TDFD
TÜRK DOĞA ve FEN DERGİSİ

TURKISH JOURNAL OF NATURE AND SCIENCE
TJNS
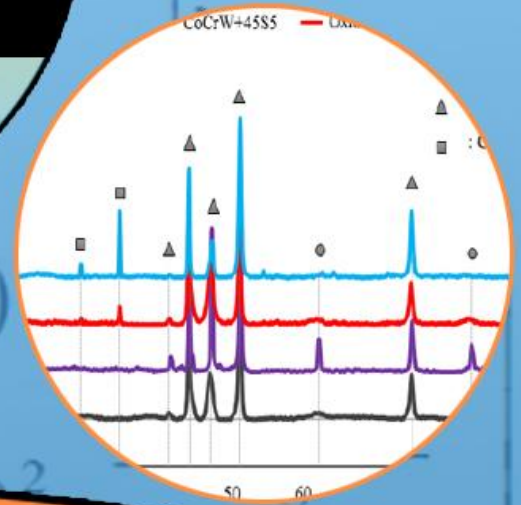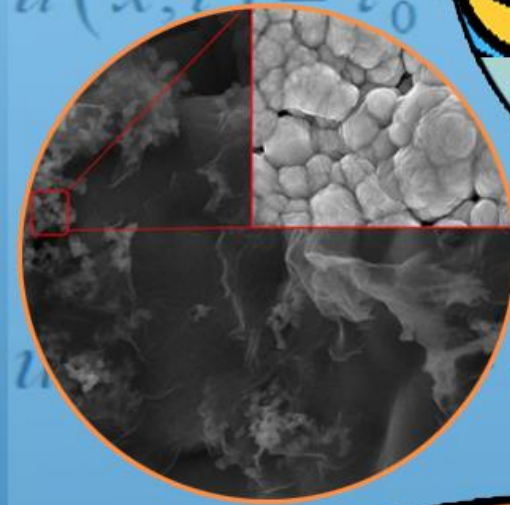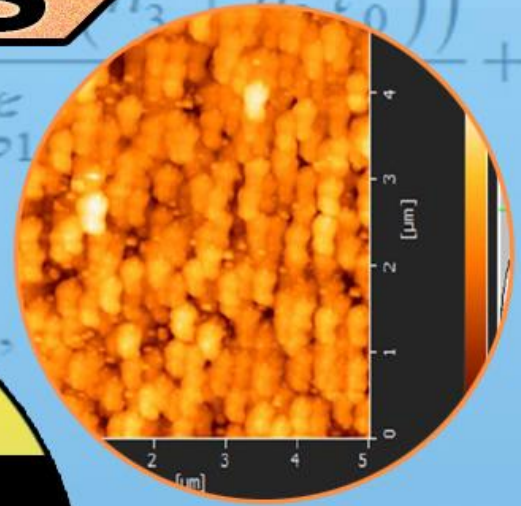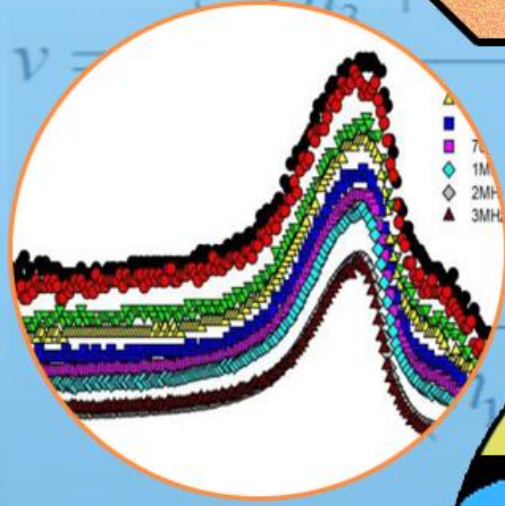
ICOLES

TÜRK DOĞA VE FEN DERGİSİ

Amaç

Türk Doğa ve Fen Dergisi, Dergipark tarafından yayınlanan Bingöl Üniversitesi Fen Bilimleri Enstitüsüne ait ulusal ve hakemli bir dergidir. Türk Doğa ve Fen Dergisi, Türkiye ve dünyanın her yerinden gelen doğa ve fen bilimlerinin her alanında özgün, yayımlanmamış, yayımlanmak üzere başka yere gönderilmemiş makale, derleme ve sempozyum değerlendirmesi gibi çalışmaların bilim alemine sunulması amacıyla kurulmuştur.

Kapsam

Türk Doğa ve Fen Dergisinde Mühendislik, Ziraat, Veterinerlik, Fen ve Doğa Bilimleri alanlarından olmak üzere Türkçe ve İngilizce hazırlanmış orijinal makale, derleme ve sempozyum değerlendirmesi gibi çalışmalar yayımlanır. Türk Doğa ve Fen Dergisi sadece online sistemde yayınlanmakta olup ayrıca kağıt baskısı bulunmamaktadır.

Merhaba…

Türk Doğa ve Fen Dergisi, Dergipark tarafından yayınlanmakta olup Bingöl Üniversitesi Fen Bilimleri Enstitüsüne aittir. Bahar ve güz dönemi olmak üzere yılda iki defa çıkarılan ulusal hakemli bir dergi olarak ilk sayısını 2012 bahar döneminde yayımlamıştır. Türk Doğa ve Fen Dergisi, Türkiye ve dünyanın her yerinden gelen doğa ve fen bilimlerinin her alanında özgün, yayımlanmamış, yayımlanmak üzere başka yere gönderilmemiş makale, derleme ve sempozyum değerlendirmesi gibi çalışmaların bilim alemine sunulması amacıyla kurulmuştur. İlk sayısından bugüne kesintisiz olarak faaliyetlerini sürdürmektedir.

Türk Doğa ve Fen Dergisi sadece online sistemde yayınlanmakta olup ayrıca kağıt baskısı bulunmamaktadır. Dergimize gelen her çalışma öncelikle Turnitin intihal programında taranmaktadır. Dergimizde editörlerin, hakemlerin ve yazarların, uluslararası yayım etik kurallarına uyması ve makalelerin yazım kurallarına uyumlu olması zorunluluğu vardır.

Yazarlar yayımlanmak üzere dergimize gönderdikleri çalışmaları ile ilgili telif haklarını zorunlu olarak Bingöl Üniversitesi Türk Doğa ve Fen Dergisi'ne devretmiş sayılırlar. Yazarlardan herhangi bir ücret talep edilmemektedir. Yazarların değerlendirmeleri, dergimizin resmi görüşü olarak kabul edilemez. Çalışmaların her türlü sorumluluğu yazarlarına aittir. Araştırma ürünleri için etik kurul raporu gerekli ise, çalışma üzerinde bu raporun alınmış olduğu belirtilmeli ve kurul raporu sisteme kaydedilmelidir. Araştırma ile ilgili intihal, atıf manipülasyonu, sahte veri uydurma vb. suistimallerin tespit edilmesi halinde yayım ve etik ilkelerine göre davranılır. Bu durumda çalışmanın yayımlanmasını önlemek, yayımdan kaldırmak ya da başka işlemler yapmak için gerekli işlemler takip edilmektedir.

Dergimizde, kaynak gösteriminde uluslararası Vancouver sistemine geçilmiştir. Ayrıca dergimiz, Creative Commons ile lisanslanmak suretiyle dergimizde yayımlanan makalelerin paylaşımı, kaynak gösterimi ve yayımlanmasında dergi ve yazar haklarını korumaya almıştır. 2018 yılı güz döneminden itibaren makaleler, uluslararası yazar kimlik numarası ORCID No'su ile yayımlanmaktadır.

Dergi ekibi, dergimizin ulusal ve uluslararası indekslerce taranan bir dergi olması yönünde çalışmalarını titizlikle sürdürmektedir. Dergimize gösterilen ilgi bu yönde bizleri teşvik etmeye devam edecektir.

Bingöl Üniversitesi Fen Bilimleri Enstitüsü tarafından yayımlanmaktadır

Türk Doğa ve Fen Dergisi
Turkish Journal of Nature and Science

İÇİNDEKİLER/CONTENTS

Electrochemical Impedance Spectroscopy Analysis of 45S5 Bioglass Coating on After Oxidation of CoCrW Alloy

Şükran Merve TÜZEMEN[1]*, **Yusuf Burak BOZKURT[1]**, **Burak ATİK[1]**, **Yakup UZUN[1]**, **Ayhan ÇELİK[1]**

[1] Atatürk University, Engineering Faculty, Machanical Engineering Department, Erzurum, Türkiye
Şükran Merve TÜZEMEN ORCID No: 0000-0003-0400-5602
Yusuf Burak BOZKURT ORCID No: 0000-0003-3859-9322
Burak ATİK ORCID No: 0000-0003-2117-9284
Yakup UZUN ORCID No: 0000-0002-5134-7640
Ayhan ÇELİK ORCID No: 0000-0002-8096-0794

Corresponding author: sukrantuzemen@atauni.edu.tr

82

Investigation of the Effect of Bioactive Glass Coating on the Corrosion Behavior of Pre-treated Ti6Al4V Alloy

Şükran Merve TÜZEMEN[1]*, **Yusuf Burak BOZKURT[1]**, **Burak ATİK[1]**, **Yakup UZUN[1]**, **Ayhan ÇELİK[1]**

[1] Atatürk University, Engineering Faculty, Machanical Engineering Department, Erzurum, Türkiye
Şükran Merve TÜZEMEN ORCID No: 0000-0003-0400-5602
Yusuf Burak BOZKURT ORCID No: 0000-0003-3859-9322
Burak ATİK ORCID No: 0000-0003-2117-9284
Yakup UZUN ORCID No: 0000-0002-5134-7640
Ayhan ÇELİK ORCID No: 0000-0002-8096-0794

Corresponding author: sukrantuzemen@atauni.edu.tr

87

On Matrix Representations of Homeomorphism Classes

Kadirhan POLAT[1]*

[1] Ağrı İbrahim Çeçen University, Faculty of Science and Letter, Department of Mathematics, Ağrı, Türkiye
Kadirhan POLAT ORCID No: 0000-0002-3460-2021

Corresponding author: kadirhanpolat@agri.edu.tr

92

Some Novel Integral Inequalities on the Co-ordinates for Geometrically Exponentially Convex Functions

Sinan ASLAN[1]*

[1] Ağrı Türk Telekom Social Sciences High School, Ağrı, Türkiye
Sinan ASLAN ORCID No: 0000-0001-5970-1926

Corresponding author: sinanaslan0407@gmail.com

96

Curves of Constant Ratio with Quasi frame in $\mathbb{E}^3$ **Rabia KALMUK[1*] (iD), Sezgin BÜYÜKKÜTÜK[2] (iD), Günay ÖZTÜRK[3] (iD)** [1] Kocaeli University, Arts and Science Faculty, Department of Mathematics, Kocaeli, Türkiye [2] Kocaeli University, Gölcük Vocational School of Higher Education, Kocaeli, Türkiye [3] İzmir Democracy University, Arts and Science Faculty, Department of Mathematics, İzmir, Türkiye Rabia KALMUK ORCID No: 0009-0009-0890-792X Sezgin BÜYÜKKÜTÜK ORCID No: 0000-0002-1845-0822 Günay ÖZTÜRK ORCID No: 0000-0002-1608-0354 *Correspondingauthor: sezgin.buyukkutuk@kocaeli.edu.tr 	**103**
Hermite-Hadamard Inequalities for a New Class of Generalized-(s,m) via Fractional Integral **Erdal GÜL[1*] (iD), Ahmet Ocak AKDEMİR[2] (iD), Abdüllatif YALÇIN[3] (iD)** [1-3] Yıldız Technical University,Faculty of Arts and Science Department of Mathematics, Istanbul, Turkey [2] Ağrı İbrahim Çeçen University, Faculty of Science and Letters, Department of Mathematics, Ağrı, Turkey Erdal GÜL ORCID No: 0000-0003-0626-0148 Ahmet Ocak AKDEMİR ORCID No: 0000-0003-2466-0508 Abdüllatif YALÇIN ORCID No: 0009-0003-1233-7540 *Corresponding author: abdullatif.yalcin@std.yildiz.edu.tr 	**109**
Characterization of a New Type of Topological Sequence Spaces and Some Properties **Gökhan MUMCU[1*] (iD), Ahmet Ocak AKDEMİR[2] (iD), Yasin ÇINAR[3] (iD)** [1] Erzincan Binali Yildirim University, Arts and Sciences Faculty, Mathematics Department, Erzincan, Türkiye [2] Agri Ibrahim Cecen University, Arts and Sciences Faculty, Mathematics Department, Agri, Türkiye [3] Batman University, Arts and Sciences Faculty, Mathematics Department, Batman, Türkiye Gökhan MUMCU ORCID No: 0000-0002-5828-1963 Ahmet Ocak AKDEMİR ORCID No: 0000-0003-2466-0508 Yasin ÇINAR ORCID No: 0009-0006-5942-2445 *Corresponding author: gokhanmumcu@outlook.com 	**116**

Türk Doğa ve Fen Dergisi
Turkish Journal of Nature and Science
www.dergipark.gov.tr/tdfd

Existence and Uniqueness Solution for a Mathematical Model with Mittag-Leffler Kernel

Mustafa Ali DOKUYUCU[1*] 🆔

[1] Ondokuz Mayıs University, Science Faculty, Mathematics Department, Samsun, Türkiye
Mustafa Ali DOKUYUCU ORCID No: 0000-0001-9331-8592

Corresponding author: mustafaalidokuyucu@gmail.com

Abstract: In this work, we analyse the fractional order West Nile Virus model involving the Atangana-Baleanu derivatives. Existence and uniqueness solutions were obtained by the fixed-point theorem. Another impressive aspect of the work is illustrated by simulations of different fractional orders by calculating the numerical solutions of the mathematical model.

Mittag-Leffler Çekirdeği ile bir Matematiksel Modelin Varlığı ve Tekliğinin Çözümü

Öz: Bu çalışmada Atangana-Baleanu türevlerini içeren kesirli dereceli Batı Nil Virüsü modelini analiz ediyoruz. Varlık ve teklik çözümleri sabit nokta teoremi ile elde edildi. Çalışmanın bir diğer etkileyici yanı ise matematiksel modelin sayısal çözümlerinin hesaplanarak farklı kesirli derecelerin simülasyonları ile ortaya konulmasıdır.

1. INTRODUCTION

Perhaps one of the most prevalent ideas in applied mathematics is the notion of a derivative. This idea was first developed to explain how quickly a particular function changes, and it was later applied to create mathematical equations that explain how situations in the actual world behave. However, the idea was updated to the idea of fractional derivatives due to the complexity of the situations in the actual world. One of the most comprehensive books on the fractional derivative was handled by I. Podlubny. Here, all fractional derivative and integral operators that have contributed to the literature are discussed in detail with all their properties [17]. Kilbas et al. have discussed the fractional derivative in a comprehensive way and the applications of the fractional derivative are also shown [11]. It quickly became apparent that the fractional derivative

notion was better suited than the local derivative for simulating real-world problems. It makes sense that many scholars have focused on creating a new definition of fractional derivative. Fractional derivative and integral have been used in many disciplines, including engineering, chemistry, physics, and others, as a result of this significant advancement [3, 4, 13]. Numerous applications made use of the Caputo fractional derivative [7]. However, due to kernel singularity, this concept has a significant flaw. We can see that this problem has been addressed by the work of Atangana and Baleanu [1], which changed the kernel. In addition, there are very important studies on the fractional derivative. For example, the stability of fractional differential equations (FDEs) whose parameters are unknown has been studied [14]. The authors [15] investigated the time and frequency domain characteristics of the circuit. Bacteria and viruses are common ways for many diseases to spread from animals to people. Carriers have

the ability to spread bacteria or viruses to others, which has the potential to cause a pandemic. The measles, sometimes called as the "Flower" pandemic, is a term used to describe the epidemic that died an estimated 5 million people between 165 and 180 AD. Between 30 and 50 million people died during the Justinian Plague (1st Plague Outbreak) in the middle of the fifth century, which was brought on by a strain of the bacterium Yersinia pestis. Throughout history, there have been numerous more outbreaks that are comparable. The Spanish flu (1918-1919), HIV/AIDS (1981present), and the yellow fever outbreak (late 1800s) are the most common causes of death among them. The number of pandemic diseases has dramatically increased in the twenty-first century. Since the early 2000s, nations, continents, and possibly the entire planet have been in danger from virus-borne epidemics including SARS, Swine flu, Ebola, and MERS. One of the most significant recent instances is the coronavirus, also known as COVID-19, which is still active today and has already claimed many lives. Throughout human history, diseases have always existed and have caused the death of people. The analysis of mathematical modeling of epidemics by fractional derivative operators has been the subject of many studies. For example, the garden equation is analyzed with both Caputo and Caputo-Fabrizio fractional derivative operators [8]. The mathematical model of the virus, named COVID-19, which has recently affected the whole world, has been analyzed in detail with the Caputo-Fabrizio fractional derivative operator, and the existence and uniqueness of its solution has been examined. Numerical solutions are also included in the study [9]. The SIQR model is solved numerically with the help of Caputo Fractional derivative operator [12].

In this study, we analyzed West Nile (WN) Virus model. Human, equine, and avian neuropathogens include the flavivirus West Nile that is spread by mosquitoes. The virus is native to Asia, Africa, Australia and Europe. Recently, it has produced significant epidemics in Israel, Romania, and Russia. The WN virus was very recently discovered in North America after being discovered there in 1999 during a meningoencephalitis pandemic in New York City. The majority of WN virus infections in humans are asymptomatic, the risk of developing severe neuroinvasive disease and dying rises with age [6].

New information regarding the dynamics and epidemiology of WNV transmission was mentioned in Hayes et al [10]. They gave the chance to do this subject investigation as well. A reaction-diffusion model was created and examined by Lewis et al [16]. for the spatial distribution of the West Nile virus. Wonham et al. [19] offered a straightforward new analytical and graphical method for calculating the essential mosquito control levels from common public health indicators. A free boundary problem with a coupled system was taken into consideration by Tarboush et al. [18] in their study of the PDE and ODE models that represent the movement of birds and mosquitoes, respectively.

2. PRELIMINARIES

Fundamental definitions relating to fractional derivatives and integral operators are to be presented in this part [1, 7, 17].

Definition 2.1 *Following is a definition of the well-known fractional order Caputo derivative [7],*

$$_a^C D_t^\varepsilon \phi(t) = \frac{1}{\Gamma(m-\varepsilon)} \int_a^t \frac{\phi^{(m)}(\rho)}{(t-\rho)^{\varepsilon+1-m}} d\rho, \qquad (1)$$

$$m-1 < \varepsilon < m \in N \quad \text{with } \emptyset \in H^1(a,b), b > a.$$

Definition 2.2 *The Riemann-Liouville (RL) fractional integral is defined as [17]:*

$$J^\varepsilon \phi(t) = \frac{1}{\Gamma(\varepsilon)} \int_a^t \phi(\rho)(t-\rho)^{\varepsilon-1} d\rho. \qquad (2)$$

Definition 2.3 *The definition of the Sobolev space of order 1 in (a,b) is [7]:*

$$H^1(a,b) = \{u \in L^2(a,b) : u' \in L^2(a,b)\}. \qquad (3)$$

Definition 2.4 *Let a function $g \in H^1(a,b)$ and $\varepsilon \in (0,1)$. The following is the definition of the AB fractional derivative in the Caputo and RL sense of order ε of g with a basis point a [1]:*

$$_a^{ABC} D_t^\varepsilon g(t) = \frac{B(\varepsilon)}{1-\varepsilon} \int_a^t g'(s) *$$
$$E_\varepsilon[\frac{\varepsilon}{1-\varepsilon}(\rho-t)^\varepsilon] d\rho, \qquad (4)$$

and

$$_a^{ABR} D_t^\varepsilon g(t) = \frac{B(\varepsilon)}{1-\varepsilon} \frac{d}{dt} \int_a^t g(\rho) *$$
$$E_\varepsilon[\frac{\varepsilon}{1-\varepsilon}(\rho-t)^\varepsilon] d\rho, \qquad (5)$$

where

$$B(\varepsilon) = 1 - \varepsilon + \frac{\varepsilon}{\Gamma(\varepsilon)},$$

Definition 2.5 *With base point a, the Atangana-Baleanu fractional integral of order ε is defined as [1]:*

$$^{AB} I_t^\varepsilon g(t) = \frac{1-\varepsilon}{B(\varepsilon)} g(t) + \frac{\varepsilon}{B(\varepsilon)\Gamma(\varepsilon)} \int_a^t g(\rho)(t-\rho)^{\varepsilon-1} d\rho.$$

2

3. THE MATHEMATICAL MODEL AND ITS DERIVATION

3.1. Classical Model

Bowman et al. [5] provided a mathematical model of the West Nile virus (WNV) in 2015. Given below is a mathematical model of how the female mosquitoes that feed on birds as intermediate hosts and disseminate the West Nile virus between humans and domestic animals.

$$\frac{dM_S(t)}{dt} = \Lambda_M - \frac{b_1\zeta_1 M_S(t)B_i(t)}{N_B(t)} - \eta_M M_S(t),$$

$$\frac{dM_i(t)}{dt} = \frac{b_1\zeta_1 M_S(t)B_i(t)}{N_B(t)} - \eta_M M_i(t),$$

$$\frac{dB_S(t)}{dt} = \Lambda_B - \frac{b_1\zeta_2 M_i(t)B_s(t)}{N_B(t)} - (\phi_B + \eta_B)B_S(t),$$

$$\frac{dB_i(t)}{dt} = \frac{b_1\zeta_2 M_i(t)B_s(t)}{N_B(t)} - (\nu_B + \phi_B + \eta_B)B_i(t),$$

$$\frac{dS(t)}{dt} = \Lambda_H - \frac{b_2\zeta_3 M_i(t)S(t)}{N_H(t)} - \eta_H S(t),$$

$$\frac{dE(t)}{dt} = \frac{b_2\zeta_3 M_i(t)S(t)}{N_H(t)} - (\gamma + \eta_H)E(t),$$

$$\frac{dI(t)}{dt} = \gamma E(t) - (\alpha + \nu_I - r + \eta_H)I(t),$$

$$\frac{dH(t)}{dt} = \alpha I(t) - (\nu_H + \mu + \eta_H)H(t),$$

$$\frac{dR(t)}{dt} = \mu H(t) + rI(t) - \eta_H R(t).$$

They fall under the first group's categories of susceptibility $S(t)$, exposure $E(t)$, infectiousness $I(t)$, hospitalization $H(t)$, and recovery $R(t)$. Alternatively, when formulated mathematically,

$$N_M(t) = M_S(t) + M_i(t), \quad N_B(t) = B_S(t) + B_i(t),$$
$$N_H(t) = S(t) + E(t) + I(t) + H(t) + R(t).$$

The recruitment rates of mosquitoes (assumed susceptible), birds (assumed susceptible), and insects (assumed susceptible) are described by the variables Λ_M, Λ_B, and Λ_H in the equation system above, respectively. The per capita rate of mosquito bites on the primary host (birds) and the per capita rate of mosquito bites on the human host are then described in b_1 and b_2, respectively. Additionally, ζ_1, ζ_2 and ζ_3 represent the likelihood that WNV will spread from an infected bird to a mosquito that is susceptible to the virus, the likelihood that WNV will spread from an infected mosquito to a bird that is susceptible to the virus, and the likelihood

that WNV will spread from mosquitoes to humans, respectively. The natural death rates for humans η_H and for animals η_M are denoted by the symbols η_M and η_H, respectively. The rate of bird migration is ϕ_B. The percentage of birds dying because of WNV is ν_B. The pace at which WNV's clinical symptoms appear is γ. The death rates of people hospitalized and those caused by the WNV are denoted by the variables ν_I and ν_H, respectively. The natural recovery rate is r, the treatment-induced recovery rate is μ, and the hospitalization rate for infectious people is α [5].

Table 1. Values of the parameters of the system (12)

Parameter	Value
γ	$[0,0.05]$
θ_2	0.03
ζ_1	0.1245
η_1	2×10^7
μ_2	0.18
β	1×10^{-9}
α	1
η_3	10
ζ_2	5
θ_3	1×10^3

3.2. Existence Solution

Using a fixed-point technique, the existence of a solution for a fractional WNV mathematical model will be investigated. The following form results when the system (7) is expressed using the ABC fractional operator:

$$_0^{ABC}\mathsf{D}_t^\varepsilon M_S(t) = \Lambda_M - \frac{b_1\zeta_1 M_S(t)B_i(t)}{N_B(t)} - \eta_M M_S(t),$$

$$_0^{ABC}\mathsf{D}_t^\varepsilon M_i(t) = \frac{b_1\zeta_1 M_S(t)B_i(t)}{N_B(t)} - \eta_M M_i(t),$$

$$_0^{ABC}\mathsf{D}_t^\varepsilon B_S(t) = \Lambda_B - \frac{b_1\zeta_2 M_i(t)B_s(t)}{N_B(t)} - (\phi_B + \eta_B)B_S(t),$$

$$_0^{ABC}\mathsf{D}_t^\varepsilon B_i(t) = \frac{b_1\zeta_2 M_i(t)B_s(t)}{N_B(t)} - (\nu_B + \phi_B + \eta_B)B_i(t),$$

$$_0^{ABC}\mathsf{D}_t^\varepsilon S(t) = \Lambda_H - \frac{b_2\zeta_3 M_i(t)S(t)}{N_H(t)} - \eta_H S(t),$$

$$_0^{ABC}\mathsf{D}_t^\varepsilon E(t) = \frac{b_2\zeta_3 M_i(t)S(t)}{N_H(t)} - (\gamma + \eta_H)E(t),$$

$$_0^{ABC}\mathsf{D}_t^\varepsilon I(t) = \gamma E(t) - (\alpha + \nu_I - r + \eta_H)I(t),$$

$$_0^{ABC}\mathsf{D}_t^\varepsilon H(t) = \alpha I(t) - (\nu_H + \mu + \eta_H)H(t),$$

$$_0^{ABC}\mathsf{D}_t^\varepsilon R(t) = \mu H(t) + rI(t) - \eta_H R(t).$$

under initial conditions that are not negative

3

$$M_{S_0}(0) = M_S(0), M_{i_0}(0) = M_i(0),$$

$$B_{i_0}(0) = B_i(0), E_0(0) = E(0), S_0(0) = S(0),$$

$$H_0(0) = H(0), I_0(0) = I(0), R_0(0) = R(0).$$

Using the definition (2.6), the system above can be expressed as follows:

$$M_S(t) - M_S(0) = \frac{1-\varepsilon}{B(\varepsilon)}\left(\Lambda_M - \frac{b_1\zeta_1 M_S(t)B_i(t)}{N_B(t)} - \eta_M M_S(t)\right)$$
$$+ \frac{\varepsilon}{B(\varepsilon)\Gamma(\varepsilon)}\int_0^t (t-y)^{(\varepsilon-1)}\left(\Lambda_M - \frac{b_1\zeta_1 M_S(y)B_i(y)}{N_B(y)} - \eta_M M_S(y)\right)dy,$$

$$M_i(t) - M_i(0) = \frac{1-\varepsilon}{B(\varepsilon)}\left(\frac{b_1\zeta_1 M_S(t)B_i(t)}{N_B(t)} - \eta_M M_i(t),\right)$$
$$+ \frac{\varepsilon}{B(\varepsilon)\Gamma(\varepsilon)}\int_0^t (t-y)^{(\varepsilon-1)}\left(\frac{b_1\zeta_1 M_S(y)B_i(y)}{N_B(y)} - \eta_M M_i(y),\right)dy,$$

$$B_S(t) - B_S(0) = \frac{1-\varepsilon}{B(\varepsilon)}\left(\Lambda_B - \frac{b_1\zeta_2 M_i(t)B_s(t)}{N_B(t)} - (\phi_B + \eta_B)B_S(t)\right)$$
$$+ \frac{\varepsilon}{B(\varepsilon)\Gamma(\varepsilon)}\int_0^t (t-y)^{(\varepsilon-1)}\left(\Lambda_B - \frac{b_1\zeta_2 M_i(y)B_s(y)}{N_B(y)} - (\phi_B + \eta_B)B_S(y)\right)dy,$$

$$B_i(t) - B_i(0) = \frac{1-\varepsilon}{B(\varepsilon)}\left(\frac{b_1\zeta_2 M_i(t)B_s(t)}{N_B(t)} - (\nu_B + \phi_B + \eta_B)B_i(t)\right)$$
$$+ \frac{\varepsilon}{B(\varepsilon)\Gamma(\varepsilon)}\int_0^t (t-y)^{(\varepsilon-1)}\left(\frac{b_1\zeta_2 M_i(y)B_s(y)}{N_B(y)} - (\nu_B + \phi_B + \eta_B)B_i(y)\right)dy,$$

$$S(t) - S(0) = \frac{1-\varepsilon}{B(\varepsilon)}\left(\Lambda_H - \frac{b_2\zeta_3 M_i(t)S(t)}{N_H(t)} - \eta_H S(t)\right)$$
$$+ \frac{\varepsilon}{B(\varepsilon)\Gamma(\varepsilon)}\int_0^t (t-y)^{(\varepsilon-1)}\left(\Lambda_H - \frac{b_2\zeta_3 M_i(y)S(y)}{N_H(y)} - \eta_H S(y)\right)dy,$$

$$E(t) - E(0) = \frac{1-\varepsilon}{B(\varepsilon)}\left(\frac{b_2\zeta_3 M_i(t)S(t)}{N_H(t)} - (\gamma + \eta_H)E(t)\right)$$
$$+ \frac{\varepsilon}{B(\varepsilon)\Gamma(\varepsilon)}\int_0^t (t-y)^{(\varepsilon-1)}\left(\frac{b_2\zeta_3 M_i(y)S(y)}{N_H(y)} - (\gamma + \eta_H)E(y)\right)dy,$$

$$I(t) - I(0) = \frac{1-\varepsilon}{B(\varepsilon)}\left(\gamma E(t) - (\alpha + \nu_I - r + \eta_H)I(t)\right)$$
$$+ \frac{\varepsilon}{B(\varepsilon)\Gamma(\varepsilon)}\int_0^t (t-y)^{(\varepsilon-1)}\left(\gamma E(y) - (\alpha + \nu_I - r + \eta_H)I(y)\right)dy,$$

$$H(t) - H(0) = \frac{1-\varepsilon}{B(\varepsilon)}\left(\alpha I(t) - (\nu_H + \mu + \eta_H)H(t)\right)$$
$$+ \frac{\varepsilon}{B(\varepsilon)\Gamma(\varepsilon)}\int_0^t (t-y)^{(\varepsilon-1)}\left(\alpha I(y) - (\nu_H + \mu + \eta_H)H(y)\right)dy,$$

$$R(t) - R(0) = \frac{1-\varepsilon}{B(\varepsilon)}\left(\mu H(t) + rI(t) - \eta_H R(t)\right)$$
$$+ \frac{\varepsilon}{B(\varepsilon)\Gamma(\varepsilon)}\int_0^t (t-y)^{(\varepsilon-1)}\left(\mu H(y) + rI(y) - \eta_H R(y)\right)dy,$$

To keep the kernels simple, one can write as follows:

4

$$M_1(t, M_S) = \Lambda_M - \frac{b_1\zeta_1 M_S(t)B_i(t)}{N_B(t)} - \eta_M M_S(t),$$

$$M_2(t, M_i) = \frac{b_1\zeta_1 M_S(t)B_i(t)}{N_B(t)} - \eta_M M_i(t),$$

$$M_3(t, B_S) = \Lambda_B - \frac{b_1\zeta_2 M_i(t)B_s(t)}{N_B(t)}$$
$$- (\phi_B + \eta_B)B_S(t),$$

$$M_4(t, B_i) = \frac{b_1\zeta_2 M_i(t)B_s(t)}{N_B(t)}$$
$$- (\nu_B + \phi_B + \eta_B)B_i(t),$$

$$M_5(t, S) = \Lambda_H - \frac{b_2\zeta_3 M_i(t)S(t)}{N_H(t)} - \eta_H S(t),$$

$$M_6(t, E) = \frac{b_2\zeta_3 M_i(t)S(t)}{N_H(t)} - (\gamma + \eta_H)E(t),$$

$$M_7(t, I) = \gamma E(t) - (\alpha + \nu_I - r + \eta_H)I(t),$$

$$M_8(t, H) = \alpha I(t) - (\nu_H + \mu + \eta_H)H(t),$$

$$M_9(t, R) = \mu H(t) + rI(t) - \eta_H R(t).$$

and

$$\Psi_1 = b_1\zeta_1 \frac{L_4}{L_{10}} + \eta_M$$

$$\Psi_2 = \eta_M$$

$$\Psi_3 = b_1\zeta_2 \frac{L_2}{L_{10}} + \phi_B + \eta_B$$

$$\Psi_4 = \nu_B + \phi_B + \eta_B$$

$$\Psi_5 = b_2\zeta_3 \frac{L_2}{L_{12}} + \eta_H$$

$$\Psi_6 = \gamma + \eta_H$$

$$\Psi_7 = \alpha + \nu_I - r + \eta_H$$

$$\Psi_8 = \nu_H + \mu + \eta_H$$

$$\Psi_9 = \eta_H$$

It is assumed that C : $M_S(t), M_i(t), B_S(t), B_i(t), S(t),$ $E(t), I(t), H(t), R(t), M_{S1}(t), M_{i1}(t), B_{S1}(t), B_{i1}(t), S_1(t),$ $E_1(t), I_1(t), H_1(t), R_1(t) \in L[0,1]$, are continuous functions, so that $\left\|M_S(t)\right\| \le L_1$, $\left\|M_i(t)\right\| \le$ L_2, $\left\|B_S(t)\right\| \le L_3$, $\left\|B_i(t)\right\| \le L_4$, $\left\|S(t)\right\| \le L_5$, $\left\|E(t)\right\| \le L_6$, $\left\|I(t)\right\| \le L_7$, $\left\|H(t)\right\| \le L_8$, $\left\|R(t)\right\| \le L_9$ respectively. Also,

$$N_B(t) = B_i(t) + B_S(t) \le L_3 + L_4 = L_{10}$$
$$N_M(t) = M_i(t) + M_S(t) \le L_1 + L_2 = L_{11}$$

Theorem 3.1 *If the assumption C is true, the kernels $M_i, i = 1,2,3,\dots,9$ satisfy the Lipschitz condition and are contraction s provided that $\Psi_i < 1$ for $(\forall \in i = 1\dots9)$*

Proof 3.1 *We now demonstrate that the Lipschitz condition is satisfied by $M_1(t, M_S)$. Let $M_S(t)$ and $M_{S_1}(t)$ be two different functions.*

$$\|M_1(t,M_S) - M_1(t,M_{S_1})\|$$
$$= \|(\Lambda_M - \frac{b_1\zeta_1 M_S B_i}{N_B} - \eta_M M_S)$$
$$- (\Lambda_M - \frac{b_1\zeta_1 M_{S_1} B_i}{N_B} - \eta_M M_{S_1})\|$$
$$\le (b_1\zeta_1 \frac{L_4}{L_{10}} + \eta_M)\|M_S - M_{S_1}\|$$
$$\le \Psi_1 \|M_S - M_{S_1}\|.$$

We demonstrate that the Lipschitz condition is satisfied by $M_2(t, M_i)$. Let's assume there are two functions, $M_i(t)$. and $M_{i_1}(t)$.

$$\|M_2(t,M_i) - M_2(t,M_{i_1})\|$$
$$= \left\|\left(\frac{b_1\zeta_1 M_S B_i}{N_B} - \eta_M M_i\right)\right.$$
$$\left. - \left(\frac{b_1\zeta_1 M_S B_i}{N_B} - \eta_M M_{i_1}\right)\right\|$$
$$\le \eta_M \|M_i - M_{i_1}\|$$
$$\le \Psi_2 \|M_i - M_{i_1}\|.$$

We demonstrate that the Lipschitz condition is satisfied by $M_3(t, B_S)$. Let's asuume there are two functions, $B_S(t)$ and $B_{S_1}(t)$.

$$\|M_3(t,B_S) - M_3(t,B_{S_1})\| = \|(\Lambda_B - \frac{b_1\zeta_2 M_i B_S}{N_B} - (\phi_B + \eta_B)B_S)$$
$$- (\Lambda_B - \frac{b_1\zeta_2 M_i B_{S_1}}{N_B} - (\phi_B + \eta_B)B_{S_1})\|$$
$$\le (b_1\zeta_2 \frac{L_2}{L_{10}} + \phi_B + \eta_B)\|B_S - B_{S_1}\|$$
$$\le \Psi_3 \|B_S - B_{S_1}\|.$$

We demonstrate that the Lipschitz condition is satisfied by $M_4(t, B_i)$. Let's asuume there are two functions, $B_i(t)$ and $B_{i_1}(t)$.

$$\|M_4(t,B_i) - M_4(t,B_{i_1})\| = \left\|\left(\frac{b_1\zeta_2 M_i B_S}{N_B} - (\nu_B + \phi_B + \eta_B)B_i\right)\right.$$
$$\left. - \left(\frac{b_1\zeta_2 M_i B_S}{N_B} - (\nu_B + \phi_B + \eta_B)B_{i_1}\right)\right\|$$
$$\le (\nu_B + \phi_B + \eta_B)\|B_i - Bi_1\|$$
$$\le \Psi_4 \|B_i - Bi_1\|.$$

We demonstrate that the Lipschitz condition is satisfied by $M_5(t, S)$. Let's asuume there are two functions, $S(t)$ and $S_1(t)$.

5

$$\|\mathsf{M}_5(t,S) - \mathsf{M}_5(t,S_1)\| \begin{aligned} &= \|(\Lambda_H - \frac{b_2\zeta_3 M_i S}{N_H} - \eta_H S) \\ &\quad - (\Lambda_H - \frac{b_2\zeta_3 M_i S_1}{N_H} - \eta_H S_1)\| \\ &\leq (b_2\zeta_3 \frac{L_2}{L_{12}} + \eta_H)\|S - S_1\| \\ &\leq \Psi_5 \|S - S_1\|. \end{aligned}$$

We demonstrate that the Lipschitz condition is satisfied by $M_6(t,E)$. Let's asuume there are two functions, $E(t)$ and $E_1(t)$.

$$\|\mathsf{M}_6(t,E) - \mathsf{M}_6(t,E_1)\| \begin{aligned} &= \|\left(\frac{b_2\zeta_3 M_i S}{N_H} - (\gamma + \eta_H)E\right) \\ &\quad - \left(\frac{b_2\zeta_3 M_i S}{N_H} - (\gamma + \eta_H)E_1\right)\| \\ &\leq (\gamma + \eta_H)\|E - E_1\| \\ &\leq \Psi_6 \|E - E_1\|. \end{aligned}$$

We demonstrate that the Lipschitz condition is satisfied by $M_7(t,I)$. Let's asuume there are two functions, $I(t)$ and $I_1(t)$.

$$\|\mathsf{M}_7(t,I) - \mathsf{M}_7(t,I_1)\| \begin{aligned} &= \|(\gamma E - (\alpha + \nu_I - r + \eta_H)I) \\ &\quad - (\gamma E - (\alpha + \nu_I - r + \eta_H)I_1)\| \\ &\leq (\alpha + \nu_I - r + \eta_H)\|I - I_1\| \\ &\leq \Psi_7 \|I - I_1\|. \end{aligned}$$

We demonstrate that the Lipschitz condition is satisfied by $M_8(t,H)$. Let's asuume there are two functions, $H(t)$ and $H_1(t)$.

$$\|\mathsf{M}_8(t,H) - \mathsf{M}_8(t,H_1)\| \begin{aligned} &= \|(\alpha I - (\nu_H + \mu + \eta_H)H) \\ &\quad - (\alpha I - (\nu_H + \mu + \eta_H)H_1)\| \\ &\leq (\nu_H + \mu + \eta_H))\|H - H_1\| \\ &\leq \Psi_8 \|H - H_1\|. \end{aligned}$$

We demonstrate that the Lipschitz condition is satisfied by $M_9(t,R)$. Let's asuume there are two functions, $R(t)$ and $R_1(t)$.

$$\|\mathsf{M}_9(t,R) - \mathsf{M}_9(t,R_1)\| \begin{aligned} &= \|(\mu H + rI - \eta_H R) \\ &\quad - (\mu H + rI - \eta_H R_1)\| \\ &\leq (\eta_H)\|R - R_1\| \\ &\leq \Psi_9 \|R - R_1\|. \end{aligned}$$

The kernels $M_i, i = 1,2,3,\dots,9$ are contractions with $\Psi_i < 1$ $I\backslash in$ $1,\dots 9$, and they satisfy the Lipschitz conditions. The proof is complete.

We rewrite the system given as follows, using the kernels $M_i, i = 1,2,3,\dots,9$ and all initial conditions being zero:

$$M_S(t) = \frac{1-\varepsilon}{B(\varepsilon)}\mathsf{M}_1(t, M_S(t)) + \frac{\varepsilon}{B(\varepsilon)\Gamma(\varepsilon)}\int_0^t (t-y)^{\varepsilon-1} \mathsf{M}_1(y, M_S(y))dy,$$

$$M_i(t) = \frac{1-\varepsilon}{B(\varepsilon)}\mathsf{M}_2(t, M_i(t)) + \frac{\varepsilon}{B(\varepsilon)\Gamma(\varepsilon)}\int_0^t (t-y)^{\varepsilon-1} \mathsf{M}_2(y, M_i(y))dy,$$

$$B_S(t) = \frac{1-\varepsilon}{B(\varepsilon)}\mathsf{M}_3(t, B_S(t)) + \frac{\varepsilon}{B(\varepsilon)\Gamma(\varepsilon)}\int_0^t (t-y)^{\varepsilon-1} \mathsf{M}_3(y, B_S(y))dy,$$

$$B_i(t) = \frac{1-\varepsilon}{B(\varepsilon)}\mathsf{M}_4(t, B_i(t)) + \frac{\varepsilon}{B(\varepsilon)\Gamma(\varepsilon)}\int_0^t (t-y)^{\varepsilon-1} \mathsf{M}_4(y, B_i(y))dy,$$

$$S(t) = \frac{1-\varepsilon}{B(\varepsilon)}\mathsf{M}_5(t, S(t)) + \frac{\varepsilon}{B(\varepsilon)\Gamma(\varepsilon)}\int_0^t (t-y)^{\varepsilon-1} \mathsf{M}_5(y, S(y))dy,$$

$$E(t) = \frac{1-\varepsilon}{B(\varepsilon)}\mathsf{M}_6(t, E(t)) + \frac{\varepsilon}{B(\varepsilon)\Gamma(\varepsilon)}\int_0^t (t-y)^{\varepsilon-1} \mathsf{M}_6(y, E(y))dy,$$

$$I(t) = \frac{1-\varepsilon}{B(\varepsilon)}\mathsf{M}_7(t, I(t)) + \frac{\varepsilon}{B(\varepsilon)\Gamma(\varepsilon)}\int_0^t (t-y)^{\varepsilon-1} \mathsf{M}_7(y, I(y))dy,$$

$$H(t) = \frac{1-\varepsilon}{B(\varepsilon)}\mathsf{M}_8(t, H(t)) + \frac{\varepsilon}{B(\varepsilon)\Gamma(\varepsilon)}\int_0^t (t-y)^{\varepsilon-1} \mathsf{M}_8(y, H(y))dy,$$

$$R(t) = \frac{1-\varepsilon}{B(\varepsilon)}\mathsf{M}_9(t, R(t)) + \frac{\varepsilon}{B(\varepsilon)\Gamma(\varepsilon)}\int_0^t (t-y)^{\varepsilon-1} \mathsf{M}_9(y, R(y))dy.$$

(10)

Next, we have the following system of equations defined via recursive formulas:

6

$$M_{S_n}(t) = \frac{1-\varepsilon}{B(\varepsilon)}\mathsf{M}_1(t, M_{S_{n-1}}(t)) + \frac{\varepsilon}{B(\varepsilon)\Gamma(\varepsilon)}\int_0^t (t-y)^{\varepsilon-1} \mathsf{M}_1(y, M_{S_{n-1}}(y))dy,$$

$$M_{i_n}(t) = \frac{1-\varepsilon}{B(\varepsilon)}\mathsf{M}_2(t, M_{i_{n-1}}(t)) + \frac{\varepsilon}{B(\varepsilon)\Gamma(\varepsilon)}\int_0^t (t-y)^{\varepsilon-1} \mathsf{M}_2(y, M_{i_{n-1}}(y))dy,$$

$$B_{S_n}(t) = \frac{1-\varepsilon}{B(\varepsilon)}\mathsf{M}_3(t, B_{S_{n-1}}(t)) + \frac{\varepsilon}{B(\varepsilon)\Gamma(\varepsilon)}\int_0^t (t-y)^{\varepsilon-1} \mathsf{M}_3(y, B_{S_{n-1}}(y))dy,$$

$$B_{i_n}(t) = \frac{1-\varepsilon}{B(\varepsilon)}\mathsf{M}_4(t, B_{i_{n-1}}(t)) + \frac{\varepsilon}{B(\varepsilon)\Gamma(\varepsilon)}\int_0^t (t-y)^{\varepsilon-1} \mathsf{M}_4(y, B_{i_{n-1}}(y))dy,$$

$$S_n(t) = \frac{1-\varepsilon}{B(\varepsilon)}\mathsf{M}_5(t, S_{n-1}(t)) + \frac{\varepsilon}{B(\varepsilon)\Gamma(\varepsilon)}\int_0^t (t-y)^{\varepsilon-1} \mathsf{M}_5(y, S_{n-1}(y))dy,$$

$$E_n(t) = \frac{1-\varepsilon}{B(\varepsilon)}\mathsf{M}_6(t, E_{n-1}(t)) + \frac{\varepsilon}{B(\varepsilon)\Gamma(\varepsilon)}\int_0^t (t-y)^{\varepsilon-1} \mathsf{M}_6(y, E_{n-1}(y))dy,$$

$$I_n(t) = \frac{1-\varepsilon}{B(\varepsilon)}\mathsf{M}_7(t, I_{n-1}(t)) + \frac{\varepsilon}{B(\varepsilon)\Gamma(\varepsilon)}\int_0^t (t-y)^{\varepsilon-1} \mathsf{M}_7(y, I_{n-1}(y))dy,$$

$$H_n(t) = \frac{1-\varepsilon}{B(\varepsilon)}\mathsf{M}_8(t, H_{n-1}(t)) + \frac{\varepsilon}{B(\varepsilon)\Gamma(\varepsilon)}\int_0^t (t-y)^{\varepsilon-1} \mathsf{M}_8(y, H_{n-1}(y))dy,$$

$$R_n(t) = \frac{1-\varepsilon}{B(\varepsilon)}\mathsf{M}_9(t, R_{n-1}(t)) + \frac{\varepsilon}{B(\varepsilon)\Gamma(\varepsilon)}\int_0^t (t-y)^{\varepsilon-1} \mathsf{M}_9(y, R_{n-1}(y))dy.$$

$$(11)$$

Additionally, each equation's difference can be expressed as follows:

$$(M_{S_{n+1}} - M_{S_n})(t) = \frac{1-\varepsilon}{B(\varepsilon)}(\mathsf{M}_1(t, M_{S_n}(t)) - \mathsf{M}_1(t, M_{S_{n-1}}(t))) + \frac{\varepsilon}{B(\varepsilon)\Gamma(\varepsilon)}\int_0^t (t-y)^{\varepsilon-1} (\mathsf{M}_1(y, M_{S_n}(y)) - \mathsf{M}_1(y, M_{S_{n-1}}(y)))dy,$$

$$(M_{i_{n+1}} - M_{i_n})(t) = \frac{1-\varepsilon}{B(\varepsilon)}(\mathsf{M}_2(t, M_{i_n}(t)) - \mathsf{M}_2(t, M_{i_{n-1}}(t))) + \frac{\varepsilon}{B(\varepsilon)\Gamma(\varepsilon)}\int_0^t (t-y)^{\varepsilon-1} (\mathsf{M}_2(t, M_{i_n}(y)) - \mathsf{M}_2(t, M_{i_{n-1}}(y)))dy,$$

$$(B_{S_{n+1}} - B_{S_n})(t) = \frac{1-\varepsilon}{B(\varepsilon)}(\mathsf{M}_3(t, B_{S_n}(t)) - \mathsf{M}_3(t, B_{S_{n-1}}(t))) + \frac{\varepsilon}{B(\varepsilon)\Gamma(\varepsilon)}\int_0^t (t-y)^{\varepsilon-1} (\mathsf{M}_3(t, B_{S_n}(y)) - \mathsf{M}_3(t, B_{S_{n-1}}(y)))dy,$$

$$(B_{i_{n+1}} - B_{i_n})(t) = \frac{1-\varepsilon}{B(\varepsilon)}(\mathsf{M}_4(t, B_{i_n}(t)) - \mathsf{M}_4(t, B_{i_{n-1}}(t))) + \frac{\varepsilon}{B(\varepsilon)\Gamma(\varepsilon)}\int_0^t (t-y)^{\varepsilon-1} (\mathsf{M}_4(y, B_{i_n}(y)) - \mathsf{M}_4(y, B_{i_{n-1}}(y)))dy,$$

$$(S_{n+1} - S_n)(t) = \frac{1-\varepsilon}{B(\varepsilon)}(\mathsf{M}_5(t, S_n(t)) - \mathsf{M}_5(t, S_{n-1}(t))) + \frac{\varepsilon}{B(\varepsilon)\Gamma(\varepsilon)}\int_0^t (t-y)^{\varepsilon-1} (\mathsf{M}_5(t, S_n(y)) - \mathsf{M}_5(t, S_{n-1}(y)))dy,$$

$$(E_{n+1} - E_n)(t) = \frac{1-\varepsilon}{B(\varepsilon)}(\mathsf{M}_6(t, E_n(t)) - \mathsf{M}_6(t, E_{n-1}(t))) + \frac{\varepsilon}{B(\varepsilon)\Gamma(\varepsilon)}\int_0^t (t-y)^{\varepsilon-1} (\mathsf{M}_6(y, E_n(y)) - \mathsf{M}_6(y, E_{n-1}(y)))dy,$$

7

$$(I_{n+1} - I_n)(t) = \frac{1-\varepsilon}{B(\varepsilon)}(M_7(t, I_n(t)) - M_7(t, I_{n-1}(t))) + \frac{\varepsilon}{B(\varepsilon)\Gamma(\varepsilon)}\int_0^t (t-y)^{\varepsilon-1}(M_7(t, I_n(y)) - M_7(t, I_{n-1}(y)))dy,$$

$$(H_{n+1} - H_n)(t) = \frac{1-\varepsilon}{B(\varepsilon)}(M_8(t, H_n(t)) - M_8(t, H_{n-1}(t))) + \frac{\varepsilon}{B(\varepsilon)\Gamma(\varepsilon)}\int_0^t (t-y)^{\varepsilon-1}(M_8(t, H_n(y)) - M_8(t, H_{n-1}(y)))dy,$$

$$(R_{n+1} - R_n)(t) = \frac{1-\varepsilon}{B(\varepsilon)}(M_9(t, R_n(t)) - M_9(t, R_{n-1}(t))) + \frac{\varepsilon}{B(\varepsilon)\Gamma(\varepsilon)}\int_0^t (t-y)^{\varepsilon-1}(M_9(t, R_n(y)) - M_9(t, R_{n-1}(y)))dy.$$

The norm of the two sides of the aforementioned equations, when taken,

$$\| (M_{S_{n+1}} - M_{S_n})(t) \| = \frac{1-\varepsilon}{B(\varepsilon)}\| (M_1(t, M_{S_n}(t)) - M_1(t, M_{S_{n-1}}(t))) \| + \frac{\varepsilon}{B(\varepsilon)\Gamma(\varepsilon)}\int_0^t (t-y)^{\varepsilon-1}\| (M_1(y, M_{S_n}(y)) - M_1(y, M_{S_{n-1}}(y))) \| dy,$$

$$\| (M_{i_{n+1}} - M_{i_n})(t) \| = \frac{1-\varepsilon}{B(\varepsilon)}\| (M_2(t, M_{i_n}(t)) - M_2(t, M_{i_{n-1}}(t))) \| + \frac{\varepsilon}{B(\varepsilon)\Gamma(\varepsilon)}\int_0^t (t-y)^{\varepsilon-1}\| (M_2(t, M_{i_n}(y)) - M_2(t, M_{i_{n-1}}(y))) \| dy,$$

$$\| (B_{S_{n+1}} - B_{S_n})(t) \| = \frac{1-\varepsilon}{B(\varepsilon)}\| (M_3(t, B_{S_n}(t)) - M_3(t, B_{S_{n-1}}(t))) \| + \frac{\varepsilon}{B(\varepsilon)\Gamma(\varepsilon)}\int_0^t (t-y)^{\varepsilon-1}\| (M_3(t, B_{S_n}(y)) - M_3(t, B_{S_{n-1}}(y))) \| dy,$$

$$\| (B_{i_{n+1}} - B_{i_n})(t) \| = \frac{1-\varepsilon}{B(\varepsilon)}\| (M_4(t, B_{i_n}(t)) - M_4(t, B_{i_{n-1}}(t))) \| + \frac{\varepsilon}{B(\varepsilon)\Gamma(\varepsilon)}\int_0^t (t-y)^{\varepsilon-1}\| (M_4(y, B_{i_n}(y)) - M_4(y, B_{i_{n-1}}(y))) \| dy,$$

$$\| (S_{n+1} - S_n)(t) \| = \frac{1-\varepsilon}{B(\varepsilon)}\| (M_5(t, S_n(t)) - M_5(t, S_{n-1}(t))) \| + \frac{\varepsilon}{B(\varepsilon)\Gamma(\varepsilon)}\int_0^t (t-y)^{\varepsilon-1}\| (M_5(t, S_n(y)) - M_5(t, S_{n-1}(y))) \| dy,$$

$$\| (E_{n+1} - E_n)(t) \| = \frac{1-\varepsilon}{B(\varepsilon)}\| (M_6(t, E_n(t)) - M_6(t, E_{n-1}(t))) \| + \frac{\varepsilon}{B(\varepsilon)\Gamma(\varepsilon)}\int_0^t (t-y)^{\varepsilon-1}\| (M_6(y, E_n(y)) - M_6(y, E_{n-1}(y))) \| dy,$$

$$\| (I_{n+1} - I_n)(t) \| = \frac{1-\varepsilon}{B(\varepsilon)}\| (M_7(t, I_n(t)) - M_7(t, I_{n-1}(t))) \| + \frac{\varepsilon}{B(\varepsilon)\Gamma(\varepsilon)}\int_0^t (t-y)^{\varepsilon-1}\| (M_7(t, I_n(y)) - M_7(t, I_{n-1}(y))) \| dy,$$

$$\| (H_{n+1} - H_n)(t) \| = \frac{1-\varepsilon}{B(\varepsilon)} \| (M_8(t, H_n(t)) - M_8(t, H_{n-1}(t))) \| + \frac{\varepsilon}{B(\varepsilon)\Gamma(\varepsilon)} \int_0^t (t-y)^{\varepsilon-1} \| (M_8(t, H_n(y)) - M_8(t, H_{n-1}(y))) \| \, dy,$$

$$\| (R_{n+1} - R_n)(t) \| = \frac{1-\varepsilon}{B(\varepsilon)} \| (M_9(t, R_n(t)) - M_9(t, R_{n-1}(t))) \| + \frac{\varepsilon}{B(\varepsilon)\Gamma(\varepsilon)} \int_0^t (t-y)^{\varepsilon-1} \| (M_9(t, R_n(y)) - M_9(t, R_{n-1}(y))) \| \, dy.$$

Theorem 3.2 *If the following inequality is reached, a solution to the West Nile Virus mathematical model (9) can be found:*

$$\Upsilon = max\{\Psi_i\} < 1, \quad i = 1,2,\ldots 9.$$

Proof 3.2 *Let us consider the following equations,*

$$K_{1n}(t) = M_{S_{n+1}}(t) - M_S(t), \qquad K_{2n}(t) = M_{i_{n+1}}(t) - M_i(t),$$

$$K_{3n}(t) = B_{S_{n+1}}(t) - B_S(t), \qquad K_{4n}(t) = B_{i_{n+1}}(t) - B_i(t),$$

$$K_{5n}(t) = S_{n+1}(t) - S(t), \qquad K_{6n}(t) = E_{n+1}(t) - E(t),$$

$$K_{7n}(t) = I_{n+1}(t) - I(t), \qquad K_{8n}(t) = H_{n+1}(t) - H(t),$$

$$K_{9n}(t) = R_{n+1}(t) - R(t).$$

We start with $K_{1n}(t)$,

$$\| K_{1n}(t) \| \le \frac{1-\varepsilon}{B(\varepsilon)} \| M_1(t, M_{S_n}(t)) - M_1(t, M_S(t) \|$$
$$+ \frac{\varepsilon}{B(\varepsilon)\Gamma(\varepsilon)} \int_0^t (t-y)^{\varepsilon-1} \| M_1(y, M_{S_n}(y)) - M_1(y, M_S(y)) \| \, dy$$
$$\le (\frac{1-\varepsilon}{B(\varepsilon)} + \frac{1}{B(\varepsilon)\Gamma(\varepsilon)}) \Psi_1 \| M_{S_n} - M_S \|$$
$$\le (\frac{1-\varepsilon}{B(\varepsilon)} + \frac{1}{B(\varepsilon)\Gamma(\varepsilon)})^n \Upsilon^n \| M_S - M_{S_1} \|.$$

$$(13)$$

Similarly,

$$\| K_{2n}(t) \| \le (\frac{1-\varepsilon}{B(\varepsilon)} + \frac{1}{B(\varepsilon)\Gamma(\varepsilon)})^n \Upsilon^n \| M_i - M_{i_1} \|,$$

$$\| K_{3n}(t) \| \le (\frac{1-\varepsilon}{B(\varepsilon)} + \frac{1}{B(\varepsilon)\Gamma(\varepsilon)})^n \Upsilon^n \| B_S - B_{S_1} \|,$$

$$\| K_{4n}(t) \| \le (\frac{1-\varepsilon}{B(\varepsilon)} + \frac{1}{B(\varepsilon)\Gamma(\varepsilon)})^n \Upsilon^n \| B_i - B_{i_1} \|,$$

$$\| K_{5n}(t) \| \le (\frac{1-\varepsilon}{B(\varepsilon)} + \frac{1}{B(\varepsilon)\Gamma(\varepsilon)})^n \Upsilon^n \| S - S_1 \|,$$

$$\| K_{6n}(t) \| \le (\frac{1-\varepsilon}{B(\varepsilon)} + \frac{1}{B(\varepsilon)\Gamma(\varepsilon)})^n \Upsilon^n \| E - E_1 \|,$$

$$\| K_{7n}(t) \| \le (\frac{1-\varepsilon}{B(\varepsilon)} + \frac{1}{B(\varepsilon)\Gamma(\varepsilon)})^n \Upsilon^n \| I - I_1 \|,$$

$$\| K_{8n}(t) \| \le (\frac{1-\varepsilon}{B(\varepsilon)} + \frac{1}{B(\varepsilon)\Gamma(\varepsilon)})^n \Upsilon^n \| H - H_1 \|,$$

$$\| K_{9n}(t) \| \le (\frac{1-\varepsilon}{B(\varepsilon)} + \frac{1}{B(\varepsilon)\Gamma(\varepsilon)})^n \Upsilon^n \| R - R_1 \|.$$

It can be found that $K_{in}(t) \to 0, i = 1,2,\ldots 9,$ as $n \to \infty$ for $\Upsilon < 1$. This completes the proof.

$$(12)$$

3.3. Uniqueness Solution

In this section, we will demonstrate the mathematical model for the West Nile Virus's uniqueness of solution.
Theorem 3.3 *In the situation where the following inequality holds true, the WNV model (9) has an unique solution:*

$$(\frac{1-\varepsilon}{B(\varepsilon)} + \frac{1}{B(\varepsilon)\Gamma(\varepsilon)}) \Psi_i \le 1, \quad i = 1,2,\ldots 9.$$

Proof 3.3 *Let us assume that the system (9) has solutions* $M_S(t), M_i(t), B_S(t), B_1(t), S(t), \ E(t), I(t), H(t), R(t)$, *as well as* $\widetilde{M_S}(t), \widetilde{M_l}(t), \widetilde{B_S}(t), \widetilde{B_l}(t), \tilde{S}(t), \tilde{E}(t), \tilde{I}(t),$ $\widetilde{H}(t), \tilde{R}(t)$. *Then, the system can also be written as,*

9

$$\tilde{M}_S(t) \quad = \frac{1-\varepsilon}{B(\varepsilon)}\mathsf{M}_1(t,\tilde{M}_S(t)) + \frac{\varepsilon}{B(\varepsilon)\Gamma(\varepsilon)}\int_0^t (t-y)^{(\varepsilon-1)}$$
$$\mathsf{M}_1(y,\tilde{M}_S(y))dy,$$

$$\tilde{M}_i(t) \quad = \frac{1-\varepsilon}{B(\varepsilon)}\mathsf{M}_2(t,\tilde{M}_i(t)) + \frac{\varepsilon}{B(\varepsilon)\Gamma(\varepsilon)}\int_0^t (t-y)^{(\varepsilon-1)}$$
$$\mathsf{M}_2(y,\tilde{M}_i(y))dy,$$

$$\tilde{B}_S(t) \quad = \frac{1-\varepsilon}{B(\varepsilon)}\mathsf{M}_3(t,\tilde{B}_S(t)) + \frac{\varepsilon}{B(\varepsilon)\Gamma(\varepsilon)}\int_0^t (t-y)^{(\varepsilon-1)}$$
$$\mathsf{M}_3(y,\tilde{B}_S(y))dy,$$

$$\tilde{B}_i(t) \quad = \frac{1-\varepsilon}{B(\varepsilon)}\mathsf{M}_4(t,\tilde{B}_i(t)) + \frac{\varepsilon}{B(\varepsilon)\Gamma(\varepsilon)}\int_0^t (t-y)^{(\varepsilon-1)}$$
$$\mathsf{M}_4(y,\tilde{B}_i(y))dy,$$

$$\tilde{S}(t) \quad = \frac{1-\varepsilon}{B(\varepsilon)}\mathsf{M}_5(t,\tilde{S}(t)) + \frac{\varepsilon}{B(\varepsilon)\Gamma(\varepsilon)}\int_0^t (t-y)^{(\varepsilon-1)}$$
$$\mathsf{M}_5(y,\tilde{S}(y))dy,$$

$$\tilde{E}(t) \quad = \frac{1-\varepsilon}{B(\varepsilon)}\mathsf{M}_6(t,\tilde{E}(t)) + \frac{\varepsilon}{B(\varepsilon)\Gamma(\varepsilon)}\int_0^t (t-y)^{(\varepsilon-1)}$$
$$\mathsf{M}_6(y,\tilde{E}(y))dy,$$

$$\tilde{I}(t) \quad = \frac{1-\varepsilon}{B(\varepsilon)}\mathsf{M}_7(t,\tilde{I}(t)) + \frac{\varepsilon}{B(\varepsilon)\Gamma(\varepsilon)}\int_0^t (t-y)^{(\varepsilon-1)}$$
$$\mathsf{M}_7(y,\tilde{I}(y))dy,$$

$$\tilde{H}(t) \quad = \frac{1-\varepsilon}{B(\varepsilon)}\mathsf{M}_8(t,\tilde{H}(t)) + \frac{\varepsilon}{B(\varepsilon)\Gamma(\varepsilon)}\int_0^t (t-y)^{(\varepsilon-1)}$$
$$\mathsf{M}_8(y,\tilde{H}(y))dy,$$

$$\tilde{R}(t) \quad = \frac{1-\varepsilon}{B(\varepsilon)}\mathsf{M}_9(t,\tilde{R}(t)) + \frac{\varepsilon}{B(\varepsilon)\Gamma(\varepsilon)}\int_0^t (t-y)^{(\varepsilon-1)}$$
$$\mathsf{M}_9(y,\tilde{R}(y))dy.$$

When the norm is determined for the two above systems of equations, first

$$\| M_S(t) - \tilde{M}_S(t) \| \quad \le \frac{1-\varepsilon}{B(\varepsilon)}\| \mathsf{M}_1(t, M_S(t)) - \mathsf{M}_1(t, \tilde{M}_S(t)) \|$$
$$+ \frac{\varepsilon}{B(\varepsilon)\Gamma(\varepsilon)}\int_0^t (t-y)^{\varepsilon-1}$$
$$\| \mathsf{M}_1(y, M_S(y)) - \mathsf{M}_1(y, \tilde{M}_S(y)) \| dy$$
$$\le \frac{1-\varepsilon}{B(\varepsilon)}\Psi_1 \| M_S - \tilde{M}_S \|$$
$$+ \frac{\Psi_1}{B(\varepsilon)\Gamma(\varepsilon)}\| M_S - \tilde{M}_S \|.$$

(15)

The following inequality can be written,

$$(\frac{1-\varepsilon}{B(\varepsilon)}\Psi_1 + \frac{\Psi_1}{B(\varepsilon)\Gamma(\varepsilon)} - 1)\| M_S - \tilde{M}_S \| \ge 0.$$

Thus, $\| M_S - \tilde{M}_S \| = 0, ise \quad M_S(t) = \tilde{M}_S(t)$ This implies
$$M_i(t) = \tilde{M}_i(t), B_S(t) = \tilde{B}_S(t), B_i(t) = \tilde{B}_i(t), S(t) = \tilde{S}(t),$$
$$E(t) = \tilde{E}(t), I(t) = \tilde{I}(t), H(t) = \tilde{H}(t), R(t) = \tilde{R}(t)$$
Thus, the model has a unique solution.

4. NUMERICAL SIMULATIONS

The Atangana-Baleanu fractional derivative [2] will be discretized using the approach for fractional differential equations in this section. The following differential equation of fractional order is first taken into consideration.
$$_0^{ABC}\mathsf{D}_t^\varepsilon x(t) = (f(t, x(t))),$$

The following equation is created when the equation (16) is arranged.

$$x(t) - x(0) = \frac{1-\varepsilon}{ABC(\varepsilon)} f(t, x(t)) + \frac{\varepsilon}{ABC(\varepsilon)\Gamma(\varepsilon)}$$
$$\int_0^t (t-\tau)^{\varepsilon-1} f(\tau, x(\tau))d\tau,$$

consequently,

$$x(t_{n+1}) - x(0) = \frac{1-\varepsilon}{ABC(\varepsilon)} f(t_n, x_n) + \frac{\varepsilon}{ABC(\varepsilon)\Gamma(\varepsilon)}$$
$$\int_0^{t_{n+1}} (t_{n+1} - t)^{\varepsilon-1} f(t, x(t))dt,$$

and at t_n

$$x(t_n) - x(0) = \frac{1-\varepsilon}{ABC(\varepsilon)} f(t_{n-1}, x_{n-1}) +$$

$$\frac{\varepsilon}{ABC(\varepsilon)\Gamma(\varepsilon)} \int_0^{t_n} (t_n - t)^{\varepsilon-1} f(t, x(t)) dt,$$

(19)

The following equation can be discovered by combining equations (18) and (19).

$$x(t_{n+1}) - x(t_n) = \frac{1-\varepsilon}{ABC(\varepsilon)} \{ f(t_n, x_n) - f(t_{n-1}, x_{n-1}) \}$$

$$+ \frac{\varepsilon}{ABC(\varepsilon)\Gamma(\varepsilon)}$$

$$\times \int_0^{t_{n+1}} (t_{n+1} - t)^{\varepsilon-1} f(t, x(t)) dt$$

$$- \frac{\varepsilon}{ABC(\varepsilon)\Gamma(\varepsilon)}$$

$$\int_0^{t_n} (t_n - t)^{\varepsilon-1} f(t, x(t)) dt$$

Thus,

$$x(t_{n+1}) - x(t_n) = \frac{1-\varepsilon}{ABC(\varepsilon)} \{ f(t_n, x_n) -$$

$$f(t_{n-1}, x_{n-1}) \} + A_{\varepsilon,1} - A_{\varepsilon,2}$$

Without loss of generality,

$$A_{\varepsilon,1} = \frac{\varepsilon f(t_n, x_n)}{ABC(\varepsilon)\Gamma(\varepsilon)h} \{ \frac{2ht_{n+1}^\varepsilon}{\varepsilon} - \frac{t_{n+1}^{\varepsilon+1}}{\varepsilon+1} \} -$$

$$\frac{\varepsilon f(t_{n-1}, x_{n-1})}{ABC(\varepsilon)\Gamma(\varepsilon)h} \{ \frac{ht_{n+1}^\varepsilon}{\varepsilon} - \frac{t_{n+1}^{\varepsilon+1}}{\varepsilon+1} \}$$

and similiarly,

$$A_{\varepsilon,2} = \frac{\varepsilon f(t_n, x_n)}{ABC(\varepsilon)\Gamma(\varepsilon)h} \{ \frac{ht_n^\varepsilon}{\varepsilon} - \frac{t_n^{\varepsilon+1}}{\varepsilon+1} \} -$$

$$\frac{f(t_{n-1}, x_{n-1})}{ABC(\varepsilon)\Gamma(\varepsilon)h}$$

As a result,

$$x_{n+1} = x_n + f(t_n, x_n)\{ \frac{1-\varepsilon}{ABC(\varepsilon)} + \frac{\varepsilon}{ABC(\varepsilon)h}$$

$$[\frac{2ht_{n+1}^\varepsilon}{\varepsilon} - \frac{t_{n+1}^{\varepsilon+1}}{\varepsilon+1}]$$

$$- \frac{\varepsilon}{ABC(\varepsilon)\Gamma(\varepsilon)h} [\frac{ht_n^\varepsilon}{\varepsilon} - \frac{t_n^{\varepsilon+1}}{\varepsilon+1}]\} + f(t_{n-1}, x_{n-1})$$

$$\times \{ \frac{\varepsilon-1}{ABC(\varepsilon)} - \frac{\varepsilon}{hABC(\varepsilon)\Gamma(\varepsilon)}$$

$$[\frac{ht_{n+1}^\varepsilon}{\varepsilon} - \frac{t_{n+1}^{\varepsilon+1}}{\varepsilon+1} + \frac{t^{\varepsilon+1}}{hABC(\varepsilon)\Gamma(\varepsilon)}]\}$$

Theorem 4.1 *Let* $x(t)$ *be a soluiton of*

$$_0^{ABC} D_t^\varepsilon x(t) = f(t, x(t)),$$

with f being continuous and bounded, the numerical solution of $x(t)$ is given as

$$x_{n+1} = x_n + f(t_n, x_n)\{ \frac{1-\varepsilon}{ABC(\varepsilon)} + \frac{\varepsilon}{ABC(\varepsilon)h}$$

$$[\frac{2ht_{n+1}^\varepsilon}{\varepsilon} - \frac{t_{n+1}^{\varepsilon+1}}{\varepsilon+1}]$$

$$- \frac{\varepsilon}{ABC(\varepsilon)\Gamma(\varepsilon)h} [\frac{ht_n^\varepsilon}{\varepsilon} - \frac{t_n^{\varepsilon+1}}{\varepsilon+1}]\} + f(t_{n-1}, x_{n-1})$$

$$\times \{ \frac{\varepsilon-1}{ABC(\varepsilon)} - \frac{\varepsilon}{hABC(\varepsilon)\Gamma(\varepsilon)}$$

$$[\frac{ht_{n+1}^\varepsilon}{\varepsilon} - \frac{t_{n+1}^{\varepsilon+1}}{\varepsilon+1} + \frac{t^{\varepsilon+1}}{hABC(\varepsilon)\Gamma(\varepsilon)}]\} + R_\varepsilon$$

where $\| R_\varepsilon \|_\infty < M$.

4.1. Numerical simulations for the model

This section presents the model's simulations. Using the method outlined in the preceding section, numerical results were obtained and graphically presented [2]. For various values of the fractional derivative, numerical results are displayed. The simulation of $M_S(t), M_i(t), B_S(t), B_i(t), S(t),$ $E(t), I(t), H(t), R(t),$ for diffeent value of ε.

11
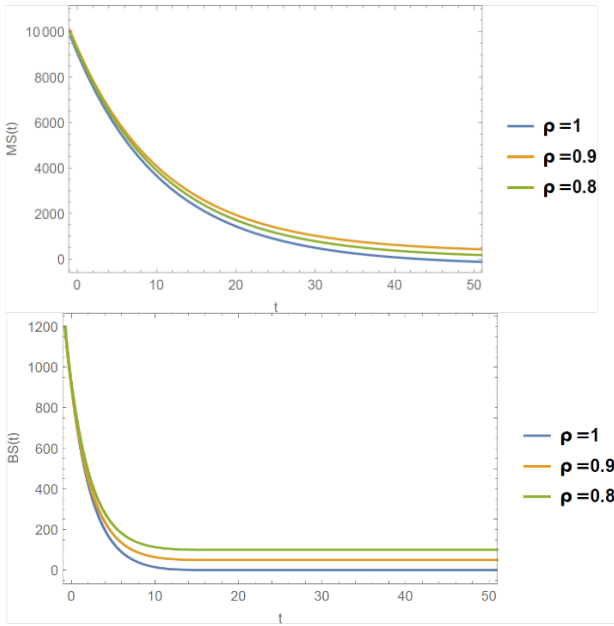
Figure 1. Simulations of the M_S and B_S function for different ε values.

In Fig.1, M_S and B_S functions are simulated. As is known, in the mathematical model, M_S and B_S represent susceptible mosquito and bird populations, respectively. It is seen that both populations decrease with time. This indicates that the susceptible population becomes infected over time. As can be expected, the suspected population in virus spreads is expected to decrease over time. The first of the important reasons for this is that a large part of the population is infected.
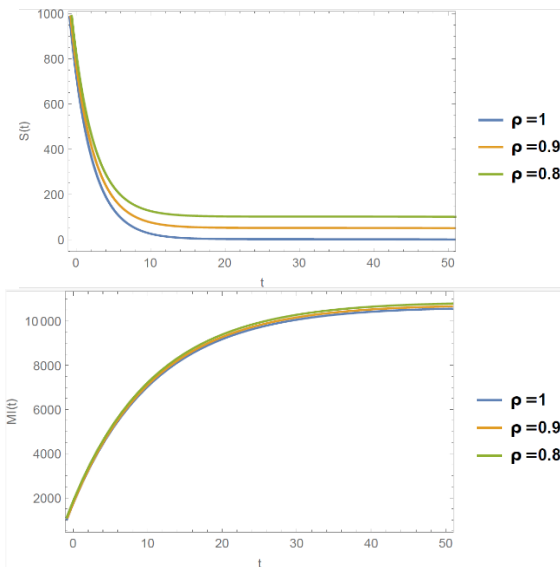
Figure 2. Simulations of the S and M_I function for different ε values.

In Fig.2, S and M_I functions are simulated. S and M_I represent susceptible human and infected mosquito populations, respectively. While the susceptible human population is decreasing over time, the infected mosquito

population is increasing. The infected mosquito population has increased over time because it has passed on the virus from an infected human or bird population. The suspected human population is also naturally declining. One of the main reasons is that they are infected.
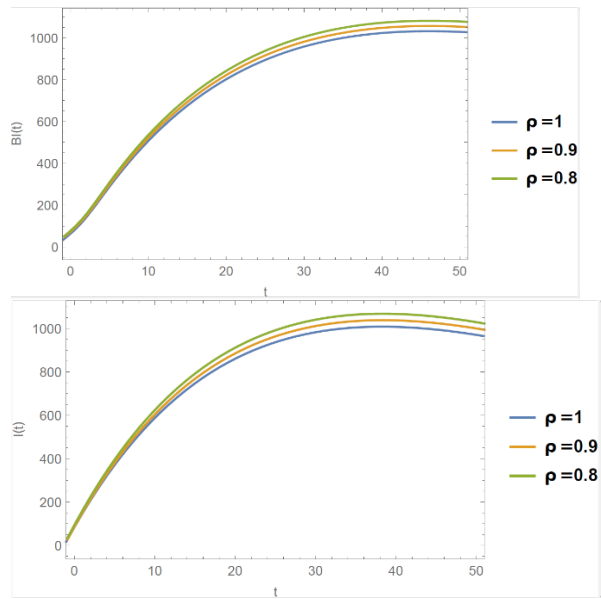
Figure 3. Simulations of the B_I and I function for different ε values.

In Fig.3, B_I and I functions are simulated. B_I and I represent susceptible infected bird populations and infectious human populations, respectively. According to the graph, it is seen that both populations have increased. Considering that the infected bird population and the virus are transmitted to humans, it is a normal situation.
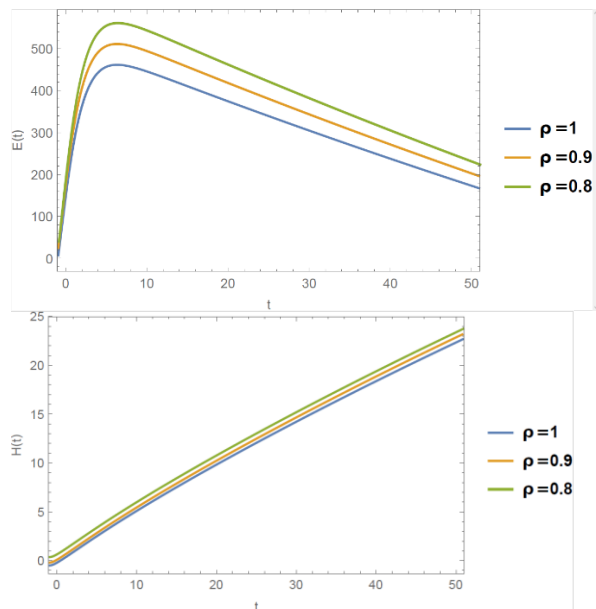
Figure 4. Simulations of the E and H function for different ε values.

In Fig.4, E and H functions are simulated. E and H represent the infected human population and the hospitalized human population, respectively. The infected human population has increased very rapidly for

12

a certain period of time and then declined after a certain time. Among the reasons for this, it can be said that the development of treatment against the virus and the discovery of a vaccine. It has been observed that the population of people treated in the hospital is constantly increasing. This clearly demonstrates the rapid spread of the virus.
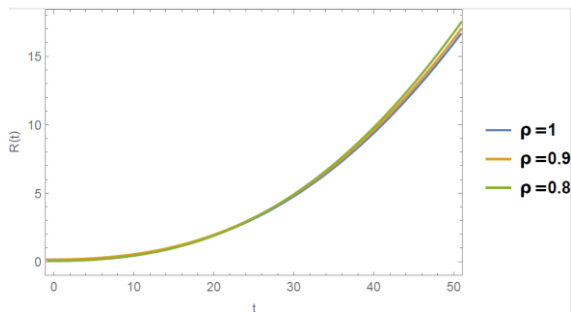
Figure 5. Simulations of the R function for different ε values.

In Fig.5, R function are simulated. R represents the recovered human population. Naturally, over time, the population of people recovering from infection is constantly increasing. This clearly shows that there is an effective treatment method against the virus

5. CONCLUSION

In this study, the West Nile Virus mathematical model was analyzed. This model is extended with the help of the Atangana-Baleanu fractional derivative operator and the existence, uniqueness and stability of its solution are analyzed. In addition, the mathematical model is solved with the Adam-Bashford numerical approach. As a result, the graphics of the mathematical model called West Nile Virus were analyzed. Three types of populations were studied in this mathematical model. These are mosquito, bird and human populations, respectively. It is easy to see how the virus affects these three populations with the help of graphs. On the other hand, the model, which was analyzed by expanding it to the Atangana-Baleanu fractional derivative, was examined for fractional derivative values of different orders. When the graphs are examined, accurate and logical results have been obtained for the fractional derivative values of different orders.
The effect of the West Nile virus affects many countries in certain periods. Even in Greece in 2022, many people were affected by this virus. If timely measures are not taken, it can cause significant damage to human metabolism and even result in death. Therefore, it is important to analyze this virus using control theory, different fractional derivative operators, and examining it with different numerical methods.

Acknowledgement

REFERENCES

[1] Atangana A, Baleanu D. New fractional derivatives with nonlocal and non-singular kernel: theory and application to heat transfer model. Thermal Science. 2016; , 20(2), 763-769.

[2] Atangana A, Owolabi KM. New numerical approach for fractional differential equations. Mathematical Modelling of Natural Phenomena. 2018;13(1):3.

[3] Bagley RL, Torvik PJ. A theoretical basis for the application of fractional calculus to viscoelasticity. Journal of Rheology. 1983 Jun 1;27(3):201-10.

[4] Bagley RL, Torvik PJ. Fractional calculus in the transient analysis of viscoelastically damped structures. AIAA journal. 1985 Jun;23(6):918-25.

[5] Bowman C, Gumel AB, Van den Driessche P, Wu J, Zhu H. A mathematical model for assessing control strategies against West Nile virus. Bulletin of mathematical biology. 2005 Sep 1;67(5):1107-33.

[6] Campbell GL, Marfin AA, Lanciotti RS, Gubler DJ. West nile virus. The Lancet infectious diseases. 2002 Sep 1;2(9):519-29.

[7] Caputo M. Linear models of dissipation whose Q is almost frequency independent—II. Geophysical Journal International. 1967 Nov 1;13(5):529-39.

[8] Dokuyucu MA. Caputo and atangana-baleanu-caputo fractional derivative applied to garden equation. Turkish Journal of Science. 2020 Mar 3;5(1):1-7.

[9] Dokuyucu M, Celik E. Analyzing a novel coronavirus model (COVID-19) in the sense of Caputo-Fabrizio fractional operator. Applied and Computational Mathematics. 2021;20(1).

[10] Hayes EB, Komar N, Nasci RS, Montgomery SP, O'Leary DR, Campbell GL. Epidemiology and transmission dynamics of West Nile virus disease. Emerging infectious diseases. 2005 Aug;11(8):1167.

[11] Kilbas AA, Srivastava HM, Trujillo JJ. Theory and applications of fractional differential equations. elsevier; 2006 Feb 16.

[12] Koca İ, Akçetin E, Yaprakdal P. Numerical approximation for the spread of SIQR model with Caputo fractional order derivative. Turkish Journal of Science. 2020;5(2):124-39.

[13] Koeller R. Applications of fractional calculus to the theory of viscoelasticity. (1984): 299-307.

[14] Koksal ME. Stability analysis of fractional differential equations with unknown parameters. Nonlinear Analysis: Modelling and Control. 2019 Feb 1;24(2):224-40.

[15] Koksal ME. Time and frequency responses of non-integer order RLC circuits. AIMS Mathematics. 2019 Jan 1;4(1):64-78.

[16] Lewis M, Rencławowicz J, den Driessche PV. Traveling waves and spread rates for a West Nile virus model. Bulletin of mathematical biology. 2006 Jan;68:3-23.

[17] Podlubny I. Fractional differential equations: an introduction to fractional derivatives, fractional differential equations, to methods of their solution

13

and some of their applications. Elsevier; 1998 Oct 27.

[18] Tarboush AK, Lin Z, Zhang M. Spreading and vanishing in a West Nile virus model with expanding fronts. Science China Mathematics. 2017 May;60:841-60.

[19] Wonham MJ, de-Camino-Beck T, Lewis MA. An epidemiological model for West Nile virus: invasion analysis and control applications. Proceedings of the royal society of London. Series B: Biological Sciences. 2004 Mar 7;271(1538):501-7.

Türk Doğa ve Fen Dergisi
Turkish Journal of Nature and Science

Investigation Of Dielectric Properties For SnO₂-PVA/n-Si Schottky Barrier Diode

Çiğdem BİLKAN[1]*

[1] Tokat Gaziosmanpaşa University, Erbaa Vocational School of Health Services, Department of Medical Services and Techniques, Tokat, Türkiye
Çiğdem BİLKAN ORCID No: 0000-0002-3347-673X

Corresponding author: cigdem.bilkan@gop.edu.tr

Abstract: The dielectric properties of SnO2-PVA nanocomposite films were examined graphically using capacitance (C) and conductivity (G/ω) data obtained over a wide frequency and voltage range at room temperature. For SnO₂-PVA/n-Si, some dielectric parameters (dielectric constants (ε', ε'') and electrical modulus (real M' and imaginary M'' parts), loss tangent (tan δ) and ac electrical conductivity (σ_{ac}) frequency and voltage dependence were calculated. As the frequency increased for each applied bias voltage, the ε', ε'' and tan δ values decreased, and it was observed that the changes in these parameters were more effective at low frequencies due to the additional loads on the interface states. While M' increases as the frequency increases due to the short-range mobility of charge carriers and has low values in the low-frequency region. The value of M'' decreases as the frequency increases due to the decrease in polarization and the density of interface states (N_{ss}) effects. While the value of electrical conductivity is almost constant at low frequencies, it increases almost exponentially at high frequencies.

SnO₂-PVA/n-Si Schottky Bariyer Diyotun Dielektrik Özelliklerinin İncelenmesi

Öz: 300 Kᵒ'de SnO₂-PVA nanokompozit filmlerin dielektrik özellikleri, geniş bir frekans ve voltaj aralığında elde edilen kapasitans (C) ve iletkenlik (G/ω) verileri kullanılarak grafiksel olarak incelenmiştir. SnO₂-PVA/n-Si için bazı dielektrik parametrelerinin (dielektrik sabitleri (ε', ε'') ve elektriksel modülüs (M' ve M''), kayıp tanjantı (tan δ) ve ac iletkenliğin hem gerçek hem de sanal kısımları (σ_{ac}), vb.), frekans ve gerilime bağımlılığı hesaplandı. Uygulanan her ön gerilim için frekans arttıkça ε', ε'' ve tan δ değerleri azalmış ve ara yüzey durumlarına gelen ilave yüklerden dolayı bu parametrelerdeki değişikliklerin düşük frekanslarda daha etkili olduğu görülmüştür. M', yük taşıyıcılarının kısa menzilli hareketliliği nedeniyle frekans arttıkça artarken, düşük frekans bölgesinde düşük değerlere sahiptir. Polarizasyon ve Ara yüzey durumların yoğunluğu (N_{ss}) etkilerinin azalması nedeniyle frekans arttıkça M'' değeri azalır. Elektriksel iletkenlik değeri düşük frekansta hemen hemen sabit iken, yüksek frekansta neredeyse katlanarak artmaktadır.

1. INTRODUCTION

Schottky barrier diodes (SBDs) are integrated circuit elements actively used in the electronics industry and technological products and have a very important place in technological developments. Many parameters affect the performance of Schottky barrier diodes, such as: preparation processes of the surfaces, interface states resulting from trap levels created by pollution atoms resulting from production, series resistance of the device, densities of the doped atoms, potential barrier in homogeneities that will occur at the interface of the two structures when contacting the metal and semiconductor, voltage and frequency applied externally to the structure, temperature of the environment where the structure is located, the existence of an polymer interlayer that separates the metal and the interface from each other and passivates the interface states that will occur [1, 2]. ε', ε'', M' and M'', tan δ, and σ_{ac} parameters are also significantly impacted by these structural parameters. Additionally, the locally active polarization mechanisms of the structure are severely affected.

Studies on the molecular orientation behaviour, relaxation, and polarization mechanisms of polymers are

currently ongoing, even though the dielectric properties of many polymers used in electronics have been investigated. One of the greatest ways is to look at dielectric loss and dielectric constant scenarios based on frequency. These computations allow for the analysis of a polymeric film's polymer structure and the voicing of opinions regarding its potential application as an interface in electrical devices.

With the implementation of a dc or ac electric field, the charges stored in the trap energy levels can be released and this can create an additional charge effect on the device [3, 4-7]. Especially, at low frequencies, for these surface states, charges can follow the ac signal. Moreover, there is less time to orient interfacial dipoles in the direction of the ac electric field [7]. This paper aims the examination of electrical and dielectric parameters of Ag/SnO$_2$-PVA/n-Si SBDs with SnO$_2$-doped PVA polymer interface layer under varying frequency and voltage at 298 K.

2. MATERIAL AND METHOD

2.1. Measurements

The fabricated structure was obtained with the use of an n-type (P-doped) single crystals silicon wafer with 300 mm thickness and 3" diameter. Wafers were cleaned in solutions of $3H_2SO_4:1H_2O_2$, 20% HF, and de-ionized water. Rectifying and ohmic contacts were deposited using Ag metal, and the back contact was annealed at 700 °C to gain the ohmic feature. SnO$_2$-PVA nanocomposite film with a thickness of 10 nm was deposited on a substrate with magnetron sputtering using a hot compacting Bi$_4$Ti$_3$O$_{12}$ powder of a stoichiometric composition as a target material.

The C-V and G/ω-V analyses of the Ag/SnO$_2$-PVA/n-Si nanocomposite structures were held at room temperature. The analyses were made between (-7) V and (+3) V and in the frequency range of 70 kHz-3 MHz using an HP 4192A LF impedance analyser (In Figure 1)

3. RESULTS

In this paper, the SnO$_2$-PVA nanostructure was fabricated, and the electrical and dielectric parameters of the structure were analysed. How electrical and dielectric properties change, especially with frequency changes (increase or decrease), has been examined graphically. The real (ε', M', tan δ, σ$_{ac}$) and imaginary (ε", M") parts of dielectric parameters were also obtained. The obtained values were examined graphically.

Four different types of polarization mechanisms are active in dielectric materials. These can be listed as follows; oriental/dipolar and interfacial polarization, atomic, electronic, or ionic [8]. Oriental/dipolar and interfacial polarizations have a large effect on dielectric properties because the dielectric constant remains almost constant at high frequencies. Interfacial polarization is very active due to the N$_{ss}$ effect when $f \leq 10^3$ Hz. In the frequency range of 10^3-10^6 Hz, dipolar and interfacial polarization

are more active because impurities and surface charges are active in this region. Atomic or ionic polarization occurs in high frequencies such as 10^{10}-10^{13} Hz. At very high frequencies such as about 10^{15} Hz, electronic polarization is especially active.
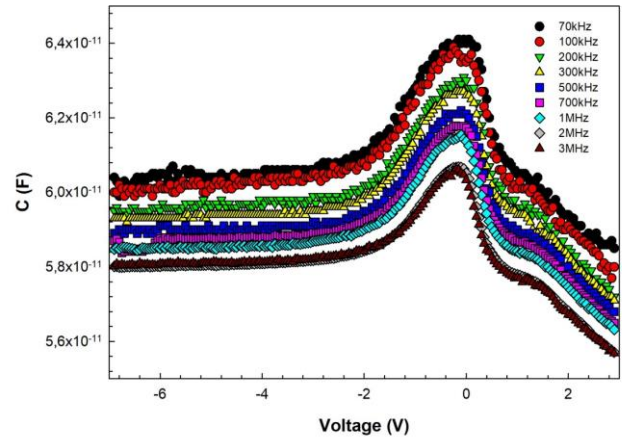
Figure 1 (a). The variation of the C-V characteristics between (-7 V)-(+3 V) of the Ag/SnO$_2$-PVA /n-Si SBDs.
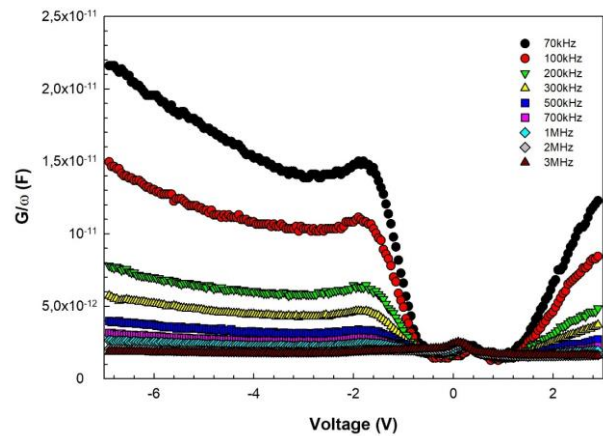
Figure 1 (b). The variation of the G/ω-V characteristics between (-7 V)-(+3 V) of the Ag/SnO$_2$-PVA /n-Si SBDs.

When a dc or ac electric field is applied, stored charges at N$_{ss}$ and trap levels may be released and create additional load on the device. For low frequencies, at the interface states, charges can follow the ac signal, and therefore the interface dipoles can orient themselves in the direction of the ac electric field in a shorter time. As a result, these charges create additional capacitance and additional conductance (C$_{ex}$ and G$_{ex}$/ω) in the measured value. With this, in the accumulation and depletion zones, investigated all parameters of the structure are high. The values of ε' and ε" were obtained from the Equations 1 and 2. The results were given in Figure 2 and 3, respectively:

$$\varepsilon' = \frac{C}{C_o} = \frac{Cd_i}{\varepsilon_o A} \tag{1}$$

$$\varepsilon'' = \frac{G}{\omega C_o} = \frac{Gd_i}{\varepsilon_o \omega A} \tag{2}$$

16

In the equations, A is the area of the diode (rectifier contact), $\varepsilon_o = 8.85 \times 10^{-12}$ F/m is the permeability of the free space charge and $C_o = \varepsilon_o A/d_i$ is the capacitance at the lowest frequency, d_i is the thickness of the intermediate polymer interface layer, ε' and ε'' components express the energies stored and lost in each cycle of the applied external electric field.

Tan δ called loss tangent value was also found by using the ε' and ε'' as in Equation 3, and the results are given in Figure 4 [8]:

$$\tan \delta = \frac{\varepsilon''}{\varepsilon'} = \frac{G}{\omega C} \qquad (3)$$
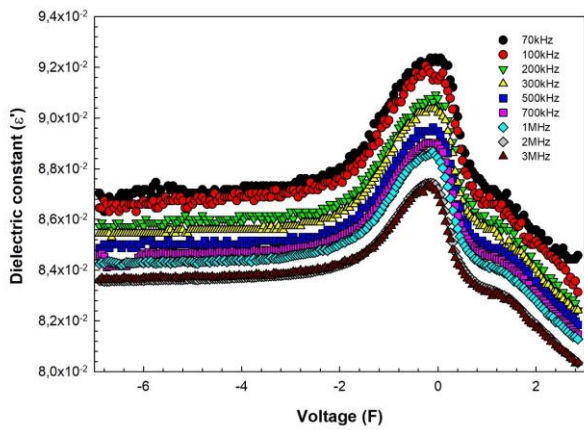
Figure 2 (a). Frequency-dependent the variation of the dielectric constant (ε') of the Ag/SnO$_2$-PVA /n-Si/Ag SBDs at room temperature.
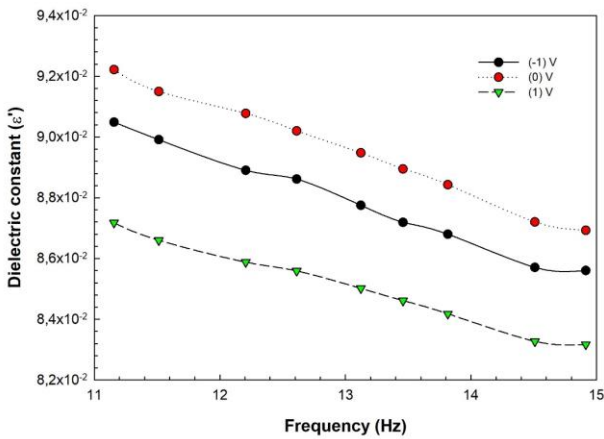
Figure 2 (b). Voltage-dependent the variation of the dielectric constant (ε') of the Ag/SnO$_2$-PVA /n-Si/Ag SBDs at room temperature.
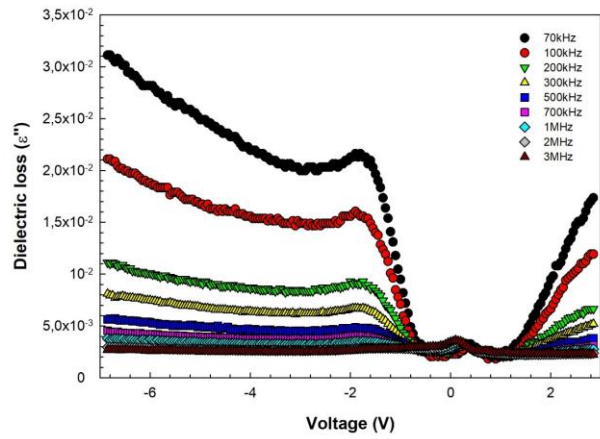
Figure 3 (a). Frequency-dependent the variation of the dielectric loss (ε'') of the Ag/SnO$_2$-PVA /n-Si SBDs at room temperature.
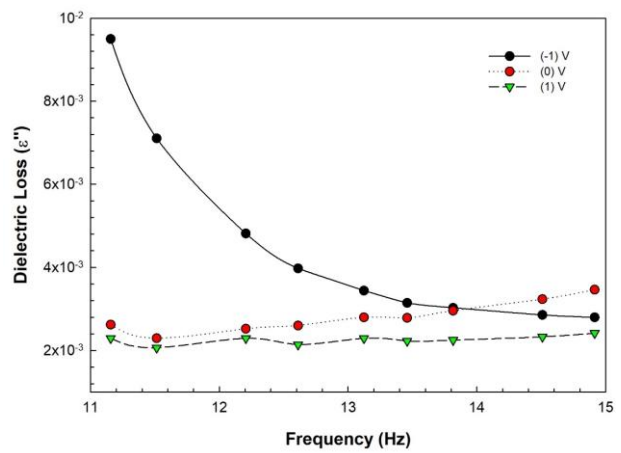
Figure 3 (b). Voltage-dependent the variation of the dielectric loss (ε'') of the Ag/SnO$_2$-PVA /n-Si SBDs at room temperature.

The fact that the parameters ε' and ε'' decrease as the frequency increases can be explained by the Debye relaxation model for the effect of dipole and interface/surface polarizations and interfacial states. For every applied bias voltage, the main dielectric parameter values ε', ε'', and tan δ have been found to decrease with increasing frequency. However, these changes are more pronounced in the depletion region, particularly at low frequencies, because of the extra carrier charges in the
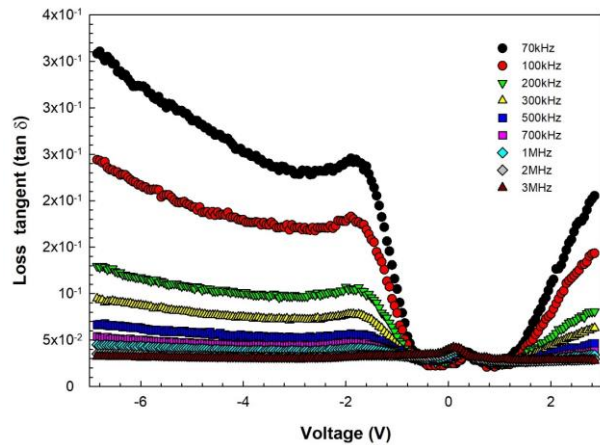
Figure 4 (a). Frequency-dependent the variation of the tan δ of the Ag/SnO$_2$-PVA /n-Si SBDs at room temperature.

17
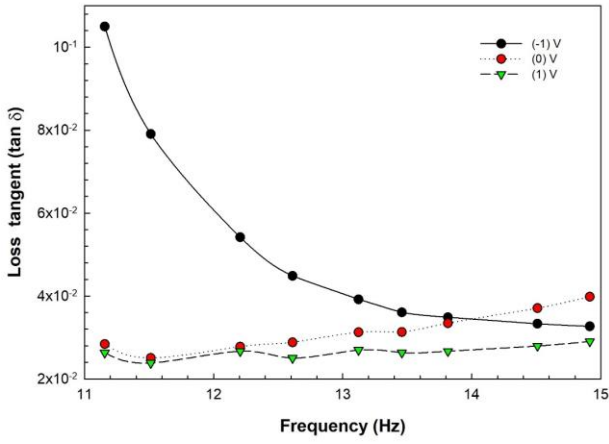
Figure 4 (b). Voltage-dependent the variation of the tan δ of the Ag/SnO$_2$-PVA /n-Si SBDs at room temperature.

surface states or traps, their relaxation times, and the polarization effect.
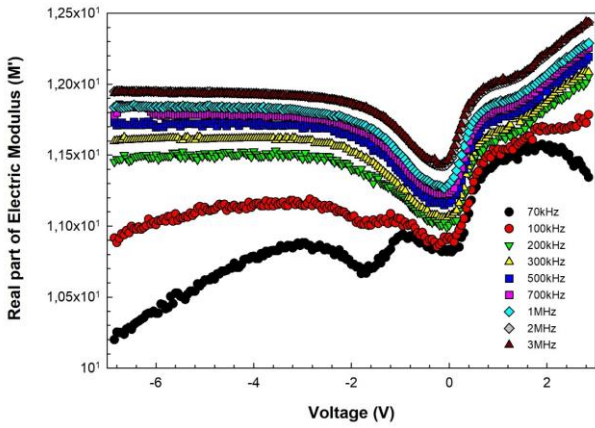
Figure 5 (a). Frequency-dependent the variation of the M' of the Ag/SnO$_2$-PVA /n-Si SBDs at room temperature.
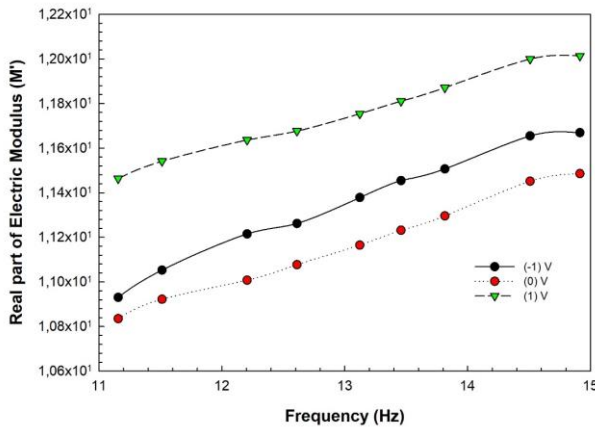
Figure 5 (b). Voltage-dependent the variation of the M' of the Ag/SnO$_2$-PVA /n-Si SBDs at room temperature.
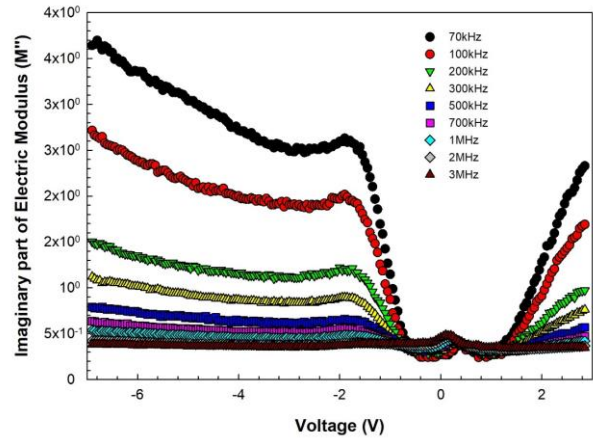
Figure 6 (a). Frequency-dependent the variation of the M" of the Ag/SnO$_2$-PVA /n-Si SBDs at room temperature.
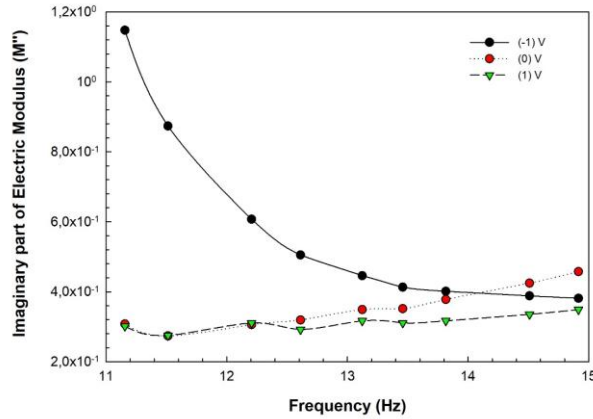
Figure 6 (b). Voltage-dependent the variation of the M" of the Ag/SnO$_2$-PVA /n-Si SBDs at room temperature.

18

Real and imaginary electric modulus M* formulas have been discussed by various authors in dielectric analysis studies of electronic materials [8]. M* expressions obtained using complex permeability (ε*=1/M*) data are shown in equations 4a and 4b.

$$M^* = M' + iM'' = \frac{\varepsilon'}{\varepsilon'^2 + \varepsilon''^2} + i\frac{\varepsilon''}{\varepsilon'^2 + \varepsilon''^2} \qquad (4)$$

Using the ε', ε", and Equation 4, M' and M" were derived and are shown in Figures 5 and 6, respectively. As we can see in Figure 5, M' values are low in the low-frequency zone but increase with frequency because of the charge carriers' short-range mobility. M" values, in contrast to M' values, fall as frequency increases. This is because as frequency rises, polarization and N$_{ss}$ effects diminish.

Dielectric relaxation is responsible for the rise in electrical modulus and dielectric properties in depletion and accumulation zones. All these characteristics decrease with increasing polarization because increasing polarization causes an increase in the number of carriers, which is proportional to the applied bias voltage [8].
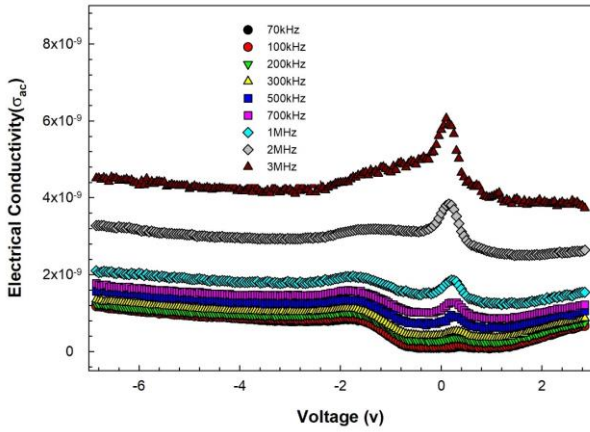
Figure 7 (a). Frequency-dependent the variation of the σ_{ac} of the Ag/SnO$_2$-PVA /n-Si SBDs at room temperature.
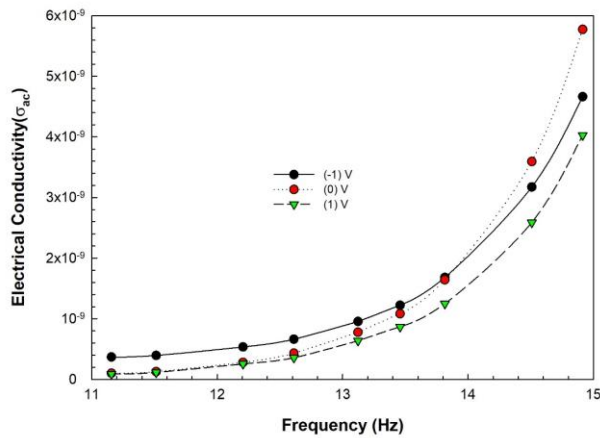
Figure 7 (b). Voltage-dependent the variation of the σ_{ac} of the Ag/SnO$_2$-PVA /n-Si SBDs at room temperature.

In order to determine the dielectric properties of the interfacial layer, the strong accumulation region is considered. In particular, in this region, the actual values of the ε'' and σ_{ac} parameters are investigated [8]. The following formulas were used to determine the diode structure's frequency- and voltage-dependent ac electrical conductivity (σ_{ac}) at room temperature. The outcomes are displayed in Figure 7:

$$\sigma_{ac} = \omega C \tan \delta (\frac{d_i}{A}) = \varepsilon'' 2\pi f \varepsilon_o = b\omega^s, \quad (1 > s > 0) \qquad (5)$$

In here, is angular frequency of the applied ac voltage, b and s are constants. Figure 7 shows σ_{ac}-V plot of the Ag/SnO$_2$-PVA /n-Si SBDs. While the value of s is almost constant at low frequencies, increases almost as exponentially and shows a peak at high frequencies which correspond to σ_{dc} and σ_{ac}, respectively.
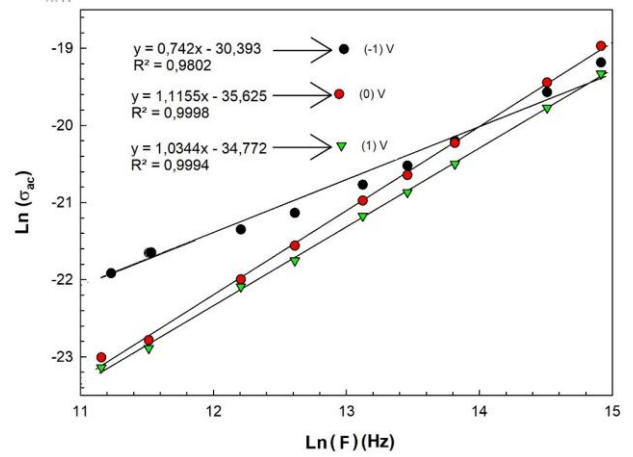
Figure 8. The Ln (σ_{ac})-Ln (F) of the Ag/SnO$_2$-PVA /n-Si SBDs at room temperature.

It is well known, that the hoping of carrier charges from one state to another state located between (SnO2-PVA) and n-Si in the forbidden band gap of the semiconductor leads to an increase in frequency-dependent ac electrical conductivity as seen in Eq. (5). To the value of s, double logarithmic ln(σ_{ac}) vs ln (f) plot was drawn for various applied bias voltage and given in Figure 8. As seen in Figure 8, the ln(σ_{ac}) vs ln (f) graph shows good linear behavior for each voltage, and its slopes (s) are found to be 0.74, 1.12, 1.03 for (-0.1V), 0V and 1V, respectively [8].

4. DISCUSSION AND CONCLUSION

19

In this study, SnO$_2$-PVA nanostructures were prepared and the electrical and dielectric properties of this structure were examined. How electrical and dielectric properties change, especially with frequency changes (increase or decrease), has been examined graphically. For interpretations, real and imaginary parts of the dielectric parameters (ε', ε'', M', M'', tan δ, and σ_{ac}, etc.) were obtained. These obtained values were examined graphically.

All obtained results confirmed that N$_{ss}$ is an important parameter in electrical and dielectric characterization processes and must be taken into consideration. It has been shown that the diode performance improves in the presence of the SnO$_2$-PVA nanocomposite interface layer and that the SnO$_2$-PVA layer can be a good alternative as a dielectric material in MPS-based devices.

Acknowledgement

REFERENCES

[1] D. Korucu, A. Turut. Temperature dependence of Schottky diode characteristics prepared with photolithography technique. International Journal of Electronics. 2014; 101:1595-1606.

[2] Ç. Bilkan, A. Gümüş, Ş. Altındal. The source of negative capacitance and anomalous peak in the forward bias capacitance-voltage in Cr/p-Si Schottky barrier diodes (SBDs). Mater Sci Semicon Proc. 2015; 39: 484-491.

[3] N. F. Mott, E. A. Dawis, Electronic Processes in Non Crystalline Materials, Clarendon Press, Oxford 1971. 437

[4] A. Kaya, S. Alialy, S. Demirezen, M. Balbaşı, S. A. Yerişkin, A. Aytimur, The investigation of dielectric properties and ac conductivity of Au/GO-doped PrBaCoO nanoceramic/n-Si capacitors using impedance spectroscopy method. Ceramics International. 2016; 42: 3322-3329.

[5] M. Mümtaz, N. A. Khan. Dielectric properties of $Cu_{0.5}Tl_{0.5}Ba_2Ca_3Cu_4O_{12}-\delta$ bulk superconductor. Physica C: Superconductivity and its Applications. 2009; 469: 728-731.

[6] S. Demirezen. Frequency-and voltage-dependent dielectric properties and electrical conductivity of Au/PVA (Bi-doped)/n-Si Schottky barrier diodes at room temperature. Appl Phys A. 2013; 112: 827-833.

[7] J. S. Lee, K. H. Choi, H. D. Ghim, S. S. Kim, D. H. Chun, H. Y. Kim, W. S. Lyoo. Role of molecular weight of atactic poly(vinyl alcohol) (PVA) in the structure and properties of PVA nanofabric prepared by electrospinning. J. Appl. Pol. Science. 2004; 93: 1638-1646

[8] Ç. Bilkan, Y. Azizian-Kalandaragh, Ş. Altındal, R. Shokrani-Havigh. Frequency and voltage dependence dielectric properties, ac electrical conductivity and electric modulus profiles in Al/Co_3O_4-PVA/p-Si structures. Physica B: Condensed Matter. 2016; 500: 154-160.

20

Türk Doğa ve Fen Dergisi
Turkish Journal of Nature and Science
www.dergipark.gov.tr/tdfd

Boric Acid Removal from Water with Alginate Based Beads and Films as Adsorbents

Kübra MOD[1] , Güler HASIRCI[2] , Nilüfer HİLMİOĞLU[3*] ,

[1] Kocaeli University, Chemical Engineering Department, Kocaeli, Türkiye
[2] Kocaeli University, Chemical Engineering Department, Kocaeli, Türkiye
[3] Kocaeli University, Chemical Engineering Department, Kocaeli, Türkiye
Kübra MOD ORCID No: 0009-0003-2103-1244
Güler HASIRCI ORCID No: 0000-0001-7435-8118
Nilüfer HİLMİOĞLU ORCID No: 0000-0002-2627-8890

*Corresponding author: niluferh@kocaeli.edu.tr

Abstract: High levels of boron cause harmful effects on humans, animals and plants. While boron is an important auxiliary nutrient for plants, excessive amounts cause toxic effects. The removal of boron in wastewater from chemical processes, industrial processes and agriculture is an important field of study. One of the most widely used methods for boron removal is adsorption method due to its low cost and ease of processing. In this study, adsorption method and sodium alginate microcapsules and sodium alginate-carbon nanotube film adsorbents were used as adsorbents for boric acid removal. In adsorption studies, sodium alginate-carbon nanotube film adsorbents with 42.11% boron removal were more efficient than sodium alginate microcapsules As a result of kinetic studies, it was found that the study was consistent with the pseudo-first order kinetic model.

Adsorban Olarak Aljinat Bazlı Küreler ve Filmler ile Sudan Borik Asit Giderimi

Öz: İnsan, hayvan ve bitkiler üzerinde borun yüksek değerlerde olması zararlı etkilere sebep olmaktadır. Bitkiler için bor önemli bir yardımcı besin iken fazla miktarda bulunması toksik etkilere yol açmaktadır. Kimyasal proseslerin, endüstriyel çalışmaların ve tarım sonucunda açığa çıkan atık suların içerisindeki borun giderilmesi önemli çalışma alanlarındandır. Borun giderilmesi için en çok kullanılan yöntemlerden biri düşük maliyet ve işlem kolaylığı sebebiyle adsorpsiyon yöntemidir. Bu çalışmada, borik asidin giderilmesi için adsorpsiyon yöntemi ve adsorban olarak sodyum aljinat mikrokapsül küreler ve sodyum aljinat-karbon nanotüp film adsorbanlar kullanılmıştır. Adsorpsiyon çalışmalarında sodyum aljinat-karbon nanotüp film adsorbanlarla, % 42.11 giderim ile sodyum aljinat mikrokapsüllerden daha verimli bor giderimi elde edilmiştir. Kinetik çalışmalar sonucunda çalışmanın yalancı birince derece kinetik model ile uyumlu olduğu bulunmuştur.

1. INTRODUCTION

Water problem is one of the biggest problems of our age. The increasing number of population, industrial zones and increasing demands, agriculture and water use are important reasons for the occurrence of water problems. In order to overcome the water problem, studies are being developed on new solutions through natural resources. For example, trying to obtain efficient clean water by separating sea water. While these and similar studies are carried out, metal products such as boron are seen in the

water obtained. In order to remove these metals from water, research is being carried out for studies that are the least harmful to nature and can achieve high efficiency. Scientists should continue these studies with the least damage to natural resources [1]. Many heavy metals are seen in wastewater as a result of chemical processes, especially in industry and agriculture. Heavy metals cause harmful effects when they penetrate into the human body or other living organisms. Boron, one of the heavy metals, is an important product for the health of humans, plants, animals and other living species. However, its high levels have a harmful effect on living things [2]. Boron, which

21

is a particularly vital supplementary food for plants, turns into a harmful effect in excessive amounts [3]. The World Health Organization (WHO) has announced the limit values for boron and set this value as 2.4 mg L^{-1} [4]. Boron has many uses. It has a wide range of uses such as hygiene materials, fire extinguishing products, medical products, personal care products, textiles, ceramics [5]. Boron does not exist alone in nature. It forms borate together with oxygen. Borax, kernite, colemanite, ulexite are borate minerals with high industrial value [6]. Although boron is a mineral found in soil and plants, it is found in high amounts only in certain countries. Turkey is the first among these countries. However, although we have high boron values, we are not ranked first in the world boron production ranking [7]. One of the compound forms of boron is boric acid. Boric acid shows weak acidic properties [8]. Boric acid is the most preferred compound among the usage areas of boron [9]. Boron removal from wastewater constitutes a wide area of study due to its high usage area. Many different techniques are used for the separation of boron from aqueous solutions. Among these methods, chemical precipitation, reverse osmosis, ion exchange and ultrafiltration are inadequate for low-value concentrations and also show high-cost characteristics. However, adsorption method, which is one of the other methods, is used more than other methods due to its ease of use and low cost [4]. Adsorption technique is the binding of multiple molecules with the ability to dissolve in different media such as gas or liquid to a solid substrate. The solid ground is the adsorbent and the substance adhering to the ground is the adsorbate. The reverse of the adsorption process is called desorption process. There are many parameters to be considered in the adsorption process such as concentration, pH, temperature, time. But one of the most important parameters is the type of adsorbent selected. Selecting the most suitable adsorbent is important to increase the efficiency of the study. When selecting the adsorbent, attention should be paid to the fact that adsorption should be at high values, it should be affordable and adsorption should take place quickly [9]. In this study, experiments were carried out separate adsorbents were used: sodium alginate beads and sodium alginate-carbon nanotube films. The adsorption study using sodium alginate microcapsules was aimed to be made more efficient by adding carbon nanotube.

Alginate obtained from algae contains mannuronic acid and guluronic acid. The reason for using sodium alginate microcapsules is that sodium alginate is a biopolymer and an environmentally friendly adsorbent. Studies in the field of nanotechnology also contribute to improving the properties of materials. Buckyballs" (spherical molecules) are formed by bonding carbon atoms in clusters of 60. When a certain number of cobalt or nickel atoms are added to the buckyballs, their form changes and they become chemically stable "nanotubes" with a wall thickness of one nanometer. Carbon nanotubes (CNTs) are characterized by their weightlessness, high stretch coefficient and being the most resistant fiber. Many studies have been carried out to obtain carbon nanotube synthesis and as a result, certain methods have emerged. These methods are carbon nanotubes obtained by synthesizing from solid carbon and gaseous carbon. Apart from these methods, other synthesis methods are being

tried for different carbon nanotubes to be obtained with different environments [10]. The carbon nanotube used in the study was preferred as an adsorbent due to the free available void spaces on its surface, its use in the literature as a good adsorbent in aqueous solutions and its low cost [11].

2. MATERIAL AND METHOD

2.1. Material

The solutions used for boron adsorption experiments in our study were obtained with boric acid (H3BO3) distilled water. Sodium alginate and carbon nanotubes were used to obtain adsorbents. CaCl$_2$ was used as cross-linker of alginate. The pH of the solutions we used during the experiment was adjusted with the help of NaOH and HCl. NaOH, D-mannitol, a few drops of phenolphthalein were added to determine the boric acid concentration by titration. Figure 1. shows the titrator used for boron adsorption and the prepared solutions.

Figure 1. Titrator used for the titration process in the study, solution prepared for boron determination (left), titrated boron solution (right).

2.2. Preparation of Alginate Microcapsule Beads

Sodium alginate was weighed and added to 100 ml, resulting in a 5% solution. The sodium alginate solution was dropped into the 0.05 M CaCl$_2$ solution for crosslinking. It was left in a magnetic stirrer overnight to complete the crosslinking reaction. After the mixing of the microcapsules was completed, they were passed through distilled water to remove CaCl$_2$. The resulting sodium alginate microcapsules were allowed to dry at room temperature. Figure 2. shows the final form of sodium alginate microcapsules.

Figure 2. Sodium alginate microcapsule beads

2.3. Preparation Of Sodium Alginate-Carbon Nanotube Films

To make boric acid adsorption more efficient, sodium alginate was mixed with carbon nanotubes. During the construction of sodium alginate-carbon nanotube film adsorbents, 0,7 g carbon nanotubes were added to 2% sodium alginate solution of the amount of sodium. The sodium alginate-carbon nanotube mixture was kept in a magnetic stirrer overnight. The resulting mixed solution was dropped into 0,01 M $CaCl_2$ for crosslinking. The sodium alginate-carbon nanotube film adsorbents were washed with distilled water to remove $CaCl_2$ and allowed to dry at an oven for a short time. Figure 3. shows the final sodium alginate-carbon nanotube film adsorbents.

Figure 3. Sodium alginate-carbon nanotube film particles

2.4. Boric Acid Determination

Since it is weakly acidic in boric acid solutions, it cannot be directly titrated with base solution. For this reason, mannitol or glycerin should be added to the solution before titration to convert boric acid into a strong monovalent acid form [13]. In our study, a stock solution was prepared for boric acid and solutions at other concentrations were obtained by diluting the stock solution. The stock solution of boron was obtained by

measuring 5.730 g of boric acid ($H3BO3$) and completing it with pure water. Stock solution concentration is 1000 mg L^{-1}. Boric acid concentration was titrated with 0.1 N NaOH by adding 1 mL boric acid solution, D-mannitol and 1-2 drops of phenolphthalein indicator until a color change occurred.

2.5. pH Effect on Boric Acid Adsorption

HCl and NaOH solutions were used to adjust the pH value of boric acid solution in adsorption studies. One of the most important parameters for boric acid solution to provide more efficient results is the pH value. Boron ions have the ability to transform into different ionic structures at various pH values. Boron removal is due to the pH-controllable tetrahydroxyborate and $B(OH)_3$ structures of boric acid. $B(OH)_3$ is rarely observed as OH- and tetrahydroxyborate at low pH values. Therefore, for low pH, boron removal occurs at lower trace fractions due to the lower affinity of $B(OH)_3$ [12].

2.6. Boron Removal in the Literature

Table 1. Literature studies on boron removal.

ADSORBENT	WORKING CONDITIONS	YIELD	REFERENCE
EGGSHELL MEMBRANE (ESM)	For adsorption results, values in the range of Ph 2-10 were analyzed. Adsorption reached high values at 35°C. Modified eggshell membrane (MESM) was also used as an adsorbent in the study. Concentration increase was seen as an important parameter.	According to the adsorption results, the highest value is 96.96% at pH 8.	[1]
ALGINATE BEADS	The adsorption study was carried out at the lowest pH 3 and the highest pH 12, and at temperatures of 20 °C and 35 °C.	50% boron adsorption was obtained.	[14]
ZIF-67	The experiment was carried out at pH 4 and temperature 25 °C, ZIF-67, boron concentration value is 0.5 mol L^{-1}.	As a result of the study, a high value of 579.80 mg g^{-1} was reached.	[15]

23

ZIF-8	Adsorption study was carried out at 45°C, lowest pH 2 and highest pH 12.	191 mg g^{-1} is the highest value found in the study.	[16]
3,4-DIHYDROXY BENZALDEHYDE-MODIFIED CHITOSAN	The boric acid concentration used in the study was 400 mg L^{-1}, pH 9.0 for DMAK and pH 5.0 for MEK. It was observed that the adsorption capacity increased with temperature and decreased with increasing temperature for MEK.	The adsorption capacity of the modified chitosan was obtained as 36.77 mg g^{-1}. This result is about 4 times higher than the boron adsorption capacity of unmodified chitosan (9.3 mg g^{-1}).	[17]
ACTIVATED CARBON	The most efficient adsorption was observed at pH 8.5. For the experiments, 0.5 g adsorbent amount was used, 30 mg B (dm³)$^{-1}$ boron concentration was carried out with 0.025 or 0.05 dm3 boron solution.	Activated carbon modified with Filtrasorb 400 (F400) has a high adsorption capacity with 51.3% removal efficiency and 0.319 mg g^{-1} adsorption capacity.	[18]
CARBON NANOTUBE IMPROVED WITH TARTARIC ACID	The highest values were obtained at pH 6. The ideal adsorbent amount was determined as 0.4 g L^{-1}. Adsorption studies were performed at concentrations of 20 mg L^{-1}.	As a result of the study, an adsorption capacity of 1.97 mg g^{-1} was obtained.	[19]

2.7. Adsorption Studies for Sodium Alginate Beads and Sodium Alginate-Carbon Nanotube Film Adsorbents

Adsorption studies were carried out with two different adsorbent microcapsules obtained with 2% sodium alginate adsorbent microcapsules and 10% carbon nanotubes added to 2% sodium alginate.
In the adsorption studies for boric acid removal with the obtained adsorbent microcapsules, Equation 1 (q) was used to calculate the adsorption percentage and Equation 2 was used to obtain the adsorption capacity [9].

$$qe = ((Co - Ce)/m)xV \qquad (1)$$

C_0 (mg L^{-1}) indicates the initial concentration for boric acid, C_e (mg L^{-1}) indicates the equilibrium concentration, q (mg g^{-1}) indicates the adsorption capacity, m (g) indicates the amount of adsorbent and V (L) indicates the solution volume.

Adsorption removal % was calculated from Equation 2 [9].

$$(\%) = ((C_0 - C_e)/C_0) \times 100 \qquad (2)$$

2.8. Adsorption Kinetic Studies for Sodium Alginate Beads and Sodium Alginate-Carbon Nanotube Film Adsorbents

Kinetic models were calculated for sodium alginate microcapsules and sodium alginate-carbon nanotube film adsorbents. Calculations for the pseudo-first-order kinetic model were obtained with the equation used by Lagergren in Equation 3., and the pseudo-second-order kinetic model was obtained with the equation shown in Equation 4 [9].

$$\log(q_e - q_t) = \log(q_e) - (k_1/2.3030)t \qquad (3)$$

q_e: Amount of adsorbed substance per gram of adsorbent at equilibrium (mg g^{-1}), q_t: Amount of adsorbed substance per gram of adsorbent at any time t (mg g^{-1}), t: Time (h), k_1: pseudo-first-order kinetic constant (h^{-1}).
The pseudo-quadratic kinetic equation is calculated using equation 4 [9].

$$t/q_t = 1/(k_2 q e^2) + t/q_e \qquad (4)$$

q_e: Adsorption capacity at equilibrium (mg g^{-1}), q_t: Adsorption capacity at time (mg g^{-1}), k_2: Pseudo second order kinetic constant (g.mg^{-1} h^{-1}), t: Time (h).

3. RESULTS

3.1. Adsorption Results for Sodium Alginate Microcapsule Beads

In line with the results, as seen in Figure 4., the highest efficient adsorption capacity q was obtained as 54 mg g^{-1} at the 24th hour. According to the data obtained as seen in Figure 5., 31.58% removal was calculated in the adsorption using sodium alginate microcapsules. Looking at Figure 4., it can be seen that adsorption did not occur in the first hour, but adsorption occurred from the 2nd hour. The highest expenditure was observed in the 23rd and 24th hours.
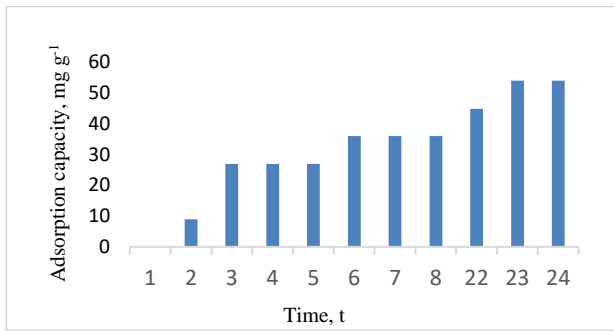
Figure 4. Adsorption capacity of sodium alginate microcapsules (experimental conditions: initial boron concentration: 1000 mg/L, adsorbent dose: 0.36 g pH: 9.66).
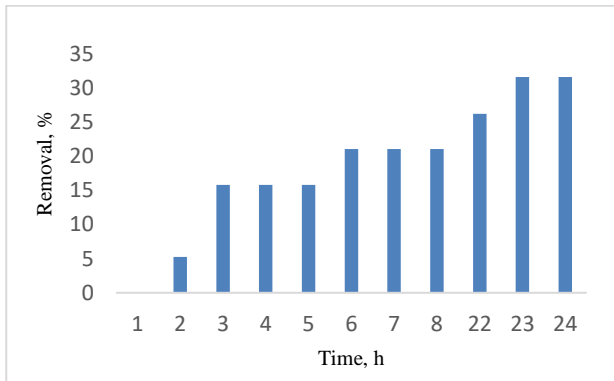
Figure 5. Boron removal % of sodium alginate microcapsules (experimental conditions: initial boron concentration: 1000 mg/L, adsorbent dose: 0.36 g pH: 9.66).

3.2. Adsorption Kinetics for Sodium Alginate Microcapsule Beads

The relationship of adsorption study with kinetic models is discussed. The graphs of the pseudo-first-order kinetic model are given in Figure 6., and the graphs of the pseudo-second-order model are given in Figure 7. It can be seen that the R^2 value of the pseudo-first order model is higher. For this reason, sodium alginate beads were found to be more suitable for the pseudo-first-order kinetic model among the two models.
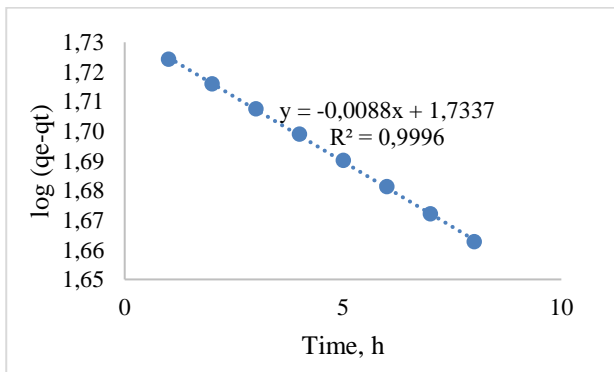
Figure 6. Pseudo-first-order kinetic model for sodium alginate microcapsule beads. Experimental conditions: 1000 mg L^{-1} concentration, 0.36 g adsorbent dosage, pH 9.66.
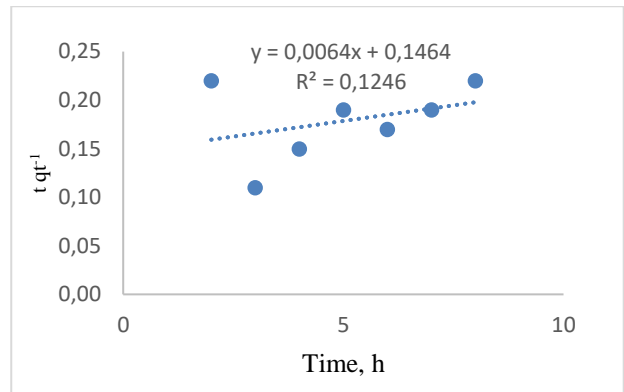
Figure 7. Pseudo- second order kinetic model for sodium alginate beads. Experimental conditions: 1000 mg L^{-1} concentration, 0.36 g adsorbent dosage, pH 9.66.

3.3. Adsorption Results of Sodium Alginate-Carbon Nanotube Film Adsorbents

As a result of the studies, it was observed that sodium alginate-carbon nanotube films reached high adsorption values. Figure 8. shows the results of adsorption capacity for sodium alginate-carbon nanotube films, and Figure 9. shows the adsorption percentage obtained. It was observed that adsorption progressed slowly in the first hours but reached the maximum value at the 23rd hour. A more effective adsorption result was obtained compared to adsorption with sodium alginate microcapsule beads.
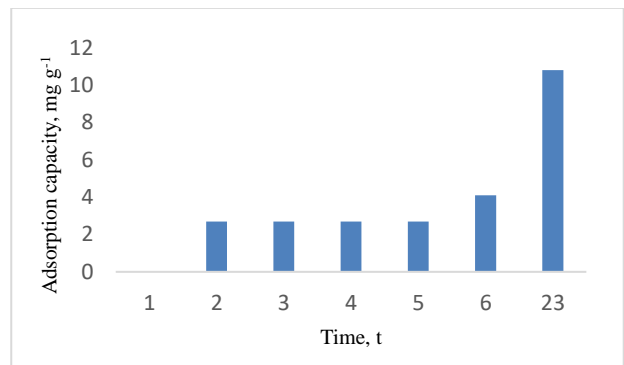
Figure 8. Adsorption capacity of sodium alginate-carbon nanotube film adsorbents (experimental conditions: initial boron concentration: 1000 mg/L, adsorbent dose: 0.36 g pH: 9.66 carbon nanotube amount: 0.7 g).
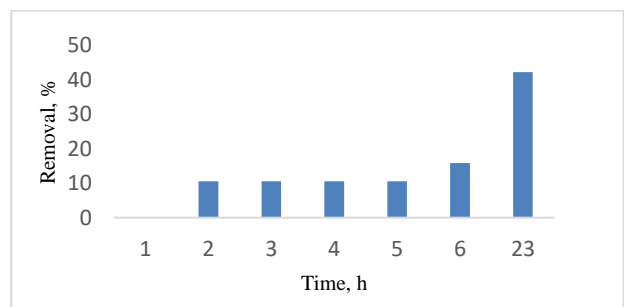
Figure 9. Boron removal % of sodium alginate-carbon nanotube film adsorbents (experimental conditions: initial boron concentration: 1000 mg/L, adsorbent dose: 0.36 g pH: 9.66 carbon nanotube amount: 0.7 g).

3.4. Adsorption Kinetics for Sodium Alginate-Carbon Nanotube Film Adsorbents

The fit of sodium alginate-carbon nanotube microcapsules with boric acid adsorption kinetic models was examined. Looking at Figure 10. and Figure 11. for the pseudo-models, it was observed that the adsorption kinetics of sodium alginate-carbon nanotube films were in agreement with the pseudo-first order kinetic model, because the pseudo-first order model that has a high R^2 value.
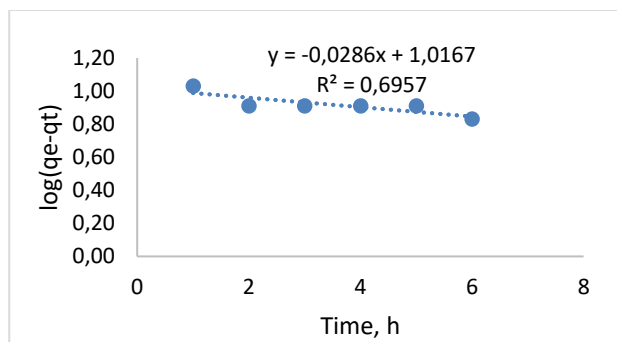
Figure 10. Pseudo-first-order kinetic model for sodium alginate /CNT film adsorbents. Experimental conditions: 1000 mg L^{-1} concentration, 0.36 g adsorbent dosage, pH 9.66, carbon nanotube amount: 0.7 g.
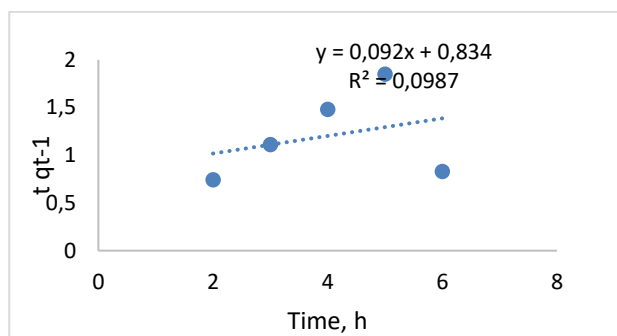
Figure 11. Pseudo-second-order kinetic model for sodium alginate /CNT film adsorbents. Experimental conditions: 1000 mg L^{-1} concentration, 0.36 g adsorbent dosage, pH 9.66, carbon nanotube amount: 0.7 g.

3.5. Comparison Of Sodium Alginate Beads And Sodium Alginate-Carbon Nanotube Films

The adsorption study showed that sodium alginate-carbon nanotube films reached higher values than sodium alginate microcapsules. As can be seen in Figure 12., 42% removal was achieved in 23 hours in adsorption with sodium alginate-carbon nanotube films. The chemical, thermal and moisture stability and large pore structures of carbon nanotube adsorbents are effective in providing efficient results. Figure 13. shows that sodium alginate microcapsules have higher q values than sodium alginate-carbon nanotube microcapsules. The reason for this is that the sodium alginate content in sodium alginate microcapsules is 5% and the sodium alginate content in sodium alginate-carbon nanotube films is 2% [11]. As a result of this study, all the results obtained with sodium alginate beads and sodium alginate-carbon nanotube films adsorbent are shown in Table 2.
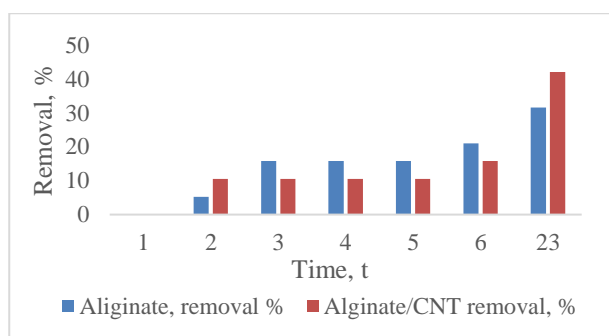
Figure 12. Comparison of adsorption removal % of sodium alginate microcapsules and sodium alginate-carbon nanotube film adsorbents (experimental conditions: initial boron concentration: 1000 mg/L, adsorbent dose: 0.36 g pH: 9.66 carbon nanotube amount: 0.7 g).
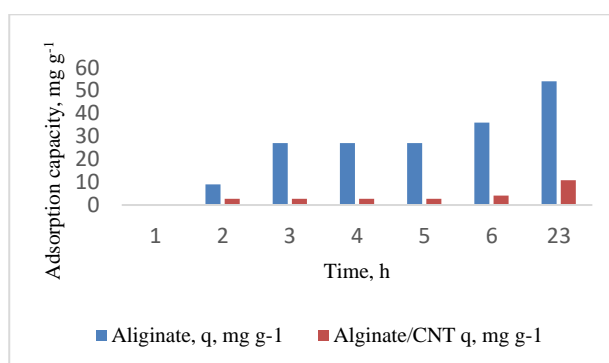
Figure 13. Comparison of adsorption capacities of sodium alginate microcapsules and sodium alginate-carbon nanotube film adsorbents (experimental conditions: initial boron concentration: 1000 mg/L, adsorbent dose: 0.36 g pH: 9.66 carbon nanotube amount: 0.7 g).

Table 2. Adsorption results for sodium alginate microcapsule beads and sodium alginate-carbon nanotube film adsorbents.

	Adsorption Removal (%)	Adsorption Capacity (mg/g)	Pseudo first order kinetic model data
Sodium Alginate Microcapsule Beads	31.58	54	k_1 : 0,02026 h^{-1} R^2 : 0.9996 $q_{e\ teorical}$: 54,16 $q_{e\ texperimental}$: 54
Sodium Alginate-Carbon Nanotube Film Adsorbents	42.11	10.8	k_1: 0, 0658 h^{-1} R^2 : 0.6957 $q_{e\ teorical}$: 10,39 $q_{e\ texperimental}$: 10,8

4. DISCUSSION AND CONCLUSION

This study is quite different from our previous adsorption studies [20, 21]. It is also seen in the literature that boron adsorption that has the low removal value is a difficult type of adsorption that takes a very long time. In our study, boric acid removal from water was studied with the help of two adsorbents. Sodium alginate microcapsule beads and sodium alginate-carbon nanotube film adsorbents were used to remove boric acid from water. As a result of the sodium alginate microcapsules and sodium alginate-carbon nanotube film adsorbents used in the study, more efficient results were obtained with adsorption studies with the adsorbent obtained by adding carbon nanotube. Maximum adsorption efficiency of 42% and adsorption capacity of 10.8 mg g^{-1} were obtained using sodium alginate-carbon nanotube film adsorbents. As a result of the kinetic studies for sodium alginate-carbon nanotube film adsorbents, the pseudo-first order kinetic model was found to be appropriate. The importance of ambient conditions for boric acid removal from water has drawn attention. It was concluded that higher pH values have better absorption results in boron removal and as the pH value of the boric acid solution increases, boron removal increases. In conclusion, compared to the studies in the literature, pH value is an important parameter for boron removal and the percentage of boron removal obtained by using sodium alginate-carbon nanotube film adsorbent is similar to the results in the literature. Sodium alginate and carbon nano tube are suitable adsorbent candidates for the removal of boron from aqueous media as they are environmentally friendly materials since alginate is a biopolymer and carbon nanotube provides high adsorption values.

Acknowledgement

REFERENCES

[1] Al-Ghouti MA, Khan M. Eggshell membrane as a novel bio sorbent for remediation of boron from desalinated water. Journal of Environmental Management. 2018;207:405–16.

[2] Gök O, Mesutoğlu ÖÇ. Ağır metallerin giderimi için düşük maliyetli adsorban olarak pirina kullanımı. Journal Of The Faculty Of Engineering And Architecture Of Gazi University. 2017;32(2):507-516.

[3] Bolaños L, Lukaszewski K, Bonilla I, Blevins D. Why boron?. Plant Physiology and Biochemistry. 2004;42:907-912.

[4] Meydan E. Boron compounds with magnetic properties and their applicatıon areas in industry. Journal of Scientific Perspectives. 2019;3(1):11-20.

[5] Bertagnolli C, Grishin A, Vincent T, Guibal E. Boron removal by a composite sorbent: Polyethylenimine/tannic acid derivative immobilized in alginate hydrogel beads. Journal of Environmental Science and Health. 2017;52(4):359-367.

[6] Çakal GÖY. Dynamic behavior of continuous flow stirred slurry reactors in boric acid production. Ankara: Middle East Technical University; 2004.

[7] Yılmaz EA. Endüstriyel atıksulardan elektrokoagülasyon yöntemi ile bor giderimi. Erzurum: Atatürk Üniversitesi; 2009.

[8] Şahin İ. Voltammetrik yöntemlerle bor tayini ve uygulamaları. Balıkesir: Balıkesir Üniversitesi; 2007.

[9] Aslan K. Borik asitin derişik sulu çözeltilerinden modifiye aktif karbon ve aljinat bazlı adsorbanlar ile giderilmesi. Isparta: Süleyman Demirel Üniversitesi; 2020.

[10] Küçükyıldırım BO, Eker AA. Karbon nanotüpler, sentezleme yöntemleri ve kullanım alanları. TMMOB MMO Mühendis ve Makina Dergisi. 2012;53(630): 34-44.

[11] Li Y, Sui K, Liu R, Zhao X, Zhang Y, Liang H, et al. Removal of methyl orange from aqueous solution by calcium alginate/multi-walled carbon nanotubes composite fibers. Energy Procedia. 2012;16:863-868.

[12] Bhagyaraj S, Al-Ghouti MA, Kasak P, Krupa I. An updated review on boron removal from water through adsorption processes. Emergent Materials. 2021;4: 1167–1186.

[13] Sarı M. Değişik minerallerin borik asit çözeltilerinde çözünme kinetiği. İstanbul: İstanbul Teknik Üniversitesi; 2008.

[14] Demey H, Barron-Zambrano J, Mhadhbi T, Miloudi H, Yang Z, Ruiz M, et al. Boron removal from aqueous solutions by using a novel alginate-based sorbent: comparison with al2o3 particles. Polymers. 2019;11(9):1509.

[15] Zhang J, Cai Y, Liu K. Extremely effective boron removal from water by stable metal organic framework zif-67. Industrial & Engineering Chemistry Research. 2019;58:4199-4207.

[16] Lyu J, Zhang N, Liu H, Zeng Z, Zhang J, Bai P, et al. Adsorptive removal of boron by zeolitic imidazolate framework: kinetics, isotherms, thermodynamics, mechanism and recycling. Separation and Purification Technology. 2017;187:67–75.

[17] Dilber Keyis. 3,4 dihidroksi benzaldehit ile modifiye edilmiş kitosan'ın hazırlanması ve sulu ortamlardan bor adsorpsiyon özelliklerinin araştırılması. Aksaray: Aksaray Üniversitesi; 2020.

[18] Kluczka J, Pudlo W, Krukiewicz K. Boron adsorption removal by commercial andmodified activated

carbons. Chemical Engineering Research and Design. 2019;147:30-42.

[19] Zohdi N, Mahdavi F, Abdullah LC, Choong TSY. Removal of boron from aqueous solution using magnetic carbon nanotube improved with tartaric acid. Journal of Environmental Health Sciences & Engineering. 2014;1–12.

[20] Oktor, K., Hilmioglu, N. Removal of ammonium from aqueous solutions by adsorption processes using environment friendly natural biopolymer chıtosan. Fresenius environmental bulletin.2021; 30: 1970-1976.

[21] Oktor, K., Yuzer, N. Y., Hasirci, G., Hilmioglu, N. . Optimization of Removal of Phosphate from Water by Adsorption Using Biopolymer Chitosan Beads. Water, Air, and Soil Pollution. 2023; 234: 271: 1-14.

Türk Doğa ve Fen Dergisi
Turkish Journal of Nature and Science
www.dergipark.gov.tr/tdfd

Performance Analysis of Span Data Type in C# Programming Language

Hakan AKDOĞAN[1*] iD , **Halil İbrahim DUYMAZ[1]** iD , **Nadir KOCAKIR[1]** iD , **Önder KARADEMİR[1]** iD

[1*] Özdilek Ev Tekstil San. ve Tic. AŞ, Özveri Ar-Ge Merkezi, Bursa, Türkiye
Hakan AKDOĞAN ORCID No: 0009-0000-5067-268X
Halil İbrahim DUYMAZ ORCID No: 0009-0005-8406-8831
Nadir KOCAKIR ORCID No: 0000-0001-7421-0631
Önder KARADEMİR ORCID No: 0000-0001-5757-7335

Corresponding author: hakan.akdogan@ozdilek.com.tr

Abstract: This study presents a comparative analysis of the Span data type in the C# programming language against other data types. Span is a data type supported in .NET Core 2.1 and later versions, and this research investigates its impact on method performance and memory usage. The primary objective of the study is to highlight the potential advantages of the Span data type for C# developers. In pursuit of this goal, the study examines the performance effects of the Span data type through comparative analyses using various methods. For instance, when comparing the StringReplace and SpanReplace methods over 1000 iterations, it is observed that SpanReplace is significantly faster. Similarly, analyses conducted on methods like Contains used in data types such as Queue, List, and Stack demonstrate the performance advantages of the Span data type. In scenarios where the Span data type is employed, it is determined that memory consumption is lower compared to other data types. These findings can assist C# programmers in understanding the potential of the Span data type and optimizing their code accordingly. The Span data type may be a more effective option, especially in data processing and performance-sensitive applications.

C# Programlama Dilinde Span Veri Türünün Performans Analizi

Öz: Bu çalışma, C# programlama dilindeki Span veri tipinin diğer veri tipleriyle karşılaştırmalı analizini sunmaktadır. Span, .NET Core 2.1 ve sonrasında desteklenen bir veri tipidir ve bu araştırma, bu veri tipinin metot performansı ve bellek kullanımı üzerindeki etkilerini araştırmaktadır. Çalışmanın temel amacı, C# geliştiricilerine Span veri tipinin potansiyel avantajlarını vurgulamaktır. Bu amaç doğrultusunda, çeşitli metotlar kullanılarak yapılan karşılaştırmalı analizlerle Span veri tipinin performans üzerindeki etkileri incelenmiştir. Örneğin, StringReplace ile SpanReplace metotları 1000 iterasyonda karşılaştırıldığında, SpanReplace'in önemli ölçüde daha hızlı olduğu görülmüştür. Benzer şekilde, Queue, List, Stack gibi veri tiplerinde kullanılan Contains metodu üzerinde yapılan analizler de Span veri tipinin performans avantajlarını göstermiştir. Span veri tipinin kullanıldığı senaryolarda, bellek tüketiminin diğer veri tiplerine göre daha düşük olduğu belirlenmiştir. Bu bulgular, C# programcıları için Span veri tipinin potansiyelini anlamalarına ve kodlarını optimize etmelerine yardımcı olabilir. Span veri tipi, özellikle veri işleme ve performans hassas uygulamalarda daha etkili bir seçenek olabilir.

1. INTRODUCTION

The ever-evolving landscape of programming languages demands a continual exploration of novel features and data types to enhance code efficiency and application performance. In this context, the present study conducts a comprehensive comparative analysis focusing on the Span data type within the C# programming language, contrasting its attributes against other prevalent data types. Span, introduced and supported in .NET Core 2.1 and subsequent versions, emerges as a key subject of investigation. This research delves into the intricate dynamics of the Span data type, aiming to discern its influence on method performance and memory utilization.

The primary objective of this study is to elucidate the latent advantages that the Span data type offers to developers immersed in the C# programming paradigm. To achieve this goal, the research employs a systematic approach, scrutinizing the performance implications of the Span data type through meticulous comparative analyses leveraging various methods.
Furthermore, the study extends its inquiry to encompass analyses of methods such as Contains, Slice, SubString, StartsWith and Replace commonly employed in data types like String, Queue, List, and Stack. The outcomes of these analyses consistently underscore the performance advantages inherent in the utilization of the Span data type. Notably, in scenarios where the Span data type finds application, discernible reductions in memory consumption are identified in contrast to other data types.

The findings of this investigation bear substantial implications for C# programmers, providing valuable insights into the untapped potential of the Span data type. Armed with this knowledge, developers can make informed decisions in optimizing their code to harness the advantages offered by the Span data type. Consequently, the Span data type emerges as a promising and more effective option, particularly in domains that demand enhanced data processing capabilities and cater to performance-sensitive applications.

2. LITERATURE REVIEW

Code effiency and application performance has been a topic of growing interest in the field of software engineering. This literature review aims to provide a comprehensive overview of existing studies, methodologies, and advancements.

The study titled "Performance Characterization of .NET Benchmarks," conducted by Deshmukh et al. [1], published in IEEE in 2021, investigates hardware performance bottlenecks in .NET applications. Employing Principal Component Analysis (PCA) and hierarchical clustering on open-source .NET and ASP.NET benchmarks, the research reveals that these applications possess distinct characteristics compared to traditional SPEC-like programs. Consequently, this dissimilarity underscores the need for consideration in architectural research. The study highlights that .NET benchmarks exhibit a significantly higher front-end dependency and analyzes the effects of managed runtime events, such as Garbage Collection (GC) and Just-in-Time (JIT) compilation.

The article titled Measuring Performance Improvements in .NET Core with BenchmarkDotNet by Almada [2], investigates the performance implications of value-type versus reference-type enumerators in C#. The author begins by highlighting how the C# compiler generates different code for the 'foreach' keyword based on the type of the collection. The critical distinction lies in whether the GetEnumerator() method returns a value type or a reference type enumerator, which significantly impacts collection iteration performance. Reference-type enumerators, associated with classes and interfaces, involve virtual calls and heap allocations, potentially affecting performance. On the other hand, value-type enumerators, exemplified by collections like List<T>, demonstrate improved performance, especially for large collections, and avoid heap allocations. The article includes benchmarking using BenchmarkDotNet, comparing the performance of iterating a List<int> when cast to IEnumerable<int> (reference-type enumerator) versus using List<int> directly (value-type enumerator).

The results indicate substantial performance differences, with value-type enumerators outperforming their reference-type counterparts. The article concludes by emphasizing the importance of considering the implications of virtual calls, recommending the use of value-type enumerators for better performance in collection iteration, and encouraging the adoption of immutable collections to avoid casting to interfaces. The benchmarks conducted on various .NET versions highlight performance improvements, providing additional motivation for transitioning to the latest versions. This insight contributes valuable considerations for developers seeking to optimize collection iteration performance in C#.

The research paper by Usman et al. [3], the authors conduct a performance analysis of searching algorithms in C#. The study focuses on evaluating the efficiency of various searching algorithms, including linear search, binary search, and brute force search, measured in terms of time complexity. The algorithms are implemented in the C family of compilers, including C#, and their performance is assessed on different machines using a sample file. The analysis considers the execution time of searching algorithms, with variations observed based on different systems and file sizes.

The results suggest that linear search exhibits better time complexity, while brute force search excels in finding all search patterns. The paper emphasizes the significance of efficient searching in programming, highlighting its importance for system throughput and efficiency. Experimental works include the development of a C# program incorporating the mentioned algorithms and a detailed examination of their performance on machines

with varying processing power. The authors conclude by discussing the implications of their findings and propose future work involving the implementation of these techniques on other compilers and exploring space complexity considerations.

Shastri et al. [4], offer a comprehensive examination of various searching and hashing algorithms, shedding light on their efficiencies in terms of time complexity. The study delves into five distinct algorithms, namely Linear Search, Binary Search, Interpolation Search, Division Method Hashing, and Mid Square Method Hashing. Through rigorous experimentation and analysis, the authors demonstrate the performance of these algorithms using Visual Studio C#. They meticulously evaluate the run-time of each algorithm across different input sizes, ranging from 10,000 to 100,000 elements, and highlight the advantages and disadvantages of each. Notably, the findings reveal that Binary Search consistently outperforms other algorithms, showcasing its superiority, particularly for large datasets. This insightful exploration contributes valuable insights to the field of algorithm analysis and aids in understanding the optimal choices for various search and hash functions in real-world applications.

Arif et al. [5], provide an empirical analysis of C#, PHP, JAVA, JSP, and ASP.Net with a focus on performance analysis based on CPU utilization. The paper underscores the significance of software development within the context of computer systems, emphasizing the need for enhanced speed and reliability in modern digital systems. Through extensive research, the authors explore the impact of different programming languages on computer performance and resource utilization, with a particular emphasis on CPU usage. Their investigation involves the development of a software application using these languages, focusing on factors such as algorithm quality, programming language selection, and SQL query optimization. The findings suggest that JAVA/JSP exhibit superior performance compared to other languages in terms of CPU usage, memory utilization, and execution time, providing valuable insights for developers and software architects aiming to optimize system performance.

Sestoft [6], explores the comparative numeric performance of C, C#, and Java across various small-scale computational tasks. While managed languages like C# and Java offer ease of use and safety, their performance in numeric computations, especially involving arrays or matrices of floating-point numbers, is comparatively inferior to that of traditional languages like C and C++. This performance gap arises due to differences in compiler optimization strategies, array access overheads, and the need for index checks in managed languages, which can incur additional execution overhead and hardware slowdowns. However, the study demonstrates that with careful optimization techniques, such as employing unsafe code in C# or leveraging high-performance virtual machines in Java, it's possible to narrow this performance gap, showcasing

the nuances and trade-offs in numeric computation across these languages.

This study presents a comparative analysis of the Span data type, supported in .NET Core 2.1 and later versions, within the context of other data types in the C# programming language. While existing literature has analyzed various aspects of .NET applications, including hardware performance bottlenecks, C# collection iteration performance, the efficiency of different search algorithms, and the impact of programming languages on CPU usage, this work specifically focuses on the effects of the Span data type on method performance and memory utilization, adding a new dimension to the discourse. Previous studies have primarily concentrated on performance comparisons of specific algorithms, programming languages, or .NET versions. In contrast, this study examines the direct impacts of utilizing the Span data type in terms of method performance and memory usage, aiming to highlight its potential advantages for C# developers. By comparatively analyzing the performance differences in specific methods such as StringReplace and SpanReplace, and the effects on memory consumption in data types (Queue, List, Stack) when methods like Contains are used, this work demonstrates that the Span data type can be a more effective option for applications with high performance sensitivity and data processing requirements. Therefore, this study significantly contributes to the existing literature by revealing the potential that the Span data type, introduced in newer versions of .NET Core, offers for code optimization within the C# programming paradigm, using academic language.

3. MATERIAL AND METHOD

3.1. Span Data Type

The methodology employed in this research revolves around a comprehensive investigation of the Span data type in C#, introduced in version 7.2 and supported in .NET Core 2.1 and subsequent releases. The primary objective of the Span data type is to efficiently handle data in memory and expedite processing procedures, making it an ideal choice for operations involving substantial datasets.

The robust aspects and limitations of the Span data type are categorized under specific headings, facilitating a more straightforward interpretation of the data collected in the study.

3.1.1. Memory management and performance

The study is focused on how Span is designed to optimize memory usage and enhance processing speed in .NET applications. Traditional collection structures often maintain data on the heap, leading to unnecessary RAM occupation and increased Garbage Collector workload. Span, however, stores data pointers on the Stack. The Stack, typically limited to around 4 MB per application, provides faster access compared to the heap. Given these considerations, the Stack offers significantly faster

access than the heap. Therefore, the ability of Span to keep data on the stack enables swift operations.

In Figure 1, the utilization of stack and heap memory for the String data type is illustrated.
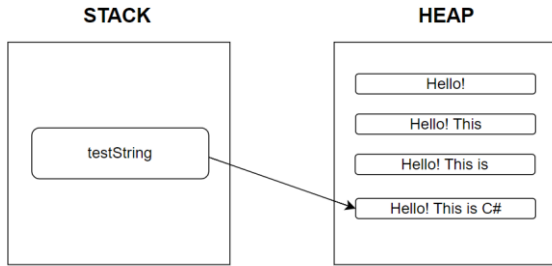
Figure 1. The way string uses stack and heap memories [7]

In Figure 2, the utilization of stack memory by the Span data type is illustrated.
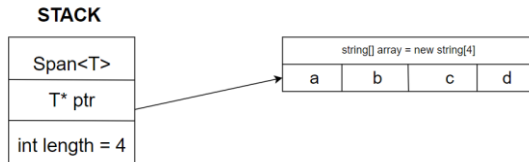
Figure 2. The way span use stack memory [8]

3.1.2. Reduced memory footprint

Span allows the usage of data on the stack without memory allocation by pointing to it. This is particularly advantageous in operations such as data copying, slicing, and sorting. Unlike traditional collections that produce new objects for such operations, Span directly accesses existing data through pointers stored on the stack. This prevents unnecessary memory allocations, contributing to more efficient application performance.

3.1.3. Memory efficiency

The study highlights the significant advantages of Span in terms of memory efficiency. For instance, when working with a string, traditional substring methods create new references in memory for each extracted portion, leading to excessive memory consumption and increased Garbage Collector activity. Span, on the other hand, maintains an offset and length on the stack, avoiding the creation of new references on the heap. This offset and length point to the desired portion of the string data on the heap, allowing operations to be completed without creating new references in memory.

3.1.4. Ref struct

The Span is categorized as a ref struct type, indicating specific limitations. Span cannot operate under any async-marked methods or Iterator methods. This restriction arises from the usage of local variables in both methods. Unlike these methods, Span avoids local

variable assignments to preserve data and disposes of data from memory when the scope is exited. Additionally, ref struct types cannot implement interfaces.

3.2. Environment and Libraries

In the conducted study, based on the information gathered about the Span data type, tests were conducted using both simulated data and real data from applications used in our company. These tests were performed using C# and .NET Framework 7.0. In order to conduct controlled iterations for testing purposes and perform data manipulation using predefined functions, the BenchmarkDotNet library was used. The performance difference between the Span data type and other included data types was revealed through these tests. All tests were conducted in the same environment, and multiple repetitions ensured the elimination of undesired conditions that could impact test results.
The physical characteristics of the testing environment and the libraries employed are presented in the below table.

3.2.1. Test environment

In Table 1, certain specifications regarding the physical environment in which the experiments were conducted, including Processor, RAM, Operating System, and the necessary library for performance measurement during the experiments, are provided.

Table 1. Test Environment

Processor	Intel(R) Core(TM) i7-8550U CPU @ 1.80GHz
RAM	16 GB
Operating System	Microsoft Windows 11 Pro
Library	BenchmarkDotNet-0.13.5

3.2.2. BenchmarkDotNet

BenchmarkDotNet is a versatile tool designed to seamlessly convert methods into benchmarks, monitor their performance, and facilitate the dissemination of reproducible measurement experiments. This library simplifies the benchmarking process, akin to composing unit tests. Its internal mechanisms leverage sophisticated techniques, notably the perfolizer statistical engine, ensuring the generation of reliable and precise results. Beyond its facilitative role, BenchmarkDotNet serves as a protective barrier against common benchmarking pitfalls, offering alerts for potential issues within benchmark design or acquired measurements. The output is presented in an intuitive format that accentuates crucial details about the experimental outcomes [9].

4. DATA ANALYSIS AND DISCUSSION

In this section, an in-depth analysis is presented concerning the performance aspects observed within the context of a online education portal project developed at Özdilek Özveri R&D Center. The examination focuses

on empirical evaluations conducted on genuine user data, exceeding a count of 80,000 records, to systematically discern the performance distinctions between the Span and List data types. Special attention is devoted to benchmark tests meticulously devised to highlight the unique performance attributes of the Span data type, particularly in the realm of data manipulation within the String data type. The dataset utilized for these benchmark tests is structured in JSON format, ensuring consistency across each test iteration. The ensuing analysis and discussion shed light on the nuanced aspects of performance exhibited by these data types in real-world applications, providing valuable insights into their respective strengths and capabilities.

The JSON data utilized in real-world data tests is presented in Figure 3 below.

```
{
    "email" : "example@gmail.com",
    "title" : "Software Assistant Specialist",
    "fullName" : "Hakan Akdoğan",
    "isActive" : true,
    "employeeNo" : "00001",
    "positionCode" : "99999",
    "isServiceData" : true,
    "expenseLocationName" : "Bursa",
    "employeeField" : "2000",
    "identityNumber" : "11111111111",
    "workerSubGroup" : "11",
    "employeeSubField" : "2008",
    "employeeSubFieldName" : "R&D",
    "employeeFieldDescription" : "Research And Development"
}
```

Figure 3. JSON User Data

4.1. User Data Benchmark Tests

4.1.1. User data contains method benchmark

Contains Method: The Contains method is used to check if a specified element is present in a collection, such as an array or list. It returns true if the element is found and false if not. This method is commonly used to determine the existence of an item in a dataset, providing a straightforward way to perform such checks in .NET applications.
In this benchmark test, the presence of the term "example" is being examined within the email field of the JSON where user data is stored [10].

As illustrated in the figure below, the Contains method applied on Span exhibited a performance approximately two times faster than when applied on List.
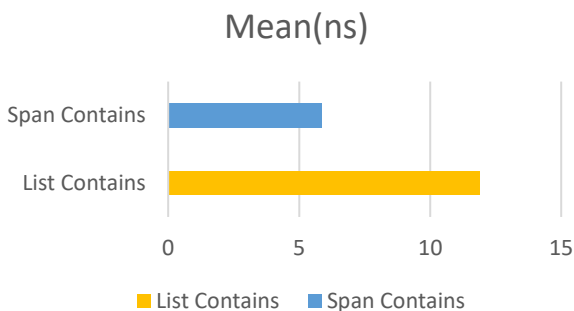
Figure 4. Contains Method Benchmark

4.1.2. User data binary search method benchmark

Binary Search Method: The Binary Search method is employed to efficiently locate a specified value within a sorted collection, such as an array or list. It follows a binary search algorithm, systematically dividing the collection in half and determining whether the sought value lies in the first or second half. This process continues until the exact position of the value is identified or it is confirmed that the value is not present in the collection. The binary search method is particularly advantageous for large datasets due to its logarithmic time complexity, resulting in faster search operations compared to linear search algorithms.
In this benchmark test, the presence of the term "example" is being examined within the email field of the JSON where user data is stored [11].

As illustrated in the figure below, the Binary Search method applied on Span concludes the operation in approximately 55 ns, whereas List completes the same operation in around 73 ns.
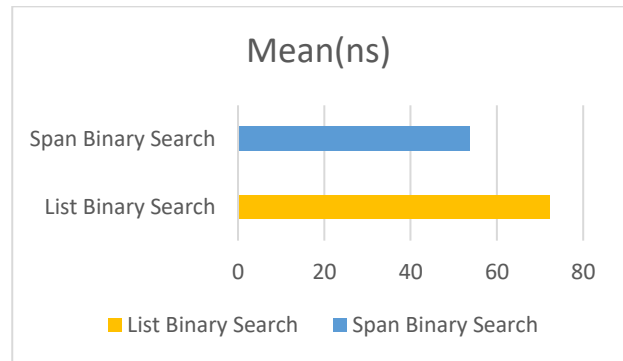
Figure 5. Binary Search Method Benchmark

4.1.3. User data slice method benchmark

Slice Method: The Slice method efficiently extracts a contiguous subset of elements from a data structure, like an array or a Span. Rather than copying elements, it creates a new view or reference to the original data, allowing for enhanced performance and reduced memory usage when working with specific data segments. This feature is particularly useful for handling large datasets with improved efficiency [12].

As illustrated in the figure below, the Slice method applied on Span accomplishes the task of cutting a JSON array in approximately 1 ns, whereas, in contrast, this operation takes around 15 ns when performed on a List.

33
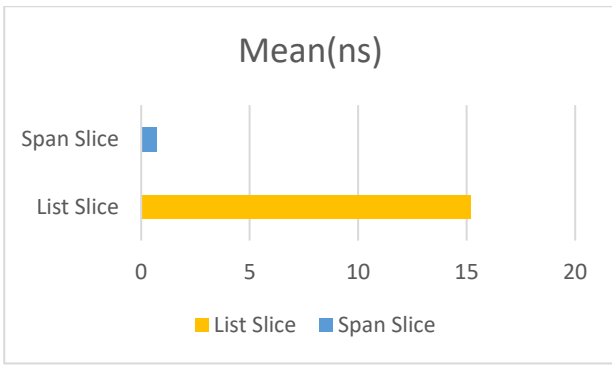
Figure 6. Slice Method

4.2. Example Data Benchmark Tests

In this section, benchmark tests have been conducted by iterating 10,000 times over the sentence 'This is an example sentence.' for performance evaluation.

4.2.1. Example data replace method benchmark

Replace Method: The Replace method is a string manipulation function that replaces all occurrences of a specified substring with another substring within a given string. It provides a straightforward way to modify string content by substituting specified patterns with desired values. The method takes two string parameters: the first represents the substring to be replaced, and the second represents the new substring. The replacement is applied to all instances of the specified substring in the original string. This function is commonly used for simple text transformations and substitutions within string data [13].

In this benchmark test, the Replace method was applied to substitute the substring "an example" with "a sample" in the sentence "This is an example sentence." As illustrated in the figure below, when applied to a Span, the operation concludes in approximately 25,000 ns, while on a String, it takes about 430,000 ns to complete. This comparison highlights the substantial performance advantage of using the Replace method with Span over String.
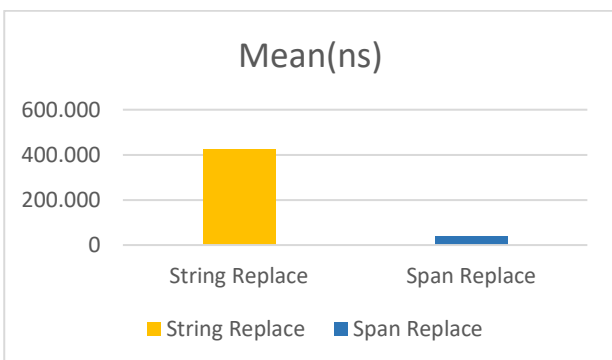
Figure 7. Replace Method

As illustrated in the graph below, when this method is applied to a Span, it performs the operation without any memory allocation, whereas when applied to a String, it allocates approximately 500,000 B of memory. This observation underscores the efficient memory handling of the method when used with Span compared to the

memory allocation associated with its application on String.
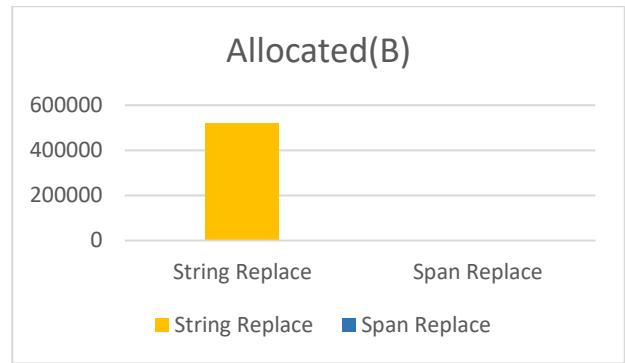
Figure 8. Replace Method Allocated Memory

4.2.2. Example data slice method benchmark

In the benchmark test, the Slice method was applied to truncate the sentence "This is an example sentence" from the first character to the 20th character, resulting in the string "This is an example se". As illustrated in the figure below, the tests conducted with the Slice method revealed that the utilization of Span is approximately 9 times faster than its counterpart using String.
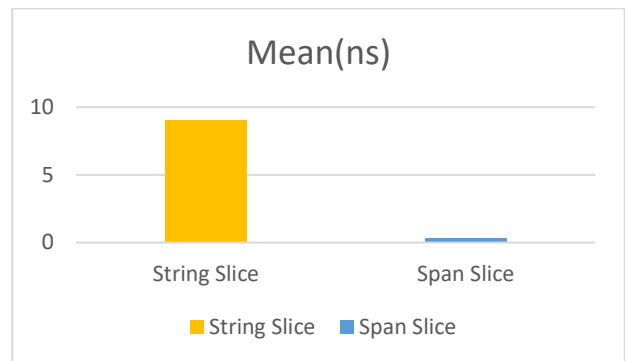
Figure 9. Slice Method

4.2.3. Example data startsWith method benchmark

StartsWith Method: The StartsWith method is used to determine whether a given string begins with a specified prefix. It returns a boolean value indicating whether the string starts with the provided prefix. This method is commonly employed to perform simple prefix-based checks in strings without the need for manual character comparisons. The result is true if the string starts with the specified prefix; otherwise, it returns false. The method is straightforward and provides a convenient way to validate the initial portion of a string in various applications, including text processing and pattern matching [14].

In this benchmark test, the StartsWith method was employed to determine whether the sentence "This is an example sentence" begins with the word "This." As illustrated in the figure below, the comparison using the StartsWith method revealed a significant performance gap. While the String implementation took nearly 38,000 ns to complete this operation, the Span implementation accomplished it in a mere 2.8 ns. This emphasizes the

34

noteworthy efficiency advantage of the Span type in performing prefix-based checks compared to traditional String operations.the benchmark test, the Slice method was applied to truncate the sentence "This is an example sentence" from the first character to the 20th character, resulting in the string "This is an example se". As illustrated in the figure below, the tests conducted with the Slice method revealed that the utilization of Span is approximately 9 times faster than its counterpart using String.
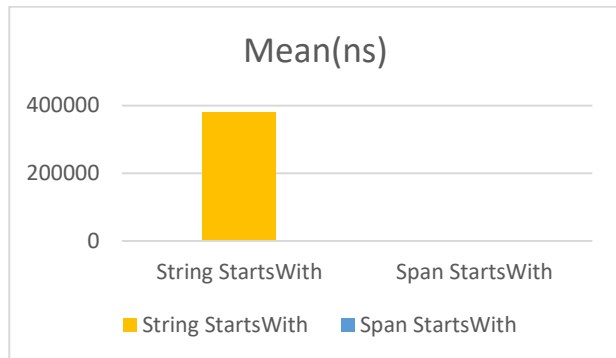
Figure 10. StartsWith Method

4. CONCLUSION

The findings from our comprehensive investigation into the Span data type in C# programming unequivocally demonstrate its superior efficiency in memory utilization and processing speed relative to traditional data types. Our research, grounded in a methodical comparative analysis of real-world and synthetic datasets, highlights the significant advantages of employing Span across various computational methods. Notably, our results reveal that SpanReplace consistently outshines StringReplace in terms of performance over 1000 iterations, thereby affirming the efficiency gains attainable with Span's adoption.

Our examination of memory consumption patterns further underscores the importance of Span, showcasing a marked reduction in memory footprint when juxtaposed with conventional data types. This facet is particularly salient in the processing of large datasets, where efficient memory management is directly linked to the overall performance of applications.
The implications of our findings extend well beyond the realm of performance enhancement. They furnish C# developers with valuable insights into codebase optimization, enabling them to leverage the full potential of the Span data type. With this knowledge, developers are better equipped to tackle the challenges of performance-sensitive applications, benefiting from the tangible improvements in speed and memory efficiency that Span offers.

Looking forward, our study serves as a robust foundation for future research focused on the Span data type. Further investigations could explore specific use cases or optimization strategies across various application domains, enriching our understanding of Span's

performance characteristics through the inclusion of empirical data from a broader array of scenarios.
In summary, our research elucidates the transformative potential of the Span data type within C# programming, heralding it as a pivotal choice for high-performance and memory-efficient applications. As the software development landscape evolves, the insights derived from our study will undoubtedly contribute to ongoing advancements in code efficiency and application performance.

REFERENCES

[1] Deshmukh R, Li R, Sen RR, Henry M, Beckwith G, Gupta G. Performance characterization of .NET benchmarks. IEEE International Symposium on Performance Analysis of Systems and Software (ISPASS); 2021 Apr. Stony Brook, NY, USA. p. 107-17. doi: 10.1109/ISPASS51385.2021.00028.

[2] Almada A. Performance of value-type vs. reference-type enumerators in C# [Internet]. 2023 Jul 22 [cited 2023 Jul 22]. Available from: https://www.linkedin.com/pulse/performance-value-type-vs-reference-type-enumerators-ant%C3%A3o-almada/

[3] Usman M, Bajwa Z, Afzal M. Performance analysis of searching algorithms in C#. International Journal for Research in Applied Science & Engineering Technology (IJRASET). 2014;2(4):511-3.

[4] Shastri S, Singh A, Mohan B, Mansotra V. Run-time analysis of searching and hashing algorithms with C# [Internet]. 2016 Dec [cited 2016 Dec]. Available from: https://www.researchgate.net/publication/311541937_Run-Time_Analysis_of_Searching_and_Hashing_Algorithms_with_C#

[5] Arif MA, Hossain MS, Nahar N, Khatun MD. An empirical analysis of C#, PHP, JAVA, JSP and ASP.Net regarding performance analysis based on CPU utilization. Banglavision Research Journal. 2014;14(1):174-88.

[6] Sestoft P. Numeric performance in C, C# and Java [Internet]. 2007 Feb 28 [cited 2007 Feb 28]. Available from: https://www.researchgate.net/publication/228380860_Numeric_performance_in_C_C_and_Java

[7] The Tech Platform. Why and how string is immutable in C# [Internet]. 2021 Oct [cited 2021 Oct]. Available from: https://www.thetechplatform.com/post/why-and-how-string-is-immutable-in-c

[8] Wickramarathna N. An introduction to writing high-performance C# using Span<T> struct [Internet]. 2021 Dec [cited 2021 Dec]. Available from: https://nishanc.medium.com/an-

introduction-to-writing-high-performance-c-using-span-t-struct-b859862a84e4

[9]   BenchmarkDotNet. BenchmarkDotNet: Powerful .NET library for benchmarking [Internet]. 2024 Jan [cited 2024 Jan]. Available from: https://github.com/dotnet/BenchmarkDotNet

[10]   CodeAcademy. Contains() [Internet]. 2023 Apr [cited 2023 Apr]. Available from: https://www.codecademy.com/resources/docs/c-sharp/strings/contains

[11]   Tripathi P. Binary search using C# [Internet]. 2023 Nov [cited 2023 Nov]. Available from: https://www.c-sharpcorner.com/blogs/binary-search-implementation-using-c-sharp1

[12]   Microsoft. ArraySegment<T>.Slice Method [Internet]. 2024 Jan [cited 2024 Jan]. Available from: https://learn.microsoft.com/en-us/dotnet/api/system.arraysegment-1.slice?view=net-8.0

[13]   Geeks for Geeks. C# | Replace() method [Internet]. 2019 May [cited 2019 May]. Available from: https://www.geeksforgeeks.org/c-sharp-replace-method/

[14]   Microsoft. String.StartsWith Method [Internet]. 2024 Jan [cited 2024 Jan]. Available from: https://learn.microsoft.com/en-us/dotnet/api/system.string.startswith?view=net-8.0

Türk Doğa ve Fen Dergisi
Turkish Journal of Nature and Science

www.dergipark.gov.tr/tdfd

Comments on Parallel Curves in 3-Dimensional Lie Group G

Ali ÇAKMAK[1*] iD , **Pelin Ezgi EPİK[2]** iD

[1] Ağrı İbrahim Çeçen University, Faculty of Sciences and Arts, Department of Mathematics, Ağrı, Türkiye
[2] Bitlis Eren University, Faculty of Sciences and Arts, Department of Mathematics, Bitlis, Türkiye
Ali ÇAKMAK ORCID No: 0000-0002-2783-9311
Pelin Ezgi EPİK ORCID No: 0009-0005-4621-0120

Corresponding author: acakmak@agri.edu.tr

Abstract: In this study, firstly, basic concepts in 3-dimensional Euclidean space and basic information about curves are given and some special curves are examined. Then, basic information about Lie algebra and Lie group basic concepts and curves are given and special curves such as helix, involute-evolute, Bertrand, Mannheim, Smarandache, are defined. Secondly, inspired by these special curves examined in the Lie group, the definitions of the parallel curve in the vector direction, the parallel curve in the direction of the vector B and the parallel curve in the direction of the linear combination of the vectors B and N of a curve according to the Frenet frame are given and characterized. Some theorems and results are obtained by finding the Frenet apparatus of these characterized curves. Finally, the findings are examined in more specific circumstances and new results are found.

3-Boyutlu Lie Grup G de Paralel Eğriler Üzerine Yorumlar

Öz: Bu çalışmada ilk olarak, 3-boyutlu Öklid uzayındaki temel kavramlar ve eğriler ile ilgili temel bilgiler verilmiş ve bazı özel eğriler incelenmiştir. Sonrasında Lie cebiri ve Lie gruplarındaki temel kavramlar ve eğriler ile ilgili temel bilgiler verilmiş helis, involüt-evolüt, Bertrand, Mannheim, Smarandache gibi özel eğrilere ait temel tanım ve teoremler verilmiştir. İkinci olarak, Lie gruplarında incelenen bu özel eğrilerden esinlenerek Lie gruplarında Frenet çatısına göre bir eğrinin N ve B vektörlerinin lineer birleşimi olan vektör yönündeki paralel eğri ve B vektörü yönündeki paralel eğri tanımları verilip karakterize edilmiştir. Karakterize edilen bu eğrilere ait Frenet elemanları bulunarak bazı teoremler ve sonuçlar elde edilmiştir. Son olarak, elde edilen bulgular daha özel hallerde incelenmiş ve yeni sonuçlar bulunmuştur.

1. INTRODUCTION

One of the predominant topics in differential geometry is the theory of curves. In studies related to the theory of curves, researchers often explore various curves such as general helices, slant helices, Salkowski curves, Bertrand curves, and more. While examining these curves, the relations between the curvatures and the Frenet apparatus are used. Consider the curve $\alpha: I \subseteq R \to E^3$ with arc-length parameterized s in three-dimensional Euclidean space. Let $\{T, N, B\}$ be the Frenet vectors of the curve α. The Frenet formulas are given by:

$$T'(s) = \kappa(s)N(s),$$
$$N'(s) = -\kappa(s)T(s) + \tau(s)B(s), \quad (1)$$
$$B'(s) = -\tau(s)N(s),$$

where $\kappa > 0$, $\tau \neq 0$ are the curvature and torsion of the curve α, and can be calculated by following:

$$\kappa = \frac{\|\alpha' \wedge \alpha''\|}{\|\alpha'\|^3},$$
$$\tau = \frac{< \alpha' \wedge \alpha'', \alpha''' >}{\|\alpha' \wedge \alpha''\|^2},$$

where $\alpha', \alpha'', \alpha'''$ are the first, second, and third-order derivations of the curve α, respectively [1].

Offset or parallel curves are defined as curves with points at a constant distance along the normal direction from a given curve in plane [2]. In the literature, the definition of a parallel curve in 3-dimensional Euclidean space appears as different definitions. The first of these is as follows:

Let a curve $\gamma = \gamma(s^*)$ with unit-speed be given, where $\tau \neq 0$. Let the β curve be the parallel curve at a distance

r from the curve γ. Let the Frenet frames of the curves γ and β be given as $\{T, N, B\}$, $\{T_\beta, N_\beta, B_\beta\}$ respectively. So, we can write the following equations:

$$\langle \beta(s) - \gamma, \beta(s) - \gamma \rangle = r^2, \tag{2}$$

$$\langle T_\beta(s), \beta(s) - \gamma \rangle = 0, \tag{3}$$

$$\langle (T_\beta{}'(s), \beta(s) - \gamma) \rangle + \langle (T_\beta(s), T_\beta(s)) \rangle = 0. \tag{4}$$

The Frenet formulas can be obtained by using the equations (1) at the point β depending on the parameter s for a curve $\beta(s)$ with unit speed where $\tau > 0$. Thus, from the equations (2), (3) and (4) we have

$$\beta(s) - \gamma = m_2 N_\beta + m_3 B_\beta, \tag{5}$$

where m_2, m_3 are the appropriate coefficients and $\beta' = T_\beta$ [3]. Another definition is as follows:

The parallel curve to a unit-speed curve $\alpha(s)$ is given by

$$\bar\alpha = \alpha(s) + rB(s). \tag{6}$$

Here, $r \neq 0$ is a real constant, $s = s(\bar s)$ is the arc-length of $\alpha(s)$ and $\bar s$ is the arc-length of the parallel curve $\bar\alpha$. B is the binormal vector of the curve $\alpha(s)$ [4].

In mathematics, a Lie group is a group that is also a differentiable manifold, characterized by the smoothness of group operations. Lie groups take their name from the Norwegian mathematician Sophus Lie, who laid the foundations of the theory of continuous transformation groups. Essentially, a Lie group is a continuous group, with its elements defined by several real parameters. Many studies have been done on the differential geometry of curves in Lie Groups [5, 6, 7, 8, 9, 10, 11].

In the present study, we discuss using the definitions of parallel curves in the literature in 3-dimensional Lie groups. It also contains theorems and results that give the relations between parallel curve pairs and special curve pairs.

2. MATERIAL AND METHOD

2.1. Fundamental Concepts in Lie Groups

Definition 2.1.1. Let G be a group and M^* is a differentiable manifold,

L_1: Every element of G coincicides with the points of M^*,

L_2: $M^* \times M^* \to M^*, (p, q) \to pq^{-1}$ is differentiable.

In such a way that the axioms are satisfied, the fundamental manifold of the Lie group is obtained as M^*, the fundamental group of the Lie group as G, and the pair (M^*, G) is obtained as the Lie group [12].

Definition 2.1.2. Let G be a Lie group and $\langle , \rangle$ be an invariant metric on G. If the Lie algebra of the Lie group G is given by g and the unit element of the Lie group G is given by e, the Lie algebra is g and the Lie algebra structure $T_g(e)$ is isomorphic. Let $\langle , \rangle$ be an invariant metric on G, and let G be the Levi-Civita connection of the Lie group $\bar V$. Here, $\forall K, L, M \in g$ is given by:

$$\langle K, [L, M] \rangle = \langle [K, L], M \rangle$$

and

$$\bar V_K L = \frac{1}{2}[K, L].$$

Assume that $\alpha: I \subset R \to G$ is a curve parameterized by arc-length, and $\{V_1, V_2, \dots, V_n\}$ is an orthonormal base of g. In this case, two vector fields along the curve can be written as $W = \sum_{i=1}^n w_i X_i$ and $Z = \sum_{i=1}^n z_i X_i$, where $w_i : I \to \mathbb{R}$ and $z_i: I \to \mathbb{R}$ are smooth functions. Lie product of two vector fields W and Z:

$$[W, Z] = \sum_{i=1}^n w_i z_j [X_i, X_j],$$

and the covariant derivative of the vector field W along the curve α is

$$D_{\alpha'} W = \dot W + \frac{1}{2}[T, W]. \tag{7}$$

Here $T = \alpha', \dot W = \sum_{i=1}^n \dot w_i X_i = \sum_{i=1}^n \frac{dw_i}{dt} X_i$. If the left invariant vector field restricted to α is W, $\dot W = 0$ [9].

Proposition 2.1.1. Assume that $\alpha(s)$ is a curve in the Lie group G, with arc-length parameter s and (T, N, B, κ, τ) is the Frenet apparatus of $\alpha(s)$. In this case, we write

$$\begin{cases} [T, N] = \langle [T, N], B \rangle B = 2\tau_G B \\ [T, B] = \langle [T, B], N \rangle N = -2\tau_G N. \end{cases} \tag{8}$$

In this case, considering that $\alpha(s)$ is a curve in G and s is the arc-length parameter of $\alpha(s)$, from the equations (7) and (8), Frenet formulae are found as follows:

$$\begin{pmatrix} \frac{dT}{ds} \\ \frac{dN}{ds} \\ \frac{dB}{ds} \end{pmatrix} = \begin{pmatrix} 0 & \kappa & 0 \\ -\kappa & 0 & \tau - \tau_G \\ 0 & -(\tau - \tau_G) & 0 \end{pmatrix} \begin{pmatrix} T \\ N \\ B \end{pmatrix}.$$

Here (T, N, B, κ, τ) is Frenet apparatus of $\alpha(s)$ in G, $\tau_G = \frac{1}{2}\langle [T, N], B \rangle$ [8].

Definition 2.1.3. Let $\alpha: I \subseteq \mathbb{R} \to G$ be a curve with arc-length parameters in the 3-dimensional Lie group G and Frenet apparatus are $\{T, N, B, \kappa, \tau\}$. The function h expressed by the equation

$$h = \frac{\tau - \tau_G}{\kappa} \tag{9}$$

is the harmonic curvature of the curve α [8].

2.2. Special Curves in 3-Dimensional Lie Groups

Definition 2.2.1. Let $\alpha: I \subseteq \mathbb{R} \to G$ be considered as a curve with arc-length parameterized in the three-dimensional Lie group and the unit left invariant vector field $X \in G$. If X and the curve α make a constant angle at all points of the curve α, that is the unit tangent vector field T at point $\alpha(s)$ on curve α is a left invariant vector field X and $\vartheta \neq \frac{\pi}{2}$ if it makes a constant angle, namely

$$\langle T(s), X \rangle = \cos \vartheta, s \in I.$$

The curve α is the general helix in the Lie group. Here, $X \in g$ and unit, T is tangent vector field of the curve α, the angle $\vartheta \neq \frac{\pi}{2}$ is the fixed angle between X and T [6].

Theorem 2.2.1. Let $\alpha: I \subseteq \mathbb{R} \to G$ be considered as a curve with arc-length parameterized in G. The curve α is general helix if and only if $\tau = c\kappa + \tau_G, c = constant$ such that $\{T, N, B, \kappa, \tau\}$ is Frenet apparatus of α [6].

Definition 2.2.2. Let G be a three-dimensional Lie group with a bi-invariant metric and the curves α, β be two curves in G. If the principal normal vector field of the

curve α and the binormal vector field of the curve β are linearly dependent at corresponding points of α and β, α is called a Mannheim curve, the curve β is called the Mannheim curve corresponding to α, and the pair $\{\alpha, \beta\}$ is referred to as a Mannheim curve pair [13].

Definition 2.2.3. Let's consider the unit speed curves $\gamma: I \subset \mathbb{R} \to G$ and $\beta: \bar{I} \subset \mathbb{R} \to G$ in G with the left-invariant metric. Let s and $\bar{s}$ be the arc-length parameters and $\{T, N, B, k_0, \varkappa_0, \alpha\}$, $\{\bar{T}, \bar{N}, \bar{B}, \bar{k}_0, \bar{\varkappa}_0, \bar{\alpha}\}$ be Frenet apparatus of γ and β respectively. If the tangent vectors at corresponding points of the γ and β curves are perpendicular to each other, that is $\langle \bar{T}, T \rangle = 0$, then the curve β is called the involute of γ and the curve γ is called the evolute of β [14].

Definition 2.2.4. Let's consider the Lie group G defined by a bi-invariant metric. If, at corresponding points of α and β, the principal normal vector field of α and the principal normal vector field of β are linearly dependent, then α is called a Bertrand curve. In this case, β is the Bertrand curve corresponding to α, and the pair $\{\alpha, \beta\}$ is referred to as a Bertrand curve pair [13].

Definition 2.2.5. Let $\alpha: I \subseteq \mathbb{R} \to G$ be a unit speed curve in three-dimensional Lie group and $\{T, N, B, \kappa, \tau\}$ be the Frenet apparatus of the curve α. In this case, the TN - Smarandache curve is $\psi(s_\psi) = \frac{1}{\sqrt{2}}(T(s) + N(s))$ [15].

3. RESULTS

In this section, starting with the consideration of parallel curve definitions in 3-dimensional Euclidean space, we will first discuss the definition of a parallel curve in G. Specifically, we will delve into the concept of a parallel curve in the direction of the vectors N and B in Lie group, and then a parallel curve in the direction of the binormal vector B of a curve will be given.

Afterwards, Frenet elements $\{T, N, B, \kappa, \tau\}$ will be obtained for the parallel curves of all two cases. In addition, some theorems and results characterizing these curves will be obtained.

3.1. Parallel Curve in the Direction of NB in 3-Dimensional Lie Groups

Definition 3.1.1. Let $\alpha: I \subseteq \mathbb{R} \to G$ be considered as a unit speed curve in the three-dimensional Lie group G and $\{T, N, B, \kappa, \tau\}$ as the Frenet apparatus of the curve α. The parallel curve of the curve α in G is

$$\rho(s_\rho) = \alpha(s) + r_1 N(s) + r_2 B(s). \tag{10}$$

Here, $r_1 \neq 0, r_2 \neq 0$ are real constants.
The Frenet frame $\{T_\rho, N_\rho, B_\rho\}$ of the parallel curve $\rho(s_\rho)$ are

$$T_\rho(s_\rho) = \frac{(1-r_1\kappa)T(s)+r_2\kappa h N(s)-r_1\kappa h B(s)}{\sqrt{(1-r_1\kappa)^2+(r_2\kappa h)^2+(r_1\kappa h)^2}}, \tag{11}$$

for

$$P_\rho = \begin{bmatrix} ((1-r_1\kappa)^2 + (r_2\kappa h)^2 \\ +(r_1\kappa h)^2)(-r_1\kappa' + r_2\kappa^2 h) \\ -(1-r_1\kappa)(-r_1\kappa' + r_1^2\kappa\kappa') \\ -(1-r_1\kappa)(r_1^2+r_2^2)(\kappa\kappa'h^2 + \kappa^2 hh') \end{bmatrix},$$

$$R_\rho = \begin{bmatrix} ((1-r_1\kappa)^2 + (r_2\kappa h)^2 \\ +(r_1\kappa h)^2) \\ (\kappa - r_1\kappa^2 + r_2\kappa'h + r_2\kappa h' + r_1\kappa^2 h^2) \\ -(r_2\kappa h)(-r_1\kappa' + r_2\kappa\kappa') \\ -(r_2\kappa h)(r_1^2+r_2^2)(\kappa\kappa'h^2 + \kappa^2 hh') \end{bmatrix},$$

$$S_\rho = \begin{bmatrix} ((1-r_1\kappa)^2 + (r_2\kappa h)^2 \\ +(r_1\kappa h)^2)(-r_2\kappa^2 h^2 - r_1\kappa'h - r_1\kappa h') \\ +(r_1\kappa h)(-r_1\kappa' + r_1^2\kappa\kappa') \\ +r_1\kappa h(r_1^2+r_2^2)(\kappa\kappa'h^2 + \kappa^2 hh') \end{bmatrix},$$

$$N_\rho(s_\rho) = \frac{1}{\sqrt{P_\rho^2+R_\rho^2+S_\rho^2}}\left(P_\rho T(s) + R_\rho N(s) + S_\rho B(s)\right) \tag{12}$$

and for $p = \sqrt{(1-r_1\kappa)^2 + (r_2\kappa h)^2 + (r_1\kappa h)^2}$ and $q = \sqrt{P_\rho^2 + R_\rho^2 + S_\rho^2}$,

$$B_\rho(s_\rho) = \frac{1}{pq}\begin{pmatrix} (r_2\kappa h S_\rho + r_1\kappa h R_\rho)T(s) \\ +(-r_1\kappa h P_\rho - (1-r_1\kappa)S_\rho)N(s) \\ +\left((1-r_1\kappa)R_\rho - r_2\kappa h P_\rho\right)B(s) \end{pmatrix}. \tag{13}$$

The curvature and torsion of the curve $\rho(s_\rho)$ are given by

$$\kappa_\rho = \|\dot{T}\| = \frac{\sqrt{P_\rho^2+R_\rho^2+S_\rho^2}}{((1-r_1\kappa)^2+(r_2\kappa h)^2+(r_1\kappa h)^2)^2} \tag{14}$$

and

$$\tau_\rho = \frac{\begin{array}{c}(r_1\kappa^2 h - r_1^2\kappa^3 h + (r_1^2+r_2^2)\kappa^3 h^3)\ell \\ +(2r_1r_2\kappa^3 h^2 + r_1\kappa'h + r_1\kappa h' - r_2\kappa^2 h^2 - r_1^2\kappa^2 h')m \\ +(\kappa - 2r_1\kappa^2 + r_2\kappa'h + r_2\kappa h' + r_1\kappa^2 h^2 + r_1^2\kappa^3 \\ -r_1r_2\kappa^2 h' - r_1^2\kappa^3 h^2 + r_2^2\kappa^3 h^2)n\end{array}}{\begin{array}{c}(r_1\kappa^2 h - r_1^2\kappa^3 h + (r_1^2+r_2^2)\kappa^3 h^3)^2 \\ +(2r_1r_2\kappa^3 h^2 + r_1\kappa'h + r_1\kappa h' - r_2\kappa^2 h^2 - r_1^2\kappa^2 h')^2 \\ +(\kappa - 2r_1\kappa^2 + r_2\kappa'h + r_2\kappa h' + r_1\kappa^2 h^2 + r_1^2\kappa^3 \\ -r_1r_2\kappa^2 h' - r_1^2\kappa^3 h^2 + r_2^2\kappa^3 h^2)^2\end{array}}, \tag{15}$$

where

$$\ell = \begin{pmatrix} -r_1\kappa'' - 3r_2\kappa\kappa'h - 2r_2\kappa^2 h' \\ +r_1\kappa^3 - r_1\kappa^3 h^2 - \kappa^2 \end{pmatrix},$$

$$m = \begin{pmatrix} \kappa' - 3r_1\kappa\kappa' + r_2\kappa''h + 2r_2\kappa'h' + r_2\kappa h'' \\ +3r_1\kappa^2 hh' + 3r_1\kappa\kappa'h^2 + r_2\kappa^3 h - r_1\kappa^3 h^3 \end{pmatrix},$$

$$n = \begin{pmatrix} \kappa^2 h - r_1\kappa^3 h + 3r_2\kappa\kappa'h^2 + 3r_2\kappa^2 hh' \\ +r_1\kappa^3 h^3 - 2r_1\kappa'h' - r_1\kappa h'' \end{pmatrix}.$$

Theorem 3.1.1. Let the curves $\alpha, \rho: I \subseteq \mathbb{R} \to G$ be considered as Frenet vector fields $\{T, N, B\}$ and $\{T_\rho, N_\rho, B_\rho\}$ respectively. The parallel curve pair (α, ρ) is involute-evolute curve pair if and only if $\kappa = \frac{1}{r_1}$.

Proof. Let the parallel curve pair (α, ρ) be involute-evolute curve pair. In this case, $\langle T, T_\rho \rangle = 0$. From the equation (11), we get

$$\langle T, T_\rho \rangle = \frac{(1-r_1\kappa)}{\sqrt{(1-r_1\kappa)^2+(r_2\kappa h)^2+(r_1\kappa h)^2}}T(s) = 0$$

which is achieved by $\kappa = \frac{1}{r_1}$
On the contrary, let's $\kappa = \frac{1}{r_1}$. If both sides of the equation (11) are made scalar product by T and $\kappa = \frac{1}{r_1}$ is written, we have $\langle T, T_\rho \rangle = 0$.

Hence, the proof is completed.

Theorem 3.1.2. Let the curve pair (α, ρ) be a parallel curve pair with the Frenet vectors $\{T, N, B\}$ and $\{T_\rho, N_\rho, B_\rho\}$ respectively. If (α, ρ) is a Bertrand curve pair, $-r_1 \kappa h P_\rho - (1 - r_1 \kappa) S_\rho = 0$.

Proof. Let the curves α and ρ be a Bertrand curve pair, where the principal normal vector field of the curve α is N and the principal normal vector field of the curve ρ is N_ρ. In this case, N and N_ρ are linearly dependent. Now, if we multiply both sides of equation (13) by N_ρ and consider that N and N_ρ are linearly dependent, we obtain
$$\frac{\left(-r_1 \kappa h P_\rho - (1 - r_1 \kappa) S_\rho\right)}{pq} = 0.$$
If the necessary adjustments are made in the last equation, we have
$$\left(-r_1 \kappa h P_\rho - (1 - r_1 \kappa) S_\rho\right) =$$
$$\left(-r_1 \kappa h \left(\begin{array}{c} \left(\begin{array}{c} (1 - r_1 \kappa)^2 + (r_2 \kappa h)^2 \\ + (r_1 \kappa h)^2 \end{array} \right)(-r_1 \kappa' + r_2 \kappa^2 h) \\ -(1 - r_1 \kappa)(-r_1 \kappa' + r_1^2 \kappa \kappa') \\ -(1 - r_1 \kappa)(r_1^2 + r_2^2)(\kappa \kappa' h^2 + \kappa^2 h h') \end{array} \right) \right)$$
$$- \left(\begin{array}{c} (1 - r_1 \kappa) \\ \left(\begin{array}{c} (1 - r_1 \kappa)^2 + (r_2 \kappa h)^2 \\ + (r_1 \kappa h)^2)(-r_2 \kappa^2 h^2 - r_1 \kappa' h - r_1 \kappa h') \\ + (r_1 \kappa h)(-r_1 \kappa' + r_1^2 \kappa \kappa') \\ + r_1 \kappa h (r_1^2 + r_2^2)(\kappa \kappa' h^2 + \kappa^2 h h') \end{array} \right) \right) = 0.$$

Specifically, when $\kappa = \frac{1}{2r_1}$ and $h = constant$, the following equation is satisfied:

$$\left(-r_1 \kappa h P_\rho - (1 - r_1 \kappa) S_\rho\right) = r_1(\kappa' h + \kappa h' - r_1 \kappa^2 h')$$
$$+ r_2(\kappa^2 h^2 - 2r_1 \kappa^3 h^2) = 0.$$

Corollary 3.1.1. It can be easily seen from Theorem 3.1.2 that if the curvature of the curve $\alpha(s)$ is κ and its torsion is τ and $\kappa = \frac{1}{2r_1}$ and $h = constant$, the curve $\alpha(s)$ is also a helix curve.

3.2. Parallel Curve in the Direction of B in 3-Dimensional Lie Groups

Definition 3.2.1. Let $\alpha: I \subseteq \mathbb{R} \to G$ be a unit-speed curve in three-dimensional Lie group G and $\{T, N, B, \kappa, \tau\}$ be the Frenet apparatus of the curve α. The parallel curve of the curve α in the direction of B is defined by
$$\wp(s_\wp) = \alpha(s) + rB(s) \tag{16}$$
where $r \neq 0$ is a real constant.
The Frenet frame $\{T_\wp, N_\wp, B_\wp\}$ of the parallel curve $\wp(s_\wp)$ are
$$T_\wp(s_\wp) = \frac{(T(s) - r\kappa h N(s))}{\sqrt{(1 + (r\kappa h)^2}}, \tag{17}$$
for
$$P_\wp = [r\kappa^2 h(1 + (r\kappa h)^2) - r\kappa' h - r\kappa h')],$$
$$R_\wp = [\kappa(1 + (r\kappa h)^2) - r\kappa' h - r\kappa h')], \tag{18}$$
$$S_\wp = [-r\kappa^2 h^2(1 + (r\kappa h)^2)],$$

$$N_\wp(s_\wp) = \frac{\sqrt{(1 + (r\kappa h)^2)}}{\sqrt{P_\wp^2 + R_\wp^2 + S_\wp^2}} \left(\begin{array}{c} P_\wp T(s) \\ + R_\wp N(s) + S_\wp B(s) \end{array} \right) \tag{19}$$
and
$$B_\wp(s_\wp) = \frac{1}{p} \left(\begin{array}{c} (-r\kappa h S_\wp) T(s) \\ + (-S_\wp) N(s) + (R_\wp + r\kappa h P_\wp) B(s) \end{array} \right), \tag{20}$$
where $p = \sqrt{P_\wp^2 + R_\wp^2 + S_\wp^2}$. The curvature and torsion of $\rho(s_\wp)$ are given by
$$\kappa_\wp = \|\dot{T}\| = \frac{\sqrt{P_\wp^2 + R_\wp^2 + S_\wp^2}}{(1 + (r\kappa h)^2)^2} \tag{21}$$
and
$$\tau_\wp = \frac{(r^2 \kappa^3 h^3)\ell + (r\kappa^2 h^2)m + (\kappa - r\kappa' h - r\kappa h' + r^2 \kappa^3 h^2)n}{(r^2 \kappa^3 h^3)^2 + (r\kappa^2 h^2)^2 + (\kappa - r\kappa' h - r\kappa h' + r^2 \kappa^3 h^2)^2}, \tag{22}$$
where
$\ell = (-\kappa^2 + 3r\kappa \kappa' h + 2r\kappa^2 h')$,
$m = (r\kappa^3 h + \kappa' - r\kappa'' h - 2r\kappa' h' - r\kappa h'' + r\kappa^3 h^3)$,
$n = (\kappa^2 h - 3r\kappa \kappa' h^2 - 3r\kappa^2 h h')$.

Corollary 3.2.1. Let the curve pair $(\alpha, \wp)$ be a parallel curve pair with the Frenet vectors $\{T, N, B\}$ and $\{T_\wp, N_\wp, B_\wp\}$ respectively, where $\wp$ is the parallel curve to α in the direction of B. The parallel curve pair $(\alpha, \wp)$ is not a Bertrand curve pair under no circumstances.

Proof. Suppose that $(\alpha, \wp)$ is a Bertrand curve pair. In this case, N and $N_\wp$ are linearly dependent. Considering the equation (20), we multiply both sides of equation (20) by $N_\wp$. Since $S_\wp = r\kappa^2 h^2(1 + (r\kappa h)^2) \neq 0$, $(\alpha, \wp)$ is not a Bertrand curve pair.

Corollary 3.2.2. Let the curve pair $(\alpha, \wp)$ be a parallel curve pair with the Frenet vectors $\{T, N, B\}$ and $\{T_\wp, N_\wp, B_\wp\}$ respectively, where $\wp$ is the parallel curve to α in the direction of B. The parallel curve pair $(\alpha, \wp)$ is not an involute-evolute curve pair under no circumstances.

Proof. Suppose that $(\alpha, \wp)$ is an involute-evolute curve pair. In this case, $T \perp T_\wp$. Considering the equation (17), we multiply both sides of equation (17) by T. Since $\langle T, T_\wp \rangle = \frac{1}{\sqrt{1 + (r\kappa h)^2}}$, $T \not\perp T_\wp$. Hence, $(\alpha, \wp)$ is not an involute-evolute curve pair.

Theorem 3.2.1. Let the curve pair $(\alpha, \wp)$ be a parallel curve pair with the Frenet frames $\{T, N, B\}$ and $\{T_\wp, N_\wp, B_\wp\}$ respectively. If the parallel curve pair $(\alpha, \wp)$ is a Mannheim curve pair, $R_\wp = 0$.

Proof. Suppose that the parallel curve pair $(\alpha, \wp)$ is a Mannheim curve pair. In this case, N and $B_\wp$ are linearly dependent. Considering the equation (19), if we multiply both sides of equation (19) by $B_\wp$, we obtain $\frac{\sqrt{(1 + (r\kappa h)^2)}}{\sqrt{P_\wp^2 + R_\wp^2 + S_\wp^2}} R_\wp = 0$. Since $\sqrt{(1 + (r\kappa h)^2)} \neq 0$, we have
$$R_\wp = (1 + (r\kappa h)^2)\kappa - r\kappa' h - r\kappa h' = 0.$$
Hence, proof is completed.
In the special case, let $\tau - \tau_G = -\frac{1}{r}$. In this case, we have

40

$$h = \frac{\tau - \tau_G}{\kappa} \Rightarrow h = -\frac{1}{r\kappa}. \qquad (23)$$

Considering the equation (23), we get the equations (18) the following as:

$$P_\wp = -2\kappa, R_\wp = 2\kappa, S_\wp = 2\kappa h = -\frac{2}{r}$$

These equations are substituted in the equation (21), we obtain

$$\kappa_\wp = \frac{\sqrt{1 + 2r^2\kappa^2}}{2r} \qquad . \qquad (24)$$

The equation (24) gives us the relationship between curvatures of the curve pair $(\alpha, \wp)$. In addition to equation (24), it can be expressed in the following theorem and result.

Theorem 3.2.2. Let the curve pair $(\alpha, \wp)$ be a parallel curve pair with the Frenet frames $\{T, N, B\}$ and $\{T_\wp, N_\wp, B_\wp\}$ respectively. If $\tau - \tau_G = -\frac{1}{r}$, the equation (17) is TN-Smarandache curve.

Proof. Substituting the equation $\tau - \tau_G = -\frac{1}{r}$ into equation (9), we get

$$h = \frac{\tau - \tau_G}{\kappa} \Rightarrow h = -\frac{1}{r\kappa}.$$

If we substitute $h = -\frac{1}{r\kappa}$ in equation (17) and we make the necessary simplifications, we have

$$T_\wp = \frac{T + N}{\sqrt{2}}.$$

Considering Definition 2.2.5. it is seen that the last equation is TN-Smarandache curve.

Corollary 3.2.3. Let consider unit-speed curve α with constant curvature κ and its parallel curve $\wp$ with the curvature $\kappa_\wp$. Since $\tau - \tau_G = -\frac{1}{r}$, the curve α is a circular helix. In this case, $\kappa_\wp = constant$ and the curve $\wp$ is a circular helix in the abelian case.

Proof. Considering equation (23), above the equations l, m, n

$$\ell = -\kappa^2, m = -\left(\frac{r^2\kappa^2 + 1}{r^2}\right), n = \kappa^2 h \qquad (25)$$

is obtained as in (25). By using equations (25) into equation (22) and if we make the necessary adjustments, we have

$$\tau_\wp = \frac{\kappa^3 h - \kappa h(-\kappa^2 - \kappa^2 h^2) + 2\kappa^3 h}{(\kappa h)^2 + (\kappa h)^2 + (2\kappa)^2}$$

Since both κ and h are constants, $\tau_\wp = constant$. Since $\tau_{G_\wp} = 0$ in the abelian case (see [6]), $\frac{\tau_\wp}{\kappa_\wp}$ is constant. So, the curve $\wp$ is obtained as a circular helix.

Finally, the following theorem can be written by taking the special case of $\kappa = \frac{1}{r}$

Theorem 3.2.3. Let the curve pair $(\alpha, \wp)$ be a parallel curve pair with the Frenet frames $\{T, N, B\}$ and $\{T_\wp, N_\wp, B_\wp\}$ respectively. Let $(\alpha, \wp)$ be Mannheim curve pair, for $\kappa = \frac{1}{r}$. In this case, $h = tan\left(\frac{s}{r} + c\right)$.

Proof. Let $\kappa = \frac{1}{r}$ and the parallel curve pair $(\alpha, \wp)$ be a Mannheim curve pair. In this case N and $B_\wp$ are linearly

dependent. Then if both sides of equation (19) are multiplied by $B_\wp$

$$R_\wp = (1 + h^2)\frac{1}{r} - h' = 0 \Rightarrow h' - \frac{(1 + h^2)}{r} = 0. \qquad (26)$$

From the solution of differential equation (26), we have

$$rh' = h^2 + 1$$

$$arctan(h) = \frac{s}{r} + c \Rightarrow h = tan\left(\frac{s}{r} + c\right).$$

This completes the proof.

4. DISCUSSION AND CONCLUSION

In this study, we investigated parallel curves in the 3-dimensional Lie group, based on the definitions of parallel curves in 3-dimensional Euclidean space. We calculated Frenet apparatus of these curves. We provided the theorems and results that reveal the relationships of the obtained parallel curves and special curves.

Finally, we examined the parallel curve pairs by adding some special cases and found interesting theorems and results.

REFERENCES

[1] O' Neill B, Elementary Differential Geometry. Academic Press, New York. 1966.
[2] Willson FN. Theoretical and Practical Graphics. The Macmillan Company. 1898.
[3] Keskin Ö, Yüksel N, Karacan MK, İkiz H. Characterization of the Parallel Curve of the Adjoint Curve in E^3. General Mathematics Notes. 2016; 35:9-18.
[4] Aldossary MT, Gazwani MA. Montion of Parallel Curves and Surfaces in Euclidean 3-Space R3. Global J. Adv. Res. Class. Mod. Geo. 2020; 9:43-56.
[5] Bozkurt Z, Gök I, Okuyucu OZ, Ekmekçi FN. Characterizations of rectifying, normal and osculating curves in three-dimensional compact Lie groups. Life Science Journal. 2013; 10: 819-823.
[6] Çiftçi Ü. A generalization of Lancret's theorem. Journal of Geometry and Physics. 2009; 59:1597-1603.
[7] Kızıltuğ S, Önder M. Associated Curves of Frenet Curves in Three-Dimensional Compact Lie Group. Miskolc Mathematical Notes 2015; 16:953-964.
[8] Okuyucu OZ, Gök I, Yaylı Y, Ekmekçi FN. Slant helices in three-dimensional Lie groups. Applied Mathematics and Computation. 2013, 221:672-683.
[9] Crouch P, Silva LF. The dynamic interpolation problem: On Riemannian manifolds, Lie groups, and symmetric spaces. J. Dyn. Control Syst. 1995; 1:177–202.
[10] Gök I, Okuyucu OZ, Yayli Y, Ekmekci N. Bertrand curves in three-dimensional Lie groups. Miskolc Mathematical Notes. 2016, 17:999–1010.

[11] Çakmak A. New Type Direction Curves in 3-Dimensional Compact Lie Group. Symmetry. 2019, 11:387.

[12] Hacısalihoğlu H. Introduction to High Differential Geometry. Fırat University, Faculty of Science Publications, Elâzığ. 2006.

[13] Okuyucu OZ. Special Curves on Some Manifolds. Ph.D. Thesis, Ankara University, Ankara, 2013.

[14] Kızılay E. Some Generalized Curves in Three Dimensional Compact Lie Groups, M.Sc. Thesis, Bilecik Seyh Edebali University, Bilecik, 2023.

[15] Değirmen C. On Curves in Three Dimensional Compact Lie Groups, M.Sc. Thesis, Bilecik Seyh Edebali University, Bilecik, 2017.

Türk Doğa ve Fen Dergisi
Turkish Journal of Nature and Science
www.dergipark.gov.tr/tdfd

Impact of 6S (5S+Safety) Implementation in Machine Workshops on Occupational Safety

Sirer ALBAYRAK¹* iD

¹ Program of Occupational Health and Safety, Ağrı İbrahim Çeçen University, Ağrı, Türkiye
Sirer ALBAYRAK ORCID No: 0000-0002-3201-1789

*Correspondingauthor: sireralbayrak@gmail.com

Abstract: In this current study, the impact of implementing 6S (5S+Safety) in the machining industry on occupational safety was investigated by selecting the chip machining section of a factory producing flywheels. To facilitate the comparison of risk levels before and after the implementation of 6S, a Fine-Kinney risk evaluation was conducted in the sawdust department before the application of 6S. The 6S implementation process took 28 days, and subsequently, a Fine-Kinney risk evaluation was performed in the sawdust department, revealing a 77.4% reduction in risks. As a result, the 77.4% reduction in accident risks indicates that the implementation of 6S, which emphasizes safety within the framework of the 5S principles, leads to a more organized, cleaner, and safer machine workshop environment. We can indicate that this approach not only reduces the risk of accidents but also enhances work efficiency, preventing time loss and material waste.

Makine Atölyelerinde 6S (5S+Safety) Uygulamasının İş Güvenliği Üzerindeki Etkisi

Öz: Bu çalışmada,6S (5S+Güvenlik)'in makine imalat sanayisinde uygulanmasının iş güvenliği üzerine etkisini belirlemek için volant dişlileri üreten bir fabrikanın talaşlı imalat bölümü seçilerek araştırma kapsamında incelenmiştir. 6S uygulaması öncesi ve sonrası risk derecelerinin karşılaştırmalarının yapılabilmesi için, talaşlı imalat bölümünde 6S uygulanmadan önce Fine-kinney risk değerlendirmesi yapılmıştır. 6S uygulama eyleminin tamamlanması 28 gün sürmüş ve akabinde talaşlı imalat bölümünde yapılan Fine-kinney risk değerlendirmesi ile risklerin %77.4 oranında azaldığı görülmüştür. Sonuç olarak, kaza risklerinin %77.4 oranında azalması,5S ilkeleri kapsamında güvenliğe vurgu yapan 6S'nin uygulanması daha organize, daha temiz ve daha güvenli bir makine atölyesi ortamına yol açtığı görülmektedir. Bu yaklaşımın yalnızca kaza riskini azaltmadığını aynı zamanda iş verimini artırdığını, zaman kaybının ve malzeme israfının da önüne geçtiğini söyleyebiliriz.

1. INTRODUCTION

Effective occupational safety practices, especially in industrial enterprises and machine workshops, play a critical role in enhancing both the health of workers and the efficiency of workplaces. The 5S system has been implemented in the industry for years. Its use not only improves the quality of a workplace but also contributes to the enhancement of occupational safety, ergonomics, elevated job standards, and increased job satisfaction and productivity [1,2,3,4]. Due to the prioritization of occupational safety in the manufacturing industry, the term '6S system' has been used for some time. Oppenheim and Felbur [4] emphasize that the 6S system, which places

greater emphasis on occupational safety than the 5S system, naturally replaces the latter. Harris and Harris [5] assert that the 6S system operates more comprehensively than the 5S system because it highlights the necessity of ensuring occupational safety, without which optimal job efficiency becomes challenging to achieve. Similarly, Badiru [6] indicates that the 6S system not only enhances quality and efficiency but also improves occupational safety. In this context, understanding and evaluating the impact of the 6S system on occupational safety represent a crucial research area to enhance health and safety standards in modern production environments.

What is 6S?

43

In 6S, Safety focuses on preventive measures to protect employees from hazardous conditions and provide them with a safe environment. Research emphasizes the significant role of safety plays in maintaining a stress-free, secure workplace environment, thereby enhancing the overall work environment [7]. 6S is a system that includes the Safety principle as an addition to the fundamental principles of the 5S application. This principle is added with the aim of increasing safety in workplaces and minimizing potential hazards. 6S encompasses six basic principles: Seiri, Seiton, Seiso, Seiketsu, Shitsuke, and Safety [8]. As the 6S System is applied either on a process or departmental basis, the Safety step aims to protect employees from occupational diseases and workplace accidents by implementing health and safety measures [9].

Importance in Machine Workshops

Machine workshops are typically places where complex machinery and equipment are intensively used. Operations such as welding, gas cutting, and casting require additional precautionary measures to reduce the number of potential incidents [10]. The 6S method is integral to industries, manufacturing, or construction activities. The implementation of the 5S+1 tools creates safer working conditions [11,12]. Implementing 6S enables operators to use personal protective equipment (PPE) and gear to prevent accidents [13].

Therefore, maintaining high safety standards in such establishments is critical for protecting the health and safety of employees. The addition of Safety in 6S implies risk identification, aiming to enhance productivity, job quality, improve occupational safety, and optimize discipline [14]. This approach, as a result of proper 6S implementation, may improve the safety of industrial units and overall conditions [15].

6S implementations not only establish physical order but also provide a strategy to strengthen the safety culture in workplaces, thereby reducing workplace accidents and hazards [6]. This article aims to thoroughly examine the impact of 6S implementation on occupational safety in a machine workshop, seeking to understand how this system can contribute to enhancing workplace safety. We believe our study could significantly contribute to elevating occupational safety standards in machine workshops.

2. MATERIAL AND METHOD

2.1. Implementation of 6S Methodology:

A risk evaluation was initially conducted in the machine workshop. This risk evaluation was carried out directly through field observation to track workers' daily work habits and verify their interactions with the surrounding environment.

According to the image of the factory which can be seen in Figure 1, to evaluate the impact of the 6S methodology on safety levels, 6S was applied in an area where risks were high due to the arrangement of finished flywheels at elevated heights, the scattered presence of raw materials, products, and waste materials in the environment, and close contact between workers and forklifts. The use of motorized industrial vehicles can contribute to increased productivity and efficiency but also poses a significant threat [16].

In the first stage, a Fine-Kinney risk evaluation was conducted to quantify the level of safety in the work area. Risk Evaluation Values were obtained by multiplying scores related to Frequency, Severity, and Probability. Once this step was completed, the 6S application was implemented, and a comparison was made between the risk evaluation conducted after the 6S implementation and the initial risk evaluation.

Although some hazards (such as manual use, ergonomics, etc.) were present during the workshop evaluation through direct observation by the assessor these hazards were not taken into account.

The completion of the 6S implementation action took approximately 28 days. To enable before-and-after comparisons, the initial state of the workshop environment was documented with photographs.

2.1.1 Seiri

The aim of Seiri is to eliminate unnecessary items and systematically organize the remaining elements for an efficient and effective workflow [17]. Therefore, a list of all materials in the workshop was compiled. Materials and equipment were categorized as essential and safe for the CNC machining process and those posing safety risks to create a clean, organized, and reliable environment. Damaged or faulty tools, unused equipment, and unnecessary materials were sent back to the factory stock for removal. The layout of CNC machines, workbenches, and other equipment was considered, integrating safety-focused elements into the Seiri process to establish a foundation for a safer and healthier working environment in the machine workshop.

2.1.2. Seiton

The Seiton stage in the 5S Lean Production system focuses on organizing and arranging items to enhance efficiency and safety [18]. In the CNC workshop, clear and unobstructed pathways were organized to facilitate the movement of workers and the transportation of materials. Easily accessible spaces were designated for frequently used tools. A systematic storage system was established to prevent tripping hazards for raw materials, ongoing projects, and finished products. A working system for the proper disposal of waste materials, such as metal shavings and scrap, was implemented to ensure a clean and safe working environment. Clear and visible safety signs indicating areas with potential hazards, emergency exits, and locations of safety equipment (fire extinguishers, first aid kits, etc.) were placed.

44

Figure 1. Picture depicting the workshop condition before the implementation of 6S.

2.1.3. Seiso

In the context of Lean production and the 5S methodology, "Seiso" represents the third S, meaning "Shine" or "Sweep." The purpose of Seiso is to keep the workplace clean and free from dirt, debris, and other contaminants [19]. In a machine workshop producing flywheels with CNC machines, Seiso involves creating cleaning practices that contribute not only to a clean workspace but also to an environment promoting safety and health. A routine plan was established to clean machine surfaces and floors to remove any oil, grease, or residues that could pose slipping hazards. Care was taken to keep storage areas clean and orderly to prevent the accumulation of dust and other pollutants on raw materials and finished products. Shelves were regularly checked and cleaned to maintain balance and prevent items from falling. These measures aimed to create a cleaner and safer machine workshop environment, reducing the risk of accidents, and enhancing overall production efficiency.

2.1.4. Seiketsu

The purpose of Seiketsu is to create and sustain standardized work practices to ensure the continued improvement achieved through Seiri, Seiton, and Seiso [20]. Detailed working procedures were prepared for each task and machine operation in the Computer Numeric Control (CNC) machine workshop. These procedures clearly defined the correct and safe way to perform tasks and use materials. Visual cues and signs were used to emphasize safety information and procedures. A checklist was created to evaluate the condition of machines, the organization of work areas, and the use of safety measures.

2.1.5. Shitsuke

Shitsuke, or self-discipline, is undoubtedly one of the most critical stages for the successful adoption of 5S. While implementing 5S is relatively simple, the challenge lies in maintaining this principle and preventing the return of old habits. Self-discipline involves employees performing their responsibilities without the need for reminders [21]. Continuous observations were made to ensure that good practices remained in the field and that all achieved results were not temporary. Regular observations were made to remind employees of the importance of sustaining these changes. Evaluations began to take place weekly after operators developed the habit of keeping their work areas clean and organized.

2.1.6. Safety

In addition to the steps of Seiri, Seiton, Seiso, Seiketsu, and Shitsuke within the 5S System, the 6S System includes the Safety step [8]. Since the 6S System can be applied at the process or department level, Safety focuses on implementing health and safety measures to protect employees from occupational diseases and workplace accidents [9]. An effort was made to create a safety culture by involving employees in the process of improving and enhancing safety measures. Visual cues, such as safety posters, signs, and bulletin boards, were used to remind employees of safety rules. Safety practices were regularly reviewed to address the evolving needs and challenges in the workshop environment.

2.2. Risk Assessment Method

In this current study, the Fine-Kinney risk analysis method was employed for risk evaluation. The Fine-Kinney Risk Evaluation Method is calculated as R = O x F x Ş, where O = Probability, F = Frequency, Ş = Severity, and R = Risk Score.

In their study conducted in 1976, Kinney and Wiruth defined 'very strong probability', which they set as a reference point with a 10-point scale, as an event that has occurred before, is possible to repeat and will occur in the future and assigned 10 to this value. They assigned another reference point, 'Low Probability', to the value 1. They gave the value of 'Almost Impossible' probability, which forms the base of the probability scale, to 0.1, and

45

the intermediate values created the scale as decreasing values depending on experience [22].

Table 1. Probability Score Ranking.

Category	Value
Almost impossible	0.1
Impossible	0.2
Weak possibility	0.5
Low probability	1
Rare but possible	3
Highly probable	6
Very strong possibility	10

Kinney and Wiruth also created a scale table for frequency values in the same study. In the frequency table, risks are classified according to their frequency of occurrence on a time basis, such as hourly, daily, or annual. As can be seen in Table 2, if the frequency of the determined risk is 'hourly', it is accepted that the risk occurs 'continuously' and the frequency value used in creating the risk value is determined as 10, which is the highest value in the table, 0.5 as the lowest value, and 3 as the middle value [22].

Table 2. Frequency (Exposure Frequency) Score Ranking.

Category	Value
Very rare (once a year or every few years)	0.5
Quite rare (once or a few times a year)	1
Rare (once or a few times a month)	2
Occasional (once or a few times a week)	3
Frequent (once or a few times a day)	6
Continuous (once or multiple times within an hour)	10

In calculating the risk score, the amount of damage resulting from the risk is taken into account in the scale table prepared for the third multiplier, severity. The severity scale table obtained as a result of this calculation is given in Table 3. In the scale created here, scoring was made by taking into account the death rate caused by violence [22].

Table 3. Damage/Consequence (Severity) Score Ranking.

Category	Value
Multiple fatalities	100
Fatal accident	40
Permanent injury	15
Significant damage	7
Minor damage	3
Near miss	1

Depending on the determined risk, probability, frequency and severity values are obtained from the relevant tables and the risk score is determined by multiplying the three parameters. Obtained risk scores are classified according to Table 4 [22].

Table 4. Risk Skor Evaluation Result.

Risk Skor	Category	Things to do
R ≥ 400	Very high risk	Tolerance for risk is unacceptable. Immediate measures should be taken.
200 ≤ R < 400	High risk	Should be improved within a few months.
70 ≤ R < 200	Significant risk	Should be carefully monitored. Improvement should be made within one year.
20 ≤ R < 70	Possible risk	Should be kept under observation. Control methods should be developed.
R < 20	Insignificant risk	No probability of causing harm. Not a priority

Table 5. Risk Evaluation Table.

Hazard Risk Level Identification Table									
Before 6S					After 6S				
Danger	P	S	F	Score	Possible risk	P	S	F	Score	Result
Knocking over of stacked gears	3	15	2	90	Significant risk	0.5	15	2	15	Insignificant risk
Forklift hitting gears	3	15	1	45	Significant risk	1	15	1	15	Insignificant risk
Forklift hitting workers	1	40	2	80	Significant risk	0.5	40	1	20	Possible risk
Storage stacking	3	15	2	90	Significant risk	0.5	15	2	15	Insignificant risk
Tripping over parts and falling	6	7	3	126	Significant risk	2	7	2	28	Possible risk
Objects falling	3	15	3	135	Significant risk	1	15	2	30	Possible risk

3. RESULTS AND DISCUSSION

As a result of creating a systematic storage area for raw materials and completed spur gears, wider safe passageways were established between forklifts and workers, eliminating the possibility of the forklift colliding with the products and minimizing the risk of accidents. The elimination of metal chips and unused scrap materials resulted in removing tripping and falling hazards. Regularly checking and organizing shelves to maintain balance and prevent objects from falling reduced the risk of objects falling from the shelves.

In the initial phase of this study, a risk evaluation was conducted in the workshop environment. To compare the scenario before and after the implementation of 5S and to understand whether there was any impact of 6S application on workshop safety after the implementation of 5S, a new risk evaluation was conducted.

The results, as seen in Figure 2, indicate that by applying 6S to the identified location and utilizing risk evaluation, it is possible to reduce the total risk by 77.4%."
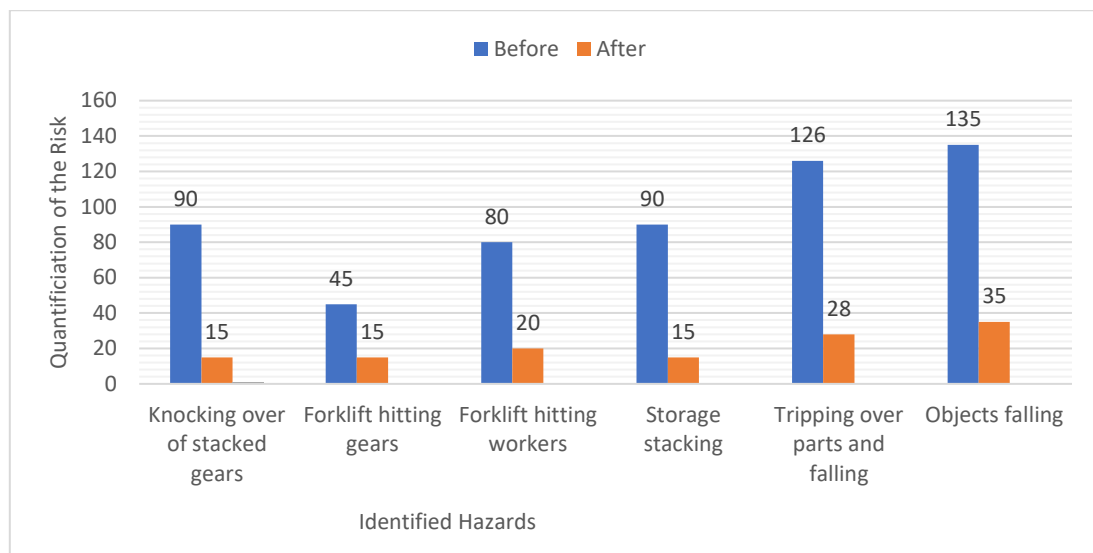
Figure 2. Risk assessment before and after 6S.

4. CONCLUSIONS

This current study investigated the application of 6S (5S+Safety) in the machine workshop of a factory producing flywheels in Konya, exploring its potential contributions to production efficiency and workplace safety conditions. The following results were obtained from the study:

The research highlighted that, in addition to being a powerful tool for organizing and optimizing the workplace environment, ensuring workplace safety is crucial. The results demonstrated that by applying 5S+1S, or 6S, in the identified location and utilizing the risk evaluation tool, it is possible to reduce the total risk by up to 77.4%. The time saved in finding tools, the reduction in wasted materials, and improvements in overall workspace efficiency were observed as benefits.

Acknowledgement

REFERENCES

[1] Rubin M. 5S for operators. Productivity Press: New York (NY); 1996.

[2] Fabrizio T, Tapping D. 5S for the Office. Organizing the Workplace to Eliminate Waste. Productivity Press: New York (NY); 2006.

[3] Koenigsaecker G. Leading the lean enterprise transformation. Productivity Press :New York (NY); 2009.

[4] Oppenheim BW, Felbur M. Lean for banks. Improving quality, productivity, and morale in financial offices. CRC Press: New York (NY); 2015.

[5] Harris C, Harris R. Developing a lean workforce. a guide for human resources, plant managers and lean coordinators. Productivity Press: New York (NY); 2007.

[6] Badiru AB. Handbook of industrial and systems engineering. CRC Press: New York (NY); 2014.

[7] Rojasra PM, Qureshi MN. International Journal of Modern Engineering Research (IJMER). 2013; 3(3): 1654-1660.

[8] Marria P, Williams SJ, Naim M. Total Quality Management & Business Excellence: 5S Creating an Efficient and Safer Work Environment. 2014; 25(12): 1410-1428. doi:10.1080/14783363.2012.704281.

[9] Gapp R, Fisher R, Kobayashi K. Implementing 5S within a Japanese Context: An Integrated Management System. Management Decision. 2008; 46 (4): 565-579. doi:10.1108/00251740810865067.

[10] Sukdeo N. Application of 6S methodology as a lean improvement tool in an ink manufacturing company, 2017 IEEE International Conference on Industrial Engineering and Engineering Management (IEEM); 2017. p. 1666–1671. doi.org/10.1109/IEEM.2017.8290176

[11] Purohit SR, Shantha V. International Journal of Scientific & Engineering Research: Implementation of 5S methodology in a manufacturing industry. 2015; 6(8): 225-231.

[12] Cabrera JL, Corpus OA, Maradiegue F, Álvarez J. Improving Quality By Implementing Lean Manufacturing: Spc, And Haccp in the Food Industry. A Case Study. S Afr J Ind Eng. 2020;31(4):194–207. https://doi.org/10.7166/31-4-2363

[13] Sommer AC, Blumenthal EZ. Survey of Ophthalmology: Implementation of Lean and Six Sigma principles in ophthalmology for improving quality of care and patient flow. 2019; 64(5):720–728. https://doi.org/10.1016/j.survophthal.2019.03.007

[14] Sârı AD, Suryoputro MR, Rahmillah FI. Materials Science and Engineering: A study of 6S workplace improvement in Ergonomic Laboratory. In IOP Conference Series Publishing; 2017, p.277 .

[15] Pacana A, Woźny A. Production engineering archives: Draft questions of 5S pre-audit with regard to health and safety standards for tires retreating plant. 2016; 13(3): 511-560.

[16] Horberry T, Larsson TJ, Johnston I, Lambert J. Applied ergonomics: Forklift safety, traffic engineering and intelligent transport systems: A case study. 2004; 35(6): 575-581.

[17] Hough R. Management services: 5S implementation methodology. 2008; 52(2): 44-45.

[18] Lanigan J. SMT Magazine: 5S provides competitive lean foundation. 2004; 70-72.

[19] Chapman CD. Quality Progress: Clean House with Lean 5S. 2005; 38 (6): 27-32.

[20] Osada T. The 5S: Five Keys to a Total Quality Environment. Tokyo: Asian Productivity Organization. 1991.

[21] Pinto JLQ, Matias JCO, Pimentel C, Azevedo SG, Govindan K, Pinto JLQ, Govindan K. Lean Manufacturing Tools: Implementation Through Lean Manufacturing Tools. 2018; 39-112.

[22] Kinney GF, Wiruth AD. Practical Risk Analysis for Safety Management (No. NWCTP- 5865). Naval Weapons Center China Lake CA. (1976).

Türk Doğa ve Fen Dergisi
Turkish Journal of Nature and Science
www.dergipark.gov.tr/tdfd

BİNGÖL UNIVERSITY

Performance Analysis of Compression Algorithms on Matrix Data: Data Transfer Optimization in Microservices Architectures

Faruk ATASOY[1*] iD **, Alper AKKAYA[1]** iD **, Nadir KOCAKIR[1]** iD **, Önder KARADEMİR[1]** iD

[1] Özdilek Ev Tekstil San. ve Tic. AŞ, Özveri Ar-Ge Merkezi, Bursa, Türkiye
Faruk ATASOY ORCID No: 0009-0005-4177-9852
Alper AKKAYA ORCID No: 0009-0007-1927-6989
Nadir KOCAKIR ORCID No: 0000-0001-7421-0631
Önder KARADEMİR ORCID No: 0000-0001-5757-7335

*Corresponding author: faruk.atasoy@ozdilek.com.tr

Abstract: With the rapid proliferation of microservices architectures these days, the efficient and fast transfer of large matrix data between services has become a significant challenge. This study presents an analysis aimed at finding solutions to this challenge. The analysis addresses the compression and decompression of large matrix data, focusing on lossless compression algorithms to optimize data transfer without data loss. The study is implemented on an example scenario. This scenario is taken from a project with a microservice architecture. In the example scenario, an image processing service developed in Python programming language generates 640x480 matrix data. After going through a compression algorithm, this data is periodically transferred to a backend service developed in C# programming language. This data is then stored in a database. In the final stage, decompression operations are performed so that this data can be used for reporting. The performance of various compression algorithms in the data compression, database storage and report generation stages is extensively tested. Within the scope of the study, tests were performed using five different compression algorithms (Gzip, Zlib, Deflate, Brotli and Bz2). The results are obtained through performance tests aimed at determining the most optimized end-to-end solution. Analyzing the performance of the compression algorithms on the example scenario, the Brotli algorithm gives the most optimal result in terms of both speed and compression size. This work makes an important contribution to data transfer optimization in microservice architectures and provides a reference for research in this area by presenting the performance analysis of various compression algorithms.

49

Veri Sıkıştırma Algoritmalarının Matris Verileri Üzerindeki Performans Analizi

Anahtar Kelimeler
Kayıpsız Veri Sıkıştırma Algoritmaları,
Veri Transferi,
Microservices,
Matris Verisi

Öz: Son zamanlarda mikroservis mimarilerinin hızla yayılmasıyla birlikte, büyük matris verilerinin hızlı ve verimli bir şekilde servisler arasında transferi, önemli bir zorluk haline gelmiştir. Bu çalışma, bu zorluğa çözüm bulmayı amaçlayan bir analiz sunmaktadır. Analiz, büyük matris verilerinin sıkıştırma ve açma işlemlerini ele almakta ve veri transferini optimize etmek için veri kaybı olmadan çalışan sıkıştırma algoritmalarına odaklanmaktadır. Çalışma, bir örnek senaryo üzerinde uygulanmıştır. Bu senaryo, mikroservis mimarisine sahip bir projeden alınmıştır. Örnek senaryoda, Python programlama dili ile geliştirilmiş bir görüntü işleme servisi, 640x480 boyutunda bir matris verisi üretmektedir. Bu veri, bir sıkıştırma algoritmasından geçtikten sonra periyodik olarak C# programlama dili ile geliştirilmiş bir back-end servise transfer edilmektedir. Bu veri daha sonra bir veritabanında depolanmaktadır. Son aşamada, bu verinin raporlama için kullanılabilmesi için açma işlemleri gerçekleştirilmektedir. Çeşitli sıkıştırma algoritmalarının performansı, veri sıkıştırma, veritabanı depolama ve rapor oluşturma aşamalarında detaylı bir şekilde test edilmiştir. Çalışma kapsamında beş farklı sıkıştırma algoritması (Gzip, Zlib, Deflate, Brotli ve Bz2) kullanılarak testler gerçekleştirilmiştir. Sonuçlar, en optimize edilmiş end-to-end çözümü belirlemeye yönelik performans testleri ile elde

edilmiştir. Örnek senaryo üzerinde sıkıştırma algoritmalarının performansını analiz ederken, Brotli algoritması hem hız hem de sıkıştırma boyutu açısından en optimal sonucu vermektedir. Bu çalışma, mikroservis mimarilerinde veri transferi optimizasyonuna önemli bir katkı sağlamakta ve çeşitli sıkıştırma algoritmalarının performans analizini sunarak bu alandaki araştırmalara referans oluşturmaktadır.

1. INTRODUCTION

The rapid evolution of information technology is replacing traditional monolithic structures with microservice architectures that seek more agile and scalable systems. By decomposing software applications into small, independent services, microservice architectures aim to accelerate development processes, provide scalability and increase flexibility.

While the rise of microservice architectures has made software applications more flexible and scalable, this transformation has also brought with it the need to efficiently transfer large data sets. The fast and efficient transfer of large data sets between services has become critical. Problems such as bandwidth consumption, latency and storage costs arise during the transfer of big data. These problems are optimized through a number of methods such as data compression and coding, protocol optimization, cache utilization, parallel processing, distributed storage, etc.

This paper aims to optimize the problems that arise during the transfer of large matrix data between microservices by using compression algorithms. It focuses on the performance of Gzip, Zlib, Bz2, Deflate and Brotli lossless compression algorithms in the compression and decompression processes of matrix data transfer between Python and C# based applications with a message broker in between. It examines data transfer at each step of the process and provides detailed performance analysis. It also discusses their performance on matrix variants with different types of data sets. The results were obtained in the context of a real-life project. In addition, this study aims to shed light on the optimization of other microservices projects with large data transfers in different data types by using compression algorithms.

The rest of the paper is organized as follows: Section 2 summarizes the literature review. Section 3 discusses the problem definition, information about compression algorithms, information about the algorithms that will be tested to solve the problem, and the types of matrices used in the testing. Section 4 presents the results of the performance tests. Section 5 contains the evaluation and comments on the final results.

2. LITERATURE REVIEW

With the rapid deployment of microservice architectures, the fast and efficient transfer of large matrix data between services emerged as a major challenge. In this context, a survey of the existing literature was conducted to gain various perspectives. Research on topics such as microservice architecture, lossless compression algorithms, matrix data, inter-service communication, etc., guided this review. Specifically, the realization of a gap in the literature concerning the optimization of large matrix data transmission between microservices motivated the investigation to fill this void. Enliçay et al. [1] undertook a study on the optimization of large datasets between microservices using the Deflate and Gzip algorithms. It was observed that no significant differences existed between the two algorithms, leading to the continued preference for the more prominent Gzip algorithm. Öztürk et al. [2] conducted tests on various NoSQL database technologies utilizing LZ4 and Zlib algorithms, finding that the Zlib algorithm, when used with MongoDB, achieved the best compression ratio. Conversely, when Snappy was employed, LevelDB yielded the fastest compression results. Deorowicz [3] provided a comprehensive examination of globally utilized compression algorithms, elucidating the differences and usage directions of these algorithms, along with underlying strategies and methods. This comparison facilitated an understanding of the appropriateness of each algorithm based on different scenarios.

Ramu [4] asserted that the adoption of microservice architecture has led to significant advancements in building scalable and flexible software systems. The study examined and evaluated the impact of microservices architecture on performance, focusing on vital elements such as inter-service communication, service discovery, data management, fault tolerance, and scalability. The findings contributed to the understanding of microservices and offered practical recommendations for architects and developers to optimize the performance of their applications. Kodituwakku and Amarasinghe [5] investigated and compared the performance of lossless data compression algorithms, evaluating their efficacy in compressing text data. The entropy of these algorithms was discussed, and an experimental comparison was conducted. Tapia et al. [6] described the transition of a project developed in monolithic architecture to the microservice level, noting the absence of mention regarding data optimization. Somashekar [7] presented effective solutions for optimizing data across microservices, focusing on optimizing the setup and layout of systems rather than the data itself. Semunigus and Pattanaik [8] analyzed differences between Huffman encoder, LZW encoder, and Arithmetic encoder, which was deemed insufficient for addressing both the analysis of matrix defects and the control of foundation disassembly. The blocks suitable for the project were identified as the high-level changes constructed with these blocks.

50

2
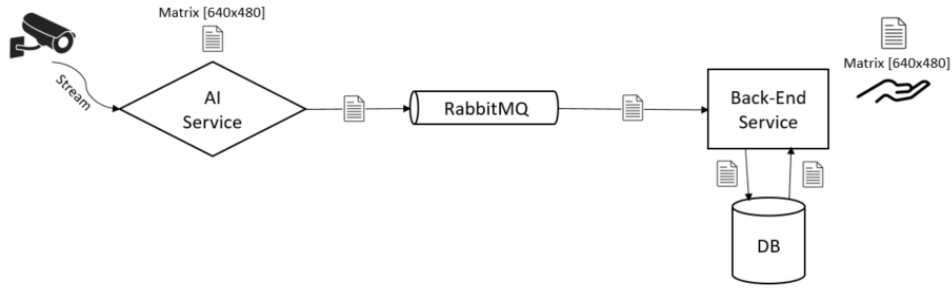
Figure 1. The journey of matrix data on the project architecture.

The mentioned studies above provide a comprehensive overview of matrix data transfer in microservices architectures. However, it is crucial to consider the limitations and gaps in the existing research in this area. This article focuses on existing studies to understand the shortcomings in the current literature and highlight how its own research aims to contribute to filling these gaps.

3. LITERATURE REVIEW

3.1. Problem Description

The system we are working on is built within the microservices architecture. The system architecture is shown in Figure 1. The end user completes the setup of the artificial intelligence service by selecting one of the previously registered cameras in the system. In the subsequent process, the Angular-based front-end communicates the necessary configuration to the .NET Core-based back-end service through APIs. After the writing process to the database, the same configurations are stored on Redis, a discrete cache mechanism, in a key-value format. Simultaneously, the service responsible for coordinating Python-based artificial intelligence services is notified using Redis's pub-sub mechanism. Once the coordinating service is notified, it retrieves the settings from the relevant Redis key and initiates the process of the heat map module based on these settings. The artificial intelligence service now monitors camera recordings via the stream URL of the relevant camera within the specified time period in the settings. At the end of the period, it publishes the movement data of detected individuals to the relevant queue in RabbitMQ, which serves as a message broker. Another C#-based back-end service, listening to this queue, receives the relevant report and writes it to the PostgreSQL database.

The journey of the data necessitating performance optimization within the architecture is addressed in Figure 1. The artificial intelligence service monitors the camera, sends the acquired data to the back-end service through RabbitMQ. Here, the data is later written to the database for use during report preparation.

All these operations are conducted to monitor, analyze, and generate reports on the movements of people visiting social areas, primarily malls and hypermarkets. The obtained data is stored in the database for later reporting. If desired, data sets are presented to end users on a daily, monthly, or yearly basis. The visualization of these data sets benefits from the heat map method.

The periodic data obtained by the artificial intelligence service is of a two-dimensional integer array type. Therefore, we can refer to it as a two-dimensional matrix. The first dimension of this matrix has a size of 640, and the second dimension has a size of 480 characters. The majority of matrix data consists of 0 parameters. Other parameters different from 0 represent the number of people passing through that point. The reason for the matrix size being 640x480 is due to the camera resolution. Due to the excess of matrix elements, the size of the data sometimes reaches megabytes. The largeness of the data has made it essential to optimize the process in terms of delays in transfer, storage costs, and resource consumption. Especially in the preparation of heat map reports, pulling, summing, and serving matrix data of 640x480, which can be tens or hundreds, from the database will result in significant resource consumption and delays.

Research has concluded that utilizing compression algorithms would be beneficial to optimize the process. Figure 2 shows that the data needs to be optimized at 4 different points.

51
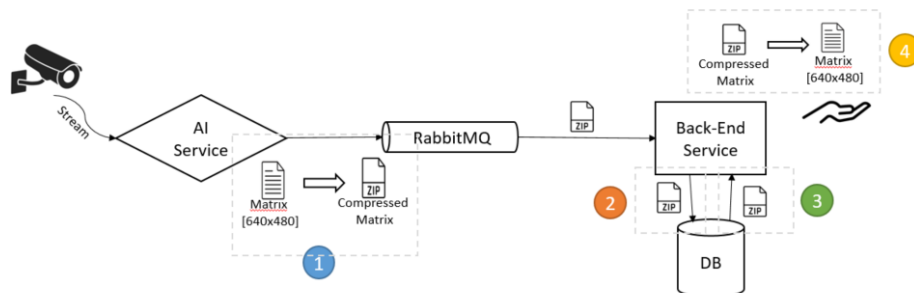
Figure 2. Showing the stages where matrix data is processed on the architecture.

3.2. Compression Algorithms

A data compression algorithm is a software or hardware method used to process data more efficiently during storage or transmission. Data compression algorithms are typically divided into two main categories. [10]
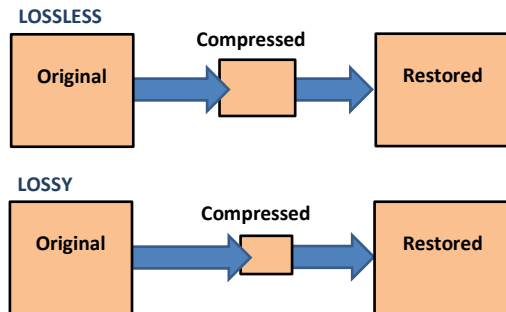
Figure 3. Behavior of compression algorithms.

The first consideration when determining algorithms to be considered for evaluation is to prefer lossless compression algorithms, as each parameter in the matrix is deemed to be highly significant. The second condition is to select algorithms that can be used in both the C# and Python programming languages. After making this distinction, the final condition to consider is the active preference and usage of algorithms in the software industry. Through literature reviews and research, we have decided to evaluate five different algorithms. Five compression algorithms (Gzip, Zlib, Deflate, Brotli, and Bz2) have been examined for data transfer optimization in micro services architectures.

3.2.1. Gzip

Gzip [11] is an algorithm developed for data compression purposes. It primarily operates using the Lempel-Ziv (LZ77) compression algorithm and Huffman coding. LZ77 analyzes the data and provides compression by identifying consecutive repeating patterns. Huffman coding adds an extra compression step by providing a shorter representation for more frequently occurring symbols. The main features of Gzip include:

• Effective Compression: It efficiently compresses data, reducing file sizes effectively.
• LZ77 and Huffman Coding: It performs compression using LZ77 and Huffman coding as fundamental algorithms.
• Usage in Web Pages: It is commonly used, especially on web servers, to compress text-based data sent to browsers. This enables faster loading of web pages.

Gzip is a widely used compression algorithm across various applications and is preferred for tasks such as data transfer over the internet and file archiving.

3.2.2. Zlib

Zlib [9] is a data compression library developed based on the Deflate algorithm. Zlib is commonly used for compression and archiving operations in the "gzip" format, although Zlib itself only encompasses compression features. The key features of Zlib include:

• Fast and Efficient Compression: Zlib reduces file sizes by compressing data quickly and efficiently.
• Portability: Zlib can be used on many different platforms and operating systems, allowing for a wide range of applications.
• Ease of Use: The Zlib library provides an easy-to-use API, facilitating the integration of compression operations for developers.

Zlib is widely utilized for data compression and archiving by web browsers, servers, databases, and many other applications.

3.2.3. Deflate

Deflate [13] is an effective algorithm used for data compression, combining two fundamental components: the LZ77 (Lempel-Ziv 1977) compression algorithm and Huffman coding.

• LZ77 (Lempel-Ziv 1977): This algorithm analyzes the data and provides compression by identifying consecutive repeating patterns. It encodes new blocks by referencing previous data blocks.
• Huffman Coding: It ensures symbols in the compressed data are represented with shorter codes. Frequently used symbols have shorter codes, while less frequently used symbols have longer codes.

The Deflate algorithm is widely used for compression and decompression operations. File formats like Gzip, Zip, and PNG can utilize the Deflate compression algorithm. Deflate is known for its fast operation, high compression ratios, and broad usability. Web browsers, file archiving, databases, and many applications prefer Deflate to optimize data transfer.

3.2.4. Brotli

Brotli [9] is a data compression algorithm developed by Google. It is designed to replace other popular compression algorithms and is specifically used to speed up the loading of web pages. Brotli aims to achieve higher compression ratios and better performance than Deflate algorithms (such as gzip and zlib). Some of its features include:

•High Compression Ratios: Brotli provides high compression ratios, especially for text-based content. This helps in delivering web pages faster and more efficiently.
• Adaptive Algorithm: Brotli uses an adaptive algorithm that can adjust the compression strategy based on the type and structure of the content. This results in more effective compression for various data types.
• Support for Web Browsers and Servers: Brotli is supported by modern web browsers and web servers. This enables faster loading of web pages, enhancing the overall user experience.

52

• Platform-Independent: Brotli can be used on different platforms and operating systems, offering a wide range of usability.

The use of Brotli plays a significant role, particularly in data transfer over the internet and web performance optimization. Faster loading of web pages contributes to an improved user experience.

3.2.5. Bz2

Bz2 is a compression algorithm and accompanying program used for data compression, also known as "bzip2." It was developed by Julian Seward. Unlike traditional compression algorithms like ZIP and Gzip, bz2 combines techniques such as Burrows-Wheeler Transform (BWT) and Huffman coding. Some of its features include:

• High Compression Ratios: Bz2 typically provides higher compression ratios compared to some other compression algorithms.
• Burrows-Wheeler Transform (BWT): This transformation reorganizes the data, highlighting repeated patterns and leading to more effective compression.
• Huffman Coding: It ensures symbols in the compressed data are represented with shorter codes. This involves shorter codes for frequently used symbols and longer codes for less frequently used symbols.
• Platform-Independent: Bz2 can be used on different platforms and operating systems.
• Data Archiving: It is commonly used for file archiving and distribution.
The bz2 compression algorithm is widely used, especially in UNIX and Linux-based systems, and users often prefer the command-line tool named "bzip2" for compression tasks.

3.3. Matrix Types Examined

The performances of these algorithms have been measured on three different large-sized matrix data sets in processes such as compression, compressing and writing to the database, compressing, writing to the database, and then reading, as well as compressing, writing to the database, reading again, and decompressing. Although the type of matrix that solves our problem is a matrix containing a large number of zeros, to shed light on and assist in future studies related to the subject, we did not limit our tests to a single type

of matrix but conducted tests on various matrix types. The general format of the examined large-sized matrix data is as follows:

• **Random Matrix**
Elements are randomly chosen integers. Example: [{1896322487, 423, 837, 29895, 5, ...}, {284997874, 5713597144, 77, 6852, ...}, ...]

• **Sequential Elements Matrix**
Elements are consecutively repeating integers. Example: [{11, 11, 22, 11, 11, 22, ...}, {11, 11, 22, 11, 11, 22, ...}, ...]

• **Matrix with Many Zeros**
Matrix with mostly zero elements, and integers. Example: [{0, 0, 598, 0, 0, 0, 85479, ...}, {0, 0, 8, 0, 0, 923559, 0, ...}, ...]

4. EXPERIMENTAL RESULTS AND DISCUSSION

Within the scope of the study, five different compression algorithms (Gzip, Zlib, Deflate, Brotli, and Bz2) underwent performance testing. These tests were focused on data compression ratios as well as compression and decompression times. All operations were performed according to the hardware and software standards shared in Table 1.

Table 1. Test Environment Components.

Sistem	Windows 11 (10.0.22000.2295/21H2/SunValley) 12th Gen Intel Core i7-1260P, 1 CPU, 16 logical and 12 physical cores, Kingston SSD snv2s2000g
.NET SDK	7.0.400
Database	PostgreSQL 15.3, compiled by Visual C++ build 1914, 64-bit
Measurement Tool	BenchmarkDotNet v0.13.7

4.1. Experimental Results

The numbered figures in Figure 4 represent the operations that will be subjected to performance testing. The location of these operations in the architecture can be found in Figure 2 in Section 3.1. The first numbered figure represents compressing the matrix, the second numbered figure represents writing the compressed matrix to the database, the third figure represents reading the compressed matrix data from the database, and the
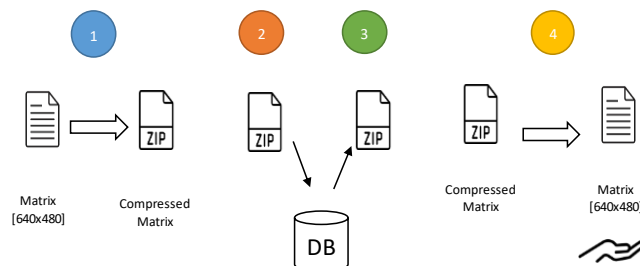
Figure 4. Operations included in the test and their numbers.

53
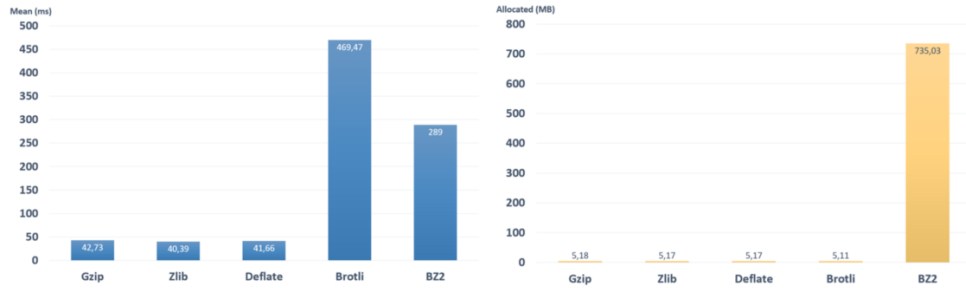
Figure 5. Complex matrix performance measurements belong to just first operation in Figure 4.

fourth and last figure represents restoring the compressed matrix data.

4.1.1. Complex matrix performance measurements

Graphs in Figure 5 compare the performance of five different compression algorithms in terms of two key metrics: processing speed and memory usage. The first graph shows the average processing time of each algorithm in milliseconds, showing that Gzip, Zlib and Deflate have similar and relatively low processing times. In contrast, Brotli's processing time is higher than all three, while BZ2 has by far the slowest processing time.

The second graph compares memory consumption in megabytes. Here again, Gzip, Zlib and Deflate show similar and quite low values in terms of memory consumption, while Brotli uses slightly more memory than these three, but the BZ2 algorithm requires a much larger amount. These results emphasize the need for an in-depth evaluation of compression processes in terms of time and memory efficiency.

These data suggest that the choice of compression algorithm should be carefully tailored to the application requirements. For example, it can be concluded that Gzip or Zlib may be preferable when speed is critical, while Brotli or BZ2 may be more appropriate in scenarios where compression ratio is more important. However, the high memory consumption and low speed of BZ2 can be a significant disadvantage, especially for real-time systems or resource-constrained environments.

Graphs in Figure 6; The first graph depicts the mean time taken by each algorithm to compress a dataset, measured in milliseconds (ms). Here, Gzip, Zlib, and Deflate show relatively similar and modest compression times at 60.44 ms, 46.65 ms, and 46.28 ms respectively,

suggesting efficient performance in time-sensitive applications. Brotli, however, takes substantially longer at 498.63 ms, which may be a trade-off for better compression ratios. BZ2 is significantly slower at 182.75 ms, indicating that while it may offer high compression ratios, it is less suitable for scenarios where time efficiency is critical.

The second graph compares the algorithms based on the amount of memory allocated during compression, measured in megabytes (MB). Gzip, Zlib, and Deflate again cluster closely together, with each requiring just over 5 MB of memory, pointing towards a low memory footprint. Brotli's memory allocation is marginally higher at 5.11 MB, which could be justified by its potentially better compression efficiency. However, BZ2 stands out with a substantially higher memory requirement of 735.03 MB, which is orders of magnitude greater than the others. This suggests that BZ2's compression technique, while perhaps yielding high compression ratios, is extremely memory-intensive, making it less feasible for systems with limited memory resources.

In summary, when considering a compression algorithm for practical use, it's crucial to weigh the trade-offs between compression time, memory usage, and compression efficiency. Gzip, Zlib, and Deflate present themselves as balanced choices for general purposes. In contrast, Brotli may be more suitable when compression efficiency outweighs the need for speed, and BZ2 might only be practical when memory resources are abundant, and compression ratio is the paramount concern.

Graphs in Figure 7; In the first graph, we examine the mean compression time in milliseconds (ms) for each algorithm. Gzip shows a mean time of 72.91 ms, Zlib at 50.21 ms, and Deflate at 49.12 ms, which are fairly close

54
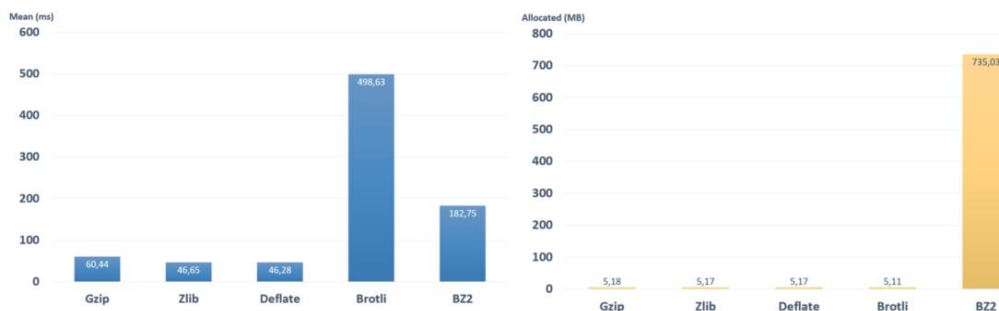
Figure 6. Complex matrix performance measurements belong to first and second operations in Figure 4.
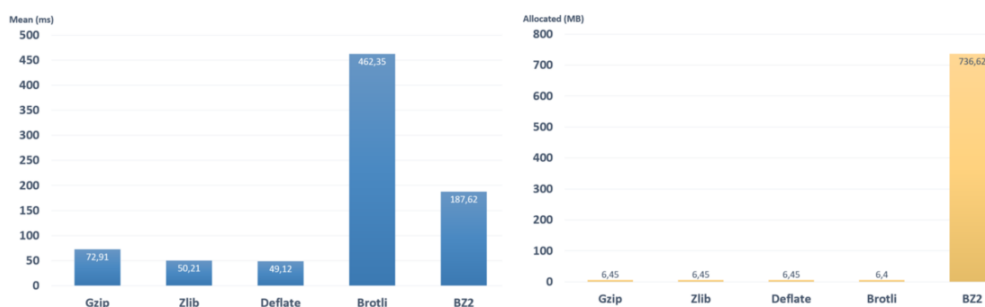
Figure 7. Complex matrix performance measurements belong to first, second and third operations in Figure 4.

in performance, indicating they could be suitable for tasks where moderate compression speed is required without significant time constraints. Brotli dramatically increases to 462.35 ms, suggesting a possible preference for a higher compression ratio at the cost of time efficiency. BZ2 is notably quicker than Brotli at 187.62 ms, but still substantially slower compared to Gzip, Zlib, and Deflate, which may make it less ideal for time-critical applications.

The second graph shows memory allocation during the compression process in megabytes (MB). Gzip, Zlib, and Deflate maintain a low memory footprint at approximately 6.45 MB each, making them practical for environments with memory usage constraints. Brotli has a similar memory requirement at 6.4 MB, slightly less than the others, which is impressive considering its compression time. BZ2, however, requires a staggering 736.62 MB of memory, which is an order of magnitude higher than its counterparts. This high memory demand could severely limit BZ2's usability, especially in systems where memory is a scarce resource.

In conclusion, while Gzip, Zlib, and Deflate offer balanced performance with low memory consumption, Brotli might be considered when the compression ratio is more important, provided that the longer compression time is acceptable. BZ2, despite its moderate compression time, may only be viable in systems where ample memory is available and the highest possible compression ratio justifies its significant memory allocation. These insights are critical when selecting an algorithm for specific use cases, particularly when balancing the need for speed, efficiency, and available system resources.

Graphs in Figure 8; The first graph details the mean compression time, revealing that Gzip, Zlib, and Deflate

take 2,422.40 ms, 2,693.30 ms, and 499.9 ms respectively. These times suggest that while Gzip and Zlib have slower compression rates, Deflate is significantly faster, almost five to six times quicker than its counterparts. Brotli and BZ2 offer even better performance at 354.2 ms and 335.8 ms, respectively, which might make them preferable in time-sensitive scenarios where efficiency is paramount.

In the second graph, memory allocation is depicted, with Gzip, Zlib, and Deflate all showing minimal differences in their memory usage, ranging between 7.63 MB to 7.62 MB. Brotli's allocation is marginally lower at 7.57 MB, which could be considered negligible in most cases. However, BZ2 demonstrates a substantial increase in memory requirements, utilizing 742.29 MB. This considerable memory usage implies that BZ2 might only be suitable in situations where memory resources are abundant and a high compression ratio is required, despite its good performance in terms of compression speed.

Overall, the graphs suggest that while Brotli and BZ2 offer the best compression times, the latter does so at a significantly higher memory cost. This data is vital when considering the operational context of these algorithms, as it highlights the need to balance compression speed with resource consumption according to specific application needs.

4.1.2. Sequential elements matrix performance measurements

Graphs in Figure 9; In the first graph, the mean compression times are relatively low for Gzip, Zlib, and Deflate, recorded at 24.46 ms, 22.99 ms, and 22.62 ms, respectively. These figures suggest a high level of efficiency, with little to differentiate between the three in

55
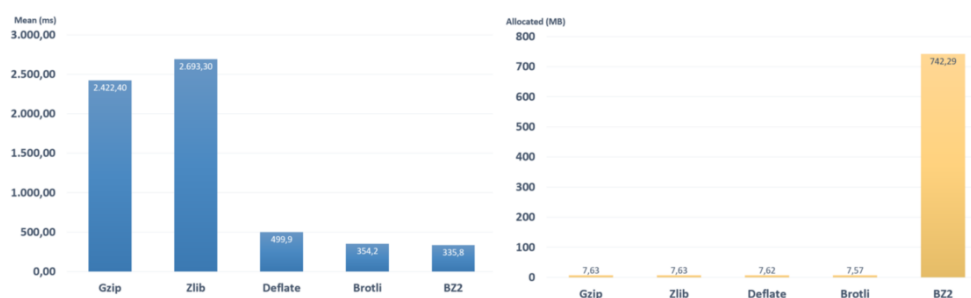
Figure 8. Complex matrix performance measurements belong to first, second, third and fourth operations in Figure 4.
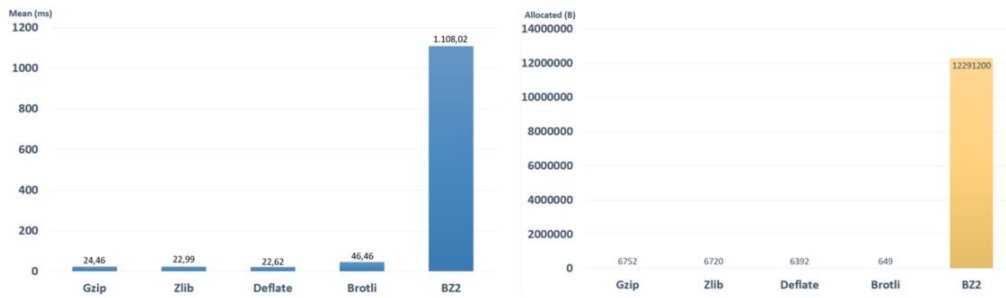
Figure 9. Sequential elements matrix performance measurements belong to just first operation in Figure 4.

terms of speed. Brotli shows a higher time of 46.46 ms, which could be attributed to its more complex compression algorithms designed for better compression ratios. BZ2, however, shows a significantly higher mean time of 1,108.02 ms, indicating that it is considerably slower than its counterparts. This would likely make BZ2 less suitable for applications where time efficiency is critical.

The second graph is particularly revealing regarding memory allocation. Gzip, Zlib, and Deflate use similar and minimal amounts of memory, with allocations at 6752 bytes, 6760 bytes, and 6392 bytes, respectively, which demonstrates their suitability for memory-constrained environments. Brotli has a slightly higher allocation at 649 bytes, which remains relatively modest. However, BZ2's memory allocation is an outlier, requiring a colossal 12,291,200 bytes. This is orders of magnitude greater than the other algorithms, suggesting it may be impractical for most applications due to its high memory demands, despite any potential benefits in compression ratio.

In summary, these visual data points emphasize the importance of considering both compression speed and memory usage when selecting an algorithm. While Gzip, Zlib, and Deflate offer the best balance for general use, Brotli might be an alternative for specific use cases that can tolerate slightly longer compression times. BZ2's high resource consumption makes it suitable only for niche applications where its compression benefits outweigh the significant memory requirements.

Graphs in Figure 10; From the first graph, we observe that Gzip, Zlib, and Deflate have quite competitive mean compression times of 25.76 ms, 23.58 ms, and 23.3 ms respectively. These small differences are unlikely to impact the choice of algorithm in scenarios where

compression time is somewhat flexible. Brotli's mean time is slightly higher at 34.87 ms, which is still within an acceptable range for many applications, considering that it typically achieves better compression ratios. BZ2, however, has a mean time of 1,153.63 ms, which is substantially higher than the others. This may limit its use to non-time-sensitive processes where compression efficiency is more critical.

In the second graph, memory allocation in kilobytes (KB) is represented, showing that Gzip, Zlib, and Deflate all have modest memory requirements at 65.13 KB, 65.1 KB, and 64.78 KB, respectively. Brotli is slightly more efficient at 59.28 KB. In stark contrast, BZ2 requires a dramatically higher amount of memory at 12,063.71 KB, which is nearly 200 times greater than its nearest competitor. This high memory allocation suggests that BZ2's use cases might be very specialized, where the benefits of its compression outweigh the cost in terms of memory usage.

The data from these graphs suggest that for most general purposes, Gzip, Zlib, and Deflate offer a good balance of speed and memory efficiency. Brotli stands out as a strong candidate when slightly higher compression times are acceptable, and memory efficiency is a priority. BZ2 appears to be a specialized tool that might be reserved for unique situations where its heavy memory use can be justified, likely in environments where memory is not a constraint and maximum compression is the primary goal.

Figure 11; From the compression time perspective, Gzip and Zlib are the quickest, with times of 26.51 ms and 21.89 ms, respectively, making them suitable for applications where speed is essential. Deflate and Brotli exhibit slightly longer compression times at 24.7 ms and 35.29 ms, respectively, with Brotli's longer time possibly

56
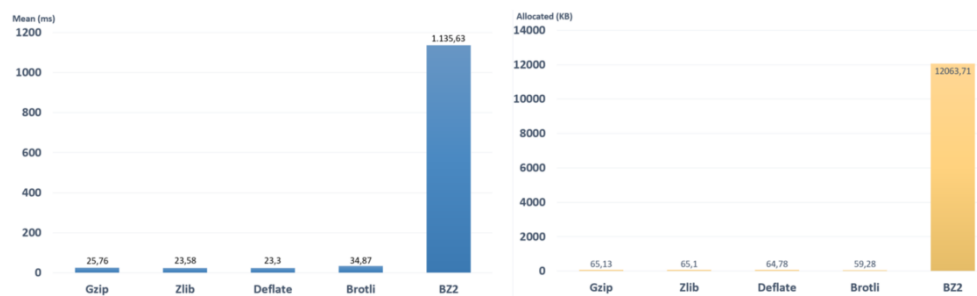
Figure 10. Sequential elements matrix performance measurements.
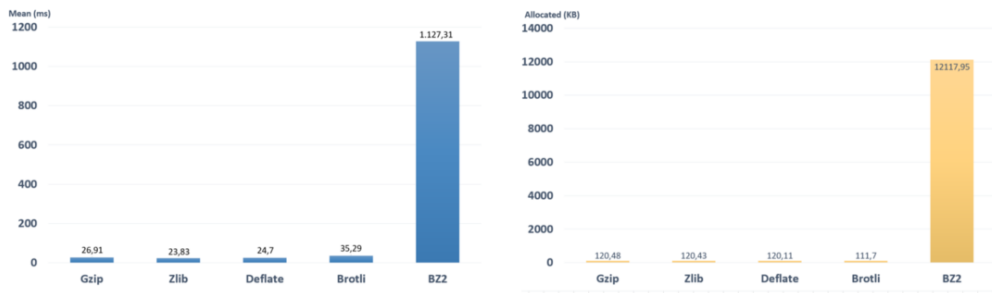
Figure 11. Sequential elements matrix performance measurements belong to first, second and third operations in Figure 4.

reflecting its focus on achieving higher compression ratios. BZ2 is the outlier, taking considerably longer at 1,127.31 ms, suggesting it might be less suited for time-sensitive processes.

The memory allocation chart shows that Gzip, Zlib, Deflate, and Brotli have similar and relatively low memory footprints, all under 1.3 MB. This is beneficial in resource-constrained environments where maintaining a small memory usage is crucial. In stark contrast, BZ2 requires a substantially larger amount of memory, at 17.27 MB, which may hinder its practicality in systems with limited memory availability.

Figure 12; Gzip and Zlib demonstrate relatively moderate compression times at 1,842.34 ms and 1,975.51 ms, respectively. Deflate follows closely, showing a time of 69.66 ms, suggesting a faster performance that could be beneficial in time-sensitive applications. Brotli shows a compression time of 1,502.17 ms, which is slower compared to Gzip and Zlib but faster than BZ2, which has the highest mean time at 11,879.34 ms, indicating it may be less efficient for rapid compression needs.

When examining memory allocation, Gzip, Zlib, Deflate, and Brotli are quite efficient, each requiring slightly over 1 MB of memory. This low memory footprint is advantageous for environments where resource conservation is essential. However, BZ2's memory requirement is much higher at 17.36 MB, making it potentially impractical for memory-constrained systems despite its slower compression time.

In an academic context, these findings would suggest that while Brotli and BZ2 have slower compression times, they might offer better compression ratios, which could be a trade-off depending on the application's requirements. However, the significantly higher memory usage of BZ2 could limit its use to systems where memory resources are not a concern.

4.1.3. Matrix With Many Zero Performance Measurements

Graphs in Figure 13; For compression time, Gzip is the fastest at 34.46 ms, closely followed by Zlib and Deflate at 29.32 ms and 30.61 ms respectively. Brotli is slightly slower at 56.54 ms, while BZ2 is the slowest at 67.27 ms.

Memory allocation shows Gzip, Zlib, and Deflate using less than 4 KB of memory, indicating high efficiency. Brotli requires slightly more at 671 bytes. BZ2, however, requires a much larger memory size of 12,197,576 bytes, which is substantially more than its counterparts.

In summary, Gzip, Zlib, and Deflate are efficient in both time and memory usage, suitable for most applications. Brotli trades off some speed for compression quality, while BZ2, due to its high memory demand, may only be practical for specific use cases where its compression benefits outweigh its resource usage.
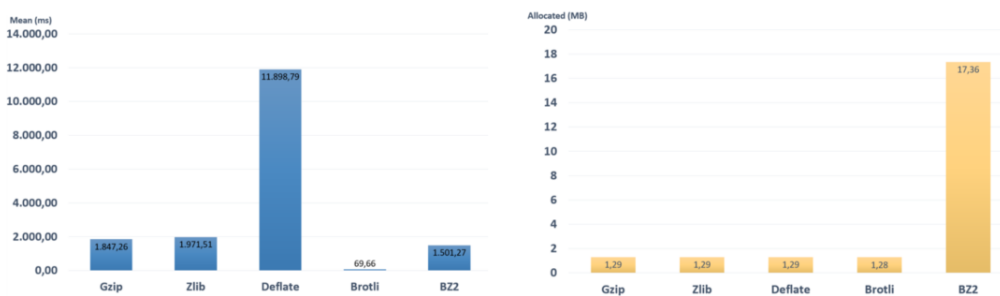
Figure 12. Sequential elements matrix performance measurements belong to first, second, third and fourth operations in Figure 4.
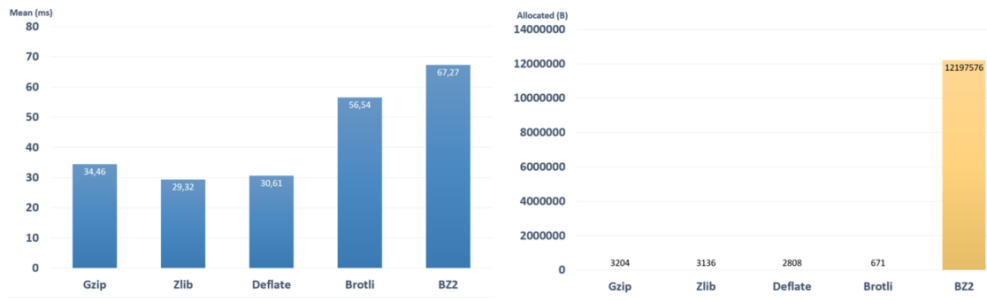
Figure 13. 4.2.3. Matrix with many zero performance measurements belong to just first operation in Figure 4.
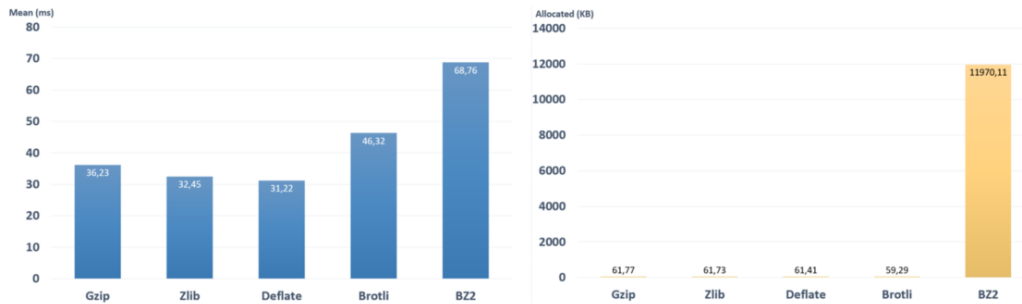
Figure 14. Matrix with many zero performance measurements belong to first and second operations in Figure 4.

Graphs in Figure 14; The mean compression times are fairly close for Gzip, Zlib, and Deflate, recorded at 36.23 ms, 32.45 ms, and 31.22 ms respectively, which suggests these algorithms are quite efficient. Brotli shows a higher time at 46.32 ms, and BZ2 is the slowest at 68.76 ms, which could be a drawback for rapid compression needs.

On the memory allocation front, Gzip, Zlib, and Deflate are comparable, requiring between 61.77 KB to 61.41 KB. Brotli is slightly more efficient at 59.29 KB. However, BZ2's memory requirement is exceptionally high at 11,970.11 KB, which may render it less practical for environments with limited memory resources.

In essence, Gzip, Zlib, and Deflate are suitable for general use, offering a good balance of speed and low memory usage. Brotli stands out as a slightly less efficient option in terms of speed but still maintains low memory use. BZ2, while slowest, may offer better compression ratios at the cost of significantly higher memory usage.

Graphs in Figure 15; Gzip has a compression time of 37.33 ms, Zlib is faster at 26.32 ms, and Deflate is very close to Zlib at 32.96 ms. Brotli is slower at 55.22 ms,

and BZ2 is the slowest at 71.6 ms.

For memory usage, Gzip, Zlib, and Deflate are nearly identical, ranging from 115.23 MB to 115.02 MB. Brotli is marginally more efficient at 111.79 MB. BZ2's memory allocation is significantly higher at 12,023.52 MB, suggesting it is less efficient in terms of memory usage.

Overall, Zlib and Deflate are the most efficient in both time and memory usage, while BZ2's high memory allocation could limit its practicality despite its compression capability.

Graphs in Figure 16; In terms of compression time, Gzip, Zlib, and Deflate exhibit high performance, with mean times of 9,452.95 ms, 11,166.46 ms, and 10,679.48 ms, respectively, indicating they are quite fast. Brotli has a lower time at 575.5 ms, and BZ2 is the most time-efficient at 62.98 ms.

Memory allocation shows that Gzip, Zlib, Deflate, and Brotli have similar low memory usage, around 1.29 MB to 1.28 MB. In stark contrast, BZ2 requires significantly more memory at 17.27 MB.
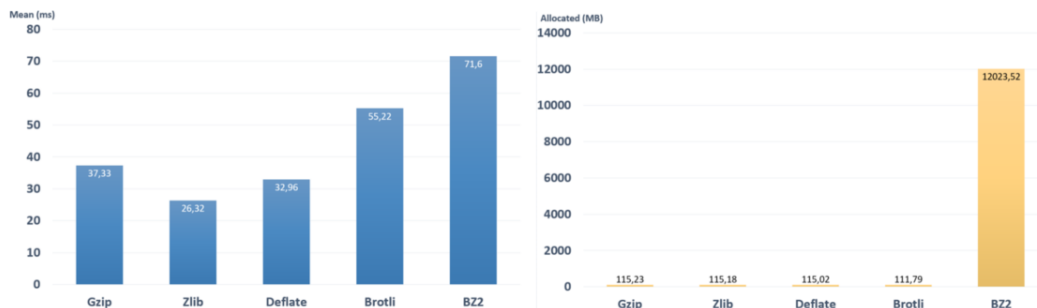
Figure 15. Matrix with many zero performance measurements belong to first, second and third operations in Figure 4.
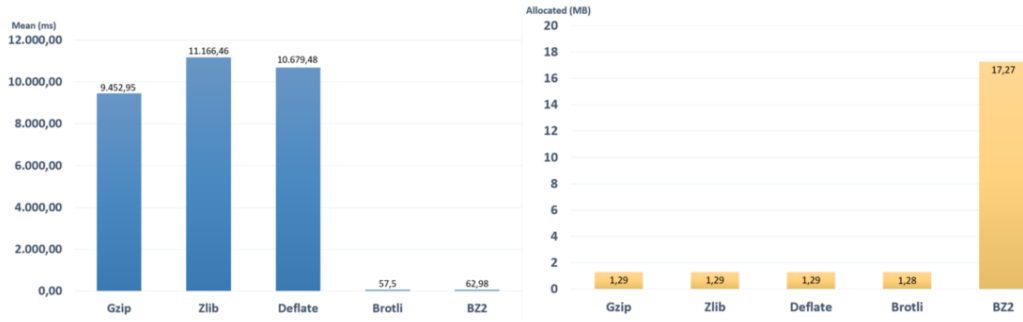
Figure 16. Matrix with many zero performance measurements belong to first, second, third and fourth operations in Figure 4.

BZ2 stands out with the lowest compression time but requires more memory, while Brotli offers a balance between efficient compression time and low memory usage. Gzip, Zlib, and Deflate, while slower, also maintain a low memory footprint.

4.2. Compression Performance Measurements

Figure 17 covers the performance of compression algorithms in minimizing the 63,684-byte matrix. As observed, the Brotli algorithm demonstrates a clear superiority compared to the others. Brotli, being the overall winner in performance tests, owes its distinction to its high compression ratio.

Figure 17. Compression ratios of algorithms.

5. DISCUSSION

The results of the experimental studies have shown that the Brotli algorithm provides the best performance. Brotli offers both a high compression ratio and fast compression and decompression times. Other algorithms either have a low compression ratio or slow processing times. These results provide a framework for the effective transfer of large matrix data in microservices architectures. An overall evaluation of the obtained results is presented below:

• Gzip, Zlib, and Deflate have been the most performant in the first three periods, providing similar results to each other.
• Brotli, despite lagging behind in performance in the first three measurements, has been the most efficient algorithm in the end-to-end test.
• While the BZ2 algorithm exhibited the worst performance in the first three periods, it yielded good results in the later periods; however, it did not meet the expected memory usage.

• The ultimate reason for Brotli being the optimal algorithm is its high compression ratio compared to others.
• Brotli algorithm provided the most optimal results for all types of matrices.

6. CONCLUSION

This study focuses on optimizing data transfer in microservices architectures and evaluates the performance of compression and decompression processes for large matrix data. The results obtained indicate that the Brotli algorithm provides the best solution in this context. It has been the most performant algorithm for three different types of matrices subjected to testing. This study serves as a reference for researchers and industry professionals interested in data transfer in microservices architectures. The provided information should not be limited to matrix-specific evaluations but should also be considered for other data formats.

59

Looking ahead, further research can expand upon this work by exploring a broader range of data formats such as text, JSON, and XML to determine the most effective compression algorithms for diverse data types. Additionally, investigating the distribution of compression and decompression tasks in distributed systems could offer insights into enhancing performance for large-scale data transfers. Embracing adaptive compression techniques and exploring hardware acceleration are promising directions that could lead to significant improvements in real-time data processing and efficiency. These future endeavors will build on the foundation laid by this study, offering a comprehensive understanding of data optimization in microservices architectures across various contexts and technologies.

Acknowledgement

REFERENCES

[1] Enliçay M, Şahin Ö, Ülger İ, Balçiçek ÖE, Baydarman MV, Taşdemir Ş. Veri Sıkıştırma Algoritmalarının Karşılaştırılması: Katılım Bankası Örneği. Konya: Selçuk Üniversitesi; 2014.

[2]   Öztürk E, Mesut A, Diri B. The performance analysis of data compression algorithms used in NoSQL databases. In: Proceedings of the International Conference on Computer Science and Engineering (UBMK 2016); 2016 Oct; Tekirdağ.

[3]   Deorowicz S. Universal lossless data compression algorithms [dissertation]. Gliwice: Silesian University of Technology; 2003.

[4]   Ramu V. Performance impact of microservices architecture. Rev Contemp Sci Acad Stud. 2023;3.

[5]   Kodituwakku SR, Amarasinghe US. Comparison of lossless data compression algorithms for text data. Indian J Comput Sci Eng. 2010;1(4):416-25.

[6]   Tapia F, et al. From monolithic systems to microservices: a comparative study of performance. Appl Sci. 2020;10(17):5797.

[7]   Somashekar G. Performance management of large-scale microservices applications [dissertation]. Stony Brook (NY): Stony Brook University; 2023.

[8]   Semunigus W, Balachandra P. Analysis for lossless data compression algorithms for low bandwidth networks. J Phys Conf Ser. 2021;1964(4).

[9]   Alakuijala J, et al. Brotli: A general-purpose data compressor. ACM Trans Inf Syst. 2018;37(1):1-30.

[10]   Bulut F. Huffman algoritmasıyla kayıpsız hızlı metin sıkıştırma. El-Cezeri. 2016;3(2).

[11]   Gailly J-l, Adler M. gzip [Internet]. Available from: http://ftp.gnu.org/gnu/gzip/gzip-1.6.tar.gz .

[12]   Zlib Compression Library [Internet]. Available from: http://www.zlib.net/ [cited 2024 Jan 10].

[13]   Deutsch P. Deflate compressed data format specification version 1.3. RFC 1951 (Informational). IETF; 1996.

Türk Doğa ve Fen Dergisi
Turkish Journal of Nature and Science

Selecting the most successfull recycling strategy over daily consumption products: application of q-Rung Orthopair Fuzzy Topsis method

Sinan ÖZTAŞ[1*] ID

[1] Ataturk University, Engineering Faculty, Industrial Engineering Department, Erzurum, Türkiye
Sinan ÖZTAŞ ORCID No: 0000-0002-9630-6586

*Corresponding author: sinanoztas@atauni.edu.tr

Abstract: Recycling is the process of collecting and reusing that helps the countries to achieve their sustainable development goals. This study, for the first time in the literature, considers the recycling of many daily consumption products as a decision-making problem with the q-rung orthopair fuzzy (q-ROF) approach. In Turkey, recycling initiatives are primarily led by the government and municipalities, involving either reprocessing in public facilities or collaboration with private enterprises. The research evaluates the effectiveness of recycling strategies, considering paper, plastic, textiles, batteries, frying oils, electronics, glass, and wood as alternative products. Criteria such as convertibility rate, resource usage for recycling, converted product lifespan, recycling process complexity, economic gain, product consumption rate, and trading opportunities are employed in the decision-making process. The q-rung orthopair fuzzy Technique for Order Preference by Similarity to Ideal Solution (q-ROFTOPSIS) method is applied to assess these criteria. Decision makers, comprising a recycling expert, a recycling business engineer, and an academician specializing in recycling studies, contribute to the evaluation. The study reveals electronic products as the most successful in recycling, while frying oils exhibit the least success.

61

En Başarılı Geri Dönüşüm Stratejisinin Gündelik Tüketim Ürünleri Üzerinden Seçilmesi: q-ROF Topsis Yöntemi Uygulaması

Anahtar Kelimeler
Geri dönüşüm,
q-ROF
Topsis,
Gündelik
tüketim
ürünleri

Öz: Dönüşüm, ülkelerin sürdürülebilir kalkınma hedeflerine ulaşmalarına yardımcı olan toplama ve yeniden kullanma sürecidir. Bu çalışma literatürde ilk kez birçok günlük tüketim ürününün geri dönüşümünü q-rung orthopair fuzzy (q-ROF) yaklaşımıyla bir karar verme problemi olarak ele almaktadır. Türkiye'de geri dönüşüm girişimlerine genellikle hükümet ve belediyeler tarafından liderlik edilmekte olup, geri dönüşüm kamu veya özel işletmelerle iş birliği içerisinde yürütülmektedir. Araştırma kâğıt, plastik, tekstil, pil, kızartma yağları, elektronik, cam ve ahşap gibi alternatif ürünleri değerlendirerek geri dönüşüm stratejilerinin etkinliğini değerlendirmektedir. Dönüştürülebilirlik oranı, geri dönüşüm için kaynak kullanımı, dönüştürülmüş ürün ömrü, geri dönüşüm sürecinin karmaşıklığı, ekonomik kazanç, ürün tüketim hızı ve ticaret fırsatları gibi kriterler karar verme sürecinde kullanılmaktadır. Bu kriterleri değerlendirmek için q-rung orthopair fuzzy topsis (q-ROFTOPSIS) yöntemi uygulanmaktadır. Karar vericiler bir geri dönüşüm uzmanı, geri dönüşüm alanında çalışan bir mühendis ve geri dönüşüm çalışmalarında uzmanlaşmış bir akademisyenden oluşmaktadır. Çalışma, elektronik ürünlerin geri dönüşümde en başarılı ürün grubu olduğunu, kızartma yağlarının ise en az başarıyı gösteren ürün grubu olduğunu ortaya koymaktadır.

1. INTRODUCTION

Recycling plays a pivotal role in mitigating environmental impact, and among the diverse array of daily consumption products, paper, plastic, textiles, and batteries stand out as critical materials to be responsibly managed. The recycling of paper not only conserves trees but also significantly reduces energy consumption compared to producing paper from raw materials. Similarly, plastics, notorious for their environmental persistence, can be transformed into new products through recycling, reducing the burden on landfills and the oceans. Textiles, often overlooked, contribute to immense waste, but recycling them can lead to the creation of sustainable fashion and insulation materials. Additionally, proper

disposal and recycling of batteries are essential to prevent hazardous materials from contaminating the soil and water. By emphasizing the recycling of these everyday items, we contribute to a circular economy that minimizes waste and conserves valuable resources.

1.1. Literature Review

The literature review for this study will be bifurcated into two distinct components: an exploration of existing research in the field of recycling and an investigation into studies that leverage q-rung orthopair fuzzy sets (q-ROFs). This division aims to provide a comprehensive understanding of both the broader context of recycling practices and the specific application of q-ROFs in decision-making processes related to recycling strategies.

1.2. Literature Review On Recycling

Several studies have addressed the intricacies of recycling programs and waste management, employing diverse methodologies and decision-making tools. Wibowo & Deng [1] focused on e-waste recycling programs, utilizing multi-criteria decision-making methods and incorporating intuitionistic fuzzy sets (IFS) to navigate uncertainties. Huang & Li [2] developed a discrete event-based simulation model to optimize household appliance recycling networks, considering system performance, economic factors, and environmental and energy indices. Chakraborty & Saha [3] tackled the multi-criteria decision-making problem of recycling lithium-ion batteries, determining the most effective system. Su et al. [4] utilized the TOPSIS method to analyze waste management in Taiwan, encompassing social, economic, and managerial aspects. Tortorella et al. [5], integrated lean production techniques with multi-criteria decision-making to optimize solid waste systems in Brazilian municipalities. Banar et al. [6] addressed the collection of electrical and electronic waste in Turkey, employing a decision-making approach with seven criteria and 16 alternatives. Zheng & Zhou [7] explored recycling processes for packaging products as a multi-criteria decision-making problem. Moro [8] delved into recycling concentrated mixtures, applying various criteria to a decision-making framework. Hadipour et al. [9] studied wastewater reuse in Iran within a decision-making context. Li et al. [10] evaluated express packaging recycling patterns using diverse multi-criteria decision-making methods. Koca & Behdioglu [11] examined recycling studies in the automotive industry, employing various criteria and decision-making methodologies. Stallkamp et al. [12] addressed the design of a recycling network for plastic waste in Europe using multi-criteria decision-making. Makarichi et al. [13] developed a multi-criteria decision-making approach to support solid waste management in Zimbabwe. Hanan et al. [14] evaluated paper recycling management systems in the Isle of Wight as a multi-criteria decision-making problem. Bhuyan et al. [15] explored recycling strategies for lithium-ion batteries in India, employing diverse multi-criteria decision-making methods in their study.

1.3. Literature Review On q-ROFs

In recent studies, various applications of q-rung orthopair fuzzy (q-ROF) methods in multi-criteria decision-making have been explored across different domains. Dinçer & Yüksel [16] assessed the risks associated with nuclear energy investments using the SWARA and ELECTRE methods, incorporating q-ROFs. Seikh & Mandal [17] focused on the location selection problem for software operating units, employing q-ROFs. Oraya et al. [18] utilized q-ROFs in a multi-criteria decision-making approach to evaluate the impact of delays in residence construction. Khan et al. [19] introduced a novel operator for stock selection in the market, applying q-ROFs to multi-criteria decision-making. Naz et al. [20] analyzed river crossing projects with q-ROFs, considering various criteria. Erdebilli et al. [21] addressed the sustainable selection of private health insurance in Turkey, employing q-ROFs. Aytekin et al. [22] identified critical lean 6 sigma methods using q-ROFs to optimize critical business processes. Pınar & Boran [23] utilized q-ROFs for supplier selection, introducing a new distance measurement model in their study. Alkan & Kahraman [24] discussed state strategies against Covid-19 using the q-ROFs TOPSIS method. Mishra & Rani [25] applied q-ROFs to select sustainable recycling pairs, while Yang & Chang [26] used q-ROFs for the optimal selection of garbage separation areas. Pınar et al. [27] employed q-ROFs in addressing the green supplier selection problem.

2. MATERIAL AND METHOD

2.1. Fuzzy Sets

Fuzyy sets (Fs): A fuzzy set *A* in the universe of discourse $X = \{x_1, x_2, \ldots, x_3\}$ is a set of ordered pairs: $A = \{\langle x, \mu_A(x) \rangle \mid x \in X\}$ where $\mu_A(x) \to [0,1]$ is the membership degree, Zadeh [28].

Intuitionistic Fuzzy Sets (IFs): An intuitionistic fuzzy set A in X can be described as: $A = \{\langle x, \mu_A(x), \nu_A(x) \rangle \mid x \in X\}$ where the functions $\mu_A(x) \to [0,1]$ and $\nu_A(x) \to [0,1]$ shows membership degree and non-membership degree of x, respectively, Atanassov [29].

Pythagorean Fuzzy Sets (PFs): Pythagorean fuzzy sets membership degree couple of values (a, b) such that $a, b \in [0,1]$ as follows: $a^2 + b^2 \leq 1$ where $a = A_Y(x)$, membership degree of x in *A* and $b = A_N(x)$ the non-membership degree of x in *A*, Yager [30].

q-Rung Orthopair Fuzzy Sets (q-ROFs): A fuzzy sets *A* of *X* given as $A = \{\langle x, \mu_A(x), \nu_A(x) \rangle \mid x \in X\}$ where $\mu_A(x) \to [0,1]$ shows membership degree and $\nu_A(x) \to [0,1]$ shows non-membership degree of $x \in X$ with condition given: $(\mu_A(x))^q + (\nu_A(x))^q \leq 1$, Yager [30].

Figure 1 represents the compression of different fuzzy sets

62
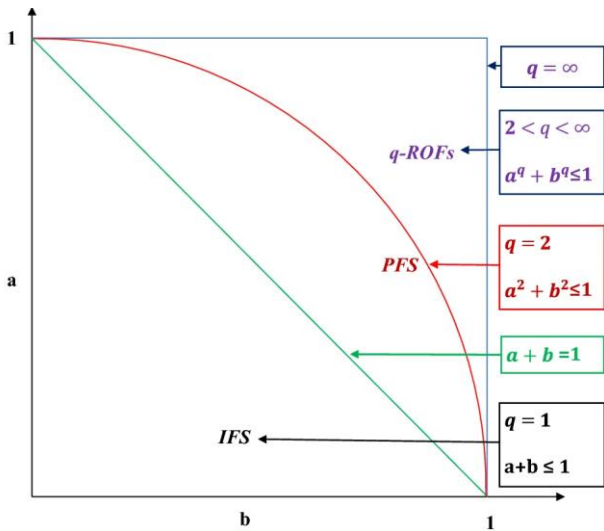
Figure 1. Comparing of fuzzy sets [23]

2.2. Topsis

TOPSIS is a multi-criteria decision-making (MCDM) method used to determine the best alternative from a set of available options. It was developed to evaluate and rank alternatives based on their proximity to the ideal solution and the remoteness from the negative solution. The method involves comparing the alternatives against both positive and negative ideal solutions to establish their relative closeness or distance.

The implementation steps for q-ROFs TOPSIS are outlined in detail below:

Step 1. Create a decision matrix with linguistic variables which's are taken from decision makers for alternatives and criteria. The set of alternatives, criteria and decision makers are shown below.

$A_i = \{A_1, A_2, \dots \dots, A_n\}$, $i = 1,2, \dots, n$ represent set of alternatives.

$C_j = \{C_1, C_2, \dots \dots, C_m\}$, $j = 1,2, \dots, m$ represent set of criteria.

$DM_k = \{DM_1, DM_2, \dots \dots, DM_t\}$, $k = 1,2, \dots, t$ represent set of decision makers weights where $DM_k > 0$ and $\sum_{k=1}^{t} DM_k = 1$

Table 1 shows linguistic scale which also used by Alkan & Kahraman [24] given below. (μ: membership degree and ν: non-membership degree).

Table 1. Linguistic scale for alternatives and criteria.

Liguistic term	Linguistic scale for alternatives and criteria	
	μ	ν
Certainly High Value-(CHV)	0,99	0,11
Very High Value-(VHV)	0,88	0,22
High Value-(HV)	0,77	0,33
Above Average Value-(AAV)	0,66	0,44
Average Value-(AV)	0,55	0,55

Under Average Value-(UAV)	0,44	0,66
Low Value-(LV)	0,33	0,77
Very Low Value-(VLV)	0,22	0,88
Certainly Low Value-(CLV)	0,11	0,99

Step 2. Convert linguistic variables as μ and ν pairs to obtain a numerical decision matrix.

Step 3. Calculate aggregated decision matrix by using equation (1) given below.

$$q - ROFWG(\tilde{Q}_1, \tilde{Q}_2, \dots \dots, \tilde{Q}_n$$

$$= \left(\prod_{i=1}^{n} \mu_{\tilde{Q}_i}^{DM_i}, \left(1 - \prod_{i=1}^{n} \left(1 - v_{\tilde{Q}_i}^q \right)^{DM_i} \right)^{\frac{1}{q}} \right) \dots \dots \dots \dots \dots \dots \dots \dots \quad (1)$$

Where q-ROFWG: q-rung orthopair fuzzy weighted geometric operator

$\tilde{Q}_i = \left(\mu_{\tilde{Q}_i}, v_{\tilde{Q}_i} \right), i = 1,2, \dots \dots, n$ be set of q-ROFNs

$q = 1,2,3, \dots$ is a value that helps to provide a stronger uncertainty and flexibility to decision makers.

Step 4. Calculate aggregated decision matrix for criteria by using equation 1.

Step 5. Calculate weighted aggregated decision matrix by using equation 2.

$$\tilde{Q}_1 \otimes \tilde{Q}_2 = \left(\mu_{\tilde{Q}_1} \mu_{\tilde{Q}_2}, \left(v_{\tilde{Q}_1}^q + v_{\tilde{Q}_2}^q - v_{\tilde{Q}_1}^q v_{\tilde{Q}_2}^q \right)^{\frac{1}{q}} \right) \dots \dots \dots \dots \dots \quad (2)$$

where $\tilde{Q}_1 = \left(\mu_{\tilde{Q}_1}, v_{\tilde{Q}_1} \right), \tilde{Q}_2 = \left(\mu_{\tilde{Q}_2}, v_{\tilde{Q}_2} \right)$ a set of q-ROFN

Step 6. Normalize the weighted aggregated decision matrix by using equation 3.

Let $\tilde{N}$ be normalized q-ROF decision matrix

$$\tilde{N} = \tilde{n}_{ij} = \left(\mu_{ij}, v_{ij} \right) = \begin{cases} \left(\mu_{ij}, v_{ij} \right), & \text{if crit. is benefit keep it as it is} \\ \left(v_{ij}, \mu_{ij}, \right), & \text{if crit. is cost than turn it to benefit} \end{cases} \quad (3)$$

Step 7. Determine q-ROF positive ideal solution (q-ROFPIS) and q-ROF negative solution (q-ROFNIS) using by equation 4. and 5.

63

$$\tilde{N}_j^* = max\{S(N_{1j}), S(N_{2j}), \dots \dots, S(N_{mj})\}, j$$
$$= 1, 2, \dots \dots, n \tag{4}$$

$$\tilde{N}_j^- = min\{S(N_{1j}), S(N_{2j}), \dots \dots, S(N_{mj})\}, j$$
$$= 1, 2, \dots \dots, n \tag{5}$$

where $S(\tilde{N})$ is the score function of q-ROFN and $S(\tilde{Q}) = \mu_{\tilde{Q}}^q - v_{\tilde{Q}}^q$

Step 8. Obtain the separation measures by calculating the distances for each alternative according to positive-ideal $(\tilde{N}^*)$ and negative-ideal solutions $(\tilde{N}^-)$. Then calculate distances between each alternatives by using Euclidean distance function 6. and 7. given below.

$$d(N_i, N^*) = \left(\frac{1}{2n} \sum_{j=1}^{n} \left(\left| \mu_{ij}^q - (\mu_j^*)^q \right|^2 \right. \right.$$
$$\left. \left. + \left| v_{ij}^q - (v_j^*)^q \right|^2 \right) \right)^{1/2} \tag{6}$$

$$d(N_i, N^-) = \left(\frac{1}{2n} \sum_{j=1}^{n} \left(\left| \mu_{ij}^q - (\mu_j^-)^q \right|^2 \right. \right.$$
$$\left. \left. + \left| v_{ij}^q - (v_j^-)^q \right|^2 \right) \right)^{1/2} \tag{7}$$

Step 9. Calculate the relative closeness coefficient (CC_i) of alternatives by using equation 8.

$$CC_i = \frac{d(N_i, N^-)}{d(N_i, N^-) + d(N_i, N^*)} \tag{8}$$

Step 10. Rank the alternatives according to final scores and select alternative which has best (CC_i) value.

3. RESULTS

The recycling landscape in Turkey shows an average waste recycling rate of 7%, with packaging materials leading at 20%. Specific product recycling rates are as follows: paper (43%), plastic (27%), glass (12%), textile products (8%), and metal products (4%). The study identifies various recycling products as alternatives, emphasizing their importance in sustainable practices.

Here is information about these products:
Paper (A1): Constituting a third of solid waste, recycling paper and cardboard is crucial for saving landfill space. One ton of paper occupies approximately 3.3 cubic meters of landfill space, making paper recycling an effective strategy for conserving space and reducing the need for additional landfills.
Plastic (A2): Recycling plastic waste extends the life of landfills and protects non-renewable raw material resources. The energy-saving impact is significant, with 14,000 kWh saved for every ton of recycled plastic.

Textiles (A3): Recycling textiles prevents pollution, reduces energy and water consumption, and minimizes landfill requirements. This is particularly important given that synthetic fibers don't decompose, and natural fibers can emit greenhouse gases.
Batteries (A4): Proper battery recycling is vital to prevent the release of toxic substances like cadmium into water and soil. Cadmium contamination poses severe health risks through the food chain and drinking water.
Frying Oil (A5): Recycling waste oils protects groundwater and soil, preventing pollution and maintaining soil fertility. It also reduces the risk of fires and prevents unpleasant odors associated with improper disposal.
Electronics (A6): Recycling electronic waste is essential to prevent environmental harm and promote the reuse of valuable materials. Electronic waste often contains harmful substances like cobalt, barium, and mercury.
Glass (A7): Producing products with recycled glass reduces CO_2 emissions and greenhouse gases by 40%, and it decreases ocean and sea pollution by 20%. Glass stands out for its infinite recyclability without quality loss.
Wood (A8): Recycling wood waste in specialized facilities ensures the efficient use of resources in wooden goods production. The key factor is ensuring that recycled wood remains free from chemicals or substances that could compromise its structural integrity.

The study evaluates alternatives based on the following criteria:
Convertibility Rate (C1): This criterion gauges the percentage of recycled products obtained from the collected waste that can undergo recycling.
Resource Usage for Recycling (C2): This criterion assesses the amount of resources required to recycle the products.
Converted Product Lifespan (C3): It indicates the average duration it takes for the converted product to become waste again.
Recycling Process Complexity (C4): This criterion encompasses the difficulty level of the conversion processes, including collecting, storing, and reprocessing the product.
Economic Gain (C5): This criterion refers to the economic contribution of the product obtained through recycling.
Product Consumption Rate (C6): It evaluates how frequently the product in question is consumed.
Trading Opportunities (C7): This criterion expresses the economic significance of the recycled product within the sector.

In conclusion, this study unfolds in a comprehensive four-part structure, commencing with the definition of alternatives and criteria crucial to the decision problem. Subsequently, the literature review immerses into the vast realm of recycling and the nuanced application of q-rung orthopair fuzzy sets (q-ROFs). The second segment illuminates the q-ROF TOPSIS method, offering a clear understanding of its methodology. Moving forward, the third chapter including results the decision problem,

employing the established criteria to evaluate the identified alternatives. Finally, the fourth and last chapter

64

culminates in presenting the study's contributions, encapsulating key findings and underscoring the research's impact on the broader field.

In this section, the success status of the recycling strategies developed by the government, a focal point of this study, will be systematically assessed using the q-rung orthopair fuzzy TOPSIS (q-ROFTOPSIS) method. The evaluation will be conducted as a decision-making problem, considering the predefined alternatives and criteria. Each step of the q-ROFTOPSIS method will be followed to provide a comprehensive analysis of the recycling strategies. This approach aims to offer a nuanced understanding of the effectiveness and performance of state-developed recycling strategies, contributing valuable insights to the broader discourse on sustainable waste management.

Step 1. Obtained linguistic evaluations by using Table 1 from 3 different decision makers and results given in Table 2.

Table 2. Linguistic decision matrix for each decision maker.

	DM1								DM2								DM3							
	A1	A2	A3	A4	A5	A6	A7	A8	A1	A2	A3	A4	A5	A6	A7	A8	A1	A2	A3	A4	A5	A6	A7	A8
C1	CHV	VHV	HV	HV	AV	AAV	HV	VLV	CHV	CHV	AV	VHV	VLV	HV	AAV	CLV	VHV	CHV	AV	HV	CLV	VHV	AAV	VLV
C2	HV	VHV	AAV	CHV	VHV	AAV	HV	AV	HV	VHV	HV	UAV	VHV	HV	AAV	LV	AV	AAV	UAV	HV	VHV	AAV	HV	LV
C3	LV	VHV	HV	UAV	CLV	AAV	UAV	AAV	UAV	AAV	VHV	AAV	UAV	HV	AV	AAV	HV	VHV	AAV	AAV	VLV	AAV	UAV	HV
C4	HV	HV	AV	LV	VHV	HV	HV	VHV	AV	AAV	HV	UAV	VHV	AAV	UAV	AV	AAV	HV	UAV	LV	CHV	HV	VHV	AV
C5	LV	UAV	LV	HV	AV	CHV	AAV	CLV	AV	UAV	UAV	HV	UAV	CHV	AV	VLV	LV	LV	VLV	AAV	UAV	CHV	VHV	VLV
C6	CHV	VHV	AAV	VHV	UAV	CHV	AAV	VLV	VHV	CHV	HV	VHV	AV	CHV	HV	LV	AAV	AV	AV	VHV	VLV	CHV	AV	UAV
C7	AAV	UAV	HV	AV	CLV	CHV	UAV	UAV	LV	CLV	AAV	UAV	CLV	VHV	VLV	LV	VLV	CLV	LV	UAV	CLV	HV	LV	VLV

Step 2 and *Step 3*.
In step 2, linguistic evaluations converted to numerical values according to Table 1. Then we calculated Table 3 by using equation 1. Q number accepted 4, and DMs weight taken into consideration as (0,33-0,33-0,34) respectively.

Table 3. Aggregated decision matrix.

	A1		A2		A3		A4		A5		A6		A7		A8	
	μ	ν	μ	ν	μ	ν	μ	ν	μ	ν	μ	ν	μ	ν	μ	ν
C1	[0,951	0,173]	[0,952	0,172]	[0,615	0,507]	[0,805	0,306]	[0,235	0,934]	[0,766	0,362]	[0,964	0,413]	[0,175	0,950]
C2	[0,687	0,446]	[0,798	0,347]	[0,605	0,539]	[0,696	0,516]	[0,880	0,220]	[0,694	0,413]	[0,732	0,378]	[0,391	0,724]
C3	[0,484	0,664]	[0,800	0,344]	[0,764	0,364]	[0,577	0,549]	[0,220	0,935]	[0,694	0,413]	[0,474	0,631]	[0,696	0,412]
C4	[0,654	0,467]	[0,732	0,378]	[0,570	0,565]	[0,363	0,741]	[0,916	0,200]	[0,732	0,378]	[0,670	0,517]	[0,642	0,501]
C5	[0,391	0,724]	[0,399	0,706]	[0,316	0,799]	[0,731	0,379]	[0,474	0,631]	[0,990	0,110]	[0,685	0,458]	[0,175	0,950]
C6	[0,830	0,342]	[0,780	0,426]	[0,653	0,468]	[0,880	0,220]	[0,374	0,762]	[0,990	0,110]	[0,653	0,468]	[0,318	0,797]
C7	[0,361	0,782]	[0,174	0,972]	[0,549	0,623]	[0,474	0,631]	[0,110	0,990]	[0,874	0,264]	[0,317	0,798]	[0,316	0,799]

Step 4. Linguistic evaluations converted to numerical values and calculated aggregated criteria weights by using equation 1. Shown in Table 4. Criteria divided into two type, cost and benefit. Criteria 2 marked as cost type and others marked benefit type.

Table 4. Linguistic evaluations of criteria for each decision maker and aggregated criteria weights.

					Type	
Criteria	DM1	DM2	DM3	Aggregated	Cost	Benefit
C1	HV	VHV	VHV	[0,842 0,272]		✓
C2	CHV	CHV	VHV	[0,951 0,173]	✓	
C3	AV	AAV	HV	[0,655 0,466]		✓
C4	LV	HV	AAV	[0,552 0,620]		✓
C5	VHV	HV	HV	[0,805 0,306]		✓
C6	UAV	AV	HV	[0,573 0,562]		✓
C7	LV	UAV	AAV	[0,459 0,670]		✓

Step 5. Weighted aggregated decision matrix calculated by using equation 2. And Table 5 shows the results.

Table 5. Weighted aggregated decision matrix.

	A1 μ	A1 ν	A2 μ	A2 ν	A3 μ	A3 ν	A4 μ	A4 ν	A5 μ	A5 ν	A6 μ	A6 ν	A7 μ	A7 ν	A8 μ	A8 ν
C1	[0,801 0,283]		[0,802 0,282]		[0,518 0,516]		[0,678 0,345]		[0,1998 0,935]		[0,645 0,388]		[0,585 0,431]		[0,147 0,950]	
C2	[0,653 0,449]		[0,759 0,352]		[0,575 0,540]		[0,662 0,518]		[0,837 0,238]		[0,661 0,416]		[0,696 0,382]		[0,372 0,725]	
C3	[0,317 0,694]		[0,524 0,496]		[0,500 0,503]		[0,378 0,605]		[0,144 0,939]		[0,455 0,523]		[0,310 0,667]		[0,455 0,523]	
C4	[0,361 0,659]		[0,404 0,637]		[0,315 0,696]		[0,200 0,798]		[0,506 0,621]		[0,404 0,637]		[0,370 0,676]		[0,355 0,670]	
C5	[0,314 0,728]		[0,321 0,711]		[0,254 0,802]		[0,588 0,413]		[0,381 0,638]		[0,797 0,307]		[0,551 0,478]		[0,141 0,950]	
C6	[0,475 0,579]		[0,447 0,600]		[0,374 0,615]		[0,504 0,565]		[0,214 0,797]		[0,567 0,562]		[0,374 0,615]		[0,182 0,825]	
C7	[0,166 0,841]		[0,080 0,978]		[0,252 0,754]		[0,218 0,757]		[0,051 0,992]		[0,402 0,673]		[0,146 0,851]		[0,145 0,852]	

Step 6. Normalized decision matrix created by equation 3. and results shown in Table 6.

Table 6. Normalized decision matrix.

	A1 μ	A1 ν	A2 μ	A2 ν	A3 μ	A3 ν	A4 μ	A4 ν	A5 μ	A5 ν	A6 μ	A6 ν	A7 μ	A7 ν	A8 μ	A8 ν
C1	[0,801 0,283]		[0,802 0,282]		[0,518 0,516]		[0,678 0,345]		[0,1998 0,935]		[0,645 0,388]		[0,585 0,431]		[0,147 0,950]	
C2	[0,449 0,653]		[0,352 0,759]		[0,540 0,575]		[0,518 0,662]		[0,238 0,837]		[0,416 0,661]		[0,382 0,696]		[0,725 0,372]	
C3	[0,317 0,694]		[0,524 0,496]		[0,500 0,503]		[0,378 0,605]		[0,144 0,939]		[0,455 0,523]		[0,310 0,667]		[0,455 0,523]	
C4	[0,361 0,659]		[0,404 0,637]		[0,315 0,696]		[0,200 0,798]		[0,506 0,621]		[0,404 0,637]		[0,370 0,676]		[0,355 0,670]	
C5	[0,314 0,728]		[0,321 0,711]		[0,254 0,802]		[0,588 0,413]		[0,381 0,638]		[0,797 0,307]		[0,551 0,478]		[0,141 0,950]	
C6	[0,475 0,579]		[0,447 0,600]		[0,374 0,615]		[0,504 0,565]		[0,214 0,797]		[0,567 0,562]		[0,374 0,615]		[0,182 0,825]	
C7	[0,166 0,841]		[0,080 0,978]		[0,252 0,754]		[0,218 0,757]		[0,051 0,992]		[0,402 0,673]		[0,146 0,851]		[0,145 0,852]	

Step 7. In this section positive ideal solution (q-ROFPIS) and q-ROF negative solution (q-ROFNIS) determined by using equation 4. and 5. Table 7 shows the results.

Table 7. Positive and negative ideal solutions.

Criteria	Positive ideal solution	Negative ideal solution
C1	[0,802 0,282]	[0,147 0,950]
C2	[0,725 0,372]	[0,238 0,837]
C3	[0,524 0,496]	[0,144 0,939]
C4	[0,506 0,621]	[0,200 0,798]
C5	[0,797 0,307]	[0,141 0,950]
C6	[0,504 0,562]	[0,182 0,825]
C7	[0,402 0,673]	[0,051 0,992]

Step 8. Separation measures calculated by using equation 6. and 7. and results given in Table 8.

Table 8. Separation measures of alternatives.

	A1	A2	A3	A4	A5	A6	A7	A8
$d(N_i, N^*)$	0,1766	0,2519	0,1922	0,1434	0,4147	0,1045	0,1762	0,3668
$d(N_i, N^-)$	0,3677	0,3641	0,3716	0,4114	0,1884	0,4502	0,3733	0,2712

Step 9 and *Step 10*. Closeness coefficient calculated by using equation 8. Table 9 shows closeness coefficient and ranking of alternatives.

Table 9. Closeness Coefficient and Ranking of Alternatives.

	A1	**A2**	**A3**	**A4**	**A5**	**A6**	**A7**	**A8**
CC_i	0,6755	0,591	0,6591	0,7416	0,3124	0,8117	0,6793	0,425
Rank	4	6	5	2	8	1	3	7
Alternatives	paper	plastic	textile	battery	frying oil	electronic	glass	wood

4. DISCUSSION AND CONCLUSION

This study delved into evaluating the success rates of strategies designed for recycling commonly consumed daily-life products, posing it as a decision-making problem. The analysis considered 8 alternatives and 7 success criteria, employing the q-rung orthopair fuzzy TOPSIS (q-ROFTOPSIS) approach. Findings indicated that electronic products ranked as the most favorable alternative, followed sequentially by batteries, glass, paper, textile, plastic, wood, and oils.

The determination of decision makers' weights can be approached at diverse levels and through varied methodologies. Alternative distance operators, such as Hamming or Hausdorff, could replace the Euclidean distance operator used in this study. The chosen q value of 4 facilitated decision-making amid uncertainty; however, different values may warrant exploration in subsequent studies to enhance the method's adaptability and robustness.

The flexibility of the methodology was evident in the acknowledgment that decision maker weights could be computed at different levels and using various methods. Furthermore, the study highlighted the potential for testing different q values in future research, emphasizing the adaptability of the approach under varying degrees of uncertainty. The decision-making process, guided by q-ROFTOPSIS, represents a valuable contribution to the field, providing a nuanced understanding of the success rates of recycling strategies for everyday consumables.

Acknowledgement

REFERENCES

[1] Wibowo, S. & Deng, H. (2015). Multi-criteria group decision making for evaluating the performance of e-waste recycling programs under uncertainty, Waste Management. Vol.40, pp 127-135.Carlson BM. Human embryology and developmental biology. 4th ed. St. Louis: Mosby; 2009.

[2] Huang, H. & Li, B. (2020). Optimization of WEEE recycling network for E-wastes based on discrete event simulation, Procedia CIRP. Vol. 90, pp 705-711.

[3] Chakraborty, S. & Saha, AK. (2020). Selection of optimal lithiumion battery recycling process: A multi-criteria group decision making approach, Journal of Energy Storage. Vol. 55, Part B, 105557.

[4] Su, J-P., Hung, M-L., Chao, C-W. & Ma, H., (2010). Applying multi-criteria decision-making to improve the waste reduction policy in Taiwan, Waste Management & Research. 28(1):20-28.

[5] Tortorella, G., Silva, G., Campos, L.M.S., Pizzeta, C., Latosinski, A. & Soares, A. (2018). "Productivity improvement in solid waste recycling centres through lean implementation aided by multi-criteria decision analysis", Benchmarking: An International Journal. Vol. 25, No. 5, pp. 1480-1499.

[6] Banar, M., Tulger, G. & Özkan, A., (2014). Plant Sıte Selectıon for Recyclıng Plants of Waste Electrıcal and Electronıc Equıpment in Turkey by Usıng Multı Crıterıa Decısıon Makıng Methods, Envıronmental Engıneerıng and Management Journal. Vol. 13, No. 1, pp. 163-172.

[7] Zheng, C. & Zhou, Y., (2022). Multi-criteria Group Decision-Making Approach for Express Packaging Recycling Under Interval-Valued Fuzzy Information: Combining Objective and Subjective Compatibilities. Int. J. Fuzzy Syst. 24, 1112–1130 (2022).

[8] Moro, C., (2023). Comparative Analysis of Multi-Criteria Decision Making and Life Cycle Assessment Methods for Sustainable Evaluation of Concrete Mixtures, Sustainability. 15, no. 17: 12746.

[9] Hadipour, A., Rajaee, T., Hadipour, V. & Seidirad, S., (2016). Multi-criteria decision-making model for wastewater reuse application: a case study from Iran. Desalination and Water Treatment. 57:30, 13857-13864.

[10] Ling, L., Anping, R. & Di, X., (2023). Proposal of a hybrid decision-making framework for the prioritization of express packaging recycling patterns, Environ Dev Sustain. 25, 2610–2647.

[11] Koca, G. & Behdioglu, S., (2019). Multi-Criteria Decision Making in Green Supply Chain Management: An Example of Automotive Main Industry, Eskısehır Osmangazı Unıversıty Journal of Economıcs and Admınıstratıve Scıences. Vol. 14(3), pp. 675-698.

[12] Stallkamp, C., Steins, J., Ruck, M., Volk, R., & Schultmann, F., (2022). Designing a Recycling Network for the Circular Economy of Plastics with Different Multi-Criteria Optimization Approaches, Sustainability. 14, no. 17: 10913.

[13] Makarichi, L., Techato, K. & Jutidamrongphan, W., (2018). Material flow analysis as a support tool for multi-criteria analysis in solid waste management decision-making, Resources, Conservation and Recycling. Vol. 139, pp. 351-365.

[14] Hanan, D., Burnley, S. & Cooke, D., (2023). A multi-criteria decision analysis assessment of waste paper management options, Waste Management. Vol. 33(3), pp. 566-573.

67

[15] Bhuyan, A., Tripathy, A., Padhy, R. K. & Gautam, A., (2022). Evaluating the lithium-ion battery recycling industry in an emerging economy: A multi-stakeholder and multi-criteria decision-making approach, Journal of Cleaner Production. Vol. 331, 130007.

[16] Dinçer, H. & Yüksel, S., (2023). Assessing the risk management-based impact relation map of nuclear energy system investments using the golden cut and bipolar q-ROF hybrid decision making model, Progress in Nuclear Energy. Vol. 165, 104911.

[17] Seikh, M., R. & Mandal, U., (2023). q-Rung Orthopair Fuzzy Archimedean Aggregation Operators: Application in the Site Selection for Software Operating Unit. Symmetry 15, no. 9: 1680.

[18] Oraya, A., F., Hana, A., C-T., Luciano, R., Patadlas, A., Baguio, I., Aro, L., J., Maturan, F. & Ocampo, L., (2023). An Integrated Multicriteria Sorting Methodology with q-Rung Orthopair Fuzzy Sets for Evaluating the Impacts of Delays on Residential Construction ProjectS. Axioms 12, no. 8: 735.

[19] Khan, R., M., Ullah, K., Karamti, H., Khan, Q. & Mahmood, T., (2023). Multi-attribute group decision-making based on q-rung orthopair fuzzy Aczel–Alsina power aggregation operators, Engineering Applications of Artificial Intelligence. Vol. 126, Part A, 106629.

[20] Naz, S., Akram, M., Davvaz, B. & Saadat A., (2023). A new decision-making framework for selecting the river crossing project under dual hesitant q-rung orthopair fuzzy 2-tuple linguistic environment, Soft Computing. Vol. 27(17), pp. 12021–12047.

[21] Erdebilli, B., Gecer, E., Yılmaz, İ., Aksoy, T., Hacıoglu, Ü., Dinçer, H. & Yüksel. S., (2023). Q-ROF Fuzzy TOPSIS and VIKOR Methods for the Selection of Sustainable Private Health Insurance Policie, Sustainability. Vol.15, No. 12: 9229

[22] Aytekin, A., Okoth, B., O., Korucuk, S., Mishra, R., A., Memiş, S., Karamaşa, Ç. & Tirkolaee, B., E., (2023). Critical success factors of lean six sigma to select the most ideal critical business process using q-ROF CRITIC-ARAS technique: Case study of food business, Expert Systems with Applications. Vol. 224, 120057.

[23] Pinar, A. & Boran, F.E., (2020). A q-rung orthopair fuzzy multi-criteria group decision making method for supplier selection based on a novel distance measure, Int. J. Mach. Learn. & Cyber. 11, 1749–1780.

[24] Alkan, N. & Kahraman, C., (2021). Evaluation of government strategies against COVID-19 pandemic using q-rung orthopair fuzzy TOPSIS method, Applied Soft Computing. Vol. 110, 107653.

[25] Mishra, A.R. & Rani, P., (2023). A q-rung orthopair fuzzy ARAS method based on entropy and discrimination measures: an application of sustainable recycling partner selection, J Ambient Intell Human Comput 14, 6897–6918.

[26] Yang, Z. & Chang, J., (2021). A multi-attribute decision-making-based site selection assessment algorithm for garbage disposal plant using interval q-rung orthopair fuzzy power Muirhead mean operator, Environmental Research. Vol. 193, 110385.

[27] Pınar, A., Daneshvar, B., R. & Özdemir, S. Y., (2021). q-Rung Orthopair Fuzzy TOPSIS Method for Green Supplier Selection Problem, Sustainability. Vol. 13, No. 2: 985.

[28] Zadeh, L.A. (1965). Fuzzy Sets, Information Control. Vol. 8, 338-353.

[29] Atanassov, K.T. (1999). Intuitionistic Fuzzy Sets. In: Intuitionistic Fuzzy Sets. Studies in Fuzziness and Soft Computing, vol 35. Physica, Heidelberg.

[30] Yager, R.R. (2016). Properties and Applications of Pythagorean Fuzzy Sets. In: Angelov, P., Sotirov, S. (eds) Imprecision and Uncertainty in Information Representation and Processing. Studies in Fuzziness and Soft Computing, vol 332. Springer, Cham. https://doi.org/10.1007/978-3-319-26302-1_9

68

Türk Doğa ve Fen Dergisi
Turkish Journal of Nature and Science
www.dergipark.gov.tr/tdfd

Determination of Pharmacokinetic and Toxicological Parameters of Some Commonly Used Statin Group Drugs

Mustafa Tuğfan BİLKAN[1*] ID , **Çiğdem BİLKAN[2]** ID

[1] Tokat Gaziosmanpaşa University, Faculty of Medical, Department of Biophysics, Tokat, Türkiye
[2] Tokat Gaziosmanpaşa University, Erbaa Vocational School of Health Services, Department of Medical Services and Techniques, Tokat, Türkiye
Mustafa Tuğfan BİLKAN ORCID No: 0000-0002-0306-1509
Çiğdem BİLKAN ORCID No: 0000-0002-3347-673X

Corresponding author: mustafa.bilkan@gop.edu.tr

Abstract: Statins work as inhibitors of the HMG-CoA reductase enzyme and are the most commonly prescribed cholesterol-lowering drug group for people with cardiovascular disease or risk. This study aimed to determine the pharmacokinetic parameters and toxicities of conventional and new-generation cholesterol drugs such as atorvastatin, fluvastatin, lovastatin, pravastatin, simvastatin, rosuvastatin and pitavastatin. Absorption, distribution, metabolism, and excretion (ADME) parameters and toxicity predictions of drugs were made using in silico modeling, which gives faster results than animal experiments and does not involve any laboratory costs. In calculations made using structural similarity, compounds' pharmacokinetic properties and toxicity predictions are obtained based on previously known structure-activity data. The study results showed that the toxicity classifications of the drugs were 5 (LD: 5000 mg/kg) for atorvastatin and 6 (LD: 8939 mg/kg) for pravastatin, respectively. The toxicity classes were found to be 4 for all the other statin group drugs. The results showed that pravastatin had the lowest toxicity among investigated cholesterol drugs, while pitavastatin and fluvastatin had the highest toxic effects. Accordingly, it is recommended that the consequences of using pravastatin and atorvastatin, cholesterol drugs with lower toxicity classes, should be investigated more seriously in terms of minimum toxic substance intake for patient groups requiring high doses of medication.

69

Yaygın Olarak Kullanılan Bazı Statin Grubu İlaçların Farmakokinetik ve Toksikolojik Parametrelerinin Belirlenmesi

Öz: Statinler, HMG-CoA redüktaz enziminin inhibitörleri olarak çalışır ve kardiyovasküler hastalığı veya riski olan kişiler için en sık reçete edilen kolesterol düşürücü ilaç grubudur. Bu çalışmada atorvastatin, fluvastatin, lovastatin, pravastatin, simvastatin, rosuvastatin ve pitavastatin gibi geleneksel ve yeni nesil kolesterol ilaçlarının farmakokinetik parametrelerinin ve toksisitelerinin belirlenmesi amaçlandı. İlaçların emilim, dağılım, metabolizma ve atılım (ADME) parametreleri ve toksisite tahminleri, hayvan deneylerine göre daha hızlı sonuç veren ve herhangi bir laboratuvar maliyeti gerektirmeyen in silico modelleme ile yapılmıştır. Yapısal benzerlik kullanılarak yapılan hesaplamalarda, bileşiklerin farmakokinetik özellikleri ve toksisite öngörüleri, önceden bilinen yapı-aktivite verilerine dayanılarak elde edilmiştir. Çalışma sonuçları, ilaçların toksisite sınıflandırmalarının atorvastatin için sırasıyla 5 (LD: 5000 mg/kg) ve pravastatin için 6 (LD: 8939 mg/kg) olduğunu gösterdi. Diğer tüm statin grubu ilaçlar için toksisite sınıfı 4 olarak belirlendi. Sonuçlar, araştırılan kolesterol ilaçları arasında pravastatinin en düşük toksisiteye sahip olduğunu, pitavastatin ve fluvastatinin ise en yüksek toksik etkilere sahip olduğunu gösterdi. Buna göre, düşük toksisite sınıfına sahip kolesterol ilaçları olan pravastatin ve atorvastatinin yüksek doz ilaç gerektiren hasta gruplarında kullanımının minimum toksik madde alımı açısından sonuçlarının daha ciddi şekilde araştırılması önerilmektedir.

1. INTRODUCTION

Cardiovascular diseases (CVDs) refer to pathologies occurring in the heart and vascular pathways and are among the important causes of death, especially in underdeveloped and developing countries [1]. One of the most critical factors of cardiovascular diseases is the increase in the level of high low-density lipoprotein (LDL) in blood, popularly referred to as bad cholesterol. LDL can cause atherosclerosis and, as a result, the development of coronary heart disease. Statins are treatment agents that control LDL cholesterol by inhibiting the HMG-CoA reductase enzyme [2, 3]. Due to these features, they provide primary protection for people at high risk of cardiovascular disease. At the same time, they are also used in secondary protection in patients who have had cardiovascular disease [4].

Nowadays, the forms of statin commonly used to keep the blood-cholesterol level in a certain balance can be listed as atorvastatin, fluvastatin, lovastatin, pravastatin, simvastatin, rosuvastatin and pitavastatin [5]. Although each of these forms of statins has different pharmacokinetic properties and activities, they also have serious side effects, such as hepatoxicity and nephrotoxicity. However, it is well known that there is no drug without side effects. In clinical use, the physician evaluates the patient's general condition, and the most appropriate drug (most effective and with the lowest side effects) is always recommended.

The most important process after taking a drug into the body is that the drug causes the least harm to the body (which can be expressed as minimum toxicity) and provides maximum benefit. Absorption, distribution, metabolism, and excretion (ADME) processes are critical in ensuring maximum benefit after the dose with minimum toxicity is given to the patient. In this respect, obtaining ADME data in pharmacokinetic processes can provide useful information at the preclinical stage of drug development. In this respect, in silico ADME calculations can show the potential of a new molecule to be used as a drug.

In this study, ADME, drug-likeness, and toxicity predictions of some important statin group drugs were performed in silico. Which drug has what kind of toxicity and LD50 values have been determined. Blood-brain barrier penetration, Caco2 and MDCK cell permeability, and HIA parameters were also obtained. From the results obtained, toxicity situations that may arise as a result of the use of drugs were interpreted.

2. MATERIAL AND METHOD

The 2D molecular structures of the statin group drugs used in this study were drawn using the MarvinSketch program [6]. In the part of in silico biological activity calculations, the ADME and drug-likeness parameters were obtained using the PreADMET [7] website. Toxicity predictions for each drug were performed using the ProTox-II [8] suite.

3. RESULTS

3.1. Molecular Structures and Mechanism of Action of Statin Group Drugs

Statins are generally divided into two groups: those produced by fermentation (type I statins) and those produced synthetically (type II statins). Lovastatin, simvastatin and pravastatin are the first three natural statins produced for clinical use [9]. Lovastatin and pravastatin were isolated from broths as a result of fermentation. Simvastatin is a semi-synthetic statin derived from lovastatin produced by fermentation. Fluvastatin, atorvastatin, pitavastatin and rosuvastatin are synthetically obtained statins. The molecular structures of the drugs are given in Figure 1.
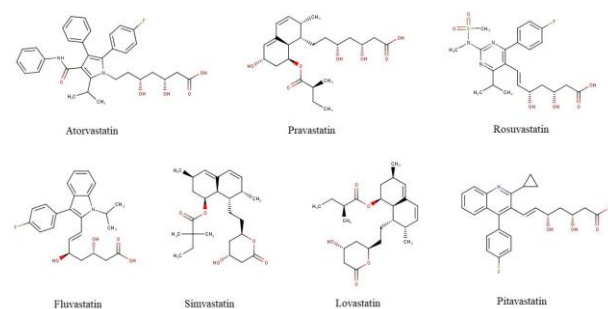
Figure 1. 2D molecular structures of statin group drugs

As can be seen from Figure 1, statins are structurally large molecules and contain many rings and chains in their structures. While lovastatin and simvastatin lack the polar 'head' group in the generalized system, these compounds are pro-drugs [10]. Their respective lactone rings are hydrolyzed in vivo to produce the corresponding hydroxyacid form. Essentially, statins bind to active moieties in the hydrophobic binding sites of the HMG-CoA reductase enzyme, which is actively used for cholesterol synthesis and competitively inhibits the functioning of this enzyme. This interaction is stronger than natural substrate binding. HMG-CoA reductase enzyme is a protein located in the HMG-CoA reductase pathway and used for cholesterol synthesis. In addition to inhibiting cholesterol synthesis, statins are also effective in regulating intracellular cholesterol levels. By reducing intracellular cholesterol levels, they increase LDL receptor synthesis in liver cells and thus accelerate the removal of LDL from the blood [11].

3.2. ADME Parameters of Statins

In medical and biological applications, there are some critical parameters in applying a molecule with therapeutic effects to the patient as a drug. These parameters are absorption, distribution, metabolism, and excretion (ADME) processes, and the optimal benefit of the drug to the patient is directly related to these factors [12]. In this respect, obtaining ADME data in pharmacokinetic processes can provide useful information at the preclinical stage of drug development. These parameters can also provide helpful information in evaluating drug effectiveness after administration. One of the ADME parameters that can be calculated in silico is Blood-brain barrier penetration (BBB), which predicts

whether compounds pass across the blood-brain barrier. The central nervous system (CNS) active compounds are more than 1.0 (Cbrain/Cblood). The second one is Caco2 cell permeability. Caco-2 cells are derived from human colon adenocarcinoma and possess multiple drug transport pathways through the intestinal epithelium. Another one is Madin-Darby canine kidney (MDCK) cells permability. It is a model mammalian cell line used in biomedical research. Middle permeability is 4~70, low permeability is less than 4, and high permeability is more than 70 nm/sec.

HIA-Human Intestinal Absorption predicts the percentage of human intestinal absorption (% HIA). Human intestinal absorption data are the sum of bioavailability and absorption evaluated from the excretion ratio or cumulative excretion in urine, bile, and feces. Well-absorbed compounds are 70~100 %.

The calculated ADME parameters for the statins examined in this study are given in Table 1.

Table 1. In silico predicted ADME parameters of the statins

Statin	Atorv	Fluv	Lov	Prav
BBB	0.673	0.174	0.664	0.067
Caco2	21.709	17.489	27.516	18.943
HIA	94.651	95.075	96.566	77.691
MDCK	0.044	0.045	0.056	0.084
Pure water solubility (mg/L)	0.115	9.045	5.458	405.165
Skin Permeability	-2.419	-2.452	-2.692	-3.080
Plasma Protein Binding	90.348	91.606	100.00	85.811
Statin	Simv	Rosuv	Pitav	
BBB	1.147	0.106	0.054	
Caco2	29.741	0.505	19.490	
HIA	96.564	90.483	95.163	
MDCK	0.047	0.105	0.055	
Pure water solubility (mg/L)	2.134	9.440	0.660	
Skin Permeability	-2.159	-2.430	-2.742	
Plasma Protein Binding	100.00	96.199	96.269	

As can be seen from the table, Simvastatin is the only statin group drug with BBB penetration above 1. It is also the cholesterol drug with the highest Caco2 value, while Rosuvastatin has the lowest value. When the calculated % HIA parameters are examined, it is seen that all of them are above 70%. However, while Pravastatin has the lowest HIA value, the absorption of other drugs is over 90%. When MDCK cell permeability values, another important ADME parameter, are examined for each drug, it is seen that they are well below 1 for all drugs, that is, all of the drugs have low permeability. One of the critical factors in the absorption and distribution of a drug within the body is water solubility. Pravastatin has the highest solubility in water, with 405.165 mg per liter, while surprisingly, the solubility for other statin group drugs is below 10 mg/L. Plasma protein binding (PPB) refers to the degree to which medications attach to blood proteins within the plasma [13]. A drug's efficacy is related to the degree to which it binds. The less bound of a drug mean the more efficiently it can diffuse through cell membranes. In this respect, Pravastatin may have higher medical efficacy than other statins, with the lowest PPB value as well as the highest water solubility.

3.3. Toxicity of the Compounds

Toxicity is the degree to which a chemical or a mixture causes harm to the organism [14]. Toxicity can refer to the damage of the toxic substance on the whole organism, or it can refer to the effect on a group of cells or an organ in the organism. One of the most important features of toxicity is the dose dependence of the effects of the toxic substance. Even substances with very high toxicity (such as snake venom) may have no toxic effects when taken in very small doses. Additionally, toxicity is a species-specific concept. Substances that show high toxicity for some species are not effective on some species.

The toxicity effects on the target tissue or cell can be measured in various units. Lethal dose (LD50) values generally determine toxicity definitions. It is a measure of toxicity, usually at the population level, that relates LD50 estimates to the probabilities of an outcome for a given individual in a population of individuals who respond differently to the same dose of toxicant [15].

The in silico predicted LD50 values of the statins are given in Table 2.

Table 2. In silico predicted ADME parameters of the statins

Statin	Predicted LD50 mg/kg	Toxicity	Predict. Toxicity Class	Molecular Structure
Atorv.	5000	Hepatotoxic	5	$C_{33}H_{35}FN_2O_5$
Fluv.	416	Hepatotoxic	4	$C_{24}H_{26}FNO_4$
Lov.	1000	Carcinogenic Immunotoxic	4	$C_{24}H_{36}O_5$
Prav.	8939	Carcinogenic Immunotoxic	6	$C_{23}H_{36}O_7$
Simv.	1000	Carcinogenic Immunotoxic	4	$C_{25}H_{38}O_5$
Rosuv.	464	Hepatotoxic Immunotoxic	4	$C_{22}H_{28}FN_3O_6S$
Pitav.	416	Hepatotoxic	4	$C_{25}H_{24}FNO_4$

Toxicity classes and LD50 (mg/kg) values are defined as follows: Class I: fatal if swallowed (LD50≤5) Class II: fatal if swallowed (5<LD50≤50) Class III: toxic if swallowed (50<LD50≤300) Class IV: harmful if swallowed (300<LD50≤2000) Class V: may be harmful if swallowed (2000<LD50≤5000) Class VI: non-toxic (LD50>5000) [8]. The LD50 values of the statins were calculated as 5000 mg/kg, 416 mg/kg, 1000 mg/kg, 8939 mg/kg, 1000 mg/kg, 464 mg/kg and 416 mg/kg, respectively. Toxicity classes were obtained as 6 for Pravastatin, 5 for Atorvastatin and 4 for all other drugs. The results show that Pravastatin has the lowest toxicity among the drugs and the predicted result was obtained as non-toxic. However, if taken in very high doses, it may have carcinogenic and immunotoxic effects. The ones showing the highest toxicity are Fluvastatin and Pitavastatin. Both drugs may exhibit hepatotoxic effects.

4. DISCUSSION AND CONCLUSION

In this study, toxicity and ADME predictions of some important statin group drugs were performed in silico. The study results show Pravastatin has the lowest toxicity among investigated cholesterol drugs. Although it is the least toxic statin, also has the lowest Human Intestinal Absorption value. The second drug with the lowest toxicity was estimated to be atorvastatin. However, atorvastatin is most preferred in treatment due to its lower

toxic effect and broader spectrum lipid carrier protein level control effect. Accordingly, it is recommended that the consequences of using pravastatin and atorvastatin, cholesterol drugs with lower toxicity classes, should be investigated more seriously in terms of minimum toxic substance intake for patient groups requiring high doses of medication. The structure-activity-related computational studies can provide useful preliminary information to researchers..

REFERENCES

[1] Civek S. ve Akman M. Dünyada ve Türkiye'de kardiyovasküler hastalıkların sıklığı ve riskin değerlendirilmesi. Jour Turk Fam Phy 2022; 13 (1): 21-28. Doi: 10.15511/tjtfp.22.00121.

[2] Alenghat FJ, Davis AM (February 2019). "Management of Blood Cholesterol". JAMA. 321 (8): 800–801. doi:10.1001/jama.2019.0015. PMC 6679800.

[3] National Clinical Guideline Centre (UK) (July 2014). Lipid Modification: Cardiovascular Risk Assessment and the Modification of Blood Lipids for the Primary and Secondary Prevention of Cardiovascular Disease. National Institute for Health and Clinical Excellence: Guidance. London: National Institute for Health and Care Excellence (UK). PMID 25340243. NICE Clinical Guidelines, No. 181 – via NIH National Library of Medicine.

[4] Endo, A. A gift from nature: the birth of the statins. Nat Med 14, 1050–1052 (2008). https://doi.org/10.1038/nm1008-1050

[5] Sweetman SC, ed. (2009). "Cardiovascular drugs". Martindale: the complete drug reference (36th ed.). London: Pharmaceutical Press. pp. 1155–1434.

[6] MarvinSketch

[7] PreADMET, https://preadmet.qsarhub.com/, (2022).

[8] ProTox-II- Prediction of Toxicity of Chemicals, (2022).

[9] Yong-Jin Wu, Heterocycles and Medicine, Progress in Heterocyclic Chemistry, 2012

[10] https://www.stereoelectronics.org/webDD/DD_05.html

[11] Furuya, Y., Sekine, Y., Kato, H., Miyazawa, Y., Koike, H., & Suzuki, K. (2016). Low-density lipoprotein receptors play an important role in the inhibition of prostate cancer cell proliferation by statins. Prostate international, 4(2), 56-60.

[12] Alan Talevi, Pablo A. M. Quiroga, (2018). ADME Processes in Pharmaceutical Sciences.

[13] Olson, R. E., & Christ, D. D. (1996). Plasma protein binding of drugs. In Annual reports in medicinal chemistry (Vol. 31, pp. 327-336). Academic Press.

[14] Libralato, G., Annamaria, V. G., & Francesco, A. (2010). How toxic is toxic? A proposal for wastewater toxicity hazard assessment. Ecotoxicology and Environmental Safety, 73(7), 1602-1611.

[15] DePass, L. R. (1989). Alternative approaches in median lethality (LD50) and acute toxicity testing. Toxicology letters, 49(2-3), 159-170./

Türk Doğa ve Fen Dergisi
Turkish Journal of Nature and Science

BİNGÖL UNIVERSITY

Synergistic Nanostructured Electrochemically Reduced Graphene Oxide/Molybdenum Trioxide Photoelectrodes For Enhanced Photoresponse

Emir ÇEPNİ[1*] iD

[1] Atatürk University, Engineering Faculty, Electronics and Electrical Engineering Department, Erzurum, Türkiye
Emir ÇEPNİ ORCID No: 0000-0001-8738-1157

Corresponding author: emircepni@atauni.edu.tr

Abstract: Photovoltaic systems that convert solar energy into electrical energy are one of the promising solutions for clean and renewable energy resources to meet the rapidly increasing energy need in the world. For this purpose, investigation of new photovoltaics with high conversion efficiency has gained importance for alternative strategies. Goal of this research is to present electrochemical synthesis and photoresponse of synergistic nanostructured electrochemically reduced graphene oxide/molybdenum trioxide photoelectrodes for proposing an alternative photovoltaic material. With this work, the obtained results indicate that electrochemically synthesized photoelectrodes are utilizable as new alternative materials for various energy production devices, such as solar cells. These interpretations can later be verified by subsequent solar cell applications.

Gelişmiş Fototepki İçin Sinerjistik Nanoyapılı Elektrokimyasal İndirgenmiş Grafen Oksit/Molibden Üçoksit Fotoelektrotlar

Anahtar Kelimeler
Fototepki,
Elektrokimyasal
indirgenmiş
grafen oksit,
Molibden trioksit,
Sinerjistik
nanoyapılı

Öz: Güneş enerjisini elektrik enerjisine dönüştüren fotovoltaik sistemler, dünyada hızla artan enerji ihtiyacının karşılanmasında temiz ve yenilenebilir enerji kaynakları için umut verici çözümlerden biridir. Bu amaç doğrultusunda yüksek dönüşüm verimliliğine sahip yeni fotovoltaiklerin araştırılması alternatif stratejiler açısından önem kazanmıştır. Bu araştırmanın amacı, alternatif bir fotovoltaik malzeme olarak sinerjistik nanoyapılı elektrokimyasal indirgenmiş grafen oksit/molibden trioksit fotoelektrotların elektrokimyasal sentezini ve fototepkisini sunmaktır. Bu çalışma kapsamında elde edilen bulgular, elektrokimyasal sentezlenen fotoelektrotların, güneş pilleri gibi çeşitli enerji üretim cihazlarında yeni alternatif malzemeler olarak kullanılabileceğini göstermektedir. Bu bulgular ileride yapılacak güneş pili uygulamalarında kullanılabilir.

1. INTRODUCTION

The demand for energy in the world is increasing day by day, but the energy resources that meet this demand are also rapidly depleting [1-3]. Statistical studies show that existing fossil resources such as coal, oil and natural gas will be insufficient after a few decades [4]. In addition, the energy produced by traditional methods using these fossil fuels negatively affects nature due to negative consequences such as global warming and environmental pollution [5,6]. Due to this situation, researchers have focused on innovative and environmentally friendly energy production studies. These studies are centered on direct electrical energy production with wind and solar energy, which are renewable energy sources. Solar energy can be easily converted into electrical energy using semiconductor-based photovoltaics [7-9]. Titanium dioxide (TiO_2) and zinc oxide (ZnO) are the metal oxides with the best photovoltaic properties among these semiconductors, and scientific studies on alternative materials continue.

Molybdenum trioxide (MoO_3) has a variety of interesting chemical, structural, optical and electrical properties among metal oxides. Its superior properties have been researched in different application areas such as gas sensor [10, 11], photocatalysis [12-14] and ion batteries [15,16]. MoO_3 can be a strong competitor to ZnO and TiO_2 in metal oxide-based photovoltaics with its improvable properties. These improvements can be achieved by composites with materials such as graphene,

which have a large specific surface area and excellent electrical conductivity [17].

Herein, we present synthesis route and characterization of synergistic nanostructured electrochemically reduced graphene oxide/molybdenum trioxide (ERGO/MoO_3) photoelectrodes and their enhanced photoresponses. Structurally and morphologically characterized FTO-ERGO/MoO_3 photoelectrodes were analyzed electrochemically and optically to indicate their photoelectric properties.

2. MATERIAL AND METHOD

A three-electrode cell (fluorine-doped tin oxide (FTO) coated glass as working electrode, Pt wire (approximately 99.95% purity) as counter electrode, and Ag/AgCl (3M KCl) as reference electrode) was used for electrochemical synthesis and measurements. X-ray diffractometer (Cu-Kα (λ=15.405 Å) (XRD), scanning electron microscope (SEM), energy dispersive X-ray spectroscopy (EDS), and UV-VIS spectroscopies were used for structural, morphological and optical analyzes.

The FTO coated glass working electrodes were cleaned by using an ultrasonic bath before all electrochemical synthesis processes with pure ethanol and distilled water. We used a mixture solution containing 10 mM MoO_3, 50 mM HCl and 2 mg mL^{-1} graphene oxide (GO) dispersion for electrochemical synthesis of ERGO/MoO_3. HCl was used to provide acidic media to increase the solubility of MoO_3 in water. MoO_3 was used as Mo^{6+} source and GO was used as ERGO precursor. Electrodeposition was carried out at -1.15 V (vs. Ag/AgCl) to reduce Mo^{+6} and GO, simultaneously, for 5 min in the presence of oxygen gas passing through the mixture solution. Then, deposited electrodes were rinsed with deionized water and dried with Ar gas. After all, the as-prepared electrodes were treated by thermal annealing at 400°C for 1 h for the formation of FTO-ERGO/MoO_3 photoelectrodes. The experimental procedure is shown in Figure 1.
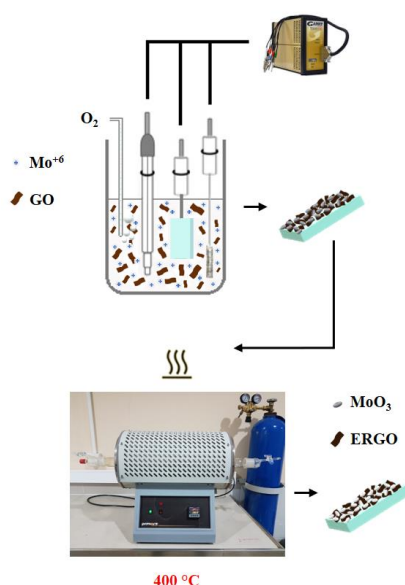
Figure 1. The schematic illustration of the experimental procedure.

3. RESULTS

Morphological properties of FTO-ERGO/MoO_3 photoelectrodes were analyzed by using SEM. SEM images of FTO-ERGO/MoO_3 photoelectrodes were given in Figure 2a. The images show the formation of MoO_3 clusters covered by ERGO on FTO electrode surface homogeneously. The elemental composition of FTO-ERGO/MoO_3 photoelectrodes was investigated by using EDS attached with SEM (Figure 2b). The detected peaks demonstrate the existence of O, Mo, and C which are forming the elemental composition of FTO-ERGO/MoO_3 photoelectrodes.

Element	Weight %	Atomic %
C K	7.22	10.71
O K	77.72	86.49
Si K	0.02	0.01
Mo L	15.04	2.79
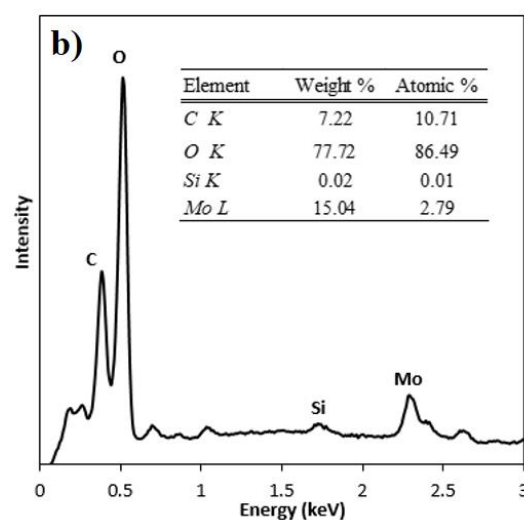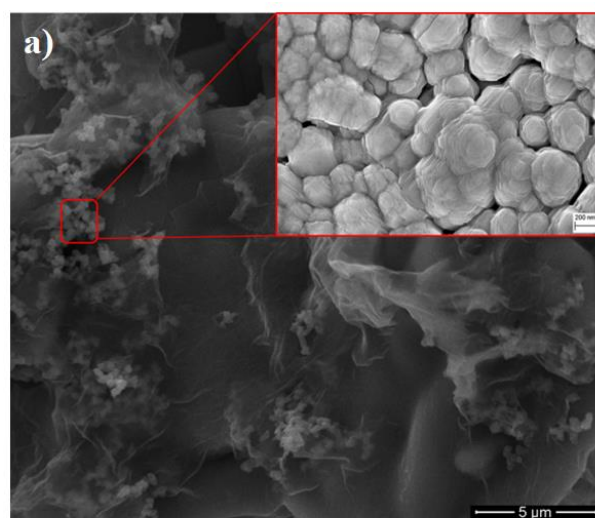
Figure 2. SEM images (a) and EDS spectra (b) of FTO-ERGO/MoO_3 photoelectrodes.

Rigaku Miniflex X-ray diffractometer (Cu-Kα (λ=15.405 Å) was utilized to investigate the crystal structure of FTO-ERGO/MoO_3. The determined peaks at 12.7°, 25.7°, 27.3°, 30.1°, and 38.9° in diffractogram (Figure 3) corresponds to (020), (040), (021), (130), and (060) planes, respectively, and promote the existence of MoO_3 with crystalline form (JCPDS No.05-0508). Additionally, the diffraction peak of ERGO at 25° was not detected in the diffractogram. This situation is related to the loss of layer stacking regularity after the composite of ERGO layers with MoO_3 particles. This

phenomenon was observed in various previous studies [18,19].
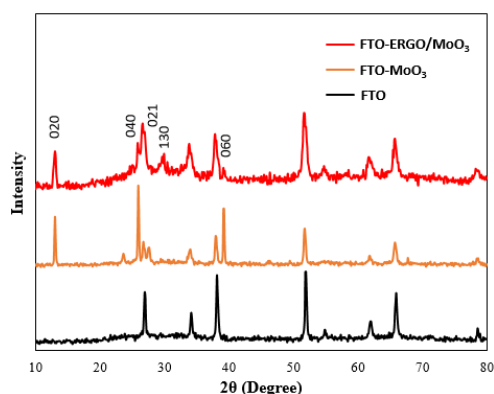
Figure 3. XRD diffractograms of FTO, FTO-MoO_3 and FTO-ERGO/MoO_3 photoelectrode.

UV-VIS spectroscopy was used to record the optical absorbance spectras for identifying and comparing the optical band-gap energies of FTO-MoO_3 and FTO-ERGO/MoO_3 photoelectrodes (Figure 4a). With the usage of Tauc plot, the band-gap value of the FTO-ERGO/MoO_3 photoelectrodes calculated as 3.03 eV whereas FTO-MoO_3 photoelectrode is 3.95 eV (Figure 4b). This decrease in the band-gap value can be attributed to the strong interaction and synergistic effect between ERGO and MoO_3 in the light of the literature [20,21].
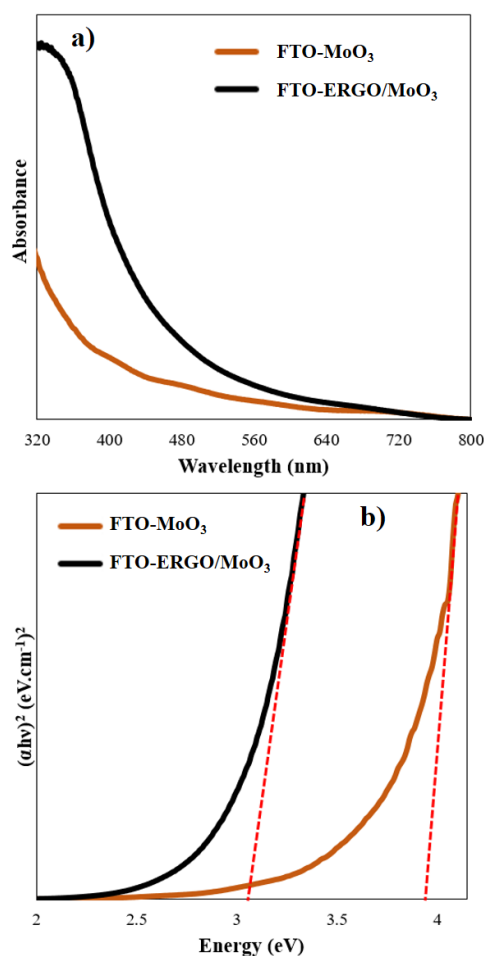
Figure 4. UV–VIS absorbance spectras (a) and Tauc plots (b) for the FTO-MoO_3 and FTO-ERGO/MoO_3 photoelectrodes.

Figure 5 shows the photocurrent–time diagrams of the FTO-MoO_3 and FTO-ERGO/MoO_3 photoelectrodes saved at 0 V for 90 s in 0.1 M Na_2SO_4 aqueous electrolyte. When the sunlight illumination is switched on, the photoresponse increases swiftly to ~24.7 $\mu A.cm^{-2}$. Further, with the light illumination switching on and off, the photoresponse rise and fall immediately.
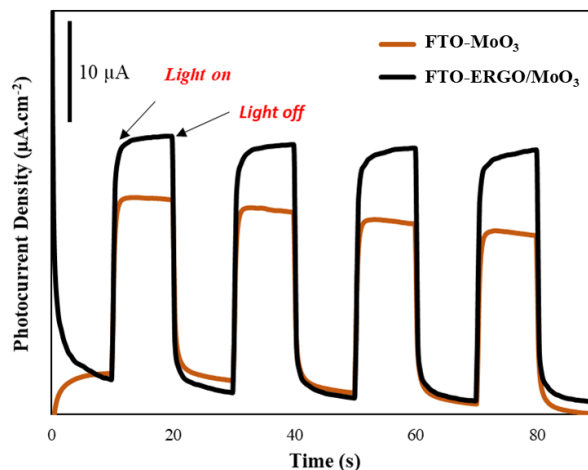
Figure 5. The photoresponse of the FTO-ERGO/MoO_3 and FTO-MoO_3 photoelectrodes in 0.1 M Na_2SO_4 aqueous electrolyte.

4. DISCUSSION AND CONCLUSION

Herein, FTO-ERGO/MoO_3 photoelectrodes were synthesized successfully by using electrochemical method. The photoelectrodes were explored with SEM, EDS, XRD and UV-VIS spectroscopic techniques for morphological, structural and optical characterization, successfully. A photocurrent density of ~24.7 $\mu A.cm^{-2}$ was obtained for FTO-ERGO/MoO_3 photoelectrode which is attributed to enhanced photoresponse compared to FTO-MoO_3. The results indicate that electrochemically synthesized FTO-ERGO/MoO_3 photoelectrodes are utilizable as new alternative materials for various energy production devices, such as solar cells.

Acknowledgement

REFERENCES

[1] Asif M, Muneer T. Energy supply, its demand and security issues for developed and emerging economies. Renewable and Sustainable Energy Reviews. 2007;11(7):1388-1413.

[2] Shahbaz M, Topcu BA, Sarıgül SS, Vo XV. The effect of financial development on renewable energy demand: The case of developing countries. Renewable Energy. 2021;178:1370-1380.

[3] Abbasi KR, Adedoyin FF, Abbas J, Hussain K. The impact of energy depletion and renewable energy on CO2 emissions in Thailand: Fresh evidence

75

from the novel dynamic ARDL simulation. Renewable Energy. 2021;180:1439-1450.

[4] Shafiee S, Topal E. When will fossil fuel reserves be diminished? Energy Policy. 2009;37(1):181-189.

[5] Yi S, Raza Abbasi K, Hussain K, Albaker A, Alvarado R. Environmental concerns in the United States: Can renewable energy, fossil fuel energy, and natural resources depletion help? Gondwana Research. 2023;117:41-55.

[6] Azni MA, Md Khalid R, Hasran UA, Kamarudin SK. Review of the Effects of Fossil Fuels and the Need for a Hydrogen Fuel Cell Policy in Malaysia. Sustainability (Switzerland). 2023;15(5):4033.

[7] Obaideen K, Olabi AG, Al Swailmeen Y, Shehata N, Abdelkareem MA, Alami AH, et al. Solar Energy: Applications, Trends Analysis, Bibliometric Analysis and Research Contribution to Sustainable Development Goals (SDGs). Sustainability. 2023;15(2):1-34.

[8] Zhang H, Lu Y, Han W, Zhu J, Zhang Y, Huang W. Solar energy conversion and utilization: Towards the emerging photo-electrochemical devices based on perovskite photovoltaics. Chemical Engineering Journal. 2020;393:124766.

[9] Awan AB, Zubair M, Memon ZA, Ghalleb N, Tlili I. Comparative analysis of dish Stirling engine and photovoltaic technologies: Energy and economic perspective. Sustainable Energy Technologies and Assessments. 2021;44:101028.

[10] Ali HM, Shokr EK, Taya YA, Elkot SA, Hasaneen MF, Mohamed WS. Amorphous molybdenum trioxide thin films for gas sensing applications. Sensors and Actuators A: Physical. 2022;335:113355.

[11] Halwar DK, Deshmane VV, Patil AV. Orthorhombic molybdenum trioxide micro-planks as carbon monoxide gas sensor. Materials Research Express. 2019;6(10):105913.

[12] Liao M, Wu L, Zhang Q, Dai J, Yao W. Controlled Morphology of Single-Crystal Molybdenum Trioxide Nanobelts for Photocatalysis. Journal of Nanoscience and Nanotechnology. 2019;20(3):1917-1921.

[13] Taya YA, Ali HM, Shokr EK, Abd El-Raheem MM, Hasaneen MF, Elkot SA, et al. Mn-doped molybdenum trioxide for photocatalysis and solar cell applications. Optical Materials. 2021;121:111614.

[14] Sharma KH, Hang DR, Bolloju S, Lee JT, Wu HF, Islam SE, et al. Two-dimensional molybdenum trioxide nanoflakes wrapped with interlayer-expanded molybdenum disulfide nanosheets: Superior performances in supercapacitive energy storage and visible-light-driven photocatalysis. International Journal of Hydrogen Energy. 2021;46(70):34663-34678.

[15] Sheng D, Liu X, Zhang Q, Yi H, Wang X, Fu S, et al. Intercalation Reaction of Molybdenum Trioxide Cathode for Rechargeable Ion Batteries. Batteries and Supercaps. 2021;6(5):e202200569.

[16] Yang C, Zhong X, Jiang Y, Yu Y. Reduced graphene oxide wrapped hollow molybdenum trioxide nanorod for high performance lithium-ion batteries. Chinese Chemical Letters. 2017;28(12):2231-2234.

[17] Yu X, Cheng H, Zhang M, Zhao Y, Qu L, Shi G. Graphene-based smart materials. Nature Reviews Materials. 2017;2:17046.

[18] Temur E, Eryiğit M, Öztürk Doğan H, Çepni E, Demir Ü. Electrochemical fabrication and reductive doping of electrochemically reduced graphene oxide decorated with TiO2 electrode with highly enhanced photoresponse under visible light. Applied Surface Science. 2022;581:152150.

[19] Pan X, Zhao Y, Liu S, Korzeniewski CL, Wang S, Fan Z. Comparing graphene-TiO2 nanowire and graphene-TiO2 nanoparticle composite photocatalysts. ACS Applied Materials and Interfaces. 2012;4:8:3944–3950.

[20] Ramesh S, Khandelwal S, Rhee KY, Hui D. Synergistic effect of reduced graphene oxide, CNT and metal oxides on cellulose matrix for supercapacitor applications. Composites Part B: Engineering. 2018;138:45-54.

[21] Qi T, Jiang J, Chen H, Wan H, Miao L, Zhang L. Synergistic effect of Fe3O4/reduced graphene oxide nanocomposites for supercapacitors with good cycling life. Electrochimica Acta. 2013;114:674-680.

H₂ Gas Response of NiO Thin Film at Different Gas Concentrations

Betül CEVİZ ŞAKAR[1]* iD

[1]Atatürk University, *East Anatolia High Technology Application and Research Center (DAYTAM), Erzurum, 25240*
Türkiye
Betül CEVİZ ŞAKAR ORCID No: 0000-0003-3298-2793

Corresponding author: betul.sakar@atauni.edu.tr

Abstract: Interest in H_2 energy, which is one of the alternative energy sources that can meet the energy needs of the increasing world population, is increasing day by day. However, dangerous properties of H_2 gas such as high flammability and explosiveness require sensitive detection of this gas. For this purpose, intensive research is being carried out on the detection of H_2 gas with high response values at low gas concentrations. In this study, the structural, morphological and H_2 gas sensing characteristics of NiO thin film, which grown on quartz substrate by RF sputtering. XRD results of the produced film revealed that the NiO film has a polycrystalline cubic structure with (101), (012), (110) and (113) diffraction planes. The lattice constant of the film was obtained as 4.226 nm, which differed by 1.274% from the theoretical values presented in the literature. From the special scanning XPS spectrum of the Ni element, the presence of peaks corresponding to Ni^{+2}, Ni^{+3} and NiOOH on the film surface was detected. SEM images revealed the existence of a homogeneous structure on the film surface consisting of structures with grain sizes of 10-20 nm. Current changes obtained at 100, 500 and 1000 ppm H_2 concentrations at 300°C showed that the produced film was sensitive to H_2 gas and the current value increased as the ppm value increased. For 1000 ppm H_2, the response value was 11.49, the response and recovery times were 239 and 286 seconds, respectively. Gas sensor measurements have also shown that the NiO film produced may have p-type conductivity.

77

NiO İnce Filmin Farklı Gaz Konsantrasyonlarında H₂ Gazı Tepkisi

Öz: Artan dünya nüfusunun enerji ihtiyacını karşılayabilecek alternatif enerji kaynaklarından biri olan H_2 enerjisine olan ilgi her geçen gün artmaktadır. Ancak H_2 gazının yüksek yanıcılık ve patlayıcılık gibi tehlikeli özellikleri bu gazın hassas bir şekilde tespit edilmesini gerektirmektedir. Bu amaçla düşük gaz konsantrasyonlarında yüksek tepki değerlerine sahip H_2 gazının tespiti üzerine yoğun araştırmalar yürütülmektedir. Bu çalışmada RF sıçratma yöntemiyle kuvars alttaş üzerinde büyütülen NiO ince filmin yapısal, morfolojik ve H_2 gazını algılama özellikleri incelenmiştir. Üretilen filmin XRD sonuçları, NiO filminin (101), (012), (110) ve (113) kırınım düzlemlerine sahip çok kristalli kübik bir yapıya sahip olduğunu ortaya çıkardı. Filmin örgü sabiti 4,226 nm olarak elde edildi ve bu değer literatürde sunulan teorik değerlerden %1,274 farklılık gösterdi. Ni elementinin özel taramalı XPS spektrumundan film yüzeyinde Ni^{+2}, Ni^{+3} ve NiOOH'ye karşılık gelen piklerin varlığı tespit edildi. SEM görüntüleri, film yüzeyinde tane boyutları 10-20 nm olan yapılardan oluşan homojen bir yapının varlığını ortaya çıkardı. 300°C'de 100, 500 ve 1000 ppm H_2 konsantrasyonlarında elde edilen akım değişimleri, üretilen filmin H_2 gazına duyarlı olduğunu ve ppm değeri arttıkça akım değerinin arttığını göstermiştir. 1000 ppm H_2 için yanıt değeri 11,49, yanıt ve iyileşme süreleri sırasıyla 239 ve 286 saniyeydi. Gaz sensörü ölçümleri ayrıca üretilen NiO filmin p tipi iletkenliğe sahip olabileceğini de göstermiştir.

1. INTRODUCTION

The need for new energy sources that can be an alternative to fossil fuels, which have serious harm to the environment and human health and whose reserves are decreasing day by day, is increasing in parallel with the increasing population. Alternative energy sources are desired to be highly efficient, low-cost, low-waste and renewable. Solar cells and hydrogen energy are the most studied types in this context. Hydrogen, which is the combustion product of water and has a huge reserve in nature, is expected to be one of the main energy sources in the future [1]. Despite its high energy efficiency, difficulties in transporting and storing hydrogen impose limitations on the practical usability of this energy source. The fact that this gas is colorless and odorless makes it impossible to detect it with human senses. In addition, when the hydrogen concentration in the environment exceeds 4%, the possibility of high explosiveness requires very sensitive detection of this gas. For this purpose, intensive research is being carried out on various semiconductors for the detection of hydrogen gas. The most prominent of these are ZnO [2], SnO_2 [3], CuO [4], TiO_2 [5] and WO_3 [6] are semiconductors. Additionally, there are studies indicating that the NiO semiconductor, whose electrical resistance increases when exposed to any reducing gas, can be a hydrogen gas sensor [7].

NiO, which has a face-centered cubic structure, has p-type semiconductor properties because the majority of the main charge carriers consist of holes. This semiconductor has a wide band gap between 3.2 and 4 eV and good chemical stability. It is used in transistors [8], light emitting diodes [9] , photodetectors [10], electrochromic devices [11] , supercapacitors [12] and gas sensors. NiO films can be produced using techniques such as direct current sputtering (DC) or radio frequency (RF) magnetron sputtering, chemical vapor deposition, pulsed laser deposition, thermal evaporation, sol-gel, chemical bath deposition, and spray pyrolysis [13].

There are some studies in the literature where NiO thin film is used as an H_2 gas sensor. The conductivity type and electrical properties of NiO thin films produced by the PLD technique were controlled by changing the pressure of O_2 gas during the growth of the film. The response of these NiO films against H_2 was found to be 12% to 14% at operating temperatures between 80–125 °C at 30000 ppm H_2 gas concentration [14]. The reactions of NiO thin films grown by DC magnetron sputtering method to H_2 gas were investigated by coating them with Pt at 3 and 5 nm. It has been observed that platinum coated on the thin film surface increases the response to H_2 gas and platinum thickness is an important parameter. The effect of different and multi-stage annealing on the response of the NiO thin film produced by the sol-gel method to H_2 gas was investigated. It has been observed that the multistage annealed NiO thin film has higher porosity and higher gas response than other thin films. The highest gas response was found to be 68% for 3000 ppm H_2 at 175 °C [15]. The response of NiO thin films produced with the DC magnetron sputter technique at different thicknesses to H_2 was investigated. It was observed that thin films grown with 50 and 100 nm thickness gave a higher response for 500 ppm H_2 gas at 250 °C, and the 50 nm thick NiO thin film gave a higher response [16].

In this study, NiO thin film was prepared on quartz substrate using a 75W RF sputtering system. Detailed characterization of the produced films was performed by XRD, XPS, FESEM and AFM. The gas response of the produced thin film was investigated for 100 ppm, 500 ppm and 1000 ppm H_2 using a current-sensitive gas sensor measurement system.

2. MATERIAL AND METHOD

In the study, NiO thin film, whose H_2 gas response was examined, was produced by RF magnetron sputtering technique. A 99.99% pure Nickel target with a diameter of 2 inches was used to enlarge the film. While enlarging, the boiler pressure was set to 3 mTorr. Sputtering was carried out at 75 W, 300 °C substrate temperature and 45 min. The distance between the target and the substrate is set to 10 cm. Before thin film growth began, the Ni target was cleaned by sputtering with argon gas for 2 minutes. After cleaning the Ni target, growth was performed on the quartz substrate by introducing oxygen gas in addition to argon. Ag contact was deposited using Interdigitated digital electrode (IDE) on NiO thin film by physical vapor deposition (PVD) system.

The crystal structure of the films was determined by XRD measurements with Panalitical Empyrean (CuKa (λ = 1.5405 Å)). Measurements were made between angles of 10°–90°, with a step interval of 0.01º. AFM (Hitachi AFM 5100N; in tapping mode) and SEM (Zeiss Sigma 300) images were taken to investigate the surface morphology of the film XPS measurements were made with the Flex Mod Specs XPS system. Hydrogen gas sensor properties of NiO thin film were determined with a Keithley 487 picoampermeter in a current-sensitive measurement system at 300°C ambient temperature, 100 ppm, 500 ppm and 1000 ppm gas flow. In these measurements, 0.5V voltage was applied to the metal contacts on the samples.

3. RESULTS AND DISCUSSION

The X-ray diffraction spectrum of NiO thin film is shown in Figure 1. The obtained diffraction peaks correspond to angles of 36.83°, 42.79°, 62.06°, 74.33°. These angle values belong to the characteristic (101), (012), (110), (113) planes of the cubic NiO compound. The interplane distance values obtained using the well-known Bragg law were calculated as 0.24, 0.21, 0.15, 0.13 Å, respectively. These data are in accordance with JPDS card: (01-078-4383). The average lattice constant of the produced thin film was calculated as 4.226 nm, which differs from the theoretical value by 1.248. The crystallite sizes calculated using the Scherrer equation for the (101), (012), (110) and (113) directions were calculated as 11.357, 10.548, 10.277 and 9.647 nm,

respectively. From XRD analyses, it can be said that there is no other formation in the structure of the NiO thin film produced and that it has a crystallization compatible with the literature.
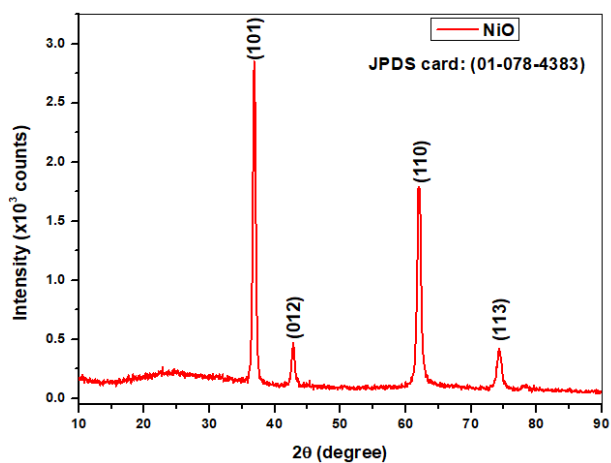
Figure 1. XRD pattern of NiO thin film.

Figure 2 shows the survey of the NiO thin film and the high-resolution XPS spectra of the O1s and Ni2p peaks. From Figure 2a, only the C1s peak is visible on the surface of the produced thin film, in addition to the characteristic peaks of nickel and oxygen This can be considered as an indication that there is no contamination other than C on the film surface. Since the binding energy of the C1s peak is 284.1 eV, a 3.3 eV shift was made in the spectrum calibration. In the O1s special scanning spectrum given in Figure 2b, two intertwined peaks are seen. After deconvolution, it can be said that these peaks correspond to the energies of 529.9 eV and 531.6 eV and belong to O^{-2} and O^{-3}. This means that there are both NiO and Ni_2O_3 structures in the structure. In the Ni2p special scan given in Figure 2c, it is seen that Ni has +2 and +3 valence, supporting the O1s spectrum. When these two spectra are evaluated together, it can be said with certainty that there is NiO and Ni_2O_3 formation on the surface.
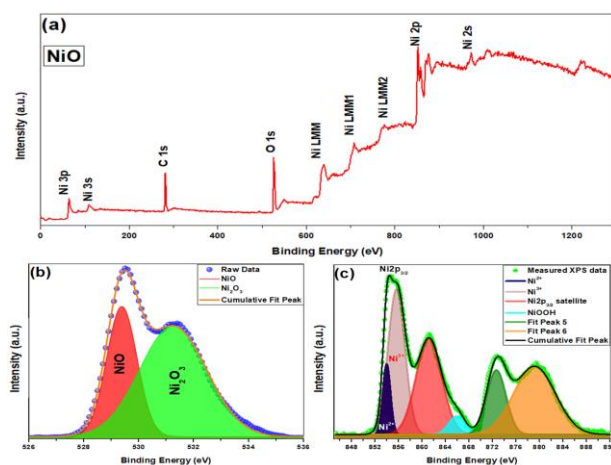
Figure 2. XPS spectra of NiO a) Survey spectrum b) High resolution O1s c) High resolution Ni2p.

SEM (Figure 3) and AFM (Figure 4) images were taken to determine the surface morphology and roughness of the NiO thin film grown by RF sputtering method. From the 20KX image given at the top of Figure 3, it can be

seen that the surface is covered quite homogeneously. In the 200 KX image (Figure 3 lower part) taken for a more detailed analysis of the film surface, a lumpy structure with 1-2 nm wide gaps between them stands out. From this 20 nm scale image, it was determined that these lump-shaped structures had a size of 10-20 nm. Additionally, these images support the formation of a polycrystalline structure, as stated in XRD analyse. From the 2D AFM image obtained for a surface area of 5x5 microns (Figure 4 upper part), spherical nanostructured formations are observed on the surface of the NiO thin film. This indicates that the lumpy structures mentioned in the SEM images are spherical. Additionally, this image also indicates that the film surface has a homogeneous structure. The 3D AFM image (Figure 4 lower part) shows that the structures extending out from the surface have generally equal heights. Surface roughness values obtained from AFM analyzes were obtained as 79.61 nm for NiO film.
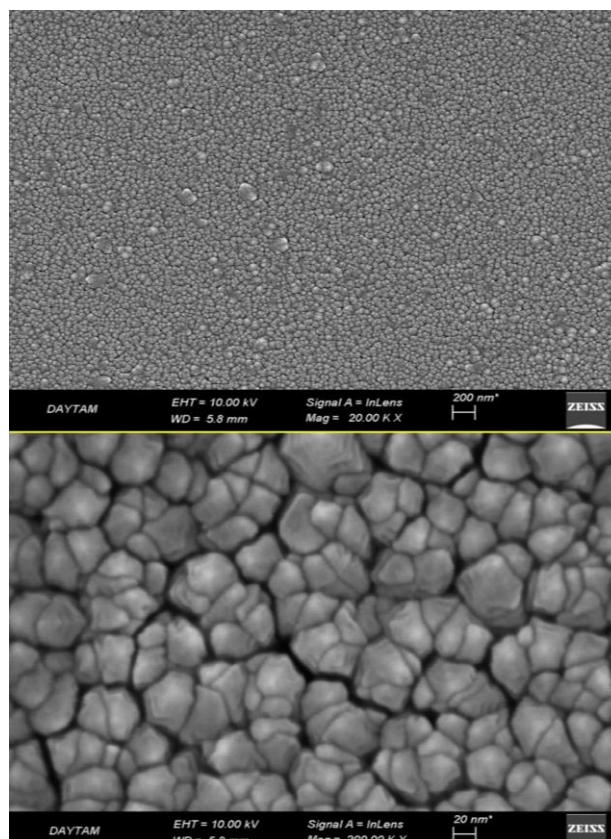
Figure 3. SEM image of NiO thin film at 20 and 200KX magnification.

The H_2 gas response of the NiO thin film obtained with the gas sensing system sensitive to current change is given in Figure 5 for different gas concentrations. In experimental measurements, H_2 gas was introduced into the environment 2 seconds after the beginning of the experiment. When 100, 500 and 1000 ppm H_2 gas was introduced, the current values measured through the sample decreased. For H_2 gas applied for 300s, current values decreased at all ppm. When the H_2 gas was cut off, the current values passing through the sample surface increased. This was repeated 3 times for each 3 different ppm values. During each cycle, the NiO thin

film showed similar evolution curves upon degassing and degassing. This is a clear indication that the produced film both responds to H_2 gas and that the gas response is repeatable. The current change at 100 ppm is quite small, and the R value calculated with the formula $R=100x(I_0-I)/I_0$ was obtained as 0.08. However, it was observed that the current changes increased significantly with increasing gas concentration. R values at 500 and 1000 ppm gas values were calculated as 3.41 and 11.49, respectively. The H_2 gas response, which shows a significant increase with increasing H_2 gas concentration, indicates that the produced NiO thin film has a linear gas response. The R^2 value of the linearity graph given in Figure 6 was calculated as 0.994. In addition, at all gas concentrations, decreasing current values when gas is applied suggest that the produced film may be p-type. As a matter of fact, when p-type semiconductors are exposed to a reducing gas such as H_2, they react with oxygen adsorbed on the surface and release electrons. The resulting electrons recombine with the holes in the structure, increasing the electrical resistance of the semiconductor. This is the main reason why the current decreases when gas is applied.
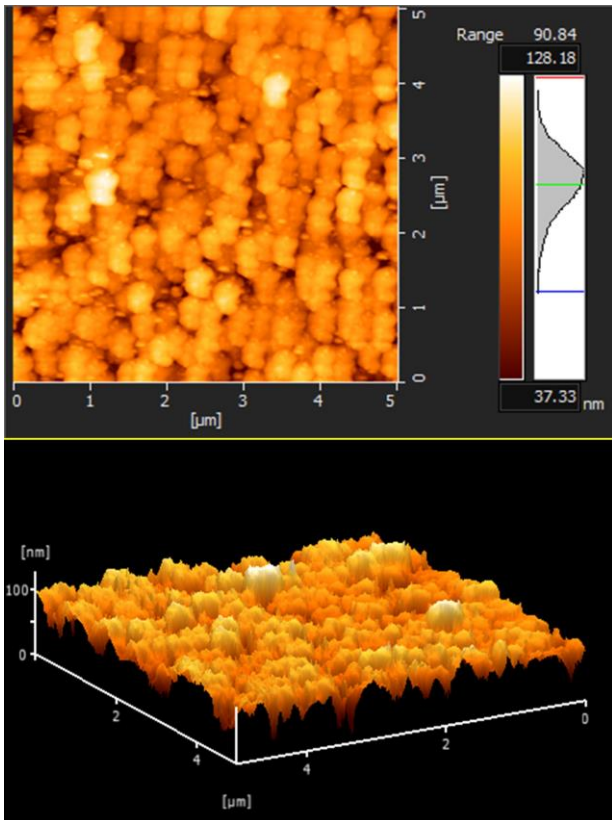
Figure 4. 2d and 3d AFM images of NiO thin film for 5x5 micron surface area.

H_2 gas response data of the produced NiO thin film at different ppm are given in Table 1. From this table, it can be seen that the response and recovery times of the film have little dependence on the gas concentration. At different gas ppm values, res and rec times are approximately 238 and 279 s, respectively. Gas response times of any material directly depend on the rate of diffusion between the gas and the element that makes up the material Since the gas responses of a single thin film at different ppm were examined in this study, there were

no significant differences in the response times as expected.
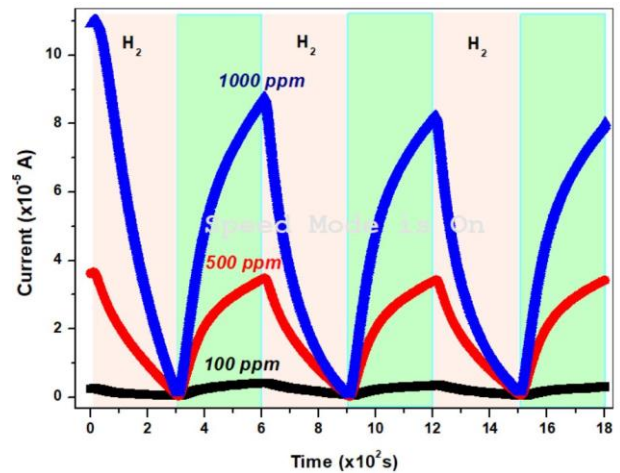
Figure 5. Current-time variation of NiO thin film for different H_2 concentrations.

Table 1. H_2 gas sensing results

H_2 concentration (ppm)	100	500	1000
τ res (s)	234	241	239
τ rec (s)	283	269	286
R	<1	3.41	11.49
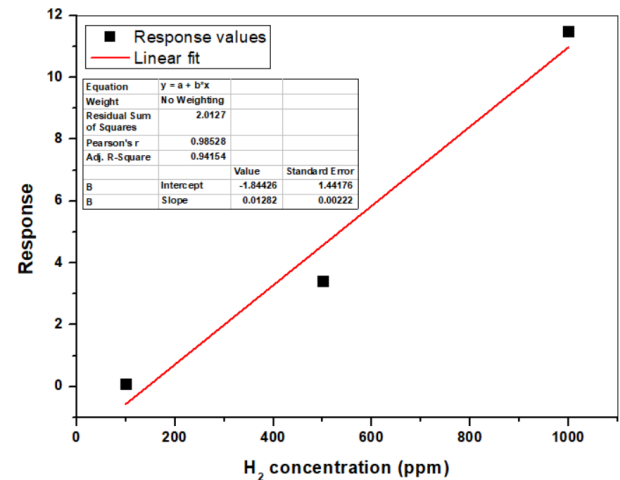
Figure 6. Linearity of NiO thin film for H_2 gas.

4. CONCLUSION

In this study, the structural and H_2 gas sensor properties of NiO thin film produced on quartz substrate by RF sputtering method were investigated. XRD measurements indicate that the structure is quite compatible with the literature and the existence of a polycrystalline cubic structure. XPS results show that NiO and Ni_2O_3 formations occur on the surface. According to the XRD and XPS results, it was revealed that no additional compounds or formations occurred in the structure, contrary to expectations. According to SEM and AFM analyses, the surface consists of very homogeneous, spherical (10—20 nm in size) nanostructures. The surface roughness value was

calculated as 79.61 nm. Although H_2 gas measurements showed that the produced films had significant response values starting from 500 ppm, the response and recovery times were not significantly affected by the gas concentration. Although the H_2 gas response of the NiO film produced is lower than other studies in the literature, it is hoped that sensors with higher response values can be obtained by obtaining the p-type NiO thin film in a more porous structure. It is also predicted that surface changes can be made to obtain shorten response and recovery times.

Acknowledgement

REFERENCES

[1]   Li Z, Yao Z, Haidry AA, et al. Resistive-type hydrogen gas sensor based on TiO2: A review. *International Journal of Hydrogen Energy* 2018; 43: 21114–21132.
[2]   Zhu L, Zeng W. Room-temperature gas sensing of ZnO-based gas sensor: A review. *Sensors and Actuators A: Physical* 2017; 267: 242–261.
[3]   Barbosa MS, Suman PH, Kim JJ, et al. Gas sensor properties of Ag- and Pd-decorated SnO micro-disks to NO2, H2 and CO: Catalyst enhanced sensor response and selectivity. *Sensors and Actuators B: Chemical* 2017; 239: 253–261.
[4]   Moon WJ, Yu JH, Choi GM. The CO and H2 gas selectivity of CuO-doped SnO2–ZnO composite gas sensor. *Sensors and Actuators B: Chemical* 2002; 87: 464–470.
[5]   Ceviz Şakar B. Influence of the Cu doping on the physical and H2 gas sensing properties of TiO2. *International Journal of Hydrogen Energy* 2023; S0360319923051005.
[6]   Mirzaei A, Kim J-H, Kim HW, et al. Gasochromic WO3 Nanostructures for the Detection of Hydrogen Gas: An Overview. *Applied Sciences* 2019; 9: 1775.
[7]   Steinebach H, Kannan S, Rieth L, et al. H2 gas sensor performance of NiO at high temperatures in gas mixtures. *Sensors and Actuators B: Chemical* 2010; 151: 162–168.
[8]   Varghese B, Reddy MV, Yanwu Z, et al. Fabrication of NiO Nanowall Electrodes for High Performance Lithium Ion Battery. *Chem Mater* 2008; 20: 3360–3367.
[9]   Zhang Y, Wang S, Chen L, et al. Solution-processed quantum dot light-emitting diodes based on NiO nanocrystals hole injection layer. *Organic Electronics* 2017; 44: 189–197.
[10]   Tsai S-Y, Hon M-H, Lu Y-M. Fabrication of transparent p-NiO/n-ZnO heterojunction devices for ultraviolet photodetectors. *Solid-State Electronics* 2011; 63: 37–41.
[11]   Purushothaman KK, Muralidharan G. Nanostructured NiO based all solid state electrochromic device. *J Sol-Gel Sci Technol* 2008; 46: 190–194.
[12]   Du D, Hu Z, Liu Y, et al. Preparation and characterization of flower-like microspheres of nano-NiO as electrode material for supercapacitor. *Journal of Alloys and Compounds* 2014; 589: 82–87.
[13]   Bonomo M. Synthesis and characterization of NiO nanostructures: a review. *J Nanopart Res* 2018; 20: 222.
[14]   Stamataki M, Tsamakis D, Brilis N, et al. Hydrogen gas sensors based on PLD grown NiO thin film structures. *phys stat sol (a)* 2008; 205: 2064–2068.
[15]   Soleimanpour AM, Hou Y, Jayatissa AH. Evolution of hydrogen gas sensing properties of sol–gel derived nickel oxide thin film. *Sensors and Actuators B: Chemical* 2013; 182: 125–133.
[16]   Predanocy M, Hotový I, Čaplovičová M. Structural, optical and electrical properties of sputtered NiO thin films for gas detection. *Applied Surface Science* 2017; 395: 208–213.

Electrochemical Impedance Spectroscopy Analysis of 45S5 Bioglass Coating on After Oxidation of CoCrW Alloy

Şükran Merve TÜZEMEN[1*] (ID), Yusuf Burak BOZKURT[1] (ID), Burak ATİK[1] (ID), Yakup UZUN[1] (ID), Ayhan ÇELİK[1] (ID)

[1] Atatürk University, Engineering Faculty, Machanical Engineering Department, Erzurum, Türkiye
Şükran Merve TÜZEMEN ORCID No: 0000-0003-0400-5602
Yusuf Burak BOZKURT ORCID No: 0000-0003-3859-9322
Burak ATİK ORCID No: 0000-0003-2117-9284
Yakup UZUN ORCID No: 0000-0002-5134-7640
Ayhan ÇELİK ORCID No: 0000-0002-8096-0794

*Corresponding author: sukrantuzemen@atauni.edu.tr

(Received: 25.01.2024, Accepted: 24.04.2024, Online Publication: 01.10.2024)

Abstract: Implants and prostheses, which are used to replace a missing or damaged structure in living organisms, must show all the necessary mechanical, tribological, electrochemical and biocompatibility properties together. CoCr alloys are often preferred biometals for their good mechanical strength and wear resistance, especially in dental and orthopedic implants. Although these alloys show good corrosion resistance in terms of electrochemical behavior as well as other good properties, when CoCr alloys come into contact with bone tissue, their surfaces show bioinert properties in terms of tissue formation between the implant and bone tissue. Therefore, both their corrosion behavior and biocompatibility properties need to be improved. In this study, CoCrW alloys produced by selective laser melting were coated with commercial 45S5 bioglass powder, a bioactive material, by electrophoretic deposition method. In order to improve the adhesion after coating, CoCrW alloys were subjected to electrochemical etching process during coating. After the coating process was completed, untreated, oxidized, untreated-coated and oxidized-coated samples were examined by electrochemical impedance spectroscopy (EIS) after open circuit potential measurements to investigate their corrosion behavior. As a result of the corrosion tests, it was determined that the oxidized-coated sample showed the best condition compared to the other samples in EIS analyzes.

82

CoCrW Alaşımının Oksidasyon Sonrasında 45S5 Biyocam Kaplamanın Elektrokimyasal Empedans Spektroskopisi Analizi

Anahtar Kelimeler
Elektrokimyasal
empedans
spektoskopisi,
45S5 Biyocam,
Oksitleme,
CoCr Alaşımı

Öz: Canlı organizmalarda eksik veya hasarlı bir yapının yerine konulması amacıyla kullanılan implant ve protezlerin gerekli tüm mekanik, tribolojik, elektrokimyasal ve biyouyumluluk özelliklerini bir arada göstermesi gerekir. CoCr alaşımları, özellikle diş ve ortopedik implantlarda iyi mekanik dayanımları ve aşınma dirençleri nedeniyle sıklıkla tercih edilen biyometallerdir. Bu alaşımlar diğer iyi özelliklerinin yanı sıra elektrokimyasal davranış açısından da iyi bir korozyon direnci göstermelerine rağmen, Cr iyonlarının alaşım yüzeyinden bir süre sonra vücuda salındığı tespit edilmiştir. Ayrıca CoCr alaşımları kemik dokusu ile temas ettiğinde yüzeyleri implant ile kemik dokusu arasında doku oluşumu açısından biyoinert özellik göstermektedir. Bu nedenle hem korozyon davranışlarının hem de biyouyumluluk özelliklerinin geliştirilmesi gerekmektedir. Bu çalışmada, seçici lazer eritme ile üretilen CoCrW alaşımları, elektroforetik biriktirme yöntemi ile biyoaktif bir malzeme olan ticari 45S5 biyocam tozu ile kaplanmıştır. Kaplama esnasında adezyonu iyileştirmek için CoCrW alaşımları kaplama öncesi elektrokimyasal oksitleme işlemine tabi tutulmuştur. Kaplama işlemi tamamlandıktan sonra, işlemsiz, oksitlenmiş, işlemsiz-kaplanmış ve oksitlenmiş-kaplanmış numuneler, korozyon davranışlarını araştırmak için açık devre potansiyeli ölçümlerinden sonra elektrokimyasal empedans spektroskopisi (EIS) ile incelenmiştir. Korozyon testlerinden önce kaplamanın yapısal

özellikleri analiz edilmiştir. Korozyon testleri sonucunda, EIS analizlerinde oksitlenmiş-kaplanmış numunenin diğer numunelere kıyasla en iyi durumu gösterdiği tespit edilmiştir.

1. INTRODUCTION

CoCrW alloys, also known as Stellite alloys, are widely used in biomedical, aerospace, space, nuclear and other industries that require superior properties such as high temperature, wear and corrosion resistance [1]. The excellent comprehensive properties of CoCrW alloy are mainly due to the low stacking fault energy of γ-Co, solid solution strengthening of Cr, W and precipitation strengthening of carbide second phase [2,3]. In addition, since these alloys are non-magnetic, radiopaque and MRI compatible, CoCrW alloys are often preferred in hip and knee prostheses and dental implants [4]. The corrosion resistance of CoCr alloys is provided by the passive oxide layer on them as in stainless steels. However, in physiological fluids, factors such as the type and chemical composition of the alloy, exposure time to aggressive ions, pH change and temperature of the biological environment affect the formation and dissolution kinetics of the passive film on CoCr alloys [5,6]. Bone tissue has a piezoelectric behavior that can change the electrochemical potential of metallic implants. These continuous and dynamic processes not only undermine surface performance, but also lead to increased debris in the implant environment. To date, in vivo wear and corrosion and debris generated from articular surfaces have been identified as one of the most important phenomena leading to implant failure [7,8]. On the other hand, some studies have shown that the release of Co^{2+}, Cr^{3+} and Cr^{6+} ions from implants made of CoCr alloys can cause hypersensitivity and inflammatory responses at the implant site [9]. In order to overcome these situations, surface treatments are applied to metallic structures. The film coated with the surface treatment affects the biocompatibility of implant materials and in recent years, bioactive coatings have become more preferred to provide osseointegration as well as corrosion prevention [10].

The electrophoretic deposition (EPD) technique is an electrochemical surface treatment that offers the possibility of coating on complex substrates at room temperature, simple and low installation cost, and the ability to form microstructurally homogeneous films of high purity. The method involves the deposition of colloidal powder particles suspended in suspension onto the substrate by means of an externally applied electric field [11]. Bioactive coatings through the EPD process have been reported in the literature in a few cases and most of the research has focused on high bioactivity hydroxyapatite and bioactive glass coatings [12,13]. The high bioactivity of bioactive glasses (BGs) is based on the release of H+ ions from the surrounding solution and ions such as Ca2+, Na+ from the structure as a result of their rapid dissolution. With the release of these ions, a bone-like hydroxyapatite layer forms on the surface of the substrate, so bioactive glasses are preferred in the field of bone tissue repair and reconstruction [14]. Studies show that a strong adhesion is formed in hydroxyapatite-coated structures by the EPD process and that the corrosion resistance of these structures in simulated body fluid (SBF) is improved compared to untreated samples [15]. However, the application of processes such as pre-coating heat treatment, etching, oxidation has been observed in the literature to increase coating adhesion and give better results in wear and corrosion tests [16].

In addition, CoCr alloys are difficult metallic materials to produce due to their high hardness, melting point and lower ductility [17]. Additive manufacturing (AM) techniques, which have been introduced in recent years with 3D printers, offer a very good solution to fabricate such intricately shaped, difficult-to-produce metallic materials. Among these techniques, selective laser melting (SLM), a powder bed fusion technique, uses computer-aided design (CAD) data to melt metal powders and fuse them layer by layer to form a structure using thermal energy from a focused and accurately controlled laser beam. SLM facilitates the production of complex and non-machinable parts in many industries such as aerospace, aviation, automotive, biomedical and defense industries. Compared to other conventional methods such as weaving and machining, SLM offers advantages such as no casting defects, dimensional accuracy, improved mechanical properties with finer grains due to rapid melting and cooling, lower production cost and less scrap [17,18]. In the literature, the mechanical, tribological and electrochemical properties of many CoCr alloys and composites after additive manufacturing have been investigated in terms of tensile strength, wear and corrosion resistance and it has been observed that they perform better than conventional manufacturing methods [19,20].

In this study, the corrosion resistance of electrochemically oxidized CoCrW alloy coated with 45S5 bioactive glass using EPD technique was analyzed by electrochemical impedance spectroscopy (EIS). The results of untreated, untreated-45S5 coated, oxidized and oxidized-45S5 coated samples were analyzed comparatively in order to observe the improvement of corrosion resistance.

2. MATERIAL AND METHOD

2.1. Materials and Surface Treatments

Samples of CoCrW alloy containing 58.85 wt% Co, 26.30 wt% Cr, 12.62 wt% W, 1.13 wt% Si and 1.1 wt% C were manufactured by the SLM method using a CONCEPT LASER MLab Cusing device with dimensions of 10x10x2 mm^3 and CoCrW powders according to ASTM F75 standard. The manufacturing was carried out using simple straight line scans with 95 W laser power directly directed to melt each layer, a layer thickness of 30 μm and a plane and contour scan speed of 1500 mm/s. After manufacturing, all samples were polished using 80, 220, 400, 800, 1200, 2000 mesh grid with SiC papers and 1 μm grain size with alumina powder respectively, then cleaned with ethanol and dried.

CoCrW alloys prepared to improve adhesion prior to the EPD process were electrochemically oxidized using 1 M H_2SO_4 solution and DC power supply and CoCrW counter electrode for 15 V-10 minutes. For the EPD process, a suspension was prepared by first mixing 99 ml distilled water, 1 ml acetic acid, 0.2 ml phosphate ester and 1 g/L 45S5 Bioglass® (containing 45% SiO_2, 24.5% CaO, 24.5% Na_2O and 6.0% P_2O_5 by weight) commercial powder using a magnetic stirrer for 2 hours. All EPD coating processes were carried out at ambient temperature with a GW GPR-30H10D Laboratory DC Power Supply using graphite as the counter electrode with a distance of approximately 2 cm between them. All samples were coated for 5 minutes at 30 V DC voltage. The phases of the untreated and coated samples were determined by X-Ray Diffraction analysis at 40 kV and 30 mA Cu Kα (λ = 1.789 Å) source diffractometer using XRD-GNR Explorer instrument.

2.2. Electrochemical Impedance Spectroscopy

Untreated, untreated-45S5 coated, oxidized and oxidized-45S5 coated CoCrW samples were subjected to corrosion tests using Gamry G750 Potentiostat/Galvanostat system in stimulated body fluid (SBF) for electrochemical investigation. The test setup was prepared as a triple electrode system using untreated and coated samples as working electrode, graphite rod as counter electrode and Ag/AgCl as reference electrode. The corrosion tests were completed by Open Circuit Potential (OCP) followed by Potantiodynamic Polarization and Electrochemical Impedance Spectroscopy (EIS) analyzes. During the test, the corrosion surface area was set to 0.5 cm2 and the time required for the Open Circuit Potential reading was set to 7200 seconds. Potantiodynamic Polarization measurements were performed with a scan rate of 1 mV/s beyond 2 V beyond the Open Circuit Potential values. The Potantiodynamic Polarization and EIS curves obtained from electrochemical analysis were examined in detail.

3. RESULTS

The XRD graph of the untreated, electrochemically oxidized, EPD coated CoCrW alloy samples coated with 45S5 bioglass and duplex (Oxidized+45S5) is given in Figure 1. XRD peaks were obtained in the range of 10°-100° for 2θ. CoCrW alloy consists of surface-centered cubic (fcc) γ- and hexagonal tight-packed (hcp) ε-phase structures [21-23]. XRD diffraction patterns show that CoCrW alloy is composed of fcc γ-phase and hcp ε-phase as seen from the peaks obtained at 41°, 43°, 47° and 51° for 2θ. The presence of $Cr2O3$ phases after the electrochemical oxidation process is seen in the XRD graph given in Figure 1 [24]. In addition, peaks belonging to 45S5 bioglass are seen in the peaks obtained as a result of XRD analysis obtained from bioglass coated surfaces with EPD technique [25].
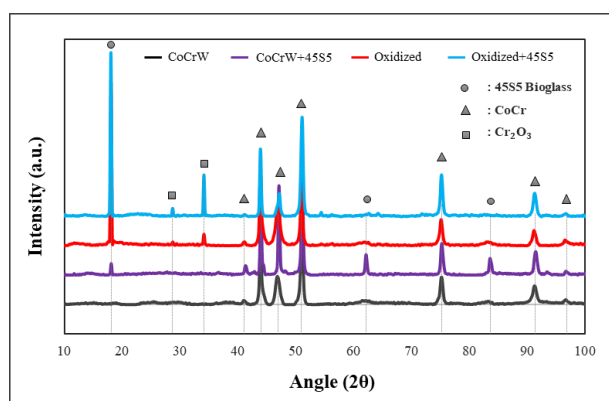
Figure 1. XRD patterns of all samples.

The corrosion behavior of all sample groups subjected to different surface treatments produced by SLM method was carried out by open circuit potential, potentiodynamic polarization and electrochemical impedance spectroscopy measurements in SBF solution at 37°C. Open circuit potential (OCP) measurements were performed for 7200 seconds for all sample groups (Figure 2a). When the OCP graphs are analyzed, it is seen that the curves are directed towards a constant value. The OCP has become stable due to the formation of a stable oxide film on the surface during the OCP measurement and the dissolution and re-formation of this oxide film at the same time [26,27]. It is also seen that the potential of the oxidized surface is higher. Figure 2b shows the potentiodynamic polarization curves for all sample groups at a scan rate of 1 mV/s. The shapes of the potentiodynamic polarization curves are generally similar to each other. Current density, anodic Tafel slope, cathodic Tafel slope, corrosion potential and corrosion rate (Ecorr, icorr, βa, βc, respectively) values of all sample groups were calculated by Tafel extrapolation method and given in Table 1.
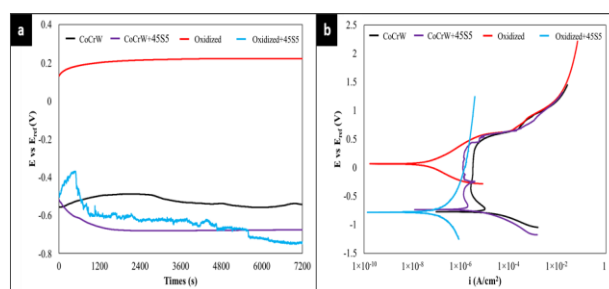
,
Figure 2. All sample groups (a) OCP and (b) Potentiodynamic polarization graphs.

Corrosion current density (icorr) is an important parameter for the corrosion mechanism. In addition, icorr is directly proportional to the corrosion rate. It can be said that corrosion resistance increases with decreasing current density [27-29]. For this reason, when the icorr values given in Table 1 are examined, it is seen that the icorr values of CoCrW+45S5 (17.34×10^{-6} A/cm²), Oxidized (57.80×10^{-9} A/cm²) and Oxidized+45S5 (11.90×10^{-9} A/cm²) samples are lower than the untreated CoCrW (195.60×10^{-9} A/cm²) sample. In addition, the highest corrosion rate was 82.30 mm/year in the untreated sample. This value shows that the untreated CoCrW sample has

lower corrosion resistance compared to the other samples in terms of both mass loss and corrosion rate. In addition, when the potentiodynamic polarization curves of untreated CoCrW and CoCrW+45S5 coated samples are examined, it is seen in Figure 2b that they show a similar passivation feature. This passivation behavior is directly related to the protective passive oxide layer formed on the surface [29].

Table 1. The values of corrosion test results for all samples.

Samples	Ecorr [mV]	icorr [A/cm^2]	Corrosion Rate [mm/year]
CoCrW	- 56.39	195.60×10^{-9}	82.30
CoCrW+45S5	- 771.50	17.34×10^{-6}	7.296
Oxidized	- 68.50	57.80×10^{-9}	20.59×10^{-3}
Oxidized+45S5	- 779	11.90×10^{-9}	4.229×10^{-3}

Bode and Nyquist curves obtained from electrochemical impedance spectroscopy before potentiodynamics in SBF solution for all sample groups are given in Figure 3 and Figure 4. Phase angle is directly proportional to corrosion. The probability of corrosion decreases with increasing phase angle [29]. In bode and nyquist curves, corrosion resistance increases with the increase of capacitive semicircle diameter [27]. Thus, when the bode curves obtained are examined, it is seen that the Oxidized + 45S5 duplex surface treated sample has high corrosion resistance.
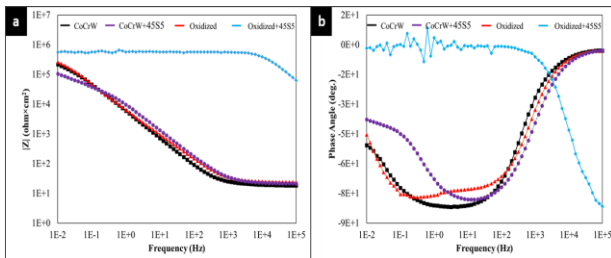
Figure 3. Bode curves for all sample groups (a) Frequency-|Z| and (b) Frequency-Phase angle curves.

It means that the corrosion resistance increases as the capacitive loop expands in Nyquist curves. Looking at the Nyquist curves given in Figure 4, it is seen that the capacitive semicircle diameter of the Oxidized+45S5 sample is considerably higher compared to the other samples. This shows that it has the highest corrosion resistance compared to other samples.
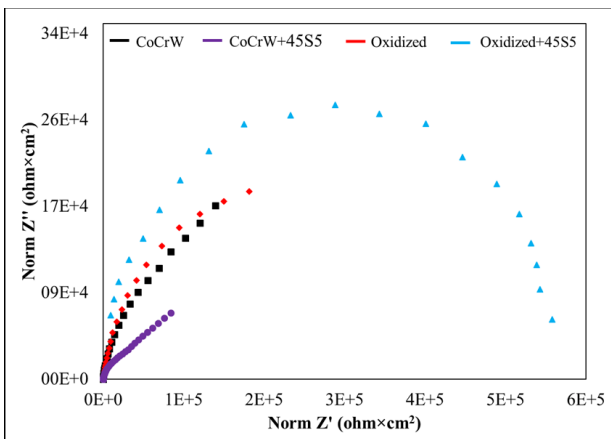
Figure 4. Nyquist curves for all samples groups

4. DISCUSSION AND CONCLUSION

Electrochemical oxidation, 45S5 Bioglass and duplex (oxidation+45S5 Bioglass) coating processes were carried out on CoCrW alloy produced by SLM. Electrochemical corrosion properties of untreated and coated surfaces were investigated in SBF solution and the results obtained are summarized below:

- ✓ According to XRD results, CoCr, Cr2O3 and 45S5 Bioglass peaks were obtained. In addition, fcc γ-phase and hcp ε-phases of untreated CoCrW alloy were found.
- ✓ In the electrochemical corrosion test results carried out in SBF solution, the highest corrosion resistance was observed on the Oxidized+45S5 coated surface with 11.90×10^{-9} A/cm^2 icorr value.
- ✓ The electrochemical corrosion performances of CoCrW+45S5, oxidation and oxidation+45S5 coatings on the surface of CoCrW alloy produced by SLM technique have been improved.

Acknowledgement

REFERENCES

[1] Kuzucu V, Ceylan M, Çelik H, Aksoy I. Microstructure and phase analyses of Stellite 6 plus 6 wt.% Mo alloy. Journal of Materials Processing Technology. 1997; 69(1–3): 257-263.

[2] Tian LY, Lizárraga R, Larsson H, Holmström E, Vitos L. A first principles study of the stacking fault energies for fcc Co-based binary alloys. Acta Materialia. 2017; 136: 215-223.

[3] Wang S, Zhan S, Hou X, Wang L, Zhang H, Zhang H, Sun Y, Huang L. Microstructure and Mechanical Property of a Multi-Scale Carbide Reinforced Co–Cr–W Matrix Composites. Crystals. 2022; 12(2):198.

[4] Yan Y, Neville A, Dowson D. Tribo-corrosion properties of cobalt-based medical implant alloys in simulated biological environments. Wear. 2007; 263(7–12): 1105-1111.

[5] Ouerd A, Alemany-Dumont C, Normand B, Szunerits S. Reactivity of CoCrMo alloy in physiological medium: Electrochemical characterization of the metal/protein interface. Electrochimica Acta. 2008; 53(13): 4461-4469.

[6] Igual Muñoz A, Mischler S. Interactive Effects of Albumin and Phosphate Ions on the Corrosion of CoCrMo Implant Alloy. J. Electrochem. Soc. 2007; 154: 10.

[7] Gittens RA, Olivares-Navarrete R, Tannenbaum R, Boyan BD, Schwartz Z. Electrical Implications of Corrosion for Osseointegration of Titanium Implants. Journal of Dental Research. 2011; 90(12): 1389-1397.

[8] Diaz I, Martinez-Lerma JF, Montoya R, Llorente I, Escudero ML, García-Alonso MC. Study of overall and local electrochemical responses of oxide films grown on CoCr alloy under biological environments. Bioelectrochemistry. 2017; 115: 1-10.

[9] Mani G. Metallic biomaterials: cobalt-chromium alloys. Murphy W, Black J, Hastings G. (Eds.), Handb. Biomater. Prop (second ed.). 159-166, 2016, Springer.

[10] Chen Q, Thouas GA. Metallic implant biomaterials. Mater Sci Eng R Rep. 2015; 87: 1-57.

[11] Boccaccini AR, Peters C, Roether JA, Eifler D, Misra SK, Minay EJ. Electrophoretic deposition of polyetheretherketone (PEEK) and PEEK/Bioglass® coatings on NiTi shape memory alloy wires. J. Mater. Sci. 2006; 41: 8152-8159.

[12] Pishbin F, Simchi A, Ryan MP, Boccaccini AR. Electrophoretic deposition of chitosan/45S5 Bioglass® composite coatings for orthopaedic applications. Surf. Coatings Technol. 2011; 205: 5260-5268.

[13] Khanmohammadi S, Ojaghi-Ilkhchi M, Farrokhi-Rad M. Evaluation of Bioactive glass and hydroxyapatite based nanocomposite coatings obtained by electrophoretic deposition. Ceramics International. 2020; 46: 26069-26077.

[14] Vichery C, Nedelec J-M. Bioactive Glass Nanoparticles: From Synthesis to Materials Design for Biomedical Applications. Materials. 2016; 9(4): 288.

[15] Khanmohammadi S, Ojaghi-Ilkhchi M, Khalil-Allafi J. Electrophoretic deposition and characterization of Bioactive glass-whisker hydroxyapatite nanocomposite coatings on titanium substrate. Surface and Coatings Technology. 2019; 378: 1-13.

[16] Pawlik A, Rehman MAU, Nawaz Q, Bastan FE, Sulka GD, Boccaccini AR. Fabrication and characterization of electrophoretically deposited chitosan-hydroxyapatite composite coatings on anodic titanium dioxide layers. Electrochim. Acta. 2019; 307: 465-473.

[17] Ozel T, Bartolo P, Ceretti E, De Ciurana Gay J, Rodriguez CA, Da Silva JVL. Biomedical devices: design, prototyping and manufacturing. 2017, John Wiley & Sons.

[18] Takaichi A, Suyalatu T, Nakamoto N, Joko N, Nomura Y, Tsutsumi S. Microstructures and mechanical properties of Co-29Cr-6Mo alloy fabricated by selective laser melting process for dental applications. J Mech Behav Biomed Mater. 2013; 21: 67-76.

[19] Mergulhão MV, Podestá CE, das Neves MDM. Valuation of mechanical properties and microstructural characterization of ASTM F75 Co-Cr alloy obtained by Selective Laser Melting (SLM) and casting techniques. Mater Sci Forum. 2017; 899: 323-328.

[20] Seyedi M, Zanotto F, Monticelli C, Balbo A, Liverani E, Fortunato A. Microstructural characterization and corrosion behaviour of SLM CoCrMo alloy in simulated body fluid. Metall Ital. 2018; 110: 45-50.

[21] Lee HW, Jung K-H, Hwang S-K, Kang S-H, Kim D-K. Microstructure and mechanical anisotropy of CoCrW alloy processed by selective laser melting. Materials Science and Engineering: A. 2019; 749: 65-73.

[22] Lu Y, Wu S, Gan Y, Zhang S, Guo S, Lin J, Lin J. Microstructure, mechanical property and metal release of As-SLM CoCrW alloy under different solution treatment conditions. Journal of the Mechanical Behavior of Biomedical Materials. 2016; 55: 179-190.

[23] Luo J, Wu S, Lu Y et al. The effect of 3 wt.% Cu addition on the microstructure, tribological property and corrosion resistance of CoCrW alloys fabricated by selective laser melting. J Mater Sci: Mater Med. 2018; 29(37).

[24] Lu Y, Lin W, Xie M, Xu W, Liu Y, Lin J, Yu C, Tang K, Liu W, Yang K, Lin J. Examining Cu content contribution to changes in oxide layer formed on selective-laser-melted CoCrW alloys. Applied Surface Science. 2019; 464: 262-272.

[25] Azzouz I, Faure J, Khlifi K, Cheikh Larbi A, Benhayoune H. Electrophoretic Deposition of 45S5 Bioglass® Coatings on the Ti6Al4V Prosthetic Alloy with Improved Mechanical Properties. Coatings. 2020; 10(12):1192.

[26] Qin P, Chen LY, Liu YJ, Zhao CH, Lu YJ, Sun H, Zhang LC. Corrosion behavior and mechanism of laser powder bed fusion produced CoCrW in an acidic NaCl solution. Corrosion Science. 2023; 213: 110999.

[27] Uzun Y., Taş B., Tüzemen Ş.M., Çelik A. The Improvement of Corrosion Performance of CoCrW Alloy with Bioglass Coating. 3rd International Natural Science, Engineering and Materials Technology Conference, NEM 2023. Gazimagusa, Cyprus (Kktc); 2023. p.182-189.

[28] Lu Y, Ren L, Xu X, Yang Y, Wu S, Luo J, Yang M, Liu L, Zhuang D, Yang K, Lin J. Effect of Cu on microstructure, mechanical properties, corrosion resistance and cytotoxicity of CoCrW alloy fabricated by selective laser melting. Journal of the Mechanical Behavior of Biomedical Materials. 2018; 81: 130-141.

[29] Lu Y, Wu S, Gan Y, Li J, Zhao C, Zhuo D, Lin J. Investigation on the microstructure, mechanical property and corrosion behavior of the selective laser melted CoCrW alloy for dental application. Materials Science and Engineering: C. 2015; 49: 517-525.

[30] Sun D, Wharton JA, Wood RJK, Ma L, Rainforth WM. Microabrasion–corrosion of cast CoCrMo alloy in simulated body fluids. Tribology International. 2009; 42(1): 99-110.

86

Türk Doğa ve Fen Dergisi
Turkish Journal of Nature and Science
www.dergipark.gov.tr/tdfd

BINGÖL UNIVERSITY

Investigation of the Effect of Bioactive Glass Coating on the Corrosion Behavior of Pre-treated Ti6Al4V Alloy

Şükran Merve TÜZEMEN[1*] iD **, Yusuf Burak BOZKURT[1]** iD **, Burak ATİK[1]** iD **, Yakup UZUN[1]** iD **, Ayhan ÇELİK[1]** iD

[1] Atatürk University, Engineering Faculty, Machanical Engineering Department, Erzurum, Türkiye
Şükran Merve TÜZEMEN ORCID No: 0000-0003-0400-5602
Yusuf Burak BOZKURT ORCID No: 0000-0003-3859-9322
Burak ATİK ORCID No: 0000-0003-2117-9284
Yakup UZUN ORCID No: 0000-0002-5134-7640
Ayhan ÇELİK ORCID No: 0000-0002-8096-0794

*Corresponding author: sukrantuzemen@atauni.edu.tr

Abstract: Titanium alloys, especially Ti6Al4V, are widely used in in-body implants due to their superior mechanical properties, corrosion resistance and biocompatibility. However, due to their higher modulus of elasticity than bone, they do not bond well with the bone structure, leading to loosening. In addition, they contain the elements Al and V, both of which are dangerous when released into the body. Therefore, these alloys are subjected to a number of surface treatments to improve their surface properties. In this study, Ti6Al4V alloys were produced by selective laser melting in dimensions of 10x10x2 mm^3 and then surface treated. The alloy surfaces were first anodized and then coated with 45S5 bioglass powder. After all surface processes, structural analyzes were performed and the effectiveness of the coating was examined. The untreated and coated samples were subjected to corrosion tests by cyclic polarization method and their corrosion behaviors were investigated.

Biyoaktif Cam Kaplamanın Ön İşlem Görmüş Ti6Al4V Alaşımının Korozyon Davranışı Üzerindeki Etkisinin Araştırılması

Öz: Titanyum alaşımları, özellikle Ti6Al4V alaşımı üstün mekanik özellikleri, korozyon direnci ve biyouyumlulukları nedeniyle vücut içi implantlarda yaygın olarak kullanılmaktadır. Bununla birlikte, bu alaşımlar sahip oldukları kemikten daha yüksek elastisite modülleri ile kemik yapısıyla iyi bağlanamazlar ve gevşemeye neden olurlar. Ayrıca, her ikisi de vücuda salındığında tehlikeli olan Al ve V elementlerini içerirler. Bu nedenle, bu alaşımlar yüzey özelliklerini iyileştirmek için bir dizi yüzey işlemine tabi tutulur. Bu çalışmada, Ti6Al4V alaşımları 10x10x2 mm^3 boyutlarında seçici lazer eritme yöntemiyle üretilmiş ve ardından yüzey işlemine tabi tutulmuştur. Alaşım yüzeyleri önce anodize edilmiş ve daha sonra 45S5 biyocam tozu ile kaplanmıştır. Tüm yüzey işlemlerinden sonra yapısal analizler yapılarak kaplamanın etkinliği incelenmiştir. İşlem görmemiş ve kaplanmış numuneler döngüsel polarizasyon yöntemi ile korozyon testlerine tabi tutulmuş ve korozyon davranışları incelenmiştir.

1. INTRODUCTION

Titanium and its alloys are among the most preferred biomaterials in implant and prosthetic applications due to their properties such as complete inertness in terms of biocompatibility in the body environment, low density, high strength, low modulus of elasticity compared to other biometals, and high corrosion and wear resistance [1,2].

Among Ti and its alloys, Ti6Al4V alloy is widely used in dental and hip prosthesis where high strength and biocompatibility are required due to many structural and biological factors. However, these alloys generally exhibit poor bioactivity and the combination of surface and tissue in contact with living tissue results in the formation of fibrous tissue [3,4]. Furthermore, due to their higher modulus of elasticity than bone, they do not adhere well

87

to the bone structure and lead to loosening, and they contain the elements Al and V, both of which are dangerous when released into the body [5]. Therefore, there are still many unresolved problems such as structural, chemical and biological incompatibilities that may lead to rejection and failure of implants and prostheses by the body. A study by Mei et al. reported that implants made of titanium alloys often fail due to bacterial invasion [6]. To overcome this situation, surface treatments such as sandblasting, acid etching, anodization or a combination of these can be applied to the surfaces of Ti and its alloys [7-9]. Among these surface treatments, anodization is an electrochemical oxidation process in which nanostructured TiO_2 nanotubes are formed on the surface [9,10]. The anodization process, like any other electrochemical process, can be easily controlled once conditions such as solution, voltage or time are optimized [11]. The type of solution (electrolyte), which is one of the control parameters, allows to impart different properties to the TiO_2 structure grown as a result of anodization [12]. In the industry and literature, the most common electrolytes known and preferred for anodizing Ti and its alloys are phosphoric acid (H_3PO_4) and sulfuric acid (H_2SO_4) [13]. However, sulfuric acid has a larger dissociation constant in water than phosphoric acid, making it easier to oxidize than phosphoric acid to form TiO_2 coatings [14]. Therefore, since the oxidation power of H_2SO_4 facilitates anodic oxidation more easily, it is possible to obtain anodized coatings with a thicker and crystalline structure. In addition, sulfate ions (SO_4^{2-}) are also known to promote the growth of bone cells [15,16].

Anodization of titanium and its alloys produces TiO_2 nanotubes on their surfaces, which provide an interface for the formation of bioactive species that promote osseointegration between bone tissue and the implant [17-19]. However, a study found that macrophage cells, which support the antibacterial effect, reduce the adhesion of anodized titanium foils to the surface [20]. Therefore, bioactive coatings with 45S5 bioglass can be applied on TiO_2 nanotubes to increase the osseointegration between the implant-bone cell tissue without disrupting the natural cell formation of the living tissue [21,22]. Bioactive glasses form bone-like hydroxyapatite layers between the implant and living tissue, allowing the formation of highly durable bonds with hard and soft tissues. In addition, many studies have reported that SiO_2, CaO, Na_2O, P_2O_5 and their derivatives in the ionic solutions of bioactive glasses increase enzyme activity and exhibit antibacterial properties [23].

Bioactive glass coatings can be made by thermochemical as flame spraying, chemical as sol-gel or electrochemical deposition as electrophoretic deposition methods. Electrophoretic deposition (EPD) offers the possibility of depositing films of desired thicknesses on a wide variety of base materials with complex forms as long as they are controlled. The basic working principle of the EPD method is known as the movement and deposition of electrostatically charged powder particles in water or an organic solvent on the surface of the base material under opposite voltage by the effect of an electric field [24]. The method is remarkable for bioactive coatings due to its

simplicity, low equipment cost, ability to deposit at room temperature, and high purity and microstructural homogeneity of the films obtained. In the literature, hydroxyapatite coatings on biometals such as 316L stainless steel, titanium and its alloys have been generally reported. In the general results of these studies, it was reported that the HA films obtained by EPD method bonded to the surface of the base material with strong adhesion. In a few of these studies, it was also reported that the HA films obtained increased corrosion resistance in simulated body fluid (SBF) compared to untreated samples [25].

Only a few studies have been conducted for coating other types of bioactive coatings by EPD technique. In this study, $10x10x2$ mm^3 Ti6Al4V alloys produced by selective laser melting (SLM) were coated with commercial 45S5 bioactive glass powder by EPD method. In the study, the electrochemical behavior of 45S5 bioglass coating on anodized Ti6Al4V alloy was investigated by corrosion tests. In this context, untreated, 45S5 bioglass coated, 45S5 bioglass coated on anodized Ti6Al4V samples were subjected to open circuit potential and cyclic polarization in stimulated body fluid (SBF) environment for corrosion tests. Before the tests, all samples were subjected to structural and morphological examinations by XRD and SEM analyses to see the effectiveness of the coating. After the tests, the current-voltage graphs obtained from cyclic polarization were interpreted and the study was completed.

2. MATERIAL AND METHOD

2.1. Materials and Surface Treatments

Selective laser melting (SLM) is an additive manufacturing method that uses a direct laser beam focused through computer-aided design (CAD) data to fuse metal powders layer by layer to form a metallic structure by melting metal powders and then laying down metal powders again and repeating these processes. Ti6Al4V samples with dimensions of $10x10x2$ mm^3 were produced with alloy powders according to ASTM B348 using the CONCEPT LASER MLab Cusing device. The fabrication parameters were 75 W laser power, 1000 mm/s plane and contour scanning speed and 25 μm layer thickness. Furthermore, the fabrication was performed using simple straightline scans to melt each layer. Ti6Al4V alloy generally contains balance % Ti, max. 6.7% Al, max. 4.5% Fe, trace amounts of O, C, H. After production, the substrates were grinded using SiC papers with 80, 220, 400, 800, 1200, 2000 mesh grid respectively, and after polished by alumina powder (grain size of 1 μm), cleaned with ethanol, and dried.

Ti6Al4V alloys were subjected to anodization process before EPD process. For the anodization process, the samples were electrochemically treated in 1 M H_2SO_4 solution by applying 10 V DC voltage for 10 minutes. Afterwards, the untreated and anodized samples were coated with 45S5 bioglass with EPD. For the EPD process, firstly suspension was prepared. The suspension was prepared with 99 ml of distilled water, 1 ml of acetic

88

acid, 0.2 ml of phosphate ester and 2 g/L 45S5 Bioglass® (containing 45% SiO_2, 24.5% CaO, 24.5% Na_2O and 6.0% $P2O5$ by weight) commercial powder. They were stirred with a magnetic stirrer for 3 min before each deposition to avoid precipitation of particles. All EPD experiments were performed at ambient temperature, graphite was used as the counter electrode and the electrodes were placed with a distance of approximately 2 cm between them. The electrodes were washed with acetone before processing. Electrophoretic Deposition proses for all samples was performed using GW GPR-30H10D Laboratory DC Power Supply with untreated and pre-treated Ti6Al4V samples as the cathode electrode and graphite as the anode electrode, applying a constant voltage of 20 V for 20 minutes. The phases on the surface of the all samples were determined X-Ray Diffraction analysis using the XRD-GNR Explorer instrument operated at 40 kV and 30 mA Cu Kα (λ = 1.789 Å) source diffractometer.

2.2. 2.2. Corrosion Tests

Untreated, untreated-45S5 coated, pretreated and pretreated-45S5 coated Ti6Al4V samples were subjected to corrosion tests in stimulated body fluid (SBF) for electrochemical investigation. The chemical composition of the stimulated body fluid is given in Table 1. The corrosion tests were completed using Gamry G750 Potentiostat/Galvanostat system, first with Open Circuit Potential (OCP) and then with Cyclic Polarization. The test setup was constructed using a triple electrode system with untreated and coated samples as working electrode, graphite rod as counter electrode and Ag/AgCl as reference electrode. During the test, the corrosion surface area was set to 1 cm2 and the time required for the Open Circuit Potential reading was set to 7200 seconds. Cyclic Polarization measurements were performed with a scan rate of 1 mV/s beyond 0.5 V beyond the Open Circuit Potential values. The polarization curves obtained from the electrochemical analysis were examined in detail.

3. RESULTS

The XRD graph of untreated Ti6Al4V, anodization, 45S5 bioglass and anodization+45S5 bioglass coated samples are given in Figure 1. Ti6Al4V alloy consists of α and β phases. In the XRD graph given in Figure 1, it is seen that a hexagonal hexagonal tightly packed (α phase) crystalline phase is dominant in the structure as seen from the peaks of the Ti6Al4V alloy sample. During SLM production, the α phases in the structure transform into α′ martensite phase due to rapid cooling. The β-Ti (volume-centered cubic) phase in the structure is too small to be detected by XRD [26,27]. When the XRD peaks of the 45S5 Bioglass sample coated on Ti6Al4V alloy with EPD were examined, the presence of $CaCO_3$ (calcite), $Na_6Ca_3Si_6O_{18}$ (sodium calcium silicate) and $CaSiO_3$ (Wollastonite) phases were detected in the structure.
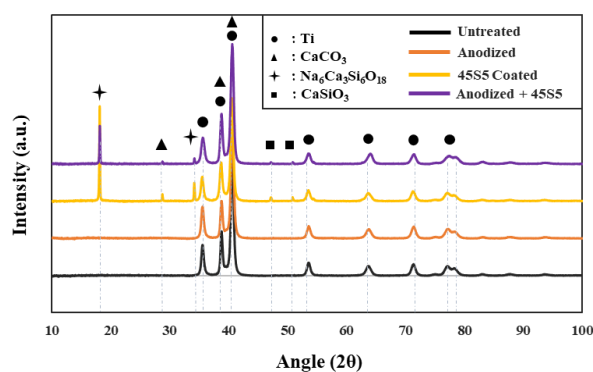
Figure 1. XRD graphs of all Ti6Al4V alloys.

The curves obtained after cyclic potentiodynamic polarization tests of all sample groups in SBF solution are shown in Figure 2. Cyclic polarization tests were carried out to determine the corrosion susceptibility of Ti6Al4V alloy produced by SLM method and samples subjected to different surface treatments. When we look at the cyclic polarization curves given in Figure 5, the hysteresis curve area formed by the untreated sample is larger than the area formed by the coated surfaces. This indicates that the untreated sample exhibits lower pitting corrosion resistance. It is seen that 45S5 bioglass coated with EPD method and 45S5 bioglass coated surfaces after anodization exhibit high pitting corrosion resistance.
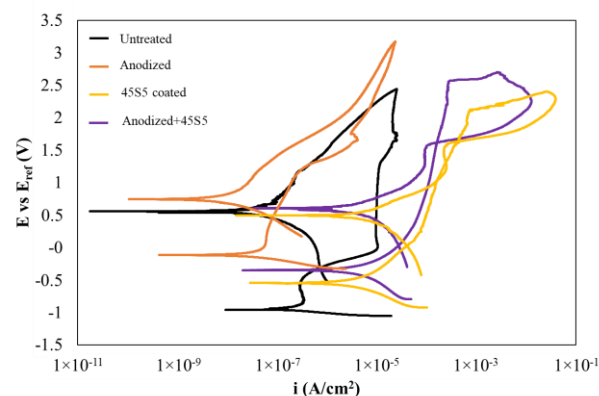
Figure 2. Cyclic polarization curves of all Ti6Al4V samples.

Anodic tafel slope (βa), cathodic tafel slope (βc), current density (icorr) and corrosion potential (Ecorr) values for all sample groups obtained from the lower arm of cyclic potentiodynamic polarization curves are given in Table 1. It is seen that the corrosion potentials (Ecorr) of the anodized, 45S5 and anodized+45S5 coated samples are even more inert when compared to the untreated sample (Table 1). The positive change in Ecorr indicates an increase in corrosion resistance [28]. The icorr values were measured as 213×10-9 A/cm2, 41.70×10-9 A/cm2, 295×10-9 A/cm2 and 88.70×10-9 A/cm2 for untreated, Anodized, 45S5 Coated and Anodized+45S5 coated samples, respectively. It is known that corrosion resistance increases with decreasing current density [29]. Thus, there is a decrease in icorr values compared to the untreated sample. According to Icorr values, the highest corrosion resistance is seen in the Anodized sample. In addition, since the surface ceramic-based coatings are applied to the samples, they act as a barrier in the

corrosive environment and cause an increase in corrosion resistance.

Table 1. The results of corrosion tests of all samples.

Samples	βa (V/decade)	βc (V/decade)	Ecorr [mV]	icorr [A/cm²]	Corrosion Rate [mm/year]
Untreated	1.663	61.90×10^{-3}	- 958	213×10^{-9}	71.92×10^{-3}
Anodized	496.60×10^{-3}	138×10^{-3}	- 113	41.7×10^{-9}	14.70×10^{-3}
45S5 Coated	35.30×10^{-3}	43.10×10^{-3}	- 545	295×10^{-9}	99.50×10^{-3}
Anodized +45S5	7.60×10^{-3}	7.50×10^{-3}	- 345	88.7×10^{-9}	29.93×10^{-3}

The high porosity of the samples produced with SLM causes the materials to exhibit low corrosion resistance. The surroundings of the pores become suitable areas for corrosion to start. Thus, it progresses between other pores and accelerates the corrosion phenomenon. For this reason, the corrosion resistance of 45S5 bioglass has been increased by oxidation and EPD method.

4. DISCUSSION AND CONCLUSION

Anodization, 45S5 Bioglass and anodization + 45S5 Bioglass coatings were applied to Ti6Al4V alloy produced by SLM technique. The corrosion behaviors of the untreated and coated surfaces were investigated. The results obtained are given below:

- ✓ According to XRD results, α-Ti and β-Ti phases were obtained. In addition, peaks belonging to CaCO3 (calcite), $Na_6Ca_3Si_6O_{18}$ (sodium calcium silicate) and $CaSiO_3$ (Wollastonite) phases were obtained for 45S5 Bioglass.
- ✓ Corrosion tests were carried out in SBF solution and cyclic potentiodynamic polarization curves were obtained. It was determined that 45S5 Bioglass coated surface and anodization + 45S5 Bioglass coated surface exhibited high pitting corrosion resistance.
- ✓ The highest corrosion resistance was observed in the anodization treated sample with a value of - 113 mV for Ecorr and 41.70×10^{-9} A/cm² for icorr.

Acknowledgement

REFERENCES

[1] Molina J, Valero-Gómez A, Belda, J, Bosch F, Bernabé-Quispe P, Tormo-Mas MA. Long-term antibacterial Ag+-release biomaterials based on anodized Ti6Al4V and silver nanoparticles. Colloids and Surfaces A: Physicochemical and Engineering Aspects. 2023; 676(B): 1-15.

[2] Atik, B., Bozkurt, Y. B., Kavasoğlu, Y. S., Kovacı, H., & Çelik, A. (2024). Pitting corrosion performance of plasma oxidized Cp-Ti and effects of fabrication methods. Surface and Coatings Technology, 130384.

[3] Zhang LC, Chen, LY. A review on biomedical titanium alloys: recent progress and prospect. Adv. Eng. Mater. 2019; 21: 1801215.

[4] Magesh S, Vasanth G, Revathi A, Geeth M. Use of nanostructured materials in implants, in: R. Narayan (Ed.). Nanobiomaterials, Nanostructured Materials for Biomedical Applications, Woodhead Publishing. 2018; 481-501.

[5] Leban MB, Kosec T, Finšgar M. Corrosion characterization and ion release in SLM-manufactured and wrought Ti6Al4V alloy in an oral environment. Corrosion Science. 2022; 209: 1-15.

[6] Mei S, Wang H, Wang W, Tong L, Pan H, Ruan C, Ma Q, Liu M, Yang H, Zhang L, Cheng Y, Zhang Y, Zhao L, Chu PK. Antibacterial effects and biocompatibility of titanium surfaces with graded silver incorporation in titania nanotubes. Biomaterials. 2014; 35: 4255-4265.

[7] He W, Yin X, Xie L, Liu Z, Li J, Zou S, Chen J. Enhancing osseointegration of titanium implants through large-grit sandblasting combined with micro-arc oxidation surface modification. J. Mater. Sci: Mater. Med. 2019; 30: 73.

[8] Herrero-Climent M, Lázaro P, Vicente Rios J, Lluch S, Marqués M, Guillem-Martí J, Gil FJ. Influence of acid-etching after grit-blasted on osseointegration of titanium dental implants: in vitro and in vivo studies. J. Mater. Sci.: Mater. Med. 2013; 24: 2047-2055.

[9] Jarosz M, Grudzień J, Kapusta-Kołodziej J, Chudecka A, Sołtys M, Sulka GD. Anodizing of titanium alloys for biomedical applications, in: G.D. Sulka (Ed.), Nanostructured Anodic Metal Oxides Synthesis and Applications. Elsevier. 2020; 211-275.

[10] Cheung KH, Pabbruwe MB, Chen W, Koshy P, Sorrell CC. Effects of substrate preparation on TiO2 morphology and topography during anodization of biomedical Ti6Al4V. Materials Chemistry and Physics. 2020; 252: 1-13.

[11] Acharya S, Suwas S, Chatterjee K. Review of recent developments in surface nanocrystallization of metallic biomaterials. Nanoscale. 2021; 13: 2286-2301.

[12] Cai Q, Paulose M, Varghese OK, Grimes CA. The effect of electrolyte composition on the fabrication of self-organized titanium oxide nanotube arrays by anodic oxidation. J. Mater. Res. 2005; 20: 230-236.

[13] Cheung KH, Pabbruwe MB, Chen W, Koshy P, Sorrell CC. Thermodynamic and microstructural analyses of photocatalytic TiO2 from the anodization of biomedical-grade Ti6Al4V in phosphoric acid or sulfuric acid. Ceramics International. 2020; 47(2): 1609-1624.

[14] Rumble JR. Electro Thermo, Solution chemistry. CRC Handbook of Chemistry and Physics, 98th Edition, CRC Press/Taylor&Francis, Boca Raton, FL. 2018; 86.

[15] Lausmaa J, Kasemo B, Mattsson H, Odelius H. Multi-technique surface charaterization of oxide

films on electropolished and anodically oxidized titanium. Appl. Surf. Sci. 1990; 45: 189-200.

[16] Tay BK, Patel VV, Bradford DS. Calcium sulfate- and calcium phosphatebased bone substitutes. Orthop. Clin. 1999; 30: 615-623.

[17] Kunze J, Müller L, Macak JM, Greil P, Schmuki P, Müller FA. Time-dependent growth of biomimetic apatite on anodic TiO2 nanotubes. Electrochim. Acta. 2008; 53: 6995-7003.

[18] Roguska A, Pisarek M, Andrzejczuk M, Lewandowska M, Kurzydlowski KJ, Janik-Czachor M. Surface characterization of Ca-P/Ag/TiO2 nanotube composite layers on Ti intended for biomedical applications. J. Biomed. Mater. Res. Part A. 2012; 100A: 1954–1962.

[19] Pawlik A, Rehman MAU, Nawaz Q, Bastan FE, Sulka GD, Boccaccini AR. Fabrication and characterization of electrophoretically deposited chitosan-hydroxyapatite composite coatings on anodic titanium dioxide layers. Electrochim. Acta. 2009; 307: 465-473.

[20] Rajyalakshmi A, Ercan B, Balasubramanian K, Webster TJ. Reduced adhesion of macrophages on anodized titanium with select nanotube surface features. Int. J. Nanomedicine. 2011; 6: 1765-1771.

[21] Boccaccini AR, Peters C, Roether JA, Eifler D, Misra SK, Minay EJ. Electrophoretic deposition of polyetheretherketone (PEEK) and PEEK/Bioglass® coatings on NiTi shape memory alloy wires. J. Mater. Sci. 2006; 41: 8152-8159.

[22] Pishbin F, Simchi A, Ryan MP, Boccaccini AR. Electrophoretic deposition of chitosan/45S5 Bioglass® composite coatings for orthopaedic applications. Surf. Coatings Technol. 2011; 205: 5260-5268.

[23] Jugowiec D, Łukaszczyk A, Cieniek Ł, Kot M, Reczyńska K, Cholewa-kowalska K, Pamuła E, Moskalewicz T. Electrophoretic deposition and characterization of composite chitosan-based coatings incorporating bioglass and sol-gel glass particles on the Ti-13Nb-13Zr alloy. Surf. Coat. Technol. 2017; 319: 33-46.

[24] Azzouz I, Faure J, Khlifi K, Cheikh Larbi A, Benhayoune H. Electrophoretic Deposition of 45S5 Bioglass® Coatings on the Ti6Al4V Prosthetic Alloy with Improved Mechanical Properties. Coatings. 2020; 10.

[25] Khanmohammadi S, Ojaghi-Ilkhchi M, Farrokhi-Rad M. Evaluation of Bioactive glass and hydroxyapatite-based nanocomposite coatings obtained by electrophoretic deposition. Ceramics International. 2020; 46: 26069-26077.

[26] Azzouz I, Faure J, Khlifi K, Cheikh Larbi A, Benhayoune H. Electrophoretic Deposition of 45S5 Bioglass® Coatings on the Ti6Al4V Prosthetic Alloy with Improved Mechanical Properties. Coatings. 2020; 10(12):1192.

[27] Uzun Y., Biçer S., Tüzemen, Ş.M., Çelik, A. Investigation of Wear Resistance of Electrophoretic Deposition onto Ti6Al4V Alloy. 3rd International Natural Science, Engineering and Materials Technology Conference, NEM 2023.Gazimagusa, Cyprus (Kktc); 2023, p. 164-172.

[28] Uzun Y. Electrochemıcal Evaluatıon Of Ti45Nb Coated Wıth 63s Bıoglass By Electrophoretıc Deposıtıon. Surface Revıew And Letters. 2023; 30(11).

[29] Bozkurt YB, Seçer Kavasoğlu Y., Atik B., Kovacı H., Uzun Y., Çelik A. Comparison study of corrosion behavior for chitosan coated Ti6Al4V alloy produced by selective laser melting and forging. Progress in Organic Coatings. 2023; 182: 107655.

Türk Doğa ve Fen Dergisi
Turkish Journal of Nature and Science
www.dergipark.gov.tr/tdfd

On Matrix Representations of Homeomorphism Classes

Kadirhan POLAT[1*] iD

[1] Ağrı İbrahim Çeçen University, Faculty of Science and Letter, Department of Mathematics, Ağrı, Türkiye
Kadirhan POLAT ORCID No: 0000-0002-3460-2021

Corresponding author: kadirhanpolat@agri.edu.tr

Keywords
Matrix
representation,
Homeomorphism
classes,
Topology.

Abstract: In this study, we investigate the matrix representations of homeomorphism classes. Considering well-known concepts such as the matrix of ones, column-sum, row-sum, one's complement, Hadamard product, and regular addition for matrices, we explore binary matrices' relationships with subsets of a finite set. The main results establish connections between matrix operations and set operations, providing insights into the structure of homeomorphism classes. The paper concludes with the formulation of a topology on a set based on specific matrix conditions.

Homeomorfizm Sınıflarının Matris Gösterimleri Hakkında

Anahtar Kelimeler
Matris
gösterimleri,
Homeomorfizm
sınıfları,
Topoloji

Öz: Bu çalışmada homeomorfizm sınıflarının matris temsillerini araştırdık. Birler matrisi, sütun toplamı, satır toplamı, birin tümleyeni, Hadamard çarpımı ve matrisler için düzenli toplama gibi iyi bilinen kavramları göz önünde bulundurarak ikili matrislerin sonlu bir kümenin alt kümeleriyle ilişkilerini araştırıyoruz. Ana sonuçlar, matris işlemleri ile küme işlemleri arasında bağlantılar kurarak homeomorfizm sınıflarının yapısına ilişkin bilgiler sağlar. Makale, belirli matris koşullarına dayalı bir küme üzerinde bir topolojinin formülasyonu ile sona ermektedir.

92

1. INTRODUCTION

R.E. Stong introduces the properties of topological spaces with a finite number of points [5]. He examines various aspects including homeomorphism classification, point-set topology properties, classification by homotopy type, and homotopy classes of mappings.

This article, which introduces a matrix representation that is completely different from that defined by R.E. Stong, aims to explore homeomorphism classes using matrix representations. Homeomorphism is a concept in mathematics that defines the transformability of topological structures, and this study investigates how these transformations can be understood through matrix representations.

We consider well-known fundamental matrix concepts such as the matrix of ones, column and row sums, and the one's complement will be introduced. These concepts will be elucidated in terms of their applicability to the analysis of homeomorphism classes. Additionally, the association of binary matrices with subsets of a set

and the expression of this relationship through matrix operations will be examined. Finally, we examine which conditions the necessary and sufficient conditions for a family to be a topology on a set depend on in the corresponding incidence matrices.

2. PRELIMINARIES

Now we introduce some basic concepts (See [1-4,6] for more detailed information).

A matrix of ones, denoted $\mathbf{1}$, is a matrix whose all entries are 1. The column-sum of a $n \times m$-matrix $\mathbf{A}$ is a row matrix each entry of which is the sum of all entries in corresponding column of $\mathbf{A}$, and denoted by $\mathrm{sum}_c(\mathbf{A})$. Similarly, the row-sum of a $n \times m$-matrix $\mathbf{A}$ is a column matrix each entry of which is the sum of all entries in corresponding row of $\mathbf{A}$, and denoted by $\mathrm{sum}_r(\mathbf{A})$. Then it is easy to see that

$$\mathrm{sum}_c(\mathbf{A}) = \mathbf{1}^t \mathbf{A} \text{ and } \mathrm{sum}_r(\mathbf{A}) = \mathbf{A}\mathbf{1}$$

where $\mathbf{1}^t$ denotes the transpose of the $n \times m$-matrix of ones $\mathbf{1}$. The one's complement of a $n \times m$-matrix $\mathbf{A}$ is

defined by $1 - \mathbf{A}$ and denoted by $\mathbf{A}^c$. We denote the maximum (the minimum) of all entries in a $n \times m$-matrix $\mathbf{A}$ by $\max \mathbf{A}(\min \mathbf{A})$.

Let $\mathbf{A}$ and $\mathbf{B}$ be two $n \times m$-matrices. The Hadamard product $\mathbf{C}$ of $\mathbf{A}$ and $\mathbf{B}$ is defined by $\mathbf{C}_{ij} = \mathbf{A}_{ij}\mathbf{B}_{ij}$ for every $i \in \{1,2,\dots,n\}$ and every $j \in \{1,2,\dots,m\}$, and denoted by $\mathbf{A} \odot \mathbf{B}$, that is,

$$(\mathbf{A} \odot \mathbf{B})_{ij} = \mathbf{A}_{ij}\mathbf{B}_{ij}.$$

Furthermore, the regular addition $\mathbf{C}$ of two column matrices $\mathbf{A}$ and $\mathbf{B}$ is defined and denoted by

$$\mathbf{A} \oplus \mathbf{B} = (\mathbf{A} + \mathbf{B}) - (\mathbf{A} \odot \mathbf{B})$$

More generally, the regular addition of a $n \times m$ matrix $\mathbf{A}$, denoted by $\oplus \mathbf{A}$, is defined by $\oplus \mathbf{A} = \oplus_j \mathbf{A}_{*j}$ where $\mathbf{A}_{*j}$ is the j-th subcolumn of $\mathbf{A}$. To put it more explicitly, $\oplus A = \mathbf{R}_m$ where $\mathbf{R}_1 = \mathbf{A}_{*1}$ and $\mathbf{R}_k = \mathbf{R}_{k-1} \oplus \mathbf{A}_{*k}$ for $k > 1$.

$\mathcal{M}_{n \times m}(\mathbb{Z})$ denotes the set of all $n \times m$-matrices over the ring $\mathbb{Z}$ of integers. We consider $\mathcal{M}_{n \times m}(\{0,1\}) \subseteq \mathcal{M}_{n \times m}(\mathbb{Z})$, that is, the class of all matrices with entries 0 and 1. A matrix $\mathbf{M} \in \mathcal{M}_{n \times m}(\{0,1\})$ is called a binary matrix.

Let X be a non-empty finite set. Consider integer-indexed elements $x_1, x_2, \dots, x_n$ of X. Then, to a subset $A \subseteq X$, we can correspond the binary n-column matrix $\mathbf{A}$ with the entries defined by

$$\mathbf{A}_{i1} = \begin{cases} 1 & \text{if } x_i \in A \\ 0 & \text{otherwise} \end{cases}$$

and called the incidence column matrix of A (with respect to the given integer-indexed set X).

Let $U_1, U_2, \dots U_{2^n}$ be integer-indexed elements of $P(X)$. To a subfamily $\mathcal{S} \subseteq P(X)$, we can correspond the binary $n \times m$-matrix $\mathcal{S}$ with the entries defined by

$$\mathcal{S}_{ij} = \begin{cases} 1 & \text{if } x_i \in U_j \in \mathcal{S} \\ 0 & \text{otherwise} \end{cases}$$

and called the incidence matrix of $\mathcal{S}$ (with respect to the integer-indexed set X and the integer-indexed power set $P(X)$).

Since X can be integer-indexed in different ways, a subset A corresponds different incidence matrices which implies that a subset A of a non-indexed set X has different incidence matrices. Similarly, by different integer indexing of X and $P(X)$, we obtain different incidence matrices of a subfamily $\mathcal{A} \subseteq P(X)$. As a result of this, if both a set X and its power set $P(X)$ are not integer-indexed, then a subfamily of $\mathcal{A} \subseteq P(X)$ has different incidence matrices.

3. MAIN RESULTS

Proposition 1. Let A be a subset of a set X. If $\mathbf{A}$ is an incidence column matrix of A, then $\mathbf{A}^c$ is an incidence matrix of A^c.

Proof. Let $\mathbf{A}$ be an incidence column matrix of set A. Then we have $\mathbf{A}_{i1} = 1$ if $x_i \in A$, otherwise $\mathbf{A}_{i1} = 0$. From the definition of one's complement of a matrix, we get $\mathbf{A}_{i1}^c = 1 - \mathbf{A}_{i1} = 1 - 1 = 0$ if $x_i \in A$, otherwise $\mathbf{A}_{i1}^c = 1 - \mathbf{A}_{i1} = 1 - 0 = 1$; or equivalently, we have $\mathbf{A}_{i1}^c = 1$ if $x_i \in A^c$, otherwise $\mathbf{A}_{i1}^c = 0$. Thus $\mathbf{A}^c$ is an incidence column matrix of A^c.

Proposition 2. Let A, B be two subsets of a set X. Let $\mathbf{A}, \mathbf{B}$ be incidence column matrices of A and B, respectively. Then the following are equivalent:
1. $A \cap B = \emptyset$
2. $\mathbf{A}^t \mathbf{B} = 0$

Proof.

$(1 \Rightarrow 2)$: Assume that $\mathbf{A}^t\mathbf{B} \neq 0$. Then

$$0 \neq \mathbf{A}^t\mathbf{B} = \sum_{i=1}^{n} \mathbf{A}_{1i}^t \mathbf{B}_{i1} = \sum_{i=1}^{n} \mathbf{A}_{i1}\mathbf{B}_{i1}$$

and so $\mathbf{A}_{i1} = \mathbf{B}_{i1} = 1$ for some $i \in \{1,2,\dots,n\}$. However, from the hypothesis $A \cap B = \emptyset$, for every $i \in \{1,2,\dots,n\}$, $\mathbf{A}_{i1} \neq \mathbf{B}_{i1}$, which leads to a contradiction. This contradiction arises from our assumption $\mathbf{A}^t\mathbf{B} \neq 0$. Thus $\mathbf{A}^t\mathbf{B} = 0$.

$(2 \Rightarrow 1)$: Assume that $A \cap B \neq \emptyset$. Then, for some $i \in \{1,2,\dots,n\}$, we have $\mathbf{A}_{i1} = 1$ and $\mathbf{B}_{i1} = 1$. On the other hand, from the hypothesis $\mathbf{A}^t\mathbf{B} = 0$, we have $\sum_{i=1}^{n} \mathbf{A}_{i1}\mathbf{B}_{i1} = 0$. Then, there exists no $i \in \{1,2,\dots,n\}$ such that $\mathbf{A}_{i1} = 1 = \mathbf{B}_{i1}$ which leads to a contradiction. This contradiction arises from our assumption $A \cap B \neq \emptyset$. Thus $A \cap B = \emptyset$.

Conclusion 3. Let A, B be incidence column matrices of subsets A and B of a set X, respectively. Then $A \cap B \neq \emptyset$ if and only if $\mathbf{A}^t\mathbf{B} \geq 1$.

Proposition 4. Let A, B be incidence column matrices of subsets A and B of a set X, respectively. Then the Hadamard product $\mathbf{A} \odot \mathbf{B}$ is an incidence column matrix of the intersection $A \cap B$.

Proof. Let A, B be incidence column matrices of subsets A and B of a set X, respectively. If $(\mathbf{A} \odot \mathbf{B})_{i1} = 1$, then the member of X corresponding $(\mathbf{A} \odot \mathbf{B})_{i1}$ belongs to both A and B and so belongs to $A \cap B$. Otherwise, it does not belong to at least one of A and B and so does not belong to $A \cap B$. Thus, the proof is completed.

Proposition 5. Let $\mathbf{A}, \mathbf{B}$ be incidence column matrices of subsets A and B of a set X, respectively. Then an incidence column matrix of the union $A \cup B$ is the regular addition $\mathbf{A} \oplus \mathbf{B}$.

Proof. Let $\mathbf{A}, \mathbf{B}$ be incidence column matrices of subsets A and B of a set X, respectively. If $(\mathbf{A} \oplus \mathbf{B})_{i1} = 0$, then the member of X corresponding $(\mathbf{A} \oplus \mathbf{B})_{i1}$ belongs to neither A nor B and so does not belong to $A \cup B$.

93

Otherwise, it belongs to at least one of A and B and so belongs to $A \cup B$. Thus, the proof is completed.

Proposition 6. Let $\mathcal{S}$ be incidence matrix of a family $\mathcal{S}$ of subsets of a set X. Then an incidence column matrix of the union $\cup \mathcal{S}$ is the regular addition $\oplus \mathcal{S}$.

Proof. Let $\mathcal{S}$ be incidence matrix of a family $\mathcal{S}$ of subsets of a set X. If $(\oplus \mathcal{S})_{i1} = 0$, then the member of X corresponding $(\oplus \mathcal{S})_{i1}$ belongs to no member of $\mathcal{S}$ and so does not belong to $\cup \mathcal{S}$. Otherwise, it belongs to at least one member of $\mathcal{S}$ and so belongs to $\cup \mathcal{S}$. Thus, the proof is completed.

Proposition 7. Let A, B be two subsets of a set X. Let $\mathbf{A}, \mathbf{B}$ incidence column matrices of A and B, respectively. Then the following are equivalent:
  1. $A \subseteq B$

Proof.

$(1 \Rightarrow 2)$: Let A be a subset of B. Then we have $A \cap B^c = \emptyset$. From Proposition 1 and Proposition 2, we have $\mathbf{A}^t \mathbf{B}^c = 0$.

$(2 \Rightarrow 1)$: Let $\mathbf{A}^t \mathbf{B}^c = 0$. Then From Proposition 1 and Proposition 2, we yield $A \cap B^c = \emptyset$, or equivalently, $A \subseteq B$.

Proposition 8. Let $\mathbf{A}, \mathbf{B}$ be incidence column matrices of subsets A and B of a set X, respectively. Then $A = B$ if and only if $\mathbf{1}^t(\mathbf{A} - \mathbf{B}) = 0$.

Proof.
$$A = B \Leftrightarrow A \subseteq B \wedge B \subseteq A$$
$$\Leftrightarrow \mathbf{A}^t \mathbf{B}^c = 0 \wedge \mathbf{B}^t \mathbf{A}^c = 0$$
$$\Leftrightarrow \mathbf{A}^t(\mathbf{1} - \mathbf{B}) = 0 \wedge \mathbf{B}^t(\mathbf{1} - \mathbf{A}) = 0$$
$$\Leftrightarrow \mathbf{A}^t \mathbf{1} - \mathbf{A}^t \mathbf{B} = 0 \wedge \mathbf{B}^t \mathbf{1} - \mathbf{B}^t \mathbf{A} = 0$$
$$\Leftrightarrow \mathbf{A}^t \mathbf{1} = \mathbf{A}^t \mathbf{B} \wedge \mathbf{B}^t \mathbf{1} = \mathbf{B}^t \mathbf{A}$$
$$\Leftrightarrow \mathbf{A}^t \mathbf{1} = \mathbf{A}^t \mathbf{B} = \mathbf{B}^t \mathbf{A} = \mathbf{B}^t \mathbf{1}$$
$$\Leftrightarrow \mathbf{A}^t \mathbf{1} = \mathbf{B}^t \mathbf{1}$$
$$\Leftrightarrow (\mathbf{A}^t - \mathbf{B}^t)\mathbf{1} = 0$$
$$\Leftrightarrow [(\mathbf{A}^t - \mathbf{B}^t)\mathbf{1}]^t = 0$$
$$\Leftrightarrow \mathbf{1}^t(\mathbf{A}^t - \mathbf{B}^t)^t = 0$$
$$\Leftrightarrow \mathbf{1}^t(\mathbf{A} - \mathbf{B}) = 0.$$

Proposition 9. Let A be a subset of a set X. Let $\mathbf{A}$ be an incidence matrix of A, and let $\mathcal{S}$ be an incidence matrix of a family $\mathcal{S}$ of subsets of X. Then the following are equivalent:
  1. $A \in \mathcal{S}$
  2. There exists $U \in \mathcal{S}$ such that $\mathbf{1}^t(\mathbf{A} - \mathbf{U}) = 0$ where $\mathbf{U}$ is an incident matrix of U.

Proof.

$(1 \Rightarrow 2)$: Let $\mathbf{A}$ be the incidence matrix of a member A of $\mathcal{S}$. Set $U = A$. Let $\mathbf{U}$ be an incident matrix of U. Then, from Proposition 8, we have $\mathbf{1}^t(\mathbf{A} - \mathbf{U}) = 0$.

$(2 \Rightarrow 1)$: Let $\mathbf{A}$ be the incidence matrix of a subset A of a set X. Consider a member U of $\mathcal{S}$ such that $\mathbf{1}^t(\mathbf{A} - $

$\mathbf{U}) = 0$ where $\mathbf{U}$ is an incident matrix of U. Then, from Proposition 8, we obtain $A = U \in \mathcal{S}$.

Theorem 10. Given a subfamily $\mathcal{T}$ of subsets of a set X. Let $\mathcal{T}$ be an incidence matrix of $\mathcal{T}$. Then $\mathcal{T}$ is a topology on X if and only if the following hold:
  1. There exists $G \in \mathcal{T}$ with an incidence column matrix $\mathbf{G}$ such that $\mathbf{1}^t \mathbf{G} = 0$.
  2. There exists $G \in \mathcal{T}$ with an incidence column matrix $\mathbf{G}$ such that $\mathbf{1}^t \mathbf{G}^c = 0$.
  3. If $\mathbf{G}, \mathbf{H}$ is incidence column matrices of members $G, H \in \mathcal{T}$, respectively, then there exists $U \in \mathcal{T}$ with an incident matrix $\mathbf{U}$ such that $\mathbf{1}^t(\mathbf{G} \odot \mathbf{H} - \mathbf{U}) = 0$.
  4. If $\mathcal{G}$ is an incidence matrix of a subfamily $\mathcal{G} \subseteq \mathcal{T}$, then there exists $U \in \mathcal{T}$ with an incident matrix $\mathbf{U}$ such that $\mathbf{1}^t[\oplus \mathbf{G} - \mathbf{U}] = 0$.

Proof. Let $\mathcal{T}$ be an incidence matrix of a subfamily $\mathcal{T}$ of subsets of a set X.

$(\Rightarrow)$: Let $\mathcal{T}$ be a topology on a set X.
  1. Since $\emptyset \in \mathcal{T}$, we have $\mathbf{1}^t \mathbf{0} = 0$ for the incidence column matrix $\mathbf{0}$ of the empty set $\emptyset$.
  2. Since $X \in \mathcal{T}$, we get $\mathbf{1}^t \mathbf{1}^c = \mathbf{1}^t \mathbf{0} = 0$ for the incidence column matrix $\mathbf{1}$ of the whole set X.
  3. Let $G, H \in \mathcal{T}$ have incidence column matrices $\mathbf{G}, \mathbf{H}$, respectively. Then, from Proposition 4, $\mathbf{G} \odot \mathbf{H}$ is an incidence column matrix of $G \cap H$. Since $G \cap H \in \mathcal{T}$, from Proposition 9, there exists $U \in \mathcal{T}$ with an incidence column matrix $\mathbf{U}$ such that $\mathbf{1}^t(\mathbf{G} \odot \mathbf{H} - \mathbf{U}) = 0$.
  4. Let $\mathcal{G}$ be an incidence matrix of a subfamily $\mathcal{G} \subseteq \mathcal{T}$. From Proposition 6, $\oplus \mathcal{G}$ is an incident column matrix of the union $\cup \mathcal{G}$. Since $\cup \mathcal{G} \in \mathcal{T}$, by Proposition 9, there exists $U \in \mathcal{T}$ with an incident matrix $\mathbf{U}$ such that $\mathbf{1}^t[\oplus \mathbf{G} - \mathbf{U}] = 0$.

$(\Leftarrow)$: (O_1) From the first item of the hypothesis, there exists $G \in \mathcal{T}$, say G_0, with an incidence column matrix $\mathbf{G}$ such that $\mathbf{1}^t \mathbf{G} = 0$. It is clear that G_0 is the empty set $\emptyset$. By Proposition 9, we have $\emptyset \in \mathcal{T}$. From the second item of the hypothesis, there exists $G \in \mathcal{T}$, say G_0, with an incidence column matrix $\mathbf{G}$ such that $\mathbf{1}^t \mathbf{G}^c = 0$. It is clear that G_0 is the whole set X. By Proposition 9, we have $X \in \mathcal{T}$.

(O_2) Let $\mathbf{G}, \mathbf{H}$ be incidence column matrices of members $G, H \in \mathcal{T}$, respectively. From the third item of the hypothesis, there exists $U \in \mathcal{T}$ with an incident matrix $\mathbf{U}$ such that $\mathbf{1}^t(\mathbf{G} \odot \mathbf{H} - \mathbf{U}) = 0$. Then, from Proposition 4 and Proposition 9, $\mathbf{G} \odot \mathbf{H}$ is an incidence column matrix of the intersection $G \cap H$ and so we have $G \cap H \in \mathcal{T}$.

(O_3) Let $\mathcal{G}$ be an incidence matrix of a subfamily $\mathcal{G} \subseteq \mathcal{T}$. From the fourth item of the hypothesis, there exists $U \in \mathcal{T}$ with an incident matrix $\mathbf{U}$ such that $\mathbf{1}^t[\oplus \mathbf{G} - \mathbf{U}] = 0$. Then, from Proposition 6 and Proposition 9, $\oplus \mathcal{G}$ is an incident column matrix of the union $\cup \mathcal{G}$ and so we have $\cup \mathcal{G} \in \mathcal{T}$.

4. CONCLUSION

We have presented a comprehensive exploration of various concepts related to matrices and subsets of a set X.

We show that it can be used the notion of incidence matrix to represent the membership relations between elements of X and subsets of X. Through propositions and theorems, we established relationships between these matrices and fundamental set operations such as intersection, union, complement, and subset relationships.

Moreover, we extended our analysis to consider families of subsets and their properties in the context of forming a topology on X. Our results provide insights into the structural properties of matrices representing subsets and lay the groundwork for further investigation into combinatorial and topological aspects of finite sets.

Acknowledgement

REFERENCES

[1] Brualdi RA, Ryser HJ, et al. Combinatorial matrix theory, volume 39. Springer; 1991.
[2] Eves HW. Elementary matrix theory. Courier Corporation; 1980.
[3] Franklin JN. Matrix theory. Courier Corporation; 2012.
[4] Ortega JM. Matrix theory: A second course. Springer Science & Business Media; 2013.
[5] Stong RE. Finite topological spaces. Transactions of the American Mathematical Society. 1966;123(2):325–340.
[6] Zhang F. Matrix theory: basic results and techniques. Springer Science & Business Media; 2011.

Türk Doğa ve Fen Dergisi
Turkish Journal of Nature and Science
www.dergipark.gov.tr/tdfd

Some Novel Integral Inequalities on the Co-ordinates for Geometrically Exponentially Convex Functions

Sinan ASLAN[1*] (ID)

[1] Ağrı Türk Telekom Social Sciences High School, Ağrı, Türkiye
Sinan ASLAN ORCID No: 0000-0001-5970-1926

Corresponding author: sinanaslan0407@gmail.com

Abstract: The main purpose of this study is to define geometrically exponentially convex functions, which are a more general version, by expanding geometrically convex functions and to create the relevant lemmas. Some properties of geometrically exponentially convex functions are proven using definitions and lemmas. While obtaining the main findings, in addition to basic analysis information, Young and Hölder inequalities, well known in the literature, were also used for the powers of some functions. In the new theorems obtained, some special results were obtained for $\alpha = 0$.

Geometrik Eksponansiyel Konveks Fonksiyonlar için Koordinatlarda Bazı Yeni İntegral Eşitsizlikler

Öz: Bu çalışmanın temel amacı geometrik konveks fonksiyonları genişleterek daha genel bir versiyonu olan geometrik eksponansiyel konveks fonksiyonları tanımlamak ve ilgili lemmaları oluşturmaktır. Geometrik eksponansiyel konveks fonksiyonların bazı özellikleri tanım ve lemmalar kullanılarak ispatlanmıştır. Ana bulguları elde ederken temel analiz bilgilerinin yanı sıra bazı fonksiyonların kuvvetleri için literatürde iyi bilinen Young ve Hölder eşitsizliklerinden yararlanılmıştır. Elde edilen yeni teoremlerde $\alpha = 0$ için bazı özel sonuçlar elde edilmiştir.

1. INTRODUCTION

In the 21st century, we see that inequalities are not only limited to mathematics, but also have an important place in many different sciences, especially engineering. For this reason, it has attracted the attention of many researchers and has been examined from different perspectives. The concept of convexity, which has an important place in inequality theory, is widely used by many researchers working in the field of inequality theory. We begin this study by giving the definition of the concept of convexity [2].

Definition 1. Let $A \subset R$. Then $\Upsilon : A \rightarrow \mathsf{R}$ is said to be convex, if

$$\Upsilon(\varpi\mu_1 + (1-\varpi)\mu_2) \leq \varpi\Upsilon(\mu_1) + (1-\varpi)\Upsilon(\mu_2) \quad (1)$$

holds for all $\mu_1, \mu_2 \in A$ and $\varpi \in [0,1]$ (Peajcariaac et al. [2]).

The main goal of studies on different types of convexity is to optimize the bounds and generalize some known classical inequalities. Based on this basic purpose, an important class of convex functions whose definition is given is exponentially convex functions and whose definition reference [1] is given as follows.

Definition 2. A function $\Upsilon : A \subseteq \mathsf{R} \rightarrow \mathsf{R}$ is said to be exponential convex function, if

$$\Upsilon\big((1-\varpi)\mu_1+\varpi\mu_2\big)\le(1-\varpi)\frac{\Upsilon(\mu_1)}{e^{\alpha\mu_1}}+\varpi\frac{\Upsilon(\mu_2)}{e^{\alpha\mu_2}} \qquad (2)$$

for all $\mu_1,\mu_2\in A,\alpha\in \mathsf{R}$ and $\varpi\in[0,1]$(Awan et al. [1]).

The definition of the concept of geometrically convex functions, which is well known in the literature and used by many researchers in their studies, is given as follows in reference [3].

Definition 3. A function $\Upsilon:A\subseteq(0,\infty)\to(0,\infty)$ is said to be a geometrically convex function, if

$$\Upsilon(\mu_1^{\varpi}\mu_2^{1-\varpi})\le\big[\Upsilon(\mu_1)\big]^{\varpi}\big[\Upsilon(\mu_2)\big]^{1-\varpi} \qquad (3)$$

for all $\mu_1,\mu_2\in A$ and $\varpi\in[0,1]$.

There are many studies in the literature about geometrically convex functions. Some of these are available in reference [4-10].

Aslan and Akdemir gave the definition of exponentially convex functions on the coordinates, which is a more general version of convex functions on coordinates, as follows in reference [11].

Definition 4. Let us consider the bidimensional interval $\Delta=[\vartheta_1,\vartheta_2]x[\vartheta_3,\vartheta_4]$ in R^2 with $\vartheta_1<\vartheta_2$ and $\vartheta_3<\vartheta_4$. The mapping $\Upsilon:\Delta\to R$ is exponentially convex on the co-ordinates on Δ, if the following inequality holds,

$$\Upsilon\big(\varpi\mu_1+(1-\varpi)\mu_3,\varpi\mu_2+(1-\varpi)\mu_4\big)$$
$$\le\varpi\frac{\Upsilon(\mu_1,\mu_2)}{e^{\alpha(\mu_1+\mu_2)}}+(1-\varpi)\frac{\Upsilon(\mu_3,\mu_4)}{e^{\alpha(\mu_3+\mu_4)}} \qquad (4)$$

for all $(\mu_1,\mu_2),(\mu_3,\mu_4)\in\Delta,\alpha\in R$ and $\varpi\in[0,1]$ (Aslan et al. [11]).

Aslan and Akdemir gave another definition of coordinates equivalent to the exponentially convex function definition as follows:

Definition 5. A function $\Upsilon:\Delta\to \mathsf{R}$ is exponentially convex function on the co-ordinates on Δ, if the following inequality holds,

$$\Upsilon\big(\varpi\mu_1+(1-\varpi)\mu_2,\omega\mu_3+(1-\omega)\mu_4\big)$$
$$\le\varpi\omega\frac{\Upsilon(\mu_1,\mu_3)}{e^{\alpha(\mu_1+\mu_3)}}+\varpi(1-\omega)\frac{\Upsilon(\mu_1,\mu_4)}{e^{\alpha(\mu_1+\mu_4)}}$$
$$+(1-\varpi)\omega\frac{\Upsilon(\mu_2,\mu_3)}{e^{\alpha(\mu_2+\mu_3)}}+(1-\varpi)(1-\omega)\frac{\Upsilon(\mu_2,\mu_4)}{e^{\alpha(\mu_2+\mu_4)}} \qquad (5)$$

for all $(\mu_1,\mu_3),(\mu_1,\mu_4),(\mu_2,\mu_3),(\mu_2,\mu_4)\in\Delta,\alpha\in \mathsf{R}$ and $\varpi,\omega\in[0,1]$ (Aslan et al. [11]).

With the definition of convex functions on coordinates, it brought to mind the question that the Hermite-Hadamard inequality could also be extended to coordinates. We see the answer to this enormous question in Dragomir's article [12]. We see the equivalent of the Hermite-Hadamard inequality in coordinates in the theorem below.

Theorem1. (Dragomir [12]) Lets assume that $\Upsilon:\Delta=[\mu_1,\mu_2]\times[\mu_3,\mu_4]\to \mathsf{R}$ is convex on the co-ordinates on Δ. Then one has the inequalit

$$\Upsilon\left(\frac{\mu_1+\mu_2}{2},\frac{\mu_3+\mu_4}{2}\right)$$
$$\le\frac{1}{(\mu_2-\mu_1)(\mu_4-\mu_3)}\int_{\mu_1}^{\mu_2}\int_{\mu_3}^{\mu_4}\Upsilon(x,y)dxdy$$
$$\le\frac{\Upsilon(\mu_1,\mu_3)+\Upsilon(\mu_1,\mu_4)+\Upsilon(\mu_2,\mu_3)+\Upsilon(\mu_2,\mu_4)}{4}. \qquad (6)$$

The above inequalities are sharp.

Theorem2. (Aslan et al. [11]) Let $\Upsilon:\Delta=[\mu_1,\mu_2]\times[\mu_3,\mu_4]\to \mathsf{R}$ be partial differentiable mapping on $\Delta=[\mu_1,\mu_2]\times[\mu_3,\mu_4]$ and $\Upsilon\in L(\Delta)$, $\alpha\in \mathsf{R}$. If Υ is exponentially convex function on the co-ordinates on Δ, then the following inequality holds;

$$\frac{1}{(\mu_2-\mu_1)(\mu_4-\mu_3)}\int_{\mu_1}^{\mu_2}\int_{\mu_3}^{\mu_4}\Upsilon(x,y)dxdy$$
$$\le\frac{\dfrac{\Upsilon(\mu_1,\mu_3)}{e^{\alpha(\mu_1+\mu_3)}}+\dfrac{\Upsilon(\mu_1,\mu_4)}{e^{\alpha(\mu_1+\mu_4)}}+\dfrac{\Upsilon(\mu_2,\mu_3)}{e^{\alpha(\mu_2+\mu_3)}}+\dfrac{\Upsilon(\mu_2,\mu_4)}{e^{\alpha(\mu_2+\mu_4)}}}{4}. \qquad (7)$$

Many studies have been carried out in the literature on exponentially convex functions and exponentially convex functions on coordinates. Some of these are given in reference [13-21].

Anderson et al. gave the following definition in (Anderson et al. [22])

Definition 6. A function $M:R^+\times R^+\to R^+$ is called a Mean function if

(1) $M(\mu_1,\mu_2)=M(\mu_2,\mu_1)$,

(2) $M(\mu_1,\mu_1)=\mu_1$,

(3) $\mu_1<M(\mu_1,\mu_2)<\mu_2$, whenever $\mu_1<\mu_2$,

(4) $M(a\mu_1,a\mu_2)=aM(\mu_1,\mu_2)$ for all $a>0$.

Let us recall special means (See [22,23,24])

1. Arithmetic Mean:

$$M(\mu_1,\mu_2)=A(\mu_1,\mu_2)=\frac{\mu_1+\mu_2}{2}.$$

2. Geometric Mean:

$$M(\mu_1,\mu_2)=G(\mu_1,\mu_2)=\sqrt{\mu_1\mu_2}\ .$$

3. Harmonic Mean:

$$M(\mu_1,\mu_2)=H(\mu_1,\mu_2)=1/A\left(\frac{1}{\mu_1},\frac{1}{\mu_2}\right).$$

4. Logarithmic Mean:

$$M(\mu_1,\mu_2)=L(\mu_1,\mu_2)=(\mu_1-\mu_2)/(\log\mu_1-\log\mu_2)$$

for $\mu_1\neq\mu_2$ and $L(\mu_1,\mu_1)=\mu_1$.

5. Identric Mean:

$$M(\mu_1,\mu_2)=I(\mu_1,\mu_2)=(1/e)\left(\mu_1^{\mu_1}/\mu_2^{\mu_2}\right)^{1/(\mu_1-\mu_2)}$$

for $\mu_1\neq\mu_2$ and $I(\mu_1,\mu_1)=\mu_1$.

Now we are in a position to put in order as:

$$H(\mu_1,\mu_2)\leq G(\mu_1,\mu_2)\leq L(\mu_1,\mu_2)$$
$$\leq I(\mu_1,\mu_2)\leq A(\mu_1,\mu_2)\leq K(\mu_1,\mu_2).$$

In [22], authors also gave a definition which is called MN-convexity as the following:

Definition 7. Let $\Upsilon:I\to(0,\infty)$ be continuous, where I is subinterval of $(0,\infty)$. Let M and N be any two Mean functions. We say Υ is MN-convex (concave) if

$$\Upsilon(M(\mu_1,\mu_2))\leq(\geq)N(\Upsilon(\mu_1),\Upsilon(\mu_2)) \qquad (8)$$

for all $\mu_1,\mu_2\in I$.

2. MAIN RESULTS

Definition 8. Let us consider the bidimensional interval $\Delta=[\mu_1,\mu_2]\times[\mu_3,\mu_4]$ in R^2 with $\mu_1<\mu_2$ and $\mu_3<\mu_4$. The mapping $\Upsilon:\Delta\to R^+$ is geometrically-exponentially convex on the co-ordinates on Δ, if the following inequality holds,

$$\Upsilon\left(\mu_1^{\varpi}\mu_3^{(1-\varpi)},\mu_2^{\varpi}\mu_4^{(1-\varpi)}\right)\leq\frac{\Upsilon^{\varpi}(\mu_1,\mu_2)}{e^{\alpha(\mu_1+\mu_2)}}\frac{\Upsilon^{(1-\varpi)}(\mu_3,\mu_4)}{e^{\alpha(\mu_3+\mu_4)}} \qquad (9)$$

for all $(\mu_1,\mu_2),(\mu_3,\mu_4)\in\Delta,\alpha\in R$ and $\varpi\in[0,1]$.

A second definition of geometrically exponentially convex functions on coordinates equivalent to the above definition can be made as follows:

Definition 9. A function $\Upsilon:\Delta\to R^+$ is geometrically exponentially convex on the co-ordinates on Δ, if the following inequality holds,

$$\Upsilon\left(\mu_1^{\varpi}\mu_2^{(1-\varpi)},\mu_3^{\omega}\mu_4^{(1-\omega)}\right)$$

$$\leq\frac{\Upsilon^{\varpi\omega}(\mu_1,\mu_3)}{e^{\alpha(\mu_1+\mu_3)}}\frac{\Upsilon^{\varpi(1-\omega)}(\mu_1,\mu_4)}{e^{\alpha(\mu_1+\mu_4)}}\frac{\Upsilon^{(1-\varpi)\omega}(\mu_2,\mu_3)}{e^{\alpha(\mu_2+\mu_3)}}\frac{\Upsilon^{(1-\varpi)(1-\omega)}(\mu_2,\mu_4)}{e^{\alpha(\mu_2+\mu_4)}} \qquad (10)$$

for all

$$(\mu_1,\mu_3),(\mu_1,\mu_4),(\mu_2,\mu_3),(\mu_2,\mu_4)\in\Delta,\alpha\in R \text{ and}$$
$$\varpi,\omega\in[0,1].$$

Lemma 1. A function $\Upsilon:\Delta\to R^+$ will be called geometrically exponentially convex on the co-ordinates on Δ, if the partial mappings $\Upsilon_{\rho_2}:[\mu_1,\mu_2]\to R$,

$$\Upsilon_{\rho_2}(u)=e^{\alpha\rho_2}f(u,\rho_2) \quad \text{and} \quad \Upsilon_{\rho_1}:[\mu_3,\mu_4]\to R,$$

$$\Upsilon_{\rho_1}(v)=e^{\alpha\rho_1}f(\rho_1,v) \qquad\qquad \text{are} \qquad\qquad \text{geometrically}$$

exponentially convex on the co-ordinates on Δ, where defined for all $\rho_2\in[\mu_3,\mu_4]$ and $\rho_1\in[\mu_1,\mu_2]$

Proof. From the definition of partial mapping Υ_{ρ_1} we can write

$$\Upsilon_{\rho_1}\left(v_1^{\varpi}v_2^{(1-\varpi)}\right)=e^{\alpha\rho_1}\Upsilon\left(\rho_1,v_1^{\varpi}v_2^{(1-\varpi)}\right)$$

$$=e^{\alpha\rho_1}\Upsilon\left(\rho_1^{\varpi}\rho_1^{(1-\varpi)},v_1^{\varpi}v_2^{(1-\varpi)}\right)$$

$$\leq e^{\alpha\rho_1}\left[\frac{\Upsilon^{\varpi}(\rho_1,v_1)}{e^{\alpha(\rho_1+v_1)}}\frac{\Upsilon^{(1-\varpi)}(\rho_1,v_2)}{e^{\alpha(\rho_1+v_2)}}\right]$$

$$=\frac{\Upsilon^{\varpi}(\rho_1,v_1)}{e^{\alpha v_1}}\frac{\Upsilon^{(1-\varpi)}(\rho_1,v_2)}{e^{\alpha v_2}}$$

$$=\frac{\Upsilon_{\rho_1}^{\varpi}(v_1)}{e^{\alpha v_1}}\frac{\Upsilon_{\rho_1}^{(1-\varpi)}(v_2)}{e^{\alpha v_2}}. \qquad (11)$$

Similarly, one can easily see that

$$\Upsilon_{\rho_2}\left(u_1^{\varpi}u_2^{(1-\varpi)}\right)\leq\frac{\Upsilon_{\rho_2}^{\varpi}(u_1)}{e^{\alpha u_1}}\frac{\Upsilon_{\rho_2}^{(1-\varpi)}(u_2)}{e^{\alpha u_2}}. \qquad (12)$$

The proof is completed.

Proposition 1. If $\Upsilon,\Phi:\Delta\to R$ are two geometrically exponentially convex functions on the co-ordinates on Δ, then $\Upsilon\Phi$ is geometrically exponentially convex functions on the co-ordinates on Δ.

Proof.

$$\Upsilon\left(\mu_1^{\varpi}\mu_2^{(1-\varpi)},\mu_3^{\omega}\mu_4^{(1-\omega)}\right)\times\Phi\left(\mu_1^{\varpi}\mu_2^{(1-\varpi)},\mu_3^{\omega}\mu_4^{(1-\omega)}\right)$$

$$\leq\frac{\Upsilon^{\varpi\omega}(\mu_1,\mu_3)}{e^{\alpha(\mu_1+\mu_3)}}\frac{\Upsilon^{\varpi(1-\omega)}(\mu_1,\mu_4)}{e^{\alpha(\mu_1+\mu_4)}}\frac{\Upsilon^{(1-\varpi)\omega}(\mu_2,\mu_3)}{e^{\alpha(\mu_2+\mu_3)}}\frac{\Upsilon^{(1-\varpi)(1-\omega)}(\mu_2,\mu_4)}{e^{\alpha(\mu_2+\mu_4)}}$$

98

$$\times \frac{\Phi^{\varpi\omega}(\mu_1,\mu_3)}{e^{\alpha(\mu_1+\mu_3)}} \frac{\Phi^{\varpi(1-\omega)}(\mu_1,\mu_4)}{e^{\alpha(\mu_1+\mu_4)}} \frac{\Phi^{(1-\varpi)\omega}(\mu_2,\mu_3)}{e^{\alpha(\mu_2+\mu_3)}} \frac{\Phi^{(1-\varpi)(1-\omega)}(\mu_2,\mu_4)}{e^{\alpha(\mu_2+\mu_4)}}$$

$$= \frac{(\Upsilon\Phi)^{\varpi\omega}(\mu_1,\mu_3)}{e^{\alpha(\mu_1+\mu_3)}} \frac{(\Upsilon\Phi)^{\varpi(1-\omega)}(\mu_1,\mu_4)}{e^{\alpha(\mu_1+\mu_4)}}$$

$$\times \frac{(\Upsilon\Phi)^{(1-\varpi)\omega}(\mu_2,\mu_3)}{e^{\alpha(\mu_2+\mu_3)}} \frac{(\Upsilon\Phi)^{(1-\varpi)(1-\omega)}(\mu_2,\mu_4)}{e^{\alpha(\mu_2+\mu_4)}} \qquad (13)$$

Therefore $\Upsilon\Phi$ is geometrically exponentially convex functions on the co-ordinates on Δ.

Theorem 3. Let $\Upsilon : \Delta = [\mu_1,\mu_2] \times [\mu_3,\mu_4] \to R^+$ be partial differentiable mapping on $\Delta = [\mu_1,\mu_2] \times [\mu_3,\mu_4]$ and $\Upsilon \in L(\Delta)$, $\alpha \in R$. If Υ is geometrically exponentially convex function on the co-ordinates on Δ, then the following inequality holds;

$$\frac{1}{(\ln\mu_2 - \ln\mu_1)(\ln\mu_4 - \ln\mu_3)} \int_{\mu_1}^{\mu_2}\int_{\mu_3}^{\mu_4} \frac{\Upsilon(\rho_1,\rho_2)}{\rho_1\rho_2} d\rho_1 d\rho_2$$

$$\leq \frac{L(\Upsilon(\mu_1,\mu_3),\Upsilon(\mu_1,\mu_4)) + L(\Upsilon(\mu_2,\mu_3)\Upsilon(\mu_2,\mu_4))}{2e^{2\alpha(\mu_1+\mu_3+\mu_1+\mu_4)}} \quad (14)$$

where $\rho_1 \in [\mu_1,\mu_2]$ and $\rho_2 \in [\mu_3,\mu_4]$ dir.

Proof. Using inequality (10), the following expression is written

$$\Upsilon\left(\mu_1^\varpi \mu_2^{(1-\varpi)}, \mu_3^\omega \mu_4^{(1-\omega)}\right)$$

$$\leq \frac{\Upsilon^{\varpi\omega}(\mu_1,\mu_3)}{e^{\alpha(\mu_1+\mu_3)}} \frac{\Upsilon^{\varpi(1-\omega)}(\mu_1,\mu_4)}{e^{\alpha(\mu_1+\mu_4)}} \frac{\Upsilon^{(1-\varpi)\omega}(\mu_2,\mu_3)}{e^{\alpha(\mu_2+\mu_3)}} \frac{\Upsilon^{(1-\varpi)(1-\omega)}(\mu_2,\mu_4)}{e^{\alpha(\mu_2+\mu_4)}} \quad (15)$$

By integrating both sides of inequality (15) with respect to ϖ,ω on $[0,1]^2$, we have

$$\int_0^1\int_0^1 \Upsilon\left(\mu_1^\varpi \mu_2^{(1-\varpi)}, \mu_3^\omega \mu_4^{(1-\omega)}\right) d\varpi d\omega$$

$$\leq \int_0^1\int_0^1 \left(\frac{\Upsilon^{\varpi\omega}(\mu_1,\mu_3)}{e^{\alpha(\mu_1+\mu_3)}} \frac{\Upsilon^{\varpi(1-\omega)}(\mu_1,\mu_4)}{e^{\alpha(\mu_1+\mu_4)}} \right.$$

$$\left. \times \frac{\Upsilon^{(1-\varpi)\omega}(\mu_2,\mu_3)}{e^{\alpha(\mu_2+\mu_3)}} \frac{\Upsilon^{(1-\varpi)(1-\omega)}(\mu_2,\mu_4)}{e^{\alpha(\mu_2+\mu_4)}} \right) d\varpi d\omega$$

$$= \frac{1}{e^{2\alpha(\mu_1+\mu_3+\mu_1+\mu_4)}}$$

$$\times \int_0^1\int_0^1 \left(\Upsilon^{\varpi\omega}(\mu_1,\mu_3)\Upsilon^{\varpi(1-\omega)}(\mu_1,\mu_4)\Upsilon^{(1-\varpi)\omega} \right.$$

$$\left. \times (\mu_2,\mu_3)\Upsilon^{(1-\varpi)(1-\omega)}(\mu_2,\mu_4) \right) d\varpi d\omega$$

$$= \frac{1}{e^{2\alpha(\mu_1+\mu_3+\mu_1+\mu_4)}}$$

$$\times \int_0^1 \frac{\Upsilon^\omega(\mu_1,\mu_3)\Upsilon^{(1-\omega)}(\mu_1,\mu_4) - \Upsilon^\omega(\mu_2,\mu_3)\Upsilon^{(1-\omega)}(\mu_2,\mu_4)}{\ln\Upsilon^\omega(\mu_1,\mu_3)\Upsilon^{(1-\omega)}(\mu_1,\mu_4) - \ln\Upsilon^\omega(\mu_2,\mu_3)\Upsilon^{(1-\omega)}(\mu_2,\mu_4)} d\omega$$

$$= \frac{1}{e^{2\alpha(\mu_1+\mu_3+\mu_1+\mu_4)}}$$

$$\times \int_0^1 L\left(\Upsilon^\omega(\mu_1,\mu_3)\Upsilon^{(1-\omega)}(\mu_1,\mu_4), \Upsilon^\omega(\mu_2,\mu_3)\Upsilon^{(1-\omega)}(\mu_2,\mu_4)\right) d\omega \quad (16)$$

If the $\rho_1 = \mu_1^\varpi \mu_2^{1-\varpi}, \rho_2 = \mu_3^\omega \mu_4^{1-\omega}$ variable is changed and the $L(a,b) < A(a,b)$ feature is taken into account, the following result is obtained.

$$\frac{1}{(\ln\mu_2 - \ln\mu_1)(\ln\mu_4 - \ln\mu_3)} \int_{\mu_1}^{\mu_2}\int_{\mu_3}^{\mu_4} \frac{\Upsilon(\rho_1,\rho_2)}{\rho_1\rho_2} d\rho_1 d\rho_2$$

$$\leq \frac{1}{e^{2\alpha(\mu_1+\mu_3+\mu_1+\mu_4)}} \times$$

$$\int_0^1 A\left(\Upsilon^\omega(\mu_1,\mu_3)\Upsilon^{(1-\omega)}(\mu_1,\mu_4), \Upsilon^\omega(\mu_2,\mu_3)\Upsilon^{(1-\omega)}(\mu_2,\mu_4)\right) d\omega$$

$$= \frac{1}{e^{2\alpha(\mu_1+\mu_3+\mu_1+\mu_4)}} \times$$

$$\int_0^1 \frac{\Upsilon^\omega(\mu_1,\mu_3)\Upsilon^{(1-\omega)}(\mu_1,\mu_4) + \Upsilon^\omega(\mu_2,\mu_3)\Upsilon^{(1-\omega)}(\mu_2,\mu_4)}{2} d\omega$$

$$= \frac{L(\Upsilon(\mu_1,\mu_3),\Upsilon(\mu_1,\mu_4)) + L(\Upsilon(\mu_2,\mu_3)\Upsilon(\mu_2,\mu_4))}{2e^{2\alpha(\mu_1+\mu_3+\mu_1+\mu_4)}} \quad (17)$$

proof is completed.

Corollary 1. If we choose $\alpha = 0$ in Theorem 2.1, the result agrees geometrically with convexity on the coordinates.

$$\frac{1}{(\ln\mu_2 - \ln\mu_1)(\ln\mu_4 - \ln\mu_3)} \int_{\mu_1}^{\mu_2}\int_{\mu_3}^{\mu_4} \frac{\Upsilon(\rho_1,\rho_2)}{\rho_1\rho_2} d\rho_1 d\rho_2$$

$$\leq \frac{L(\Upsilon(\mu_1,\mu_3),\Upsilon(\mu_1,\mu_4)) + L(\Upsilon(\mu_2,\mu_3)\Upsilon(\mu_2,\mu_4))}{2} \quad (18)$$

where $\rho_1 \in [\mu_1,\mu_2]$ and $\rho_2 \in [\mu_3,\mu_4]$ dir.

Theorem 4. Let $\Upsilon : \Delta = [\mu_1,\mu_2] \times [\mu_3,\mu_4] \to R^+$ be partial differentiable mapping on $\Delta = [\mu_1,\mu_2] \times [\mu_3,\mu_4]$ and $\Upsilon \in L(\Delta)$, $\alpha \in R$. If $|\Upsilon|$ is geometrically exponentially convex function on the co-ordinates on Δ, $p > 1$ then the following inequality holds;

$$\left|\frac{1}{(\ln\mu_2-\ln\mu_1)(\ln\mu_4-\ln\mu_3)}\int_{\mu_1}^{\mu_2}\int_{\mu_3}^{\mu_4}\frac{\Upsilon(\rho_1,\rho_2)}{\rho_1\rho_2}d\rho_1 d\rho_2\right|$$

$$\leq\left(\frac{1}{e^{2p\alpha(\mu_1+\mu_3+\mu_1+\mu_4)}}\right)^{\frac{1}{p}}$$

$$\times\left(\frac{L\left(|\Upsilon(\mu_1,\mu_3)|^q|\Upsilon(\mu_1,\mu_4)|^q\right)+L\left(|\Upsilon(\mu_2,\mu_3)|^q|\Upsilon(\mu_2,\mu_4)|^q\right)}{2}\right)^{\frac{1}{q}} \quad (19)$$

where $\rho_1\in[\mu_1,\mu_2]$, $\rho_2\in[\mu_3,\mu_4]$ and $p^{-1}+q^{-1}=1$ dir.

Proof. Using inequality (10), the following expression is written

$$\Upsilon\left(\mu_1^{\varpi}\mu_2^{(1-\varpi)},\mu_3^{\omega}\mu_4^{(1-\omega)}\right)$$

$$\leq\frac{\Upsilon^{\varpi\omega}(\mu_1,\mu_3)}{e^{\alpha(\mu_1+\mu_3)}}\frac{\Upsilon^{\varpi(1-\omega)}(\mu_1,\mu_4)}{e^{\alpha(\mu_1+\mu_4)}}\frac{\Upsilon^{(1-\varpi)\omega}(\mu_2,\mu_3)}{e^{\alpha(\mu_2+\mu_3)}}\frac{\Upsilon^{(1-\varpi)(1-\omega)}(\mu_2,\mu_4)}{e^{\alpha(\mu_2+\mu_4)}} \quad (20)$$

If the absolute value of both sides of inequality (20) is taken and integrated with respect to ϖ,ω on $[0,1]^2$, we can write

$$\left|\int_0^1\int_0^1\Upsilon\left(\mu_1^{\varpi}\mu_2^{(1-\varpi)},\mu_3^{\omega}\mu_4^{(1-\omega)}\right)d\varpi d\omega\right|$$

$$\leq\int_0^1\int_0^1\left|\begin{pmatrix}\frac{\Upsilon^{\varpi\omega}(\mu_1,\mu_3)}{e^{\alpha(\mu_1+\mu_3)}}\frac{\Upsilon^{\varpi(1-\omega)}(\mu_1,\mu_4)}{e^{\alpha(\mu_1+\mu_4)}}\\\times\frac{\Upsilon^{(1-\varpi)\omega}(\mu_2,\mu_3)}{e^{\alpha(\mu_2+\mu_3)}}\frac{\Upsilon^{(1-\varpi)(1-\omega)}(\mu_2,\mu_4)}{e^{\alpha(\mu_2+\mu_4)}}\end{pmatrix}\right|d\varpi d\omega \quad (21)$$

In inequality (21), apply Hölder's inequality to the right side of the inequality and $\rho_1=\mu_1^{\varpi}\mu_2^{1-\varpi},\rho_2=\mu_3^{\omega}\mu_4^{1-\omega}$ variable is changed , we get

$$\left|\frac{1}{(\ln\mu_2-\ln\mu_1)(\ln\mu_4-\ln\mu_3)}\int_{\mu_1}^{\mu_2}\int_{\mu_3}^{\mu_4}\frac{\Upsilon(\rho_1,\rho_2)}{\rho_1\rho_2}d\rho_1 d\rho_2\right|$$

$$\leq\left(\int_0^1\int_0^1\frac{1}{e^{2p\alpha(\mu_1+\mu_3+\mu_1+\mu_4)}}d\varpi d\omega\right)^{\frac{1}{p}}$$

$$\times\left(\int_0^1\int_0^1\left(|\Upsilon(\mu_1,\mu_3)|^{\varpi\omega q}|\Upsilon(\mu_1,\mu_4)|^{\varpi(1-\omega)q}\right.\right.$$
$$\left.\left.\times|\Upsilon(\mu_2,\mu_3)|^{(1-\varpi)\omega q}|\Upsilon(\mu_2,\mu_4)|^{(1-\varpi)(1-\omega)q}\right)d\varpi d\omega\right)^{\frac{1}{q}}$$

$$=\left(\frac{1}{e^{2p\alpha(\mu_1+\mu_3+\mu_1+\mu_4)}}\right)^{\frac{1}{p}}$$

$$\times\left(\int_0^1 L\left(|\Upsilon(\mu_1,\mu_3)|^{\omega q}|\Upsilon(\mu_1,\mu_4)|^{(1-\omega)q},|\Upsilon(\mu_2,\mu_3)|^{\omega q}|\Upsilon(\mu_2,\mu_4)|^{(1-\omega)q}\right)d\omega\right)^{\frac{1}{q}}$$

Because of the $L(a,b)<A(a,b)$ property, we can write

$$\left|\frac{1}{(\ln\mu_2-\ln\mu_1)(\ln\mu_4-\ln\mu_3)}\int_{\mu_1}^{\mu_2}\int_{\mu_3}^{\mu_4}\frac{\Upsilon(\rho_1,\rho_2)}{\rho_1\rho_2}d\rho_1 d\rho_2\right|$$

$$\leq\left(\frac{1}{e^{2p\alpha(\mu_1+\mu_3+\mu_1+\mu_4)}}\right)^{\frac{1}{p}}$$

$$\times\left(\int_0^1 A\left(|\Upsilon(\mu_1,\mu_3)|^{\omega q}|\Upsilon(\mu_1,\mu_4)|^{(1-\omega)q},|\Upsilon(\mu_2,\mu_3)|^{\omega q}|\Upsilon(\mu_2,\mu_4)|^{(1-\omega)q}\right)d\omega\right)^{\frac{1}{q}}$$

$$=\left(\frac{1}{e^{2p\alpha(\mu_1+\mu_3+\mu_1+\mu_4)}}\right)^{\frac{1}{p}}$$

$$\times\left(\int_0^1\frac{|\Upsilon(\mu_1,\mu_3)|^{\omega q}|\Upsilon(\mu_1,\mu_4)|^{(1-\omega)q}+|\Upsilon(\mu_2,\mu_3)|^{\omega q}|\Upsilon(\mu_2,\mu_4)|^{(1-\omega)q}}{2}d\omega\right)^{\frac{1}{q}}$$

$$=\left(\frac{1}{e^{2p\alpha(\mu_1+\mu_3+\mu_1+\mu_4)}}\right)^{\frac{1}{p}}$$

$$\times\left(\frac{L\left(|\Upsilon(\mu_1,\mu_3)|^q|\Upsilon(\mu_1,\mu_4)|^q\right)+L\left(|\Upsilon(\mu_2,\mu_3)|^q|\Upsilon(\mu_2,\mu_4)|^q\right)}{2}\right)^{\frac{1}{q}}. \quad (22)$$

Proof is completed.

Corollary 2. If we choose $\alpha=0$ in Theorem 4, the result agrees geometrically with convexity on the coordinates.

$$\left|\frac{1}{(\ln\mu_2-\ln\mu_1)(\ln\mu_4-\ln\mu_3)}\int_{\mu_1}^{\mu_2}\int_{\mu_3}^{\mu_4}\frac{\Upsilon(\rho_1,\rho_2)}{\rho_1\rho_2}d\rho_1 d\rho_2\right|$$

$$\leq\left(\frac{L\left(|\Upsilon(\mu_1,\mu_3)|^q|\Upsilon(\mu_1,\mu_4)|^q\right)+L\left(|\Upsilon(\mu_2,\mu_3)|^q|\Upsilon(\mu_2,\mu_4)|^q\right)}{2}\right)^{\frac{1}{q}} \quad (23)$$

where $\rho_1\in[\mu_1,\mu_2]$, $\rho_2\in[\mu_3,\mu_4]$ and $p^{-1}+q^{-1}=1$ dir.

Theorem 5. Let $\Upsilon:\Delta=[\mu_1,\mu_2]\times[\mu_3,\mu_4]\to R^+$ be partial differentiable mapping on $\Delta=[\mu_1,\mu_2]\times[\mu_3,\mu_4]$ and $\Upsilon\in L(\Delta),\ \alpha\in R$. If $|\Upsilon|$ is geometrically exponentially convex function on the co-ordinates on Δ, $p>1$ then the following inequality holds;

$$\left|\frac{1}{(\ln\mu_2-\ln\mu_1)(\ln\mu_4-\ln\mu_3)}\int_{\mu_1}^{\mu_2}\int_{\mu_3}^{\mu_4}\frac{\Upsilon(\rho_1,\rho_2)}{\rho_1\rho_2}d\rho_1 d\rho_2\right|$$

$$\leq \frac{1}{pe^{2p\alpha(\mu_1+\mu_3+\mu_1+\mu_4)}}$$

$$+ \frac{L\left(\left|\Upsilon(\mu_1,\mu_3)\right|^q\left|\Upsilon(\mu_1,\mu_4)\right|^q\right)+L\left(\left|\Upsilon(\mu_2,\mu_3)\right|^q\left|\Upsilon(\mu_2,\mu_4)\right|^q\right)}{2q} \quad (24)$$

where $\rho_1 \in [\mu_1, \mu_2]$, $\rho_2 \in [\mu_3, \mu_4]$ and $p^{-1}+q^{-1}=1$ dir.

Proof. Using inequality (10), the following expression is written

$$\Upsilon\left(\mu_1^{\varpi}\mu_2^{(1-\varpi)}, \mu_3^{\omega}\mu_4^{(1-\omega)}\right)$$

$$\leq \frac{\Upsilon^{\varpi\omega}(\mu_1,\mu_3)}{e^{\alpha(\mu_1+\mu_3)}}\frac{\Upsilon^{\varpi(1-\omega)}(\mu_1,\mu_4)}{e^{\alpha(\mu_1+\mu_4)}}\frac{\Upsilon^{(1-\varpi)\omega}(\mu_2,\mu_3)}{e^{\alpha(\mu_2+\mu_3)}}\frac{\Upsilon^{(1-\varpi)(1-\omega)}(\mu_2,\mu_4)}{e^{\alpha(\mu_2+\mu_4)}} \quad (25)$$

If the absolute value of both sides of inequality (20) is taken and integrated with respect to ϖ, ω on $[0,1]^2$, we can write

$$\left|\int_0^1\int_0^1 \Upsilon\left(\mu_1^{\varpi}\mu_2^{(1-\varpi)}, \mu_3^{\omega}\mu_4^{(1-\omega)}\right)d\varpi d\omega\right|$$

$$\leq \int_0^1\int_0^1 \left|\begin{pmatrix}\frac{\Upsilon^{\varpi\omega}(\mu_1,\mu_3)}{e^{\alpha(\mu_1+\mu_3)}}\frac{\Upsilon^{\varpi(1-\omega)}(\mu_1,\mu_4)}{e^{\alpha(\mu_1+\mu_4)}}\\ \times \frac{\Upsilon^{(1-\varpi)\omega}(\mu_2,\mu_3)}{e^{\alpha(\mu_2+\mu_3)}}\frac{\Upsilon^{(1-\varpi)(1-\omega)}(\mu_2,\mu_4)}{e^{\alpha(\mu_2+\mu_4)}}\end{pmatrix}\right| d\varpi d\omega \quad (26)$$

In inequality (26), apply Young's inequality to the right side of the inequality and $\rho_1 = \mu_1^{\varpi}\mu_2^{1-\varpi}, \rho_2 = \mu_3^{\omega}\mu_4^{1-\omega}$ variable is changed, we get

$$\left|\frac{1}{(\ln\mu_2-\ln\mu_1)(\ln\mu_4-\ln\mu_3)}\int_{\mu_1}^{\mu_2}\int_{\mu_3}^{\mu_4}\frac{\Upsilon(\rho_1,\rho_2)}{\rho_1\rho_2}d\rho_1 d\rho_2\right|$$

$$\leq \frac{1}{p}\left(\int_0^1\int_0^1 \frac{1}{e^{2p\alpha(\mu_1+\mu_3+\mu_1+\mu_4)}}d\varpi d\omega\right)$$

$$+\frac{1}{q}\left(\begin{array}{c}\int_0^1\int_0^1\left(\left|\Upsilon(\mu_1,\mu_3)\right|^{\varpi\omega q}\left|\Upsilon(\mu_1,\mu_4)\right|^{\varpi(1-\omega)q}\right.\\ \left.\times\left|\Upsilon(\mu_2,\mu_3)\right|^{(1-\varpi)\omega q}\left|\Upsilon(\mu_2,\mu_4)\right|^{(1-\varpi)(1-\omega)q}\right)d\varpi d\omega\end{array}\right)$$

$$=\frac{1}{pe^{2p\alpha(\mu_1+\mu_3+\mu_1+\mu_4)}}$$

$$+\frac{1}{q}\left(\int_0^1 L\left(\left|\Upsilon(\mu_1,\mu_3)\right|^{\omega q}\left|\Upsilon(\mu_1,\mu_4)\right|^{(1-\omega)q},\left|\Upsilon(\mu_2,\mu_3)\right|^{\omega q}\left|\Upsilon(\mu_2,\mu_4)\right|^{(1-\omega)q}\right)d\omega\right) \quad (27)$$

Because of the $L(a,b) < A(a,b)$ property, we can write

$$\left|\frac{1}{(\ln\mu_2-\ln\mu_1)(\ln\mu_4-\ln\mu_3)}\int_{\mu_1}^{\mu_2}\int_{\mu_3}^{\mu_4}\frac{\Upsilon(\rho_1,\rho_2)}{\rho_1\rho_2}d\rho_1 d\rho_2\right|$$

$$\leq \frac{1}{pe^{2p\alpha(\mu_1+\mu_3+\mu_1+\mu_4)}}+$$

$$\frac{1}{q}\left(\int_0^1 A\left(\left|\Upsilon(\mu_1,\mu_3)\right|^{\omega q}\left|\Upsilon(\mu_1,\mu_4)\right|^{(1-\omega)q},\left|\Upsilon(\mu_2,\mu_3)\right|^{\omega q}\left|\Upsilon(\mu_2,\mu_4)\right|^{(1-\omega)q}\right)d\omega\right)$$

$$=\frac{1}{pe^{2p\alpha(\mu_1+\mu_3+\mu_1+\mu_4)}}$$

$$+\left(\int_0^1\frac{\left|\Upsilon(\mu_1,\mu_3)\right|^{\omega q}\left|\Upsilon(\mu_1,\mu_4)\right|^{(1-\omega)q}+\left|\Upsilon(\mu_2,\mu_3)\right|^{\omega q}\left|\Upsilon(\mu_2,\mu_4)\right|^{(1-\omega)q}}{2q}d\omega\right)$$

$$=\frac{1}{pe^{2p\alpha(\mu_1+\mu_3+\mu_1+\mu_4)}}$$

$$+\frac{L\left(\left|\Upsilon(\mu_1,\mu_3)\right|^q\left|\Upsilon(\mu_1,\mu_4)\right|^q\right)+L\left(\left|\Upsilon(\mu_2,\mu_3)\right|^q\left|\Upsilon(\mu_2,\mu_4)\right|^q\right)}{2q} \quad (28)$$

proof is completed.

Corollary 3. If we choose $\alpha = 0$ in Theorem 5, the result agrees geometrically with convexity on the co-ordinates.

$$\left|\frac{1}{(\ln\mu_2-\ln\mu_1)(\ln\mu_4-\ln\mu_3)}\int_{\mu_1}^{\mu_2}\int_{\mu_3}^{\mu_4}\frac{\Upsilon(\rho_1,\rho_2)}{\rho_1\rho_2}d\rho_1 d\rho_2\right|$$

$$\leq \frac{1}{p}+\frac{L\left(\left|\Upsilon(\mu_1,\mu_3)\right|^q\left|\Upsilon(\mu_1,\mu_4)\right|^q\right)+L\left(\left|\Upsilon(\mu_2,\mu_3)\right|^q\left|\Upsilon(\mu_2,\mu_4)\right|^q\right)}{2q} \quad (29)$$

where $\rho_1 \in [\mu_1, \mu_2]$, $\rho_2 \in [\mu_3, \mu_4]$ and $p^{-1}+q^{-1}=1$ dir.

Acknowledgement

REFERENCES

[1] Awan MU, Noor MA, Noor KI. Hermite-Hadamard Inequalities for Exponentially Convex Functions, Appl. Math. Inf. Sci. 2018; 12, No. 2, 405-409.

[2] Peajcariaac JE, Tong YL. Convex functions, partial orderings, and statistical applications. Academic Press;1992.

[3] Niculescu CP. Convexity according to the geometric mean. Math. Inequal. Appl. 2000; 3(2): 155-167.

[4] Özdemir ME, Yıldız Ç, Gürbüz M. A note on geometrically convex functions. Journal of Inequalities and Applications. 2014(1): 1-12.

[5] Xi BY, Bai RF, Qi F. Hermite-Hadamard type inequalities for the m− and (α, m) - geometrically convex functions. Aequationes mathematicae, 2012; 84(3): 261-269.

101

[6] Özdemir ME. Inequalities on geometrically convex functions. arXiv preprint arXiv: 2013; 1312.7725.

[7] Dokuyucu M, Aslan S. Some New Approaches for Geometrically Convex Functions. 9ROXPH. 2022; 156.

[8] Rashid S, Akdemir AO, Ekinci A, Aslan S. Some Fractional Integral Inequalities for Geometrically Convex Functions. In 3rd International Conference on Mathematical and Related Sciences: Current Trends and Developments Proceedings Book. (2020, November). (p. 246).

[9] Butt SI, Ekinci A, Akdemir AO, Aslan S. Inequalities for Geometrically Convex Functions. In 3rd International Conference on Mathematical and Related Sciences: Current Trends and Developments Proceedings Book. (2020, November). (Vol. 1, p. 238).

[10] Akdemir AO, Dutta H. (2020). New integral inequalities for product of geometrically convex functions. In 4th International Conference on Computational Mathematics and Engineering Sciences (CMES-2019) 4 (pp. 315-323). Springer International Publishing.

[11] Aslan S, Akdemir AO. (2022, August). Exponentially convex functions on the co-ordinates and related integral inequalities. In Proceedings of the 8th International Conference on Control and Optimization with Industrial Applications (Vol. 2, pp. 120-122).

[12] Dragomir SS. On Hadamard's inequality for convex functions on the co-ordinates in a rectangle from the plane, Taiwanese Journal of Math., 5, 2001, 775-788.

[13] Aslan S. (2023). Eksponansiyel konveks fonksiyonlar için koordinatlarda integral eşitsizlikler. PhD thesis, Doktora Tezi, Ağrı İbrahim Çeçen Üniversitesi, Lisansüstü Eğitim Enstitüsü.

[14] Akdemir AO, Aslan S, Dokuyucu MA, Çelik E. (2023). Exponentially Convex Functions on the Coordinates and Novel Estimations via Riemann-Liouville Fractional Operator. Journal of Function Spaces, 2023.

[15] Aslan S, Akdemir AO. (2023). Exponential $s-$Convex Functions in the First Sense on the Co-ordinates and Some Novel Integral Inequalities. Turkish Journal of Science, 8(2), 85-92.

[16] Aslan S, Akdemir AO, Dokuyucu MA. (2022). Exponentially $m-$ and $(\alpha, m)-$ Convex Functions on the Coordinates and Related Inequalities. Turkish Journal of Science, 7(3), 231-244.

[17] Akdemir AO, Aslan S, Set E. (2022, October). Some New Inequalities for Exponentially Quasi-Convex Functions on the Coordinates and Related Hadamard Type Integral Inequalities. In 5th International Conference on Mathematical and Related Sciences Book of Proceedings (p. 120).

[18] Akdemir AO, Aslan S, Ekinci A. (2022, October). Some New Inequalities for Exponentially P-Functions on the Coordinates. In 5th International Conference on Mathematical and Related Sciences Book of Proceedings (94-108).

[19] Nie D, Rashid S, Akdemir AO, Baleanu D, Liu JB. On some new weighted inequalities for differentiable exponentially convex and exponentially quasi-convex functions with applications. Mathematics. 2019;7(8), 727.

[20] Rashid S, Noor MA, Noor KI, Akdemir AO. Some new generalizations for exponentially s-convex functions and inequalities via fractional operators. Fractal and fractional. 2019;3(2): 24.

[21] Rashid S, Safdar F, Akdemir AO, Noor MA, Noor KI. Some new fractional integral inequalities for exponentially m-convex functions via extended generalized Mittag-Leffler function. Journal of Inequalities and Applications. 2019; 1-17.

[22] Anderson GD, Vamanamurthy MK, Vuorinen M. Generalized convexity and inequalities, J. Math. Anal. Appl., 335 (2007), 1294-1308.

[23] Bullen PS. Handbook of Means and Their Inequalities, Math. Appl., vol. 560, Kluwer Academic Publishers, Dordrecht, 2003.

[24] Bullen PS, Mitrinović DS, Vasic PM. Means and Their Inequalities, Reidel, Dordrecht; 1988.

Türk Doğa ve Fen Dergisi
Turkish Journal of Nature and Science
www.dergipark.gov.tr/tdfd

Curves of Constant Ratio with Quasi frame in $\mathbb{E}^3$

Rabia KALMUK[1*] (iD), Sezgin BÜYÜKKÜTÜK[2] (iD), Günay ÖZTÜRK[3] (iD)

[1] Kocaeli University, Arts and Science Faculty, Department of Mathematics, Kocaeli, Türkiye
[2] Kocaeli University, Gölcük Vocational School of Higher Education, Kocaeli, Türkiye
[3] İzmir Democracy University, Arts and Science Faculty, Department of Mathematics, İzmir, Türkiye
Rabia KALMUK ORCID No: 0009-0009-0890-792X
Sezgin BÜYÜKKÜTÜK ORCID No: 0000-0002-1845-0822
Günay ÖZTÜRK ORCID No: 0000-0002-1608-0354

Correspondingauthor: sezgin.buyukkutuk@kocaeli.edu.tr

Keywords
Constant
ratio curve,
Position
vector,
Quasi frame

Abstract: In the present study we handle a regular unit speed curve by means of the position vector given by the vectorial equation $\gamma(s) = m_0\, t(s) + m_1 n_q(s) + m_2 b_q(s)$ where $b_q(s)$, $n_q(s)$ and $t(s)$ are quasi frame vectors. Firstly, we analysis these curves and investigate to being constant ratio curve. Then, we give the parameterizations of T-constant and N- constant curve in accordance with quasi frame. Further, we get the conditions for a regular curve to correspond to be a W- curve *in* $\mathbb{E}^3$.

$\mathbb{E}^3$ Uzayında Quasi Çatısına Göre Sabit Oranlı Eğriler

103

Anahtar Kelimeler
Sabit oranlı
eğri,
Pozisyon
vektörü,
Quasi çatısı

Öz: Bu çalışmada, $b_q(s)$, $n_q(s)$ ve $t(s)$ quasi çatı vektörleri olmak üzere pozisyon vektörü $\gamma(s) = m_0\, t(s) + m_1 n_q(s) + m_2 b_q(s)$ vektörel denklemi ile verilen birim hızlı eğriyi ele aldık. İlk olarak eğriyi inceleyerek sabit oranlı olma durumunu araştırdık. Sonrasında T-sabit ve N-sabit eğrilerin parametrizasyonlarını verdik. Ayrıca, bir regüler eğrinin W-eğrisine karşılık gelme koşulunu elde ettik.

1. INTRODUCTION

In $3-$ dimensional Euclidean space, the rectifying curves that located on rectifying plane are defined by B. Y. Chen [3]. The binormal vector field and tangent vector field spans the related plane. Chen also presents a simple classification in this paper. In study [5], the connection between centrodes (that is of great importance in kinematics, mechanics) and rectifying curves is mentioned. Moreover, in $3-$ dimensional Minkowski space, the rectifying curves are examined in [8, 11, 12, 14].

In Euclidean $3-$ space, the rectifying curves can be written as

$$\gamma(s) = \lambda(s)t(s) + \mu(s)b(s), \qquad (1)$$

where $\lambda(s)$ and $\mu(s)$ are curvature functions [13].

Non $-$ degenerate and continuously $3-$ times differentiable curves can be considered for creating the Frenet frame. Namely, there is a possibility that second derivative vanishes. In this station, instead of this, the new frame is needed.

Quasi frame is more useful than Frenet frame, Bishop frame, etc. For example, the quasi frame can also be defined on a straight line. The structure of the q $-$ frame is the same whether the curve unit speed or not, and the q $-$ frame can be easily determined [7].

For a regular curve given by a position vector, the sum of its normal and tangent component can be considered as

$$\gamma = \gamma^T + \gamma^N \qquad (2)$$

(see, [1]). If $\frac{\|\gamma^T\|}{\|\gamma^N\|}$ is equal to a constant, such curves are called as curves of constant ratio [1]. Here $\|\gamma^N\|$ and $\|\gamma^T\|$, are the norms or the lengths of γ^N and γ^T, respectively. As can be seen from here, the constancy of the ratio $\frac{\|\gamma^T\|}{\|\gamma\|}$ also corresponds to the same definition [2].

In particular, since the expression $\| \mathrm{grad}\ (\| \gamma \|) \|$ is equal to the related ratio, satisfying the condition

$$\| \mathrm{grad}\ (\| \gamma \|) \| = c \qquad (3)$$

on the curve means that it has a constant ratio. In addition to these explanations, a W- curve is known as a curve which has constant principle curvatures and was named by F. Klein and S. Lie in study [15]. It is also called as a helix or a screw line in $\mathbb{E}^n$.

Here, we consider a curve in Euclidean 3–space as a linear combination of the q–frame as

$$\gamma(s) = m_0 t(s) + m_1(s) n_q(s) + m_2(s) b_q(s). \qquad (4)$$

In this equation, m_0, m_1, and m_2 are curvature functions. Based on the curvature functions, we investigate whether a unit–speed curve is of constant ratio, T–constant, N–constant or a W–curve in $\mathbb{E}^3$.

2. BASIC CONCEPTS

Suppose the unit speed regular curve is denoted by $\gamma : I \subset \mathbb{R} \to \mathbb{E}^3$. The tangent unit vector is known as $\gamma'(s) = t(s)$ also $\kappa_1 = \|\gamma''(s)\|$ is the first Frenet curvature. In the case $\kappa_1 \neq 0$, the unit normal vector field satisfies $n'(s) + \kappa_1(s)t(s) = \kappa_2(s)b(s)$. Here, b is the binormal vector field (the second principle normal) and the second Frenet curvature is indicated by κ_2 given by $b'(s) = -\kappa_2(s)n(s)$. Hence, the Serret − Frenet formulae is

$$t'(s) = \kappa_1(s)n(s)$$

$$n'(s) = -\kappa_1(s)t(s) + \kappa_2(s)b(s) \qquad (5)$$

$$b'(s) = -\kappa_2(s)n(s)$$

(see, [9])

Moreover, a new frame Quasi is an alternative to Frenet frame consists by a projection vector l, the tangent vector $t(s)$, quasi-normal $n_q(s)$, and quasi-binormal $b_q(s)$. Then, the quasi frame vectors are given by

$$t(s) = \gamma'(s)$$

$$n_q(s) = \frac{t(s) \times l}{\|t(s) \times l\|}$$

$$b_q(s) = t(s) \times n_q(s)$$

where the projection vector l is chosen as $l = (1, 0, 0)$ (can also be chosen as (0, 1, 0), (0, 0, 1). Hence, the transition from Frenet frame vectors to Quasi frame vectors is

$$\begin{bmatrix} t \\ n_q \\ b_q \end{bmatrix} = \begin{bmatrix} 1 & 0 & 0 \\ 0 & \cos\alpha & \sin\alpha \\ 0 & -\sin\alpha & \cos\alpha \end{bmatrix} \begin{bmatrix} t \\ n \\ b \end{bmatrix} \qquad (7)$$

where α is the angle between the quasi−normal vector field n_q and the principle normal vector field n. Inversely, we write

$$\begin{bmatrix} t \\ n \\ b \end{bmatrix} = \begin{bmatrix} 1 & 0 & 0 \\ 0 & \cos\alpha & -\sin\alpha \\ 0 & \sin\alpha & \cos\alpha \end{bmatrix} \begin{bmatrix} t \\ n_q \\ b_q \end{bmatrix} \qquad (8)$$

Consequently, by the use of these relations, the quasi frame formulae is given by

$$\begin{bmatrix} t' \\ n_q' \\ b_q' \end{bmatrix} = \begin{bmatrix} 0 & k_1 & k_2 \\ -k_1 & 0 & k_3 \\ -k_2 & -k_3 & 0 \end{bmatrix} \begin{bmatrix} t \\ n_q \\ b_q \end{bmatrix} \qquad (9)$$

where $k_1 = -\langle t, n_q' \rangle$, $k_2 = -\langle t, b_q' \rangle$, $k_3 = \langle n_q', b_q \rangle$ are the quasi curvatures[6].

3. CLASSIFICATION OF CURVES WITH RESPECT TO Q - FRAME IN $\mathbb{E}^3$

Let $\gamma : I \to \mathbb{E}^3$ be a unit speed regular curve in $\mathbb{E}^3$. Then the position vector can be considered as a combination of its quasi frame as

$$\gamma(s) = m_0(s)t(s) + m_1(s)n_q(s) + m_2(s)b_q(s) \qquad (10)$$

where m_0, m_1 and m_2 are curvature functions of the curve $\gamma(s)$, the derivative of the position vector is

$$\gamma'(s) = m_0' t(s) + m_0 t'(s) + m_1' n_q(s) + m_1 n_q'(s) + m_2' b_q(s) + m_2 b_q'(s) \qquad (11)$$

Using Quasi frame formulas, we write

$$\gamma'(s) = m_0' t(s) + m_0(k_1 n_q(s) + k_2 b_q(s)) + m_1' n_q(s) + m_1(-k_1 t(s) + k_3 b_q(s)) + m_2' b_q(s) + m_2(-k_2 t(s) - k_3 n_q(s)) \qquad (12)$$

It follows that

$$\gamma'(s) = (m_0' - k_1 m_1 - k_2 m_2)t(s) + (m_1' + k_1 m_0 - k_3 m_2)n_q(s) + (m_2' + k_2 m_0 + k_3 m_1)b_q(s)$$

$$= t(s) \qquad (13)$$

Hence, we obtain

$$m_0' - k_1 m_1 - k_2 m_2 = 1$$

$$m_1' + k_1 m_0 - k_3 m_2 = 0 \qquad (14)$$

$$m_2' + k_2 m_0 + k_3 m_1 = 0$$

Lemma 3.1. Let $\gamma : I \rightarrow \mathbb{E}^3$ be a unit speed regular curve in $\mathbb{E}^3$ with the vectorial equation(10). Then the position vector. γ satisfies the curvature conditions in the equation system (14).

Corollary 3.2. Suppose that, a regular unit speed curve in $\mathbb{E}^3$ is denoted by $\gamma : I \rightarrow \mathbb{E}^3$. Then, γ corresponds to a $W-$curve if and only if it satisfes the differential equation

$$m_0''(s) = -(k_1^2 + k_2^2)m_0(s) + k_3(k_1 m_2(s) - k_2 m_1(s))$$

where the principle curvatures k_i, $i = 1, 2, 3$ are real constants.

Proof. Assume, the regular and unit speed curve γ satisfies the equation system (14). If k_1, k_2 and k_3 are chosen real constants in (14), using the first equation, one can write

$$m_0''(s) = k_1 m_1' + k_2 m_2' \qquad (15)$$

Combining (15) with the second and third equation of (14), we obtain the result.

3.1. Constant −ratio curves with quasi frame

Definition 3.3. Suppose that a regular unit speed curve in $\mathbb{E}^3$ is denoted by $\gamma : I \subset \mathbb{R} \rightarrow \mathbb{E}^3$. Then the relation

$$\gamma = \gamma^T + \gamma^N \qquad (16)$$

is valid. In case of $\|\gamma^T\| : \|\gamma^N\|$ is a real constant, then γ is defined as a constant ratio curve.In other words, for these curves, the related constant ratio can be considered as $\|\gamma^T\| : \|\gamma\|$ [1].

In addition, $grad(\|\gamma(s)\|)$ is calculated by

$$grad(\|\gamma(s)\|) = \frac{d(\|\gamma(s)\|)}{ds}\gamma'(s) = \frac{<\gamma(s),\gamma'(s)>}{\|\gamma(s)\|}\gamma'(s) \qquad (17)$$

where $\gamma' = T$ is the tangent vector field of γ [2].

The next consequence classifies constant - ratio curves.

Theorem 3.4. Suppose, a regular unit speed curve is denoted by $\gamma : I \subset \mathbb{R} \rightarrow \mathbb{E}^n$ in $\mathbb{E}^n$. Then γ is of constant ratio satisfying $\|\gamma^T\| : \|\gamma\| = c \Leftrightarrow \|grad\rho\| = c$ where c is a real constant.

Especially, we know that for a curve of constant ratio we have $\|grad(\|\gamma(s)\|)\| = c \leq 1$.

The next theorem, which is a result of equation (17), is important in classifying constant ratio curves.

Theorem 3.5.[4] For a regular unit speed curve $\gamma : I \subset \mathbb{R} \rightarrow \mathbb{E}^n$, $\|grad(\|\gamma(s)\|)\| = c$ ($c = const.$) if and only if the following three statements are valid:

(i) $\|grad\rho\| = 0 \Leftrightarrow \gamma$ (I) is included in a hypersphere whose center is the origin.

(ii) $\|grad\rho\| = 1 \Leftrightarrow \gamma$ (I) is congruent to line segment (pass through the origin).

(iii) $\|grad\rho\| = c \Leftrightarrow \rho = \|\gamma(s)\| = cs$, $0 < c < 1$

The following result provides a classification of constant ratio curves according to quasi frame in$\mathbb{E}^3$:

Proposition 3.6. Let $\gamma : I \rightarrow \mathbb{E}^3$ be a unit speed regular curve according to q − frame in $\mathbb{E}^3$. In case of the curve is of constant ratio then its position vector is given by

$$\gamma(s) = c^2 st(s) + \frac{(c^2-1)k_1 \pm k_2\sqrt{(k_1^2+k_2^2)(1-c^2)c^2s^2-(c^2-1)^2}}{k_1^2+k_2^2}n_q(s)$$
$$+ \frac{(c^2-1)k_2 \pm k_1\sqrt{(k_1^2+k_2^2)(1-c^2)c^2s^2-(c^2-1)^2}}{k_1^2+k_2^2}b_q(s) \qquad (18)$$

Proof. Let $\gamma : I \rightarrow \mathbb{E}^3$ be a unit speed regular curve given by the vectorial equation (10). Then the equation system(14) holds. If the curve is of constant ratio, then

$$\frac{\|\gamma^T\|}{\|\gamma\|} = c = \text{const.}$$

$$\frac{m_0}{cs} = c$$

$$m_0 = c^2 s$$

Putting $m_0 = c^2 s$ in (14), multiplying the second equation of (14) with m_1 and multiplying the third equation of (14) with m_2, we get

$$c^2 s(k_1 m_1 + k_2 m_2) + m_1' m_1 + m_2' m_2 = 0$$

Using the frst equation of (14), we yield

$$m_1^2 + m_2^2 = c^2 s^2 (1 - c^2) \qquad (19)$$

By the use of the first equation of (14) and substituting $m_2 = \frac{c^2-1-k_1 m_1}{k_2}$ into (19), we obtain

$$m_1 = \frac{(c^2-1)k_1 \pm k_2\sqrt{(k_1^2+k_2^2)(1-c^2)c^2s^2-(c^2-1)^2}}{k_1^2+k_2^2}$$

and

$$m_2 = \frac{(c^2-1)k_2 \pm k_1\sqrt{(k_1^2+k_2^2)(1-c^2)c^2s^2-(c^2-1)^2}}{k_1^2+k_2^2}$$

This completes the proof.

105

3.2. T − Constant curves with quasi frame

Defnition 3.7. Suppose, a regular unit speed curve in $\mathbb{E}^3$ is denoted by $\gamma : I \subset \mathbb{R} \to \mathbb{E}^3$. If the length of the tangent component of the curve $(\|\gamma^T\|)$ is constant, then the curve is called T − constant curve [2]. Especially, if $\|\gamma^T\| = 0$, then the curve is called as T − constant curve of first kind, if not, second kind [10].

Corollary 3.8. Let $\gamma : I \to \mathbb{E}^3$ be a unit speed regular curve according to q-frame in Euclidean 3 − space. Then, it is a T-constant curve of first kind if and only if the curvature functions m_1 and m_2 satisfies:

$$m_1^2 + m_2^2 = c_1 \tag{20}$$

Proof. Let $\gamma : I \to \mathbb{E}^3$ be a unit speed reguler curve given by the vectorial equation (10). The equation system (14) is hold if γ is T − constant curve of first kind, then $m_0 = 0$ in (14):

$$k_1 m_1 + k_2 m_2 = -1 \tag{21}$$

$$m_1' = k_3 m_2 \tag{22}$$

$$m_2' = -k_3 m_1 \tag{23}$$

By the use of (22) and (23), we write

$$\frac{m_1'}{m_1} = -\frac{m_2'}{m_2} = k_3$$

$$m_1' m_1 + m_2' m_2 = 0$$

Therefore, we obtain

$$m_1^2 + m_2^2 = c_1$$

This completes the proof.

Proposition 3.9. Let $\gamma : I \to \mathbb{E}^3$ be a unit speed regular curve according to q − frame in Euclidean 3 − space. It is congruent to T − constant curve of first kind if and only if it has the parameterization

$$\gamma(s) = \frac{-k_1 \pm k_2 \sqrt{(k_1^2 + k_2^2)c_1 - 1}}{k_1^2 + k_2^2} n_q(s) + \frac{-k_2 \pm k_1 \sqrt{(k_1^2 + k_2^2)c_1 - 1}}{k_1^2 + k_2^2} b_q(s) \tag{24}$$

where c_1 is a real constant.

Proof. Let γ be a T − constant curve of first kind. Then, the equation (20) is satisfied:

$$m_2^2 = c_1 - m_1^2 \tag{25}$$

With the help of (21), one can put $m_2 = -\frac{1 + k_1 m_1}{k_2}$ into (25). Then, the curvature functions are

$$m_1 = \frac{-k_1 \pm k_2 \sqrt{(k_1^2 + k_2^2)c_1 - 1}}{k_1^2 + k_2^2} \tag{26}$$

and

$$m_2 = \frac{-k_2 \pm k_1 \sqrt{(k_1^2 + k_2^2)c_1 - 1}}{k_1^2 + k_2^2} \tag{27}$$

This completes the proof.

Theorem 3.10. Let γ be a T − constant curve of first kind. Then the quasi curvatures k_1, k_2, k_3 satisfies the relation:

$$\left[\frac{-k_1 \pm k_2 \sqrt{(k_1^2 + k_2^2)c_1 - 1}}{k_1^2 + k_2^2} \right]' = k_3 \left[\frac{-k_2 \pm k_1 \sqrt{(k_1^2 + k_2^2)c_1 - 1}}{k_1^2 + k_2^2} \right] \tag{28}$$

Proof. By putting (26) and (27) into (22), we obtain the desired result.

Corollary 3.11. Let $\gamma : I \to \mathbb{E}^3$ be a unit speed regular curve according to q − frame in Euclidean 3 − space. Then it is a T − constant curve of second kind if and only if the curvature functions m_1 and m_2 satisfies:

$$2c_1 s + c_2 = m_1^2 + m_2^2 \tag{29}$$

Proof. Let γ be a unit speed regular curve given by the vectorial equation(10). If it is T − constant curve of second kind, $m_0 = c_1$. Hence, the equation system (14) turns into

$$k_1 m_1 + k_2 m_2 = -1 \tag{30}$$

$$m_1' = k_3 m_2 - k_1 c_1 \tag{31}$$

$$m_2' = -k_3 m_1 - k_2 c_1 \tag{32}$$

Multipiying (31) with m_1 and multiplying (32) with m_2, sum of them are

$$m_1 + m_2' m_2 = -c_1(k_1 m_1 + k_2 m_2) \tag{33}$$

Therefore, by the use of (30), we yield

$$m_1' m_1 + m_2' m_2 = c_1$$

and

$$m_1^2 + m_2^2 = 2c_1 s + c_2$$

Proposition 3.12. Let $\gamma : I \to \mathbb{E}^3$ be a unit speed regular curve according to q − frame in Euclidean 3 − space. It is congruent to T − constant curve of second kind if and only if it has the parameterization

$$\gamma(s) = c_1 t(s) + \frac{-k_1 \pm k_2 \sqrt{(k_1^2 + k_2^2)(2c_1 s + c_2) - 1}}{k_1^2 + k_2^2} n_q(s) + \frac{-k_2 \pm k_1 \sqrt{(k_1^2 + k_2^2)(2c_1 s + c_2) - 1}}{k_1^2 + k_2^2} b_q(s) \tag{34}$$

where c_1, c_2 are real constants.

Proof. Let γ be a T − constant curve of second kind ($m_0 = c_1$). Then, the equation (29) is satisfied. With the help of (21), one can put $m_2 = -\frac{1 + k_1 m_1}{k_2}$ into (29). Then, the curvature functions are

106

$$m_1 = \frac{-k_1 \pm k_2 \sqrt{(k_1^2 + k_2^2)(2c_1 s + c_2) - 1}}{k_1^2 + k_2^2} \quad (35)$$

and

$$m_2 = \frac{-k_2 \pm k_1 \sqrt{(k_1^2 + k_2^2)(2c_1 s + c_2) - 1}}{k_1^2 + k_2^2} \quad (36)$$

This completes the proof.

3.3. N − Constant curves with quasi frame

Definition 3.13. Suppose, a regular unit speed curve in $\mathbb{E}^3$ is denoted by $\gamma : I \subset \mathbb{R} \rightarrow \mathbb{E}^3$. If the length of the normal component of the curve $\|\gamma^N\|$ is constant, then the curve is called N − constant curve [2]. Especially, if $\|\gamma^N\| = 0$, then the curve is called as N−constant curve of first kind, if not, second kind.

So, for a N – constant curve γ in $\mathbb{E}^3$

$$\left\| \gamma^N(s) \right\|^2 = m_1^2(s) + m_2^2(s) \quad (37)$$

becomes a constant function. Therefore, by differentiation

$$m_1' m_1 + m_2' m_2 = 0 \quad (38)$$

For the N − constant curves of first kind we give the following result.

Lemma 3.14. : Let $\gamma : I \rightarrow \mathbb{E}^3$ be a unit speed regular curve according to q − frame in Euclidean 3 − space. If it is congruent to N − constant curve, then the following equation system is hold:

$$m_0' - k_1 m_1 - k_2 m_2 = 1,$$
$$m_1' + k_1 m_0 - k_3 m_2 = 0,$$
$$m_2' + k_2 m_0 + k_3 m_1 = 0, \quad (39)$$
$$m_1' m_1 + m_2' m_2 = 0.$$

Theorem 3.15. Let γ be a N − constant curve of first kind. Then it corresponds to a straight line.

Proof. Let γ be a N − constant curve of first kind. Then

$$m_1^2 + m_2^2 = 0$$

Hence, we write $m_1 = 0$, $m_2 = 0$. The position vector is given by $\gamma(s) = m_0 t(s)$. Since the curve is along to its tangent, it corresponds to a straight line.

Proposition 3.16. Let $\gamma : I \rightarrow \mathbb{E}^3$ be a unit speed regular curve with respect to quasi frame in $\mathbb{E}^3$. Then it is congruent to N − constant curve of second kind if and only if it is a T − constant curve of first kind or the position vector is given by

$$\gamma(s) = (s + b)t(s) + \frac{k_1^2 + k_2^2}{k_1' k_2 - k_1 k_2' - (k_1^2 + k_2^2)k_3} n_q(s) + \frac{-k_1(k_1^2 + k_2^2)}{k_2(k_1' k_2 - k_1 k_2') - (k_1^2 + k_2^2)k_3} b_q(s)$$

Proof. Let γ be a N − constant curve of second kind. Then the equation system (39) is satisfied. Multiplying the second equation of (39) with m_1 and multiplying the third equation of (39) with m_2, the sum of these relations are

$$m_0(k_1 m_1 + k_2 m_2) = 1$$

Using the first equation of (39), we obtain $m_0 (m_0' - 1) = 0$. If $m_0 = 0$, then it corresponds to a T − constant curve of first kind.

If $m_0' = 1$, then putting $m_0 = s + b$ into (39) we get

$$k_1 m_1 + k_2 m_2 = 0$$

Substituting $m_2 = \frac{-k_1 m_1}{k_2}$ into the second equation of (39), we write

$$m_1' = \frac{-k_1 k_3}{k_2} m_1 - k_1(s + b) \quad (40)$$

Also, substituting $m_2 = \frac{-k_1 m_1}{k_2}$ into the third equation of (39), we write

$$\left[\frac{-k_1 m_1}{k_2} \right]' + k_2(s + b) + k_3 m_1 = 0$$

$$\left[\frac{-k_1}{k_2} \right]' m_1 - \frac{k_1}{k_2} m_1' + k_2(s + b) + k_3 m_1 = 0 \quad (41)$$

Combining (40) and (41), we yield

$$m_1 = \frac{k_1^2 + k_2^2}{k_1' k_2 - k_1 k_2' - (k_1^2 + k_2^2)k_3}$$

Since $m_1 = -\frac{k_1}{k_2} m_1$, then

$$m_2 = \frac{-k_1(k_1^2 + k_2^2)}{k_2(k_1' k_2 - k_1 k_2' - (k_1^2 + k_2^2)k_3)}$$

This completes the proof.

REFERENCES

[1] Chen BY. Constant ratio Hypersurfaces. Soochow J. Math. 2001; 28: 353-362.
[2] Chen BY. Convolution of Riemannian manifolds and its applications. Bull. Aust. Math. Soc. 2002; 66: 177-191.

[3]   Chen BY. When does the position vector of a space curve always lies in its rectifying plane? Amer. Math. Monthly 2003; 110: 147-152.

[4]   Chen BY. More on convolution of Riemannian manifolds. Beitrage Algebra und Geom. 2003; 44: 9-24.

[5]   Chen BY and Dillen F. Rectifying curves as centrodes and extremal curves. Bull. Inst. Math. Acedemia Sinica 2005; 33: 77-90.

[6]   Ekici C., Göksel M. B., Dede M., Smarandache curves according to q − frame in Minkowski 3 − space, Conference Proceedings of Science and Technology, 2019; 2(2): 110 118.

[7]   Elshenhab A. M., Moazz O., Dassios I., Elsharkawy A., Motion along a space curve with a quasi frame in Euclidean 3 − space: Acceleration and Jerk, Symetry 2022; 14: 1610.

[8]   Ezentaş R and Türkay S. Helical versus of rectifying curves in Lorentzian spaces. Dumlıpınar Univ. Fen Bilim. Esti. Dergisi 2004; 6: 239-244.

[9]   Gray A. Modern differential geometry of curves and surface. USA: CRS Press Inc., 1993.

[10] Gürpınar S, Arslan K, Öztürk G. A Characterization of Constant − ratio Curves in Euclidean 3 − space E3. Acta Universtatis Apulensis, Mathematics and Informatics. 2015; 44: 39-51.

[11] Ilarslan K, Nesovic E and Petrovic TM. Some characterization of rectifying curves in the Minkowski 3 − space. Novi Sad J. Math. 2003; 32: 23-32.

[12] Ilarslan K and Nesovic E. On rectifying curves as centrodes and extremal curves in the Minkowski 3 − space E3 1. Novi. Sad. J. Math. 2007; 37: 53-64.

[13] Ilarslan K and Nesovic E. Some characterization of rectifying curves in the Euclidean space E4. Turk. J. Math. 2008; 32: 21-30.

[14] Ilarslan K and Nesovic E. Some characterization of null, pseudo-null and partially null rectifying curves in Minkowski space − time. Taiwanese J. Math. 2008; 12: 1035-1044.

[15] Klein F. and Lie S. Uber diejenigen ebenenen kurven welche durch ein geschlossenes system von einfach un endlich vielen vartauschbaren linearen Transformationen in sich ¨ ubergehen. Math. Ann. 1871; 4: 50-84.

Türk Doğa ve Fen Dergisi
Turkish Journal of Nature and Science
www.dergipark.gov.tr/tdfd

Hermite-Hadamard Inequalities for a New Class of Generalized-(s,m) via Fractional Integral

Erdal GÜL¹* (ID) **, Ahmet Ocak AKDEMİR²** (ID) **, Abdüllatif YALÇIN³** (ID)

¹⁻³ Yıldız Technical University, Faculty of Arts and Science Department of Mathematics, Istanbul, Turkey
² Ağrı İbrahim Çeçen University, Faculty of Science and Letters, Department of Mathematics, Ağrı, Turkey
Erdal GÜL ORCID No: 0000-0003-0626-0148
Ahmet Ocak AKDEMİR ORCID No: 0000-0003-2466-0508
Abdüllatif YALÇIN ORCID No: 0009-0003-1233-7540

Corresponding author: abdullatif.yalcin@std.yildiz.edu.tr

Abstract: This paper defines a new generalized (s,m)-σ convex function using the σ convex functions and provides some applications and exact results for this kind of functions. The new definition of the (s,m)-σ convex function class is used to obtain the Hermite Hadamard type integral inequalities existing in the literature, and new integral inequalities are obtained with the help of the σ-Riemann-Liouville fractional integral. Additionally, a new Hermite-Hadamard type fractional integral inequality is constructed using the σ-Riemann-Liouville fractional integral.

Genelleştirilmiş (s,m) Fonksiyonların Yeni Bir Sınıfı İçin Kesirli İntegral Yoluyla Hermite-Hadamard Eşitsizlikler

Öz: Bu makale, σ konveks fonksiyon sınıfını kullanarak yeni bir genelleştirilmiş (s,m)-σ konveks fonksiyonu tanımlamakta ve bu tür fonksiyonlar için bazı uygulamalar ve kesin sonuçlar sunmaktadır. Literatürde var olan Hermite Hadamard tipi integral eşitsizliklerini elde etmek için (s,m)-σ konveks fonksiyon sınıfının yeni tanımından yararlanılmış ve σ-Riemann-Liouville kesirli integrali yardımıyla yeni integral eşitsizlikleri elde edilmiştir. Ek olarak, σ-Riemann-Liouville kesirli integrali kullanılarak yeni bir Hermite-Hadamard tipi kesirli integral eşitsizliği oluşturuldu.

1. INTRODUCTION

Mathematics is a tool that serves both pure and applied sciences. Its history is as old as human history and it sheds light on how to express and solve problems. Mathematics employs various concepts and their relations for solving the problems. It defines spaces and algebraic structures built on spaces, creating structures that contribute to human life and nature. The concept of function is

fundamental in mathematics, and researchers have focused on developing new function classes and classifying the space of functions. One of this classes of functions is the convex function, which has applications in statistics, inequality theory, convex programming, and numerical analysis. A convex function is defined as a function where the line segment between any two points on the graph of the function lies above or on the graph. This definition ensures that the function is always 'curving upwards' and has no local maxima. The use of convex functions in various fields is due to their unique properties, such as their ability to model optimization problems and their connection to the theory of convex sets.

2. MATERIAL AND METHOD

Definition 2.1: [14,15] Let $\mathcal{H}$ be an interval in $\mathbb{R}$. Then, $\Omega: \mathcal{H} \to \mathbb{R}, \emptyset \neq \mathcal{H} \subseteq \mathbb{R}$ is said to be convex if

$$\Omega(\xi u + (1 - \xi)v) \leq \xi \Omega(u) + (1 - \xi)\Omega(v)$$

for all $u, v \in \mathcal{H}$ and $\xi \in [0, 1]$.

Definition 2.2: [6] For some fixed $s \in (0, 1]$ and $m \in [0, 1]$ a mapping $\Omega : \mathcal{H} \subset [0, \infty) \to \mathbb{R}$ is said to be $(s, m)-$ convex in the second sense on $\mathcal{H}$ if

$$\Omega(\xi u + m(1 - \xi)v) \leq \xi^s \Omega(u) + m(1 - \xi)^s \Omega(v)$$

holds for all $u, v \in \mathcal{H}$ and $\xi \in [0, 1]$.

Definition 2.3: [13] Let $\mathcal{H}$ be an interval in $\mathbb{R}$. Then, $\Omega: \mathcal{H} \to \mathbb{R}, \emptyset \neq \mathcal{H} \subseteq \mathbb{R}$ is said to be quasi convex if

$$\Omega(\xi u + (1 - \xi)v) \leq sup\{\Omega(u), \Omega(v)\}$$

holds for all $u, v \in \mathcal{H}$ and $\xi \in [0, 1]$.

The theory of convexity is important in various fields of pure and applied sciences. Therefore, the classical concepts of convex sets and convex functions have been extended in different directions. For further information, we refer [1,2,14]. The theory of convexity has also attracted many researchers due to its close relation with the theory of inequalities. The concept of convex functions can be used to derive many well-known inequalities. For further details, please refer to [3,15]. One of the most studied results among these inequalities is the Hermite-Hadamard inequality, which provides a necessary and sufficient condition for a function to be convex. The inequality reads as follows:

Definition 2.4: Let $\Omega: \mathcal{H} \subseteq \mathbb{R} \to \mathbb{R}$ be a convex mapping defined on the interval $\mathcal{H}$ of real numbers and $u, v \in \mathcal{H}$, with $u < v$. Then, one has

$$\Omega\left(\frac{u + v}{2}\right) \leq \frac{1}{v - u}\int_u^v \Omega(x)\, dx$$
$$\leq \frac{\Omega(u) + \Omega(v)}{2}. \tag{1}$$

This double inequality is called the Hermite-Hadamard inequality.

This fragment of text discusses the Hermite-Hadamard inequality for convex functions and introduces a new class of convex sets and functions called σ-convex sets and $\sigma -$ convex functions, respectively. The new class of convex sets and functions was introduced by Wu et al. in [4]. The definitions of σ-convex sets and σ-convex functions are explained as the followings:

Definition 2.5: A function $\Omega: \mathcal{H} \to \mathbb{R}$ is said to be σ-convex function with respect to strictly monotonic continuous function σ if

$$\Omega\left(\Psi_{[\sigma]}(u, v)\right) = \xi \Omega(v) + (1 - \xi)\Omega(u) \ \ \forall u, v \in \mathcal{H},$$
$$\xi \in [0, 1].$$

Definition 2.6: A set $\mathcal{H} \subseteq \mathbb{R}$ is said to be σ–convex set with respect to strictly monotonic continuous function σ if

$$\Psi_{[\sigma]}(u, v) = \sigma^{-1}\left(\xi \sigma(v) + (1 - \xi)\sigma(u)\right) \in \mathcal{H} \ \ \forall u, v$$
$$\in \mathcal{H}, \xi \in [0, 1].$$

Note that the function Ψ is called strictly σ-convex on $\mathcal{H}$ if the above inequality is true as a strict inequality for each distinct u and $v \in \mathcal{H}$ and for each $\xi \in (0, 1)$.

Fractional analysis has been known since ancient times. However, it has recently become a more popular subject in mathematical analysis and applied mathematics. The question of whether a solution exists when the order is fractional in a differential equation has led to the development of many derivative and integral operators. By defining the derivative and integral operators in fractional order, researchers have proposed more effective solutions for physical phenomena using new operators with general and strong kernels. This has provided mathematics and applied sciences with several operators that differ in terms of locality and singularity, as well as generalized operators with memory effect properties. The initial inquiry into the impact of a fractional order in a differential equation has now developed into the challenge of elucidating physical phenomena and identifying the most efficient fractional operators to offer practical solutions to real-world issues. Introducing fractional derivative and integral operators have made significant contributions to fractional analysis and these new operators have been effectively used in various fields by numerous researchers (see [17-18]).

The definition of the Riemann-Liouville fractional integral, as given in the literature, is:

Definition 2.7: Let $\Omega \in \mathcal{L}^1(u, v)$. The Riemann Liouville integrals $I_{u^+}^\alpha \Omega$ and $I_{v^-}^\alpha \Omega$ of order $\alpha > 0$ with $a \geq 0$ are defined by

$$I_{u^+}^\alpha \Omega(x) = \frac{1}{\Gamma(\alpha)}\int_u^x \Omega(\xi)(x - \xi)^{\alpha-1} dt, \quad x > u$$

and

$$I_{v^-}^\alpha \Omega(x) = \frac{1}{\Gamma(\alpha)}\int_x^v \Omega(\xi)(\xi - x)^{\alpha-1} dt, \quad v > x.$$

110

Definition 2.8: Let $(u,v) \subseteq \mathbb{R}$, $\sigma(x)$ be an increasing and positive function on $(u,v]$ and $\sigma'(x)$ be continuous on (u,v). Then, the left-sided and right-sided $\sigma -$ Riemann-Liouville fractional integrals of a function Ω with respect to the function $\sigma(x)$ on $[u,v]$ are respectively defined by [7,8]:

$$I_{u^+}^{\alpha:\varphi}\Omega(x)$$
$$= \frac{1}{\Gamma(\alpha)} \int_u^x \Omega(\xi)\varphi'(\xi) \left(\varphi(x) - \varphi(\xi)\right)^{\alpha-1} dt$$

$$I_{v^-}^{\alpha:\varphi}\Omega(x)$$
$$= \frac{1}{\Gamma(\alpha)} \int_x^v \Omega(\xi)\varphi'(\xi) \left(\varphi(\xi) - \varphi(x)\right)^{\alpha-1} dt, \qquad \alpha > 0.$$

It can be observed that if φ is specialised by $\varphi(x) = x$, then the σ –Riemann-Liouville fractional integral operators are reduced to the classical Riemann-Liouville fractional integral operators.

The fractional Hermite-Hadamard integral inequalities [4,9] are given by:

$$\Omega\left(\frac{u+v}{2}\right) \leq \frac{\Gamma(\alpha+1)}{2(v-u)^\alpha} \left[I_{u^+}^\alpha \Omega(v) + I_{v^-}^\alpha \Omega(u)\right]$$
$$\leq \frac{\Omega(u) + \Omega(v)}{2}.$$

In their recent work, Mohammed et al. [5] utilised this novel convex function for a fractional operator to present the new findings:

Theorem 2.1: Let $\Omega : [u,v] \subseteq \mathbb{R} \to \mathbb{R}$ be an integrable σ-convex function and $\Omega \in \mathcal{L}^1(u,v)$ with $0 \leq u < v$. If the function σ is increasing and positive on $[u,v]$ and $\sigma'(x)$ is continuous on (u,v), then for $\alpha > 0$

$$\Omega\left(\sigma^{-1}\left(\frac{\sigma(u)+\sigma(v)}{2}\right)1\right)$$
$$\leq \frac{\Gamma(\alpha+1)}{2\left(\sigma(v)-\sigma(u)\right)^\alpha} \left[I_{u^+}^{\alpha:\varphi}\Omega(v)\right.$$
$$\left.+ I_{v^-}^{\alpha:\varphi}\Omega(u)\right] \leq \frac{\Omega(u) + \Omega(v)}{2}.$$

Theorem 2.2: Let $\Omega : [u,v] \subseteq \mathbb{R} \to \mathbb{R}$ be an integrable σ-convex function and $\Omega \in \mathcal{L}^1(u,v)$ with $0 \leq u < v$. If the function σ is increasing and positive on $[u,v]$ and $\sigma'(x)$ is continuous on (u,v), then for $\alpha > 0$, we have

$$\Omega\left(\sigma^{-1}\left(\frac{\varphi(u)+\varphi(v)}{2}\right)\right)$$
$$\leq \frac{2^{\alpha-1}\Gamma(\alpha+1)}{\left(\sigma(v)-\sigma(u)\right)^\alpha} \left[I_{\sigma^{-1}\left(\frac{\varphi(u)+\varphi(v)}{2}\right)^+}^{\alpha:\varphi}\Omega(v)\right.$$
$$\left.+ I_{\sigma^{-1}\left(\frac{\varphi(u)+\varphi(v)}{2}\right)^-}^{\alpha:\varphi}\Omega(u)\right] \leq \frac{\Omega(u) + \Omega(v)}{2}.$$

3. RESULTS

Definition 3.1: For some fixed $s \in (0,1]$ and $m \in [0,1]$ a mapping $\Omega : \mathcal{H} \subset [0,b] \to \mathbb{R}^\alpha$ with $b > 0$ is said to be generalized $\sigma - (s,m)-$ convex if

$$\Psi_{[\sigma]}(x,y) - (s,m)$$
$$= \Omega\left(\sigma^{-1}(\xi\sigma(x)\right.$$
$$\left.+ m(1-\xi)\sigma(y))\right) \qquad (2)$$
$$\leq \xi^{\alpha s}\Omega(x)$$
$$+ m^\alpha(1-\xi)^{\alpha s}\Omega(y)$$

holds for all $x,y \in \mathcal{H}$ and $\xi \in [0,1]$.

Remark 3.1: If we take $\alpha = 1$ and $\sigma^{-1}(x) = x$ then, we get Definition 2.2 in [6].

Remark 3.2: If we take $\alpha = 1$, $s = 1$ and $m = 1$ then, we get Definition 2.5 in [4].

Remark 3.3: If we take $\alpha = s = m = 1$ and $\sigma(x) = x$ then, we get the concept of classical convex functions.

Moreover, if we take $\xi = \frac{1}{2}$ in (2), then the generalized $\Psi_{[\sigma]}(x,y) - (s,m)$ convex functions become Jensen-type generalized $\sigma - (s,m)$ convex functions as follows:

$$\Omega\left(\sigma^{-1}\left(\frac{\varphi(x)+m\varphi(y)}{2}\right)\right) \leq \frac{\Omega(x)+m^\alpha \Omega(y)}{2^{s\alpha}}.$$

For all $x,y \in \mathcal{H}$ and $\xi \in [0,1]$ and for some fixed $s \in (0,1]$ and $m \in [0,1]$.

Some special cases are obtained as follows.

Case-1
If we take $\sigma^{-1}(x) = \ln x$, then we get geometrically (s,m)-convex function as in [10]

$$\Omega(x^t y^{1-t}) \leq \xi^s \Omega(x) + m(1-\xi)^s \Omega(y)$$
holds for all $x,y \in \mathcal{H}$ and $t \in [0,1]$.

Cese-2
If we take $\sigma^{-1}(x) = \frac{1}{x}$, then we get harmonically (s,m)-convex function as in [11]

$$\Omega\left(\frac{mxy}{mtx+(1-\xi)y}\right) \leq \xi^s \Omega(x) + m(1-\xi)^s \Omega(y)$$

holds for all $x,y \in \mathcal{H}$ and $\xi \in [0,1]$.

Proposition 3.1: For $s \in (0,1]$ and $m \in [0,1]$ if $\Omega, \mathcal{L} : \mathcal{H} \to \mathbb{R}^\alpha$ are generalized $\sigma - (s,m) -$ convex functions, then we have the following statements:

$\Omega + \mathcal{L}$ is a generalized $\sigma - (s,m)-$ convex functions.
$\zeta^\alpha \Omega$ is a generalized $\sigma - (s,m)-$ convex functions.

111

Proof: Since Ω and $\mathcal{L}$ are generalized $-(s,m)-$ convex functions on $\mathcal{H}$ and $\xi \in [0,1]$, we have

$$(\Omega + \mathcal{L})\left(\sigma^{-1}\big(\xi\sigma(x) + m(1-\xi)\sigma(y)\big)\right)$$
$$= \Omega\left(\sigma^{-1}\big(\xi\sigma(x) + m(1-\xi)\sigma(y)\big)\right)$$
$$+ \mathcal{L}\left(\sigma^{-1}\big(\xi\sigma(x) + m(1-\xi)\sigma(y)\big)\right)$$
$$\leq \xi^{\alpha s}\Omega(x) + m^{\alpha}(1-\xi)^{\alpha s}\Omega(y)$$
$$+ \xi^{\alpha s}\mathcal{L}(x) + m^{\alpha}(1-\xi)^{\alpha s}\mathcal{L}(y)$$
$$= \xi^{\alpha s}(\Omega + \mathcal{L})(x)$$
$$+ m^{\alpha}(1-\xi)^{\alpha s}(\Omega + \mathcal{L})(y)$$

Hence, $\Omega + \mathcal{L}$ is a generalized $-(s,m)-$ convex functions on $\mathcal{H}$.
Since, Ω and $\mathcal{L}$ are generalized $-(s,m)-$ convex functions on $\mathcal{H}$ and $\xi \in [0,1]$, $\zeta \in \mathbb{R}_+$, we have

$$\zeta^{\alpha}\Omega\left(\sigma^{-1}\big(\xi\sigma(x) + m(1-\xi)\sigma(y)\big)\right)$$
$$\leq \zeta^{\alpha}[\,\xi^{\alpha s}f(x) + m^{\alpha}(1-\xi)^{\alpha s}f(y)]$$
$$= \xi^{\alpha s}(\zeta^{\alpha}\Omega)(x) + (\zeta^{\alpha}\Omega)(y)$$

and, so $\zeta^{\alpha}\Omega$ is a generalized $-(s,m)-$ convex functions on $\mathcal{H}$.

3.1 New Results on Generalized $\sigma - (s,m)$-Convexity

This section is devoted to establish some generalized Hermite– Hadamard type fractional integral inequalities via generalized $\sigma - (s,m)$ –convex.

Theorem 3.1: Let $\Omega : [u,v] \subseteq \mathbb{R} \to \mathbb{R}$ be an integrable $\sigma - (s,m)$-convex function and $\Omega \in \mathcal{L}^1(u,v)$ with $0 \leq u < v$, $m \in (0,1]$. If the function σ is increasing and positive on $[u,v]$ and $\varphi'(x)$ is continuous on (u,v), then for $\alpha > 0$, we have

$$\Omega\left(\sigma^{-1}\left(\frac{\sigma(u) + m\sigma(v)}{2}\right)\right)$$
$$\leq \frac{1}{2^{\alpha s}\big(\sigma(u) - m\sigma(v)\big)}\left[\int_{mv}^{u}\Omega(x)\,\sigma'(x)dx\right.$$
$$\left. + m^{\alpha}\int_{v}^{mu}\Omega(x)\,\sigma'(x)dx\right]$$
$$\leq \frac{[\Omega(u) + \Omega(v) + m^{\alpha}(\Omega(u/m) + \Omega(v/m))]}{2^{\alpha s}(\alpha s + 1)} \quad (3)$$

Proof: To prove the first inequality of (3), assume that Ω is a $\sigma - (s,m)$ convex function

$$\Omega\left(\sigma^{-1}\big(\xi\sigma(x) + m(1-\xi)\sigma(y)\big)\right)$$
$$\leq \xi^{\alpha s}\Omega(x) + m^{\alpha}(1-\xi)^{\alpha s}\Omega(y).$$

If we take $\xi = \frac{1}{2}$, we obtain

$$\Omega\left(\sigma^{-1}\left(\frac{\sigma(x) + m\sigma(y)}{2}\right)\right)$$
$$\leq \frac{\Omega(x) + m^{\alpha}\Omega(y)}{2^{s\alpha}}. \quad (4)$$

Let us set $x = \sigma^{-1}\big(\xi\sigma(u) + m(1-\xi)\sigma(v)\big)$ and $y = \sigma^{-1}\big(\xi\sigma(v) + m(1-\xi)\sigma(u)\big)$ in (4), one has

$$2^{\alpha s}\Omega\left(\sigma^{-1}\left(\frac{\sigma(u) + m\sigma(v)}{2}\right)\right)$$
$$\leq \Omega\left(\sigma^{-1}\big(\xi\sigma(u) + m(1-\xi)\sigma(v)\big)\right)$$
$$+ m^{\alpha}\Omega\big(\sigma^{-1}\big(\xi\sigma(v)$$
$$+ m(1-\xi)\sigma(u)\big)\big).$$

Integrating this inequality with respect to ξ over $[0,1]$, we have

$$\Omega\left(\sigma^{-1}\left(\frac{\sigma(u) + m\sigma(v)}{2}\right)\right)$$
$$\leq \int_{0}^{1}\Omega\left(\sigma^{-1}\big(\xi\sigma(u) + m(1-\xi)\sigma(v)\big)\right)d\xi$$
$$+ m^{\alpha}\int_{0}^{1}\Omega\big(\sigma^{-1}\big(\xi\sigma(v)$$
$$+ m(1-\xi)\sigma(u)\big)\big)d\xi$$
$$= \frac{1}{2^{\alpha s}}\left[\frac{1}{\sigma(u) - m\sigma(v)}\int_{mv}^{u}\Omega(x)\,\sigma'(x)dx\right.$$
$$\left. + \frac{m^{\alpha}}{m\sigma(u) - \sigma(v)}\int_{v}^{mu}\Omega(x)\,\sigma'(x)dx\right]. \quad (5)$$

The first inequality has been proved. To prove the second inequality, we will use the definition of the $\sigma - (s,m)$ convex function as follow:

$$\Omega\left(\sigma^{-1}\big(\xi\sigma(u) + m(1-\xi)\sigma(v)\big)\right)$$
$$\leq \xi^{\alpha s}\Omega(u) + m^{\alpha}(1-\xi)^{\alpha s}\Omega(v/m)$$
and
$$\Omega\left(\sigma^{-1}\big(\xi\sigma(v) + m(1-\xi)\sigma(u)\big)\right)$$
$$\leq \xi^{\alpha s}\Omega(v) + m^{\alpha}(1-\xi)^{\alpha s}\Omega\left(\frac{u}{m}\right).$$

By addition, we have

$$\Omega\left(\sigma^{-1}\big(\xi\sigma(u) + m(1-\xi)\sigma(v)\big)\right)$$
$$+ \Omega\left(\sigma^{-1}\big(\xi\sigma(v) + m(1-\xi)\sigma(u)\big)\right)$$
$$\leq [\Omega(u) + \Omega(v)]\,\xi^{\alpha s}$$
$$+ \left[\Omega\left(\frac{u}{m}\right) + \Omega\left(\frac{v}{m}\right)\right]m^{\alpha}(1-\xi)^{\alpha s}.$$

Integrating this inequality with respect to ξ over $[0,1]$, we have

$$\left[\frac{1}{\sigma(u) - m\sigma(v)}\int_{mv}^{u}\Omega(x)\,\sigma'(x)dx\right.$$
$$\left. + \frac{m^{\alpha}}{m\sigma(u) - \sigma(v)}\int_{v}^{mu}\Omega(x)\,\sigma'(x)dx\right]$$
$$\leq [\Omega(u) + \Omega(v)]\frac{1}{\alpha s + 1}$$
$$+ \left[\Omega\left(\frac{u}{m}\right) + \Omega\left(\frac{v}{m}\right)\right]\frac{m^{\alpha}}{\alpha s + 1}. \quad (6)$$

112

By combining the last two inequalities (5) and (6), the desired result is obtained as:

$$\Omega\left(\sigma^{-1}\left(\frac{\sigma(u)+m\sigma(v)}{2}\right)\right)$$

$$\leq \frac{1}{2^{\alpha s}}\left[\frac{1}{\sigma(u)-m\sigma(v)}\int_{mv}^{u}\Omega(x)\,\sigma'(x)dx\right.$$

$$\left.+\frac{m^{\alpha}}{m\sigma(u)-\sigma(v)}\int_{v}^{mu}\Omega(x)\,\sigma'(x)dx\right]$$

$$\leq[\Omega(u)+\Omega(v)]\frac{1}{\alpha s+1}+\left[\Omega\left(\frac{u}{m}\right)+\Omega\left(\frac{v}{m}\right)\right]\frac{m^{\alpha}}{\alpha s+1}.$$

This completes the proof.

Corollary 3.1: If we take $m = 1$ and $\alpha = 1$, then we obtain Theorem 5 in [12].

Corollary 3.2: If we take $\sigma(x) = x$, $s = m = \alpha = 1$, then inequality (3) reduces to inequality (1).

Theorem 3.2: Let $\Omega:[u,v]\subseteq\mathbb{R}\to\mathbb{R}$ be an integrable $\sigma-(s,m)$-convex function and $\Omega\in\mathcal{L}^1(u,v)$ with $0\leq u<v$, $m\in(0,1]$. If the function σ is increasing and positive on $[u,v]$ and $\sigma'(x)$ is continuous on (u,v), then for $\alpha > 0$, we have

$$\Omega\left(\sigma^{-1}\left(\frac{\sigma(u)+m\sigma(v)}{2}\right)\right)$$

$$\leq\frac{\Gamma(\alpha+1)}{2^{\alpha s}}\left[\frac{1}{(m\sigma(v)-\sigma(u))^{\alpha}}I_{(u)^+}^{\alpha:\varphi}\Omega(mv)\right.$$

$$\left.+\frac{1}{(\sigma(v)-m\sigma(u))^{\alpha}}I_{(v)^-}^{\alpha:\varphi}\Omega(mu)\right]$$

$$\leq\frac{[\Omega(u)+\Omega(v)]}{2^{\alpha s}(\alpha s+\alpha)}$$

$$+\frac{\left[\Omega\left(\frac{u}{m}\right)+\Omega\left(\frac{v}{m}\right)\right]m^{\alpha}}{2^{\alpha s}}\frac{\Gamma(\alpha+1)\Gamma(\alpha s+1)}{\Gamma(\alpha+\alpha s+1)}. \quad (7)$$

Proof: To prove the first inequality of (7), assume that Ω is $\sigma-(s,m)$ convex function, then we can write

$$\Omega\left(\sigma^{-1}\left(\xi\sigma(x)+m(1-\xi)\sigma(y)\right)\right)$$
$$\leq\xi^{\alpha s}\Omega(x)+m^{\alpha}(1-\xi)^{\alpha s}\Omega(y).$$

If we take $\xi=\frac{1}{2}$, we obtain

$$\Omega\left(\sigma^{-1}\left(\frac{\sigma(x)+m\sigma(y)}{2}\right)\right) \quad (8)$$

$$\leq\frac{\Omega(x)+m^{\alpha}\Omega(y)}{2^{s\alpha}}.$$

Substituting $x=\sigma^{-1}\left(\xi\sigma(u)+m(1-\xi)\sigma(v)\right)$ and $y=\sigma^{-1}\left(\xi\sigma(v)+m(1-\xi)\sigma(u)\right)$ into (8), we get

$$2^{\alpha s}\Omega\left(\sigma^{-1}\left(\frac{\sigma(u)+m\sigma(v)}{2}\right)\right)$$

$$\leq\Omega\left(\sigma^{-1}(\xi\sigma(u)\right.$$
$$+m(1-\xi)\sigma(v))\big)$$
$$+m^{\alpha}\Omega\left(\sigma^{-1}(\xi\sigma(v)\right.$$
$$+m(1-\xi)\sigma(u))\big). \quad (9)$$

Multiplying both sides of (9) by $\xi^{\alpha-1}$, then integrating the resulting inequality with respect to t over $[0,1]$, we get

$$\frac{2^{\alpha s}}{\alpha}\Omega\left(\sigma^{-1}\left(\frac{\sigma(u)+m\sigma(v)}{2}\right)\right)$$

$$\leq\int_{0}^{1}\xi^{\alpha-1}\Omega\left(\sigma^{-1}(\xi\sigma(u)\right.$$
$$+m(1-\xi)\sigma(v))\big)d\xi$$
$$+\int_{0}^{1}\Omega\left(\sigma^{-1}(\xi\sigma(v)\right.$$
$$+m(1-\xi)\sigma(u))\big)\xi^{\alpha-1}d\xi.$$

By changing the variables, $\lambda=\sigma^{-1}\left(\xi\sigma(u)+m(1-\xi)\sigma(v)\right)$ and $\eta=\sigma^{-1}\left(\xi\sigma(v)+m(1-\xi)\sigma(u)\right)$, then the last inequality becomes

$$\Omega\left(\sigma^{-1}\left(\frac{\sigma(u)+m\sigma(v)}{2}\right)\right)$$

$$\leq\frac{1}{(m\sigma(v)-\sigma(u))^{\alpha}}\int_{u}^{mv}\Omega(\lambda)\varphi'(\lambda)\left(m\varphi(v)\right.$$
$$-\varphi(\lambda))^{\alpha-1}d\lambda$$
$$+\frac{1}{(\sigma(v)-m\sigma(u))^{\alpha}}\int_{mu}^{v}\Omega(\eta)\varphi'(\eta)\left(\varphi(\eta)\right.$$
$$-m\varphi(u))^{\alpha-1}d\eta$$

$$=\frac{\Gamma(\alpha+1)}{2^{\alpha s}}\left[\frac{1}{(m\sigma(v)-\sigma(u))^{\alpha}}I_{(u)^+}^{\alpha:\varphi}\Omega(mv)\right.$$

$$+\frac{1}{(\sigma(v)-m\sigma(u))^{\alpha}}I_{(v)^-}^{\alpha:\varphi}\Omega(mu)\bigg]. \quad (10)$$

In this way, the first inequality is proved.
To prove the second inequality, we use the definition of the $\sigma-(s,m)$ convex function as:

$$\Omega\left(\sigma^{-1}\left(\xi\sigma(u)+m(1-\xi)\sigma(v)\right)\right)$$
$$\leq\xi^{\alpha s}\Omega(u)+m^{\alpha}(1-\xi)^{\alpha s}\Omega(v/m)$$
and
$$\Omega\left(\sigma^{-1}\left(\xi\sigma(v)+m(1-\xi)\sigma(u)\right)\right)$$
$$\leq\xi^{\alpha s}\Omega(v)+m^{\alpha}(1-\xi)^{\alpha s}\Omega\left(\frac{u}{m}\right).$$

By addition, we have

113

$$\Omega\left(\sigma^{-1}\big(\xi\sigma(u) + m(1-\xi)\sigma(v)\big)\right)$$
$$+ \Omega\left(\sigma^{-1}\big(\xi\sigma(v)\right.$$
$$+ m(1-\xi)\sigma(u)\big)\right)$$
$$\leq [\Omega(u) + \Omega(v)]\,\xi^{\propto s}$$
$$+ \left[\Omega\left(\frac{u}{m}\right) + \Omega\left(\frac{v}{m}\right)\right] m^{\propto}(1 \qquad (11)$$
$$- \xi)^{\propto s}.$$

Multiplying both sides of (11) by $\xi^{\alpha-1}$, then integrating the resulting inequality with respect to ξ over $[0,1]$, we can obtain

$$\int_0^1 \xi^{\alpha-1}\Omega\left(\sigma^{-1}\big(\xi\sigma(u) + m(1-\xi)\sigma(v)\big)\right)d\xi$$
$$+ \int_0^1 \Omega\left(\sigma^{-1}\big(\xi\sigma(v)\right.$$
$$+ m(1-\xi)\sigma(u)\big)\right)\xi^{\alpha-1}d\xi$$
$$\leq \int_0^1 [\Omega(u) + \Omega(v)]\,\xi^{\propto s+\alpha-1}d\xi$$
$$+ \int_0^1 [\Omega(u/m) + \Omega(v/m)]m^{\propto}(1$$
$$- \xi)^{\propto s}d\xi.$$

Hence,

$$\frac{\Gamma(\alpha + 1)}{2^{\propto s}}\left[\frac{1}{\big(m\sigma(v) - \sigma(u)\big)^{\alpha}}I_{(u)^+}^{\alpha:\varphi}\Omega(v)\right.$$
$$\left. + \frac{1}{\big(\sigma(v) - m\sigma(u)\big)^{\alpha}}I_{(v)^-}^{\alpha:\varphi}\Omega(u)\right]$$
$$\leq \frac{[\Omega(u) + \Omega(v)]}{2^{\propto s}(\propto s + \alpha)}$$
$$+ \frac{\left[\Omega\left(\frac{u}{m}\right) + \Omega\left(\frac{v}{m}\right)\right]m^{\propto}}{2^{\propto s}}\frac{\Gamma(\alpha + 1)\Gamma(\propto s + 1)}{\Gamma(\alpha+\propto s + 1)}.$$

This completes the proof.

Corollary 3.3: If we take $m = 1$ and $\propto = 1$, then we obtain Theorem 8 in [12].

Corollary 3.4: If we take $\sigma(x) = x$, $m = 1$ and $\alpha = \propto = 1$, then we get the classical Hermite–Hadamard inequality under s-convex function proved by Dragomir and Fitzpatrick [16].

Corollary 3.5: If we take $\sigma(x) = x$, $s = \alpha = m = \propto = 1$, then inequality (7) reduces to inequality (1).

4. DISCUSSION AND CONCLUSION

This paper introduces a new class of generalized $(s,m) - \sigma$ convex functions, extending the concept of σ-convexity within the framework of fractional calculus. By employing the σ-Riemann-Liouville fractional integral, we derived novel Hermite-Hadamard type inequalities, which generalize existing results and introduce new fractional inequalities. These findings provide valuable insights into the relationship between convexity and fractional operators. The flexibility of the new $(s,m) - \sigma$ convex functions enables further exploration in fractional calculus, particularly with different fractional operators. Future research could investigate the extension of these results to other operators, such as the Atangana-Baleanu integral, expanding the applications of these inequalities. In conclusion, the results obtained here represent a meaningful contribution to fractional analysis and its applications, offering a foundation for further studies in this field.

REFERENCES

[1] Anderson G.D, Vamanamurthy M.K, Vuorinen M. Generalized convexity and inequalities. Journal of Mathematical Analysis and Applications. 2007; 335(2), 1294–1308.

[2] Youness EA. E-convex sets, E-convex functions and E-convex programming. Journal of Optimization Theory and Applications. 1999; 102(2), 439–450.

[3] Du TS, Li YJ, Yang ZQ. A generalization of Simpson's inequality via differentiable mapping using extended (s, m)-convex functions. Applied Mathematics and Computation. 2017; 293, 358–369.

[4] Wu S, Awan MU, Noor MA, Iftikhar K. On a new class of convex functions and integral inequalities. Journal of Inequalities and Applications. 2019; 131.

[5] Mohammed PO, Abdeljawad T, Zeng S, Kashuri A. Fractional Hermite-Hadamard integral inequalities for a new class of convex functions. Symmetry. 2020; 12, 1485.

[6] Park J. Generalization of Ostrowski–type inequalities for differentiable real (s,m)-convex mappings. Far East Journal of Mathematical Sciences. 2011; 49(2), 157-171.

[7] Kilbas AA, Srivastava HM, Trujillo, JJ. Theory and Applications of Fractional Differential Equations; North-Holland Mathematics Studies, Volume 204. Elsevier Sci. B.V, Amsterdam, The Netherlands; 2006.

[8] Osler TJ. The Fractional Derivative of a Composite Function. SIAM Journal on Mathematical Analysis 1970; 1, 288–293.

[9] Sarikaya MZ, Set E, Yaldiz H, Başak N. Hermite-Hadamard's inequalities for fractional integrals and related fractional inequalities. Mathematical and Computer Modelling. 2013; 57, 2403–2407.

[10] Akdemir AO, Özdemir ME, Ardıç MA, Yalçın A. Some new generalizations for GA -convex functions. Filomat, 2017; 31(4), 1009–1016.

[11] Xu JZ, Raza U. Hermite–Hadamard Inequalities for Harmonic (s, m)-Convex Functions. Mathematical Problems in Engineering, Article ID1470837, 7 pages. 2020.

[12] Sahoo SK, Tariq M, Ahmad, H, Kodamasingh B, Shaikh, AA, Botmart T, El-Shorbagy MA. Some

Novel Fractional Integral Inequalities over a New Class of Generalized Convex Function. Fractal and Fractional, 2022; 6, 42.

[13] Dragomir SS, Pecaric J, Persson LE. Some inequalities of Hadamard type. Soochow Journal of Mathematics. 1995; 21(3), 335–341.

[14] Beckenbach EF. Convex functions. Bulletin of the American Mathematical Society. 1948; 54(5), 439–461.

[15] Mitrinović DS, Lacković IB. Hermite and convexity. Aequationes Mathematicae. 1985; 28(1), 229–232.

[16] Dragomir SS, Fitzpatrick S. The Hadamard inequalities for s-convex functions in the second sense. Demonstratio Mathematica. 1999; 32, 687–696.

[17] Akdemir, AO, Dutta, H, Yüksel, E, Deniz, E. Inequalities for m-Convex Functions via ψ -Caputo Fractional Derivatives. Matematical Methods and Modelling in Applied Sciences, 2020; Vol. 123, 215-224, Springer Nature Switzerland.

[18] Deniz, E, Akdemir, AO, Yüksel, E. New Extensions of Chebyshev-Pòlya-Szegö Type Inequalities via Conformable Integrals. AIMS Mathematics, 2019; 4(6), 1684-1697.

Türk Doğa ve Fen Dergisi
Turkish Journal of Nature and Science
www.dergipark.gov.tr/tdfd

Characterization of a New Type of Topological Sequence Spaces and Some Properties

Gökhan MUMCU[1*] iD **, Ahmet Ocak AKDEMİR[2]** iD **, Yasin ÇINAR[3]** iD

[1] Erzincan Binali Yildirim University, Arts and Sciences Faculty, Mathematics Department, Erzincan, Türkiye
[2] Agri Ibrahim Cecen University, Arts and Sciences Faculty, Mathematics Department, Agri, Türkiye
[3] Batman University, Arts and Sciences Faculty, Mathematics Department, Batman, Türkiye
Gökhan MUMCU ORCID No: 0000-0002-5828-1963
Ahmet Ocak AKDEMİR ORCID No: 0000-0003-2466-0508
Yasin ÇINAR ORCID No: 0009-0006-5942-2445

Corresponding author: gokhanmumcu@outlook.com

Abstract: Examination of spaces in the field of functional analysis, especially revealing their topological and algebraic structures, is very important in terms of forming a basis for studies in the field of pure mathematics and applied sciences. In this context, topology, which was widely used only in the field of geometry at the beginning, gave a solid foundation to the fields in which it was used by causing methodological changes in all branches of mathematics over time. Frechet-Coordinate space (FK space) is a concept that has a functional role in fields such as topological sequence spaces and summability. Topological vector spaces are described as linear spaces defined by a topology that provides continuous vector space operations. If this vector space has a complete metric space structure, it is called Frechet space, and if it has a topology with continuous coordinate functions, it is called Frechet-Coordinate (FK) space. The theory of FK spaces has gained more importance in recent years and has found applications in various fields thanks to the efforts of many researchers. If the topology of an FK space can be derived from the norm, this space is called as a BK space. In this study, $cs_0^\lambda(\Delta)$, $cs^\lambda(\Delta)$, and $bs^\lambda(\Delta)$ difference sequence spaces are defined, and it is revealed that these spaces are BK spaces. In addition, considering the topological properties of these spaces, some spaces that are isomorphic and their duals have been determined.

116

Yeni Tip Topolojik Dizi Uzaylarının Karakterizasyonu ve Bazı Özellikleri

Öz: Fonksiyonel analiz alanında uzayların incelenmesi, özellikle topolojik ve cebirsel yapılarının ortaya konulması, pür matematik ve uygulamalı bilimler alanındaki çalışmalara temel oluşturması açısından oldukça önemlidir. Bu bağlamda başlangıçta sadece geometri alanında yaygın olarak kullanılan topoloji, zamanla matematiğin tüm dallarında metodolojik değişikliklere neden olarak kullanıldığı alanlara sağlam bir temel kazandırmıştır. Frechet-Koordinat uzayı (FK uzayı), topolojik dizi uzayları ve toplanabilirlik gibi alanlarda işlevsel rolü olan bir kavramdır. Topolojik vektör uzayları, sürekli vektör uzayı işlemlerini sağlayan bir topoloji tarafından tanımlanan lineer uzaylar olarak tanımlanır. Bu vektör uzayı tam bir metrik uzay yapısına sahipse Frechet uzayı, sürekli koordinat fonksiyonlarına sahip bir topolojiye sahipse Frechet-Koordinat (FK) uzayı olarak adlandırılır. FK uzayları teorisi, son yıllarda daha da önem kazanmış ve birçok araştırmacının çabaları sayesinde çeşitli alanlarda uygulama alanı bulmuştur. Bir FK uzayının topolojisi normdan türetilebiliyorsa, bu uzaya BK uzayı denir. Bu çalışmada ise $cs_0^\lambda(\Delta)$, $cs^\lambda(\Delta)$ ve $bs^\lambda(\Delta)$ fark dizi uzayları tanımlanmıştır ve bu uzayların BK uzayları olduğu sonucuna ulaşılmıştır. Ayrıca bu uzayların topolojik özellikleri dikkate alınarak bu uzaylara izomorf olan bazı uzaylar ve bu uzayların dualleri belirlenmiştir.

1. INTRODUCTION AND PRELIMINARIES

The main motivation point in the studies conducted in functional analysis and topology is to obtain the expansions and generalizations of spaces, to reveal their various properties and finally to form a new space. Researchers working in this field have used various methods to serve this purpose. By using the domain of an infinite triangular matrices, which is one of these methods, on standard sequence spaces, many new sequence spaces have been created by using Cesaro matrix and Nörlund matrix (see the papers [1], [2]). Sequence spaces are one of the subjects that have been the focus of attention of many researchers due to the topological and algebraic structure they contain. Much researches have been made on the basis of the properties of these sequence spaces and their contribution to the field. Especially in studies in the field of summability theory, topological sequence spaces and difference sequence spaces have contributed to obtaining functional results.

The concept of difference sequence space has been introduced by Kızmaz in [3] as follows:
Suppose that $X = l_\infty, c, c_0$. Then,
$$X(\Delta) = \{x = (x_k) \in w: \Delta x = (\Delta x_k) = (x_k - x_{k+1}) \in X\}$$
will be called the difference sequence space.

In [5], this sequence spaces have been extended by Et as following:
$$X(\Delta^2) = \{x = (x_k) \in w: \Delta^2 x = (\Delta^2 x_k) = (x_k - x_{k+1}) \in X\}.$$

By a similar methodology, the authors have given modification of these spaces for the integer m as:
$$X(\Delta^m) = \{x = (x_k) \in w: \Delta^m x \in X\}$$
where $\Delta^0 x = (x_k \Delta^m x = (\Delta^m x_k - \Delta^m x_{k+1})$ and $\Delta^m x_k = \sum_{v=0}^{m} (-1)^v \binom{m}{v} x_{k+v}$.

On all of these efforts, another motivated generalization has been established by Et and Esi (see [7]) as follows:
Suppose that $v = (v_k)$ is a sequence for complex numbers.
$$X(\Delta_v^m) = \{x = (x_k) \in w: \Delta_v^m x \in X\}$$
where $m, k \in \mathbb{N}$
$$\Delta_v^0 x = v_k x_k \Delta_v^m x = (\Delta_v^m x_k - \Delta_v^m x_{k+1})$$
and
$$\Delta_v^m x_k = \sum_{i=0}^{m} (-1)^i \binom{m}{i} v_{k+i} x_{k+i}.$$

Sequence spaces are an important concept in mathematical analysis and play a methodologically functional key role in the work of many researchers. Although it was known as a branch of topology used only in geometry in the beginning, it has become a structure that contributes to all pure and applied sciences in time. The theory of FK spaces is a structure used in sequence spaces, summability, and matrix transformations as a topological subject. Topological vector spaces are linear spaces with a topology that enables continuous vector space operations. If this vector space has a complete metric space structure, it is called Frechet space, and if it also has a topology with continuous coordinate functions, it is called Frechet-Coordinate space (FK space).

By ω, we mean the vector space containing all real- or complex-valued sequences that are topologized through coordinatewise convergence. Any vector subspace of ω is said to be a sequence space. A sequence space X with a locally convex topology τ is referred to as a K-space if the inclusion mapping $(X, \tau) \to \omega$ is continuous when ω has the topology of coordinatewise convergence. Additionally, if τ is complete and metrizable, (X, τ) is referred to be an FK-space. A BK-space is an FK-space with a normable topology. For further results on these concepts, see the papers [4-14].

2. MATRIX TRANSFORMATIONS

In this section, we will present some lemmas related to the matrix transformations by introducing matrix transformations in the sequence spaces.

Definition 1 *([13]) Suppose that $A = (a_{nk})$ is a infinite matrix with real or complex terms and $x = (x_k)$ is a sequence. For $n \in N$, the following sequences are convergent*
$$(Ax)_n = \sum_{k=0}^{\infty} a_{nk} x_k$$
then, the sequence $((Ax)_n)$ is called the transformation sequence obtained by the matrix A of the sequence (x_k).
In the sequel of the paper, every negative index term such as λ_{-1} and x_{-1} will be assumed to be equal to zero.

Lemma 2.1 *([16]) $A = (a_{nk}) \in (cs_0: l_1)$ if and only if the following condition holds:*
$$\sup_{N,K \in F} \left| \sum_{n \in N} \sum_{k \in K} (a_{nk} - a_{n,k+1}) \right| < \infty. \quad (2.1)$$

Lemma 2.2 *([16]) $A = (a_{nk}) \in (cs: l_1)$ if and only if the following condition holds:*
$$\sup_{N,K \in F} \left| \sum_{n \in N} \sum_{k \in K} (a_{nk} - a_{n,k-1}) \right| < \infty. \quad (2.2)$$

Lemma 2.3 *([16]) $A = (a_{nk}) \in (bs: l_1)$ if and only if the following condition holds:* $\forall k \in \mathbb{N}$
$$\lim_k a_{nk} = 0. \quad (2.3)$$

Lemma 2.4 *([16]) $A = (a_{nk}) \in (cs_0: c)$ if and only if the condition*
$$\sup_n \sum_k |a_{nk} - a_{n,k+1}| < \infty \quad (2.4)$$
will be held and for $\forall k \in \mathbb{N}$, the following limit will be existed
$$\lim_k (a_{nk} - a_{n,k+1}). \quad (2.5)$$

Lemma 2.5 *([16]) $A = (a_{nk}) \in (cs: c)$ if and only if the following condition holds:* $\forall k \in \mathbb{N}$
$$\lim_k a_{nk} \text{ is exist.} \quad (2.6)$$

Lemma 2.6 *([16]) $A = (a_{nk}) \in (bs: c)$ if and only if the following condition holds:* $\forall k \in \mathbb{N}$
$$\sum_k |a_{nk} - a_{n,k-1}| \text{ is convergent.} \quad (2.7)$$

Lemma 2.7 *([16]) $A = (a_{nk}) \in (cs_0: l_\infty)$ if and only if the condition that is given in (2.4) is satisfied.*

Lemma 2.8 *([16]) $A = (a_{nk}) \in (cs_0: l_\infty)$ if and only if*
$$\sup_n \sum_k |a_{nk} - a_{n,k-1}| < \infty. \quad (2.8)$$

Lemma 2.9 *([16]) $A = (a_{nk}) \in (bs: l_\infty)$ if and only if the conditions of (2.3) and (2.4) are satisfied.*

Lemma 2.10 *([16]) $A = (a_{nk}) \in (cs_0: l_p)$ if and only if*
$$\sup_k \sum_n \left| \sum_{k \in K} (a_{nk} - a_{n,k+1}) \right|^p < \infty \quad (2.9)$$
for $1 < p < \infty$.

Lemma 2.11 *([16])* $A = (a_{nk}) \in (cs : l_p)$ *if and only if*

$$\sup_k \sum_n \left| \sum_{k \in K} (a_{nk} - a_{n,k-1}) \right|^p < \infty \qquad (2.10)$$

for $1 < p < \infty$.

Lemma 2.12 $A = (a_{nk}) \in (bs : l_p)$ *if and only if the conditions of (2.3) and (2.9) are satisfied.*

3. DIFFERENCE SEQUENCE SPACES

In this section, we will define the sequence spaces $cs_0^\lambda(\Delta), cs^\lambda(\Delta)$ and $bs^\lambda(\Delta)$, then we will show that these spaces are BK-spaces. In addition, we will calculate the Schauder bases of $cs_0^\lambda(\Delta), cs^\lambda(\Delta)$ spaces and obtain the duals of $cs_0^\lambda(\Delta), cs^\lambda(\Delta)$ and $bs^\lambda(\Delta)$.

Definition 2 *([3]) Suppose that $\Delta x = (a_k - a_{k+1})$ for any sequence $x \in w$. Assume that X is any sequnce space, the difference sequence spaces can be defined as:*

$$\Delta x = \{x = (x_k) \in w : \Delta x \in X\}.$$

In [17], Mursaleen ve Noman have defined the spaces c_0^λ, c^λ and l_∞^λ by using the domain of $\wedge = (\lambda_{nk})$ for $\forall n, k \in N$

$$\lambda_{nk} = \begin{cases} \frac{\lambda_k - \lambda_{k-1}}{\lambda_n}, & 0 \leqslant k \leqslant n, \\ 0, & k > n, \end{cases} \qquad (3.1)$$

on c_0, c and l_∞ where $\lambda = (\lambda_k)$ is an increasing sequence with the following assumptions:

$$0 < \lambda_0 < \lambda_1 < \lambda_2 \dots , \text{ve} \lim_{k \to \infty} \lambda_k = \infty$$

Then, in [4], the authors established the following sequence spaces as follows:

$$cs^\lambda = \left\{ x = (x_k) \in w : \lim_{m \to \infty} \sum_{n=0}^{m} \frac{1}{\lambda_n} \sum_{k=0}^{n} (\lambda_k - \lambda_{k-1}) x_k, exist \right\},$$

$$cs_0^\lambda = \left\{ x = (x_k) \in w : \lim_{m \to \infty} \sum_{n=0}^{m} \frac{1}{\lambda_n} \sum_{k=0}^{n} (\lambda_k - \lambda_{k-1}) x_k = 0 \right\},$$

$$bs^\lambda = \left\{ x = (x_k) \in w : \sup_m \left| \sum_{n=0}^{m} \frac{1}{\lambda_n} \sum_{k=0}^{n} (\lambda_k - \lambda_{k-1}) x_k \right| < \infty \right\}$$

by using the domain of $\wedge = (\lambda_{nk})$ on cs, cs_0 and bs.

Now, it is time to define the difference sequence spaces of $cs_0^\lambda(\Delta), cs^\lambda(\Delta)$ and $bs^\lambda(\Delta)$ by using the sequence spaces cs_0^λ, cs^λ and bs^λ with matrix transformations:

$$cs_0^\lambda(\Delta) = \left\{ x = (x_k) : \lim_{m \to \infty} \sum_{n=0}^{m} \frac{1}{\lambda_n} \sum_{k=0}^{n} (\lambda_k - \lambda_{k-1})(x_k - x_{k-1}) = 0 \right\},$$

$$cs^\lambda(\Delta) = \left\{ x = (x_k) : \lim_{m \to \infty} \sum_{n=0}^{m} \frac{1}{\lambda_n} \sum_{k=0}^{n} (\lambda_k - \lambda_{k-1})(x_k - x_{k-1}) \, exist \right\},$$

$$bs^\lambda(\Delta) = \left\{ x = (x_k) : \sup_m \left| \sum_{n=0}^{m} \frac{1}{\lambda_n} \sum_{k=0}^{n} (\lambda_k - \lambda_{k-1})(x_k - x_{k-1}) \right| < \infty \right\}.$$

Let us define a new matrix as for $n, k \in N$:

$$\bar{\lambda}_{nk} = \begin{cases} \dfrac{(\lambda_k - \lambda_{k-1}) - (\lambda_{k+1} - \lambda_k)}{\lambda_n}, & k < n, \\[2mm] \dfrac{\lambda_n - \lambda_{n-1}}{\lambda_n}, & k = n, \\[2mm] 0, & k > n, \end{cases}$$

that is obtained by multiplying $\wedge = (\lambda_{nk})$ and difference matrix.

Here, we can consider these new difference sequence spaces as the domain of $\bar{\wedge} = (\bar{\lambda}_{nk})$ on the sequence spaces, namely: $cs_0^\lambda(\Delta) = (cs_0)_{\bar{\wedge}}, \; cs^\lambda(\Delta) = (cs)_{\bar{\wedge}}, \; bs^\lambda(\Delta) = (bs)_{\bar{\wedge}}$.

$$(\bar{\wedge} x)_n = \frac{1}{\lambda_n} \sum_{k=0}^{n} (\lambda_k - \lambda_{k-1})(x_k - x_{k-1}). \qquad (3.2)$$

Theorem 3.1 *The spaces $cs_0^\lambda(\Delta), cs^\lambda(\Delta)$ and $bs^\lambda(\Delta)$ are linear spaces. Besides, the spaces are BK$-$spaces with the following norm:*

$$\|x\|_{bs^\lambda(\Delta)} = \|\bar{\wedge} x\|_{bs} = \sup_m \left| \sum_{n=0}^{m} (\bar{\wedge} x)_n \right|.$$

Proof. Firstly, we will prove that $cs_0^\lambda(\Delta)$ is a linear space. For $x, y \in cs_0^\lambda(\Delta)$ and α, β scalars, we will show that $\alpha x + \beta y \in cs_0^\lambda(\Delta)$. Let us consider

$$cs_0^\lambda(\Delta) = \{x = (x_k) \in w : \bar{\wedge} x \in cs_0\}$$

and $\bar{\wedge} x, \; \bar{\wedge} y \in cs_0$. For all $m \in N$, we can write

$$\sum_{n=0}^{m} \bar{\wedge}_n (\alpha x + \beta y)$$

$$= \sum_{n=0}^{m} \frac{1}{\lambda_n} \sum_{k=0}^{n} (\lambda_k - \lambda_{k-1})(\alpha x_k + \beta y_k - \alpha x_{k-1} - \beta y_{k-1})$$

$$= \alpha \sum_{n=0}^{m} \frac{1}{\lambda_n} \sum_{k=0}^{n} (\lambda_k - \lambda_{k-1})(x_k - x_{k-1})$$

$$+ \beta \sum_{n=0}^{m} \frac{1}{\lambda_n} \sum_{k=0}^{n} (\lambda_k - \lambda_{k-1})(y_k - y_{k-1})$$

$$= \alpha \sum_{n=0}^{m} \bar{\wedge}_n (x) + \beta \sum_{n=0}^{m} \bar{\wedge}_n (y).$$

If we set $m \to \infty$ in the last step, we have

$$\lim_{m \to \infty} \sum_{n=0}^{m} \bar{\wedge}_n (\alpha x + \beta y) = 0.$$

Then, we obtain $\bar{\wedge} (\alpha x + \beta y) \in cs_0$, namely $\alpha x + \beta y \in cs_0^\lambda(\Delta)$. This implies that $cs_0^\lambda(\Delta)$ is alinear space. By a similar argument, one can show that $cs^\lambda(\Delta)$ is a linear space. We omit the details. It is clear to show that $bs^\lambda(\Delta)$ is a linear space as following:

$$\sup_m \left| \sum_{n=0}^{m} \bar{\wedge}_n (\alpha x + \beta y) \right|$$

118

$$= \sup_m \left| \sum_{n=0}^m \frac{1}{\lambda_n} \sum_{k=0}^n (\lambda_k - \lambda_{k-1})(\alpha x_k + \beta y_k - \alpha x_{k-1} \right.$$
$$\left. - \beta y_{k-1}) \right|$$

$$\leqslant |\alpha| \sup_m \left| \sum_{n=0}^m \frac{1}{\lambda_n} \sum_{k=0}^n (\lambda_k - \lambda_{k-1})(x_k - x_{k-1}) \right|$$
$$+ |\beta| \sup_m \left| \sum_{n=0}^m \frac{1}{\lambda_n} \sum_{k=0}^n (\lambda_k - \lambda_{k-1})(y_k - x_{yk-1}) \right|$$
$$= |\alpha| \sup_m \left| \sum_{n=0}^m \bar{\lambda}_n(x) \right| + |\beta| \sup_m \left| \sum_{n=0}^m \bar{\lambda}_n(y) \right|$$

for $x, y \in bs^\lambda(\Delta)$ and α, β scalars. Then, from the definition of $bs^\lambda(\Delta)$, we can write $\bar{\lambda} x, \bar{\lambda} y \in bs$. Therefore, for $\bar{\lambda} x, \bar{\lambda} y \in bs$, we provide

$$\sup_m \left| \sum_{n=0}^m \bar{\lambda}_n(\alpha x + \beta y) \right| < \infty.$$

This completes the proof. Also, one can say that these spaces are $BK-$spaces.

Theorem 3.2 *The sequence spaces $cs_0^\lambda(\Delta), cs^\lambda(\Delta)$ and $bs^\lambda(\Delta)$ are isometrically isomorphic to the sequence spaces cs_0, cs and bs, respectively, namely $cs_0^\lambda(\Delta) \cong cs_0, \ cs^\lambda(\Delta) \cong cs$ and $bs^\lambda(\Delta) \cong bs$.*

Proof. Assume that $X = \{cs, cs_0, bs\}$ and $X^\lambda(\Delta) = \{cs^\lambda(\Delta), cs_0^\lambda(\Delta), bs^\lambda(\Delta)\}$. To prove the result, we must show the existence of linear, injective and surjective mapping as:

$$T: X^\lambda(\Delta) \to X$$
$$x \to T(x) = \bar{\lambda}(x) = y.$$

For $x = (x_j), u = (u_j) \in X^\lambda(\Delta)$ and α, β scalars, we cam write

$$T(\alpha x + \beta u) = \bar{\lambda}(\alpha x + \beta u)$$
$$= \alpha \bar{\lambda}(x) + \beta \bar{\lambda}(u)$$
$$= \alpha T(x) + \beta T(u).$$

Then, T is linear.

Let we prove that T is injective. We must prove that if $Tx = \theta$, then $x = \theta$. If we assume that $Tx = \theta$, then we have

$$k = 0, x_0 = 0,$$
$$k = 1, x_1 = 0,$$
$$\vdots$$
$$k = n, x_n = 0.$$

This implies that $x = \theta$.

Let us consider $y = (y_k) \in X$ and the sequence $x = (x_k(\Delta))$ is defined as:

$$x_k(\Delta) := \sum_{j=0}^k \sum_{i=j-1}^j (-1)^{j-i} \frac{\lambda_i}{\lambda_j - \lambda_{j-1}} y_i; \ (k \in N). \quad (3.3)$$

Then, for $\forall k \in N$, we have

$$x_k(\Delta) - x_{k-1}(\Delta) = \sum_{i=k-1}^k (-1)^{k-i} \frac{\lambda_i}{\lambda_k - \lambda_{k-1}} y_i.$$

By using (3.2), for $\forall n \in \mathbb{N}$, we get

$$(\bar{\lambda} x)_n = \frac{1}{\lambda_n} \sum_{k=0}^n (\lambda_k - \lambda_{k-1})(x_k - x_{k-1})$$
$$= \frac{1}{\lambda_n} \sum_{k=0}^n \sum_{i=k-1}^k (-1)^{k-i} \lambda_i y_i = y_n$$

Therefore, we obtain $\bar{\lambda} x = y$. Since $y = (y_k) \in X$ we provide $\bar{\lambda} x \in X$. T is surjective. Finally, by using

$$\|Tx\|_{bs} = \|y(\lambda)\|_{bs} = \|\bar{\lambda} x\|_{bs} = \|x\|_{bs^\lambda(\Delta)}$$

we conclude that T is a linear, bijective and surjective mapping.

The Schauder basis of $cs_0^\lambda(\Delta)$ ve $cs^\lambda(\Delta)$ will be presented in the following result.

Remark 1 *Suppose that $\alpha_k(\lambda) = (\bar{\lambda} x)_k$ for $\forall k \in N$. Let us define the sequence $b^{(k)}(\lambda) = \left\{ b_n^{(k)}(\lambda) \right\}_{n=0}^\infty$ as*

$$b_n^{(k)}(\lambda) = \begin{cases} 0, & n < k, \\ \dfrac{\lambda_k}{\lambda_k - \lambda_{k-1}}, & n = k, \\ \dfrac{\lambda_k}{\lambda_k - \lambda_{k-1}} - \dfrac{\lambda_k}{\lambda_{k+1} - \lambda}, & n > k, \end{cases}$$

for $k \in N$. In this case, the sequence $\left\{ b^{(k)}(\lambda) \right\}_{k=0}^\infty$ is the Schauder basis of the spaces $cs_0^\lambda(\Delta)$ and $cs^\lambda(\Delta)$. Thus, $\forall x \in cs_0^\lambda(\Delta)$ or the sequence $cs^\lambda(\Delta)$ has a unique form as follows:

$$x = \sum_k a_k(\lambda) b^{(k)}(\lambda).$$

4. THE INCLUSION RELATIONS

In this section, we will present some inclusion relations of the spaces $cs_0^\lambda(\Delta), cs^\lambda(\Delta)$ and $bs^\lambda(\Delta)$.

Theorem 4.1 *The inclusion relations hold as*
$$cs_0^\lambda(\Delta) \subset cs^\lambda(\Delta) \subset bs^\lambda(\Delta).$$

Proof. It is obvious that $cs_0^\lambda(\Delta) \subset cs^\lambda(\Delta) \subset bs^\lambda(\Delta)$. To prove the sharpness of these inclusion relations, let us consider the following sequence:

$$x_k = \sum_{i=0}^k \frac{\frac{1}{(i+2)(i+3)} \lambda_i - \frac{1}{(i+1)(i+2)} \lambda_{i-1}}{\lambda_i - \lambda_{i-1}}, \quad (\forall k \in \mathbb{N}).$$

For $n \in \mathbb{N}$, we can write

$$(\bar{\Lambda} x)_n = \frac{1}{\lambda_n} \sum_{k=0}^n (\lambda_k - \lambda_{k-1})(x_k - x_{k-1})$$
$$= \frac{1}{\lambda_n} \sum_{k=0}^n \left(\frac{1}{(k+2)(k+3)} \lambda_k - \frac{1}{(k+1)(k+2)} \lambda_{k-1} \right)$$
$$= \frac{1}{(n+2)(n+3)}.$$

Then, for $m \in \mathbb{N}$, we have

$$\sum_{n=0}^m (\bar{\Lambda} x)_n = \frac{1}{2} - \frac{1}{m+3}.$$

If we set $m \to \infty$, we get

$$\sum_{n=0}^\infty (\bar{\Lambda} x)_n = \frac{1}{2}.$$

This shows that $\bar{\Lambda} x \in cs, \ cs_0$. We conclude that $cs_0^\lambda(\Delta) \subset cs^\lambda(\Delta)$ is sharp.

Now, to show the sharpness of the inclusion $cs^\lambda(\Delta) \subset bs^\lambda(\Delta)$, we can write

$$y_k = \sum_{i=0}^k (-1)^i \left(\frac{\lambda_i + \lambda_{i-1}}{\lambda_i - \lambda_{i-1}} \right), \quad (\forall k \in \mathbb{N}).$$

For all $n \in \mathbb{N}$, we have

$$\sum_{n=0}^{m} (\overline{\Lambda}y)_n = \sum_{n=0}^{m} \frac{1}{\lambda_n} \sum_{k=0}^{n} (-1)^k (\lambda_k + \lambda_{k-1})$$

$$= \sum_{n=0}^{m} (-1)^n.$$

Then, $\overline{\Lambda}y \in bs, cs$. This implies that $cs^\lambda(\Delta) \subset bs^\lambda(\Delta)$ is sharp.

Theorem 4.2 *The inclusion $cs^\lambda(\Delta) \subset c_0^\lambda(\Delta)$ is sharp.*

Proof. Since, we know that when $x \in cs^\lambda(\Delta)$, $\overline{\Lambda}x \in cs$ therefore $\overline{\Lambda}x \in c_0$. The inclusion $cs^\lambda(\Delta) \subset c_0^\lambda(\Delta)$ is valid.

To demonsrate the sharpness of the inclusion relation, we define the sequence as

$$x_k = \sum_{i=0}^{k} \frac{1}{i+1}; \qquad (k \in \mathbb{N}).$$

Therefore, we have

$$\Delta x = (x_k - x_{k-1}) = \left(\frac{1}{k+1}\right) \in c_0$$

and $\Delta x \in c_0^\lambda$. This implies that $x \in c_0^\lambda(\Delta)$.

For all $n \in \mathbb{N}$, we get

$$(\overline{\Lambda}x)_n = \frac{1}{\lambda_n} \sum_{k=0}^{n} \frac{\lambda_k - \lambda_{k-1}}{k+1}$$

$$\geqslant \frac{1}{\lambda_n(n+1)} \sum_{k=0}^{n} (\lambda_k - \lambda_{k-1})$$

$$= \frac{1}{n+1}.$$

Then, $\overline{\Lambda}x \notin cs$ and so $x \notin cs^\lambda(\Delta)$. Since x belongs to $c_0^\lambda(\Delta)$ spaces but not to $cs^\lambda(\Delta)$, we can write $cs^\lambda(\Delta) \subset c_0^\lambda(\Delta)$.

5. DUAL SPACES

In this section, we will determine the $\alpha-, \beta-$ and $\gamma-$ duals of the sequence spaces $cs_0^\lambda(\Delta), cs^\lambda(\Delta)$ and $bs^\lambda(\Delta)$.

Theorem 5.1 *For $n, k \in \mathbb{N}$ the matrix $B^\lambda = (b_{nk}^\lambda)$ can be defined as*

$$b_{nk}^\lambda = \begin{cases} \left(\frac{\lambda_k}{\lambda_k - \lambda_{k-1}} - \frac{\lambda_k}{\lambda_{k+1} - \lambda_k}\right) a_n, & k < n, \\ \frac{\lambda_n}{\lambda_n - \lambda_{n-1}} a_n, & k = n, \\ 0, & k > n. \end{cases}$$

Then, we have $\{cs_0^\lambda(\Delta)\}^\alpha = \{bs^\lambda(\Delta)\}^\alpha = f_1^\lambda$ and $\{cs^\lambda(\Delta)\}^\alpha = f_2^\lambda$ where

$$f_1^\lambda = \left\{ a = (a_n) \in w: \sup_{N,K\in\mathcal{F}} \left|\sum_{n\in N} \sum_{k\in K} (b_{nk}^\lambda - b_{n,k+1}^\lambda)\right| < \infty \right\} \tag{5.1}$$

and

$$f_2^\lambda = \left\{ a = (a_n) \in w: \sup_{N,K\in\mathcal{F}} \left|\sum_{n\in N} \sum_{k\in K} (b_{nk}^\lambda - b_{n,k-1}^\lambda)\right| < \infty \right\}. \tag{5.2}$$

Proof. Let $a = (a_n) \in w$. Then, by using the relation (3.3) we have

$$a_n x_n = \sum_{k=0}^{n} \sum_{j=k-1}^{k} (-1)^{k-j} \frac{\lambda_j}{\lambda_k - \lambda_{k-1}} a_n y_j$$

$$= \sum_{k=0}^{n} \left(\frac{\lambda_k}{\lambda_k - \lambda_{k-1}} y_k - \frac{\lambda_{k-1}}{\lambda_k - \lambda_{k-1}} y_{k-1}\right) a_n$$

$$= \sum_{k=0}^{n-1} \left(\frac{\lambda_k}{\lambda_k - \lambda_{k-1}} - \frac{\lambda_k}{\lambda_{k+1} - \lambda_k}\right) y_k a_n + \frac{\lambda_n}{\lambda_n - \lambda_{n-1}} y_n a_n$$

$$= (B^\lambda y). \tag{5.3}$$

Thus, by the equation (5.3) when $x = (x_k) \in cs_0^\lambda(\Delta)$, $ax = (a_n x_n) \in \ell_1$ if and only if $y = (y_k) \in cs_0$ with $B^\lambda y \in \ell_1$. Namely, $a = (a_n) \in \{cs_0^\lambda(\Delta)\}^\alpha$ if and only if $B^\lambda \in (cs_0: \ell_1)$. By using Lemma 2.1, with the matrix B^λ instead of A, we show that $a = (a_n) \in \{cs_0^\lambda(\Delta)\}^\alpha$ if and only if

$$\sup_{N,K\in\mathcal{F}} \left|\sum_{n\in N} \sum_{k\in K} (b_{nk}^\lambda - b_{n,k+1}^\lambda)\right| < \infty. \tag{5.4}$$

Indeed for all $n \in \mathbb{N}$, if we have

$$\lim_k b_{nk}^\lambda = 0$$

then the condition of Lemma 2.3 holds. This implies that $\{cs_0^\lambda(\Delta)\}^\alpha = \{bs^\lambda(\Delta)\}^\alpha = f_1^\lambda$.

Similarly, by using the equation (5.3) it is obvious that $a = (a_n) \in \{cs^\lambda(\Delta)\}^\alpha$ if and only if $B^\lambda \in (cs: \ell_1)$. Consequently, if we set the matrix B^λ instead of the matrix A in Lemma 2.2, $a = (a_n) \in \{cs^\lambda(\Delta)\}^\alpha$ if and only if

$$\sup_{N,K\in\mathcal{F}} \left|\sum_{n\in N} \sum_{k\in K} (b_{nk}^\lambda - b_{n,k-1}^\lambda)\right| < \infty. \tag{5.5}$$

Thus, we provide $\{cs^\lambda(\Delta)\}^\alpha = f_2^\lambda$. This completes the proof.

Theorem 5.2 *For all $k \in \mathbb{N}$ and*

$$\overline{a}_k(n) = \lambda_k \left[\frac{a_k}{\lambda_k - \lambda_{k-1}} + \left(\frac{1}{\lambda_k - \lambda_{k-1}} - \frac{1}{\lambda_{k+1} - \lambda_k}\right) \sum_{j=k+1}^{n} a_j \right]$$

$$(k < n),$$

let us define the sets of $f_3^\lambda, f_4^\lambda, f_5^\lambda, f_6^\lambda, f_7^\lambda$ and f_8^λ as follows

$$f_3^\lambda = \left\{ a = (a_k) \in w: \sup_n \sum_{k=0}^{n-2} |\overline{a}_k(n) - \overline{a}_{k+1}(n)| < \infty \right\},$$

$$f_4^\lambda = \left\{ a = (a_k) \in w: \sup_k \left|\frac{\lambda_k}{\lambda_k - \lambda_{k-1}} a_k\right| < \infty \right\},$$

$$f_5^\lambda = \left\{ a = (a_k) \in w: \lim_{n\to\infty} (\overline{a}_k(n) - \overline{a}_{k+1}(n)) \text{ exist } (k \in \mathbb{N}) \right\},$$

$$f_6^\lambda = \left\{ a = (a_k) \in w: \sum_{j=k}^{\infty} a_j \text{ exist } (k \in \mathbb{N}) \right\},$$

$$f_7^\lambda = \left\{ a = (a_k) \in w: \sum_{k=0}^{\infty} |\overline{a}_k(n) - \overline{a}_{k+1}(n)| \text{ convergent} \right\},$$

$$f_8^\lambda = \left\{ a = (a_k) \in w: \lim_{k\to\infty} \left(\frac{\lambda_k}{\lambda_k - \lambda_{k-1}} a_k\right) \text{ convergent} \right\}.$$

Then, we have $\{cs_0^\lambda(\Delta)\}^\beta = f_3^\lambda \cap f_4^\lambda \cap f_5^\lambda, \{cs^\lambda(\Delta)\}^\beta = f_3^\lambda \cap f_4^\lambda \cap f_6^\lambda$ and $\{bs^\lambda(\Delta)\}^\beta = f_6^\lambda \cap f_7^\lambda \cap f_8^\lambda$.

Proof. Assume that $a = (a_k) \in w$ be a sequence and for all $n, k \in \mathbb{N}$ the matrix $T^\lambda = (t_{nk}^\lambda)$ is given as

$$(t_{nk}^\lambda) = \begin{cases} \bar{a}_k(n) & k < n, \\ \dfrac{\lambda_n}{\lambda_n - \lambda_{n-1}} a_n & k = n, \\ 0 & k > n. \end{cases}$$

Then, we consider

$$\sum_{k=0}^{n} a_k x_k = \sum_{k=0}^{n} \left[\sum_{j=0}^{k} \sum_{i=j-1}^{j} (-1)^{j-i} \frac{\lambda_i}{\lambda_j - \lambda_{j-1}} y_i \right] a_k$$

$$= \sum_{k=0}^{n-1} \lambda_k \left[\frac{a_k}{\lambda_k - \lambda_{k-1}} \right.$$

$$+ \left(\frac{1}{\lambda_k - \lambda_{k-1}} \right.$$

$$\left. - \frac{1}{\lambda_{k+1} - \lambda_k} \right) \sum_{j=k+1}^{n} a_j \Bigg] y_k$$

$$+ \frac{\lambda_n}{\lambda_n - \lambda_{n-1}} a_n y_n$$

$$= \sum_{k=0}^{n-1} \bar{a}_k(n) y_k + \frac{\lambda_n}{\lambda_n - \lambda_{n-1}} a_n y_n$$

$$= (T^\lambda y)_n; \qquad (n \in \mathbb{N}). \qquad (5.6)$$

From the equation (5.6) when $x = (x_k) \in cs_0^\lambda(\Delta)$, $ax = (a_n x_n) \in cs$ if and only if when $y = (y_k) \in cs_0$, $T^\lambda y \in c$. Namely, $a = (a_n) \in \{cs_0^\lambda(\Delta)\}^\beta$ if and only if $T^\lambda \in (cs_0 : c)$. Thus, from Lemma 2.4, we have

$$\sup_n \sum_{k=0}^{n-2} |\bar{a}_k(n) - \bar{a}_{k+1}(n)| < \infty, \qquad (5.7)$$

$$\sup_n \left| \frac{\lambda_n}{\lambda_n - \lambda_{n-1}} a_n \right| < \infty \qquad (5.8)$$

and we get

$$\lim_{n \to \infty} (\bar{a}_k(n) - \bar{a}_{k+1}(n)) \quad \text{(there exist for } k \in \mathbb{N}). \quad (5.9)$$

Then, $\{cs_0^\lambda(\Delta)\}^\beta = f_3^\lambda \cap f_4^\lambda \cap f_5^\lambda$.

Similarly, from the equation of (5.6), $a = (a_n) \in \{cs^\lambda(\Delta)\}^\beta$ if and only if $T^\lambda \in (cs : c)$. Then, we get (5.7) and (5.8) from Lemma 2.5. From the condition (2.6), we have

$$\sum_{j=k}^{\infty} a_j \text{ there exist for all } (k \in \mathbb{N}). \qquad (5.10)$$

This implies that $\{cs_0^\lambda(\Delta)\}^\beta = f_3^\lambda \cap f_4^\lambda \cap f_6^\lambda$.

Finally, from the equation (5.6) $a = (a_n) \in \{bs^\lambda(\Delta)\}^\beta$ if and only if $T^\lambda \in (bs : c)$. Then for all $n \in \mathbb{N}$, since

$$\lim_{k \to \infty} t_{nk}^\lambda = 0$$

the condition that is given in Lemma 2.6 holds. Also, by the condition (2.6) we can see that (5.10) is valid. From (2.7), we can write

$$\sum_{k=0}^{\infty} |\bar{a}_k(n) - \bar{a}_{k+1}(n)| \text{ convergent,} \quad (5.11)$$

$$\lim_{k \to \infty} \left(\frac{\lambda_n}{\lambda_n - \lambda_{n-1}} a_n \right) \text{ exist.} \qquad (5.12)$$

We conclude that $\{bs^\lambda(\Delta)\}^\beta = f_6^\lambda \cap f_7^\lambda \cap f_8^\lambda$.

6. CONCLUSION

As a result, we defined non-absolute type difference sequence spaces $cs_0^\lambda(\Delta)$, $cs^\lambda(\Delta)$ and $bs^\lambda(\Delta)$ based on the definitions of cs_0^λ, cs^λ and bs^λ sequence spaces defined by Kaya and Furkan in 2015, and the difference

sequence space defined by Kızmaz (1981), and show that the difference sequence spaces $cs_0^\lambda(\Delta)$, $cs^\lambda(\Delta)$ and $bs^\lambda(\Delta)$ are BK-spaces. Additionally, it is defined that these spaces are isomorphic to the spaces, cs_0, cs and bs respectively, and their Schauder basis are given. Also, the classes of matrix transformations from the spaces, $cs_0^\lambda(\Delta)$, $cs^\lambda(\Delta)$ and $bs^\lambda(\Delta)$ to the spaces l_∞, c and c_0 are characterized, where $1 \leq p \leq \infty$. Finally, some inclusion relations are examined and the $\alpha -$, $\beta -$ and $\gamma -$duals of these sequence spaces are calculated. This article provides a significant contribution to the field of functional analysis and topology by establishing that the sequence spaces $cs_0^\lambda(\Delta)$, $cs^\lambda(\Delta)$ and $bs^\lambda(\Delta)$ are BK spaces. The implications of this result extend to applied sciences and topology, offering a new perspective on sequence space theory and its practical applications. This work opens new avenues for studying topological sequence spaces and their properties, with potential applications in diverse fields.

REFERENCES

[1] Ng PN, Lee PY. Cesaro sequence spaces of non-absolute type. Commentationes Mathematicae Prace Matematyczne. 1978; 20(2): 429-433.

[2] Wang CS. On Nörlund sequence spaces. Tamkang Journal of Mathematics. 1978; 9(2): 269-274.

[3] Kızmaz H. On Certain Sequence Spaces. Canadian Mathematical Bulletin. 1981; 24(2): 169-76.

[4] Kaya M, Furkan H. Some Topological and Geometric Properties of Some New Spaces of λ-Convergent and Bounded Series. Journal of Function Spaces. 2015; 1-10.

[5] Et M. On Some Difference Sequence Spaces. Turkish Journal of Mathematics. 1993; 17: 18-24.

[6] Et M, Çolak R. On Some Generalized Difference Sequence Spaces. Soochow Journal of Mathematics. 1995; 21: 377-386.

[7] Et M, Esi A. On Köthe-Toeplitz Duals of Generalized Difference Sequence Spaces. Bulletin of the Malaysian Mathematical Sciences Society. 2000; 23: 25-32.

[8] Maddox IJ. Elements of functional analysis. Cambridge University Press Cambridge. 1970; 1-246.

[9] Başar F. Summability Theory and Its Applications. Bentham Science Publishers Istanbul; 2011.

[10] Kreyszig E. Introductory Functional Analysis with Applications. John Wiley and Sons New York; 1978.

[11] Kantorovich LV, Akilov GP. Functional Analysis in Normed Spaces. Pergamon Press Oxford; 1982.

[12] Wilansky A. Summability through Functional Analysis. Mathematics Studies Amsterdam; 1984.

[13] Malkowsky E, Pawan K.J. Sequence Spaces and Applications. Narosa Publishing House New Delhi India; 1999.

[14] Boos J. Classical and Modern Method in Summability. Oxford University Press; 2000.

[15] Garling DJH. The $\beta-$ and $\alpha-$ Duality of Sequence Spaces. Proceedings – Cambridge Philosophical Society 1967; 63: 963-981.

[16] Stieglitz M, Tietz H. Matrix transformationen von Folgenraumen Eine Ergebnisubersict. Math. Z. 1977; 154: 1-16.

[17] Mursaleen M, Noman AK. On the Spaces of $\lambda-$ Convergent and Bounded Sequences. Thai Journal of Mathematics. 2010; 8(2): 311–329.

[18] Mursaleen M, Noman AK. On some new difference sequence spaces of non-absolute type. Mathematical and Computer Modelling. 2010; 52: 603-617.